University of Nottingham
UK | CHINA | MALAYSIA

Department of Mechanical, Material and Manufacturing Engineering

Numerical Simulation of Novel Flow Control Strategies for a Vertical Stabiliser

Mahmud Jamil Muhammad

(MSc, BEng)

Thesis submitted to the University of Nottingham for the degree of Doctor of Philosophy.

March 2024

DECLARATION

I hereby declare that this thesis is entirely original and written by me. Any literature cited in this work that is not my own is appropriately acknowledged for academic integrity. To the best of my knowledge, this content has not been submitted for the award of a degree anywhere else. I confirm that this is my diligent work throughout my PhD journey.

Mahmud Jamil Muhammad

March 2024

ACKNOWLEDGEMENT

As I embarked on my Ph.D. journey, unforeseen challenges arose just a few months later with the onset of the COVID-19 pandemic. I am incredibly grateful for the unwavering financial support and guidance of my supervisor, Professor Kwing-So Choi, as I navigated this uncharted terrain. Additionally, Professor Xuerui Mao provided invaluable insights that significantly shaped my first year. I would also like to express my special thanks to Dr Yaxing Wang for his generosity in sharing knowledge.

I am deeply thankful to my wife, children, parents and colleagues, whose unwavering support and understanding have been my pillars of strength. Without their love and encouragement, this journey would not have been possible.

I sincerely thank the Petroleum Technology Development Fund (PTDF), my sponsors, for their invaluable support in funding my PhD research. Also, I express my appreciation and gratitude for the funding from the Clean Sky2 and Airbus EU-funded TailSurf project, which provided me with the experimental data and the model designs. I deeply appreciate all those mentioned above for their contributions to my Ph.D. pursuit, especially during these challenging times.

Mahmud Jamil Muhammad

March 2024

ABSTRACT

The flow control strategy is crucial in aerodynamics, especially in studying laminar to turbulent boundary layer separation. It also contributes to enhancing the side force coefficient and reduction of drag force coefficient. The vertical tailplane is a significant part of an aircraft's structure, providing directional control and stability. To improve the directional control and stability of the vertical tailplane, this project aims to investigate a new strategy of flow control devices using rudder-mounted slat and leading-edge undulation. The study numerically investigates the effect of separation using a Reynolds Number of 1.69×10^5.

The study compared various turbulence models and high-fidelity large eddy simulation (LES) for baseline with zero rudder deflection. The transition k-kl-ω model and LES produced better predictions, proving robustness in predicting transition-related flow. The experimental data is used to validate the turbulence models and LES results for drag and side force coefficients. The comparison shows that all turbulence models can accurately predict the side force and drag force coefficients when the flow is attached and at lower sideslip angles. In addition, the S-A turbulence model performed better than all the turbulence models except the transition k-kl-ω model in predicting the force coefficients.

Also, this study investigates the aerodynamic effect of a rudder-mounted slat on a vertical stabiliser. The numerical results showed that the side force coefficient increased by up to 4% while the drag coefficient was unchanged when the rudder deflection angle was set to $\delta = 30°$. LES results suggested that the rudder-mounted slat can increase the circulation around the vertical stabiliser, showing that the flow from the upstream recirculating regions was drawn towards the rudder surface. Associated changes in the turbulent flow field, including the mean and turbulent flow field and the vortical structure, are also presented to help understand the flow control mechanism by the rudder-mounted slat.

Lastly, the impact of the leading-edge undulation at rudder deflection δ = 30° and sideslip angle of β = 8°, which aimed to enhance aerodynamic performance and reduce separation, was investigated. The numerical results of the modified and baseline configurations were compared using velocity and streamlines at the lower, peak, and upper trough regions. These regions of the modified single bump were found to show additional flow attachment compared to the baseline. Notably improving aerodynamics around peaks and troughs, this design showcased enhanced aerodynamic performance and favourable flow characteristics on the vertical tailplane.

Table of Contents

LIST OF FIGURES

LIST OF TABLES

1. Chapter one

INTRODUCTION

1.1 Introduction

The vertical tailplane is part of the empennage structure of the aeroplane, which is made up of the stabiliser and the movable rudder (Fig.1.1). The role of the vertical tailplane is crucial in the design of an aeroplane because the vertical stabiliser provides directional stability. In contrast, the rudder is important in the control aspect. The conventional design of the vertical tailplane is complex from the design consideration because of the asymmetrical flow that exists from the wing and fuselage. The conventional design of the vertical tailplane affects the aeroplane's performance due to the downwash effect and interference that directly decreases the side force and increases the drag coefficient. The instability generated may lead to a rudder loss of control, which makes the aircraft difficult to control. The vertical tailplane experiences a separation region towards its trailing edge at higher sideslip and rudder deflection angles, impacting its performance.

The idea of flow control on aircraft started several decades ago. In 1964, the challenges of a fighter jet aircraft's interference, stability, and control were thoroughly investigated by McKinney et al. (1964). The knowledge of flow control in aircraft design is essential to understanding the transition from laminar to turbulent boundary layer, increase of side force and decrease of drag force coefficients. The critical instability of the transition between the laminar region and the turbulent boundary layer can dramatically affect the flow phenomenon. Aerodynamic flow control aims to modify the flow behaviour to improve performance. This can be achieved using active or passive control techniques such as plasma actuators and slats.

This study investigated two passive flow control techniques: leading-edge slat and single bump undulation. The slat is mounted at the rudder's leading edge, while the bioinspired undulation is implemented on the stabiliser's leading edge. This study's primary goal of flow control is to increase the side force coefficient and reduce the effect of separation onset of the flow from the laminar region to the turbulent boundary layer region using CFD and LES with wind tunnel experimental validation.

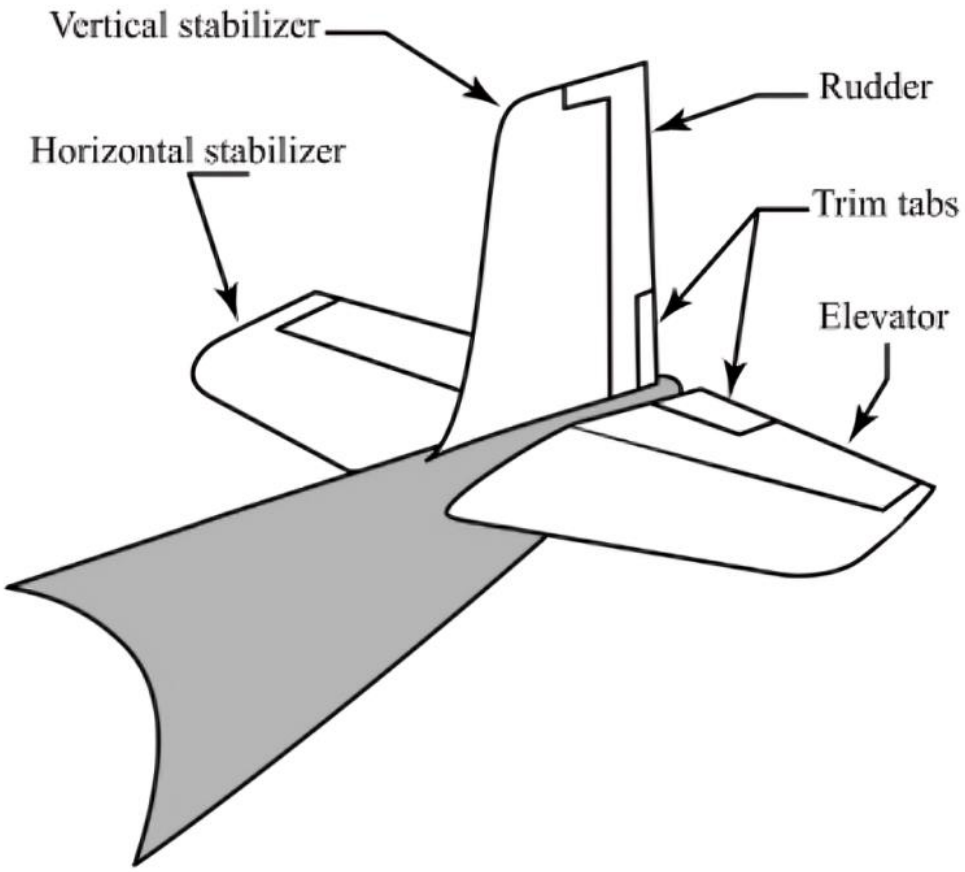

Fig. 1.1: A complete Empennage Structure (Ciliberti et al. 2017).

Flow control research has extensively investigated the impact of separation suppression. Multiple researchers have experimented with modifying the aerofoil's shape along the suction surface to combat the negative effects of the separation. These techniques have significantly improved the flow field by enhancing the aerodynamic force coefficients. Furthermore, passive and active devices have proven to be even more effective in mitigating the detrimental effects of separation caused by the formation of large vortices. The effectiveness of these methods suggests that flow control can play a vital role in enhancing the aerodynamic performance of aerofoils and, consequently, the overall efficiency of aircraft and other similar applications.

The aerospace industry cannot rely solely on the output from the wind tunnel experiment alone. The widely accepted experimental method adopted in the aerospace industry benchmark effectively utilises a wind tunnel setup. The discovery of CFD has found a breakthrough in the design and analysis of aerodynamic research (Rizzi and Luckring 2021). Hence, implementing CFD using different models has gained acceptance and confidence in aerodynamic research. Therefore, incorporating the operation of CFD codes with wind tunnel experiments is the most accurate and fast-growing aerodynamics research method (Schaeffler et al. 2010).

Computational Fluid Dynamics (CFD) employs numerical methods to investigate the airflow interaction with specific structural bodies. Modern aircraft design facilitates extensive research and innovative advancements in understanding the flow field around aircraft structures (Alonso et al. 2009). Harnessing the computational capabilities represents a breakthrough that addresses design challenges encountered in the engineering design process (Obayashi 1998; Hoburg and Abbeel 2014). Solving engineering design problems can be approached through theoretical, experimental, and numerical methods. Leveraging computational resources in the early stages of the design process ensures the verification and validation of results, contributing to a more robust final implementation of the design process.

Turbulence modelling is an important tool in the CFD method that aims to simulate complex flow behaviours. The models are crucial in many applications but limited in others. No universal turbulence model in CFD can be suited to all turbulence flows with the required accuracy. The common categories of turbulence modelling involve the Reynolds-averaged Navier-Stokes (RANS). The choice of the models and methods depends on the application, accuracy, computational cost, and experimental validation.

This study underlines the significance of employing high-fidelity simulation, particularly LES, to explore the prominent coherent structures around the vertical tailplane at larger deflection angles. The utilisation of LES offers enhanced flow field visualisation capabilities compared to the traditional CFD approaches because of its spatial resolution to capture smaller turbulent structures. Without full details of the flow physics from the

experimental data, the LES is considered an ideal method to highlight the actual features of the flow concerning the evolution and reduction of separation characteristics.

1.2 Objectives and the Thesis Structure

This project aims to use CFD to investigate the optimum flow control devices developed in the EU TailSurf project to understand the flow field associated with improved performance of the vertical tailplane (TailSurf 2019). Our focus in CFD will be a thorough analysis of the complex three-dimensional flow separation reduction and delay of the stall angle, which invariably enhances aerodynamic performance. To verify the effectiveness of these technologies, we will conduct a Reynolds-averaged Navier-Stokes equation (RANS) and large eddy simulation (LES) using High-performance computing (HPC).

We used different turbulence models to understand the flow characteristics around the vertical tailplane to achieve our goals. Then, we studied the passive flow control technique using a rudder-mounted slat to mitigate the effects of separation. Finally, we investigated the leading-edge undulation technique to suppress separation effects and delay the stall angle of the VTP. All the results obtained from the simulation were compared with the wind tunnel results for the same model at the same flow conditions and Reynolds number.

As far as we know, the study of vertical tailplanes with rudder-mounted slats has not been reported before. In addition, the single bump undulation inspired by the humpback whales is also a novel idea that bridges a gap in the leading-edge study. Both leading-edge modifications are considered to improve the aerodynamic performance, delay stall and separation effect.

The thesis comprises seven chapters, each contributing significantly to the study. Chapter 2 provides an in-depth review of past studies on vertical tailplane research, including a detailed investigation into the causes and control of flow separation and the effects of Kelvin-Helmholtz instability around an aerofoil. It also compares different control strategies based on their performance on aerodynamic efficiency. In Chapter 3, the methodology utilised in the study, including numerical model techniques, is reported. The chapter also presents the turbulence models used in the simulation. Chapter 4

describes the baseline validation of the turbulence models and large eddy simulations compared with experimental data. Chapter 5 focuses on implementing the rudder-mounted slat passive flow control technique on the VTP. Chapter 6 discusses the contribution of a leading-edge single bump undulation implementation on the VTP. Lastly, Chapter 7 summarises the findings and suggests recommendations for future studies.

1.3 Significance of Study

This study significantly contributes to knowledge by exploring and comparing the effectiveness of novel flow control devices on the vertical tailplane via numerical investigations. Specifically, the rudder-mounted slat and single bump undulation performance is evaluated compared to an unmodified baseline case. Notably, a unique design approach is employed, with a rudder-mounted slat applied at a 30% span from the tip side, expanding the understanding of slat functionality beyond traditional high-lift studies (Olson et al. 1979; Arra et al. 2021).

Moreover, the application of a bioinspired single bump undulation design, drawing inspiration from Humpback whale flipper-like structures, is explored, unlike previous research primarily focusing on rectangular wing shapes (Hansen et al. 2011). The few that used swept tapered wings reported a degradation in aerodynamic performance at the pre-stall angle (Bolzon et al. 2014). The effectiveness of the undulation design on a tapered vertical tailplane is investigated, demonstrating its potential for enhancing aerodynamic performance, particularly at pre-stall angles.

Significant benefits of single bump undulation are revealed in addressing challenges associated with separation and pre-stall angles, where previous undulation research has encountered limitations. Remarkably, visual insights into the flow patterns and skin friction lines are provided through numerical simulations using the large eddy simulation (LES) method, further validating the efficacy of these novel flow control strategies.

This study contributes novel insights into applying flow control devices on the vertical tailplane. It showcases their potential to enhance aerodynamic performance and addresses longstanding challenges. Through rigorous

numerical analysis, the understanding of innovative flow control techniques and their implications for aircraft design and performance optimisation is advanced.

2. Chapter two

LITERATURE REVIEW

A REVIEW OF COMPUTATIONAL AERODYNAMICS AND VERTICAL TAILPLANE

2.1 Introduction

This chapter reviews computational aerodynamics in modern aircraft design, focusing on vertical tailplane characteristics. Computational aerodynamics involves numerical methods to investigate the flow around an aerodynamic body. The vertical tailplane is an important component of the aircraft that contributes to the stability and control of the plane using the vertical stabiliser and rudder, respectively. The interference with the downwash generated by the fuselage and wing result in heightened instability and potential loss of control for the aircraft. The relationship between the downwash interference and the aerodynamic performance of the vertical tailplane is given in detail.

The selection of numerical methods holds great importance in computational aerodynamics. This study comprehensively examines and evaluates various turbulence models, specifically the widely used Reynolds averaged Navier-Stokes equations (RANS) and the Large Eddy Simulation (LES). Additionally, this research delves deeply into the limitations of the RANS approach in predicting separation. It highlights the importance of utilising high-fidelity methods that resolve large-scale eddies and model smaller eddies using subgrid scales. This leads to more accurate separation predictions compared to the RANS model.

Employing control devices that delay flow separation to improve aerodynamic performance is essential for aerospace industry applications. As a rule of thumb, the design of a control device should be economical and less complex to handle and maintain. As discussed in this section, the fundamental objective of aerodynamic flow control is to modify flow behaviour and enhance performance using active and passive control techniques. It is shown that different strategies played a role in controlling the separation and increasing overall aerodynamic performance.

2.2 Vertical Tailplane

The functions of the vertical and horizontal tails are almost similar; the interplay between them ensures smooth and safe flight. The vertical tail function is directional stability and control, while the horizontal tail function is longitudinal stability and control. The control forms of the vertical tail design originate from the rudder, while the horizontal tail originates from the elevator attachment. The design consideration of the two tails is closely related to each other and should be monitored for effectiveness and maximum efficiency.

As mentioned earlier, the vertical tailplane is crucial in controlling and stabilising an aircraft. The analysis of the vertical tailplane typically involves studying the interference effects between its surrounding components, such as the wing body and the horizontal wing of the aircraft (Ciliberti et al. 2017). Interference arises when there is interaction between the vertical tailplane and the plane's fuselage. The interference starts from the wing, which affected the tail's effective angle of attack. This effect leads to an instability of the vertical tailplane and a loss of control. Stability is an inevitable phenomenon experienced by aircraft during flight, and it can be managed and monitored under aviation flight standards (Airbus 2005).

However, the downwash effect influences the horizontal tail's design location. In Fig. 2.1, the region 1 is the safest for design consideration to avoid this interference, followed by the region 3, and the last one, the region 2, is not recommended. Hence, the freestream velocity is given by V_∞ while the main wing stall angle is α_s and the wing incidence is denoted by i_w. It is a general concept that lift, and drag are generated concurrently, but the drag's effect influences the maximum lift generated.

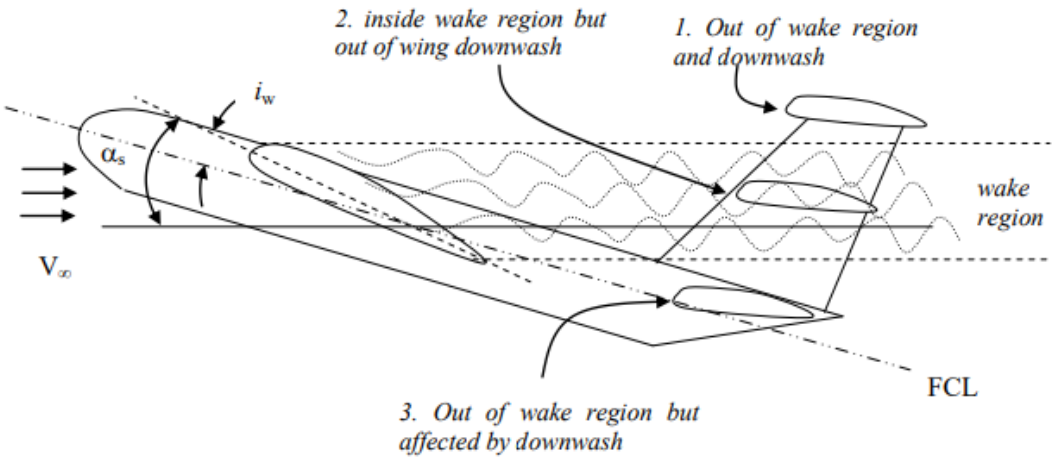

Fig. 2.1: An aerofoil section of the wing showing the effect of downwash (Sadraey 2012).

Moreover, the rudder deflection of the vertical tailplane determines the maximum design parameter for the vertical tailplane configurations. Due to its design, the rudder provides powerful directional control as a crucial control part of the tail. The effectiveness of the rudder design depends on selecting the appropriate chord of the root and tip side of the vertical tailplane (Nicolosi et al. 2012). The optimum performance of the vertical tailplane can be determined by selection and analysis of the rudder deflection and the sideslip angle. These parameters are used to ensure directional stability and aircraft control. Variations in rudder deflection and sideslip angles provide a baseline reference for evaluating the vertical tail's impact on aerodynamic performance. Fig 2.2 shows a complete parameter of the VTP and the detail of the profile of the aerofoil thickness is described in (Smith 2000; Qin et al. 2004). The directional stability, rudder, and sideslip angle have been reported to affect the directional stability and control of the aircraft. The parameters in Fig. 2.2 are described as follows:

C_t – tip chord

C_r – root chord

CP_{vt} – Centre of pressure

h – vertical stabilizer height

Λ_{LE} – leading-edge sweep angle

Λ_{TE} – trailing edge sweep angle

C_{rudder} – rudder chord

h_{MAC} – vertical stabiliser mean aerodynamic chord height.

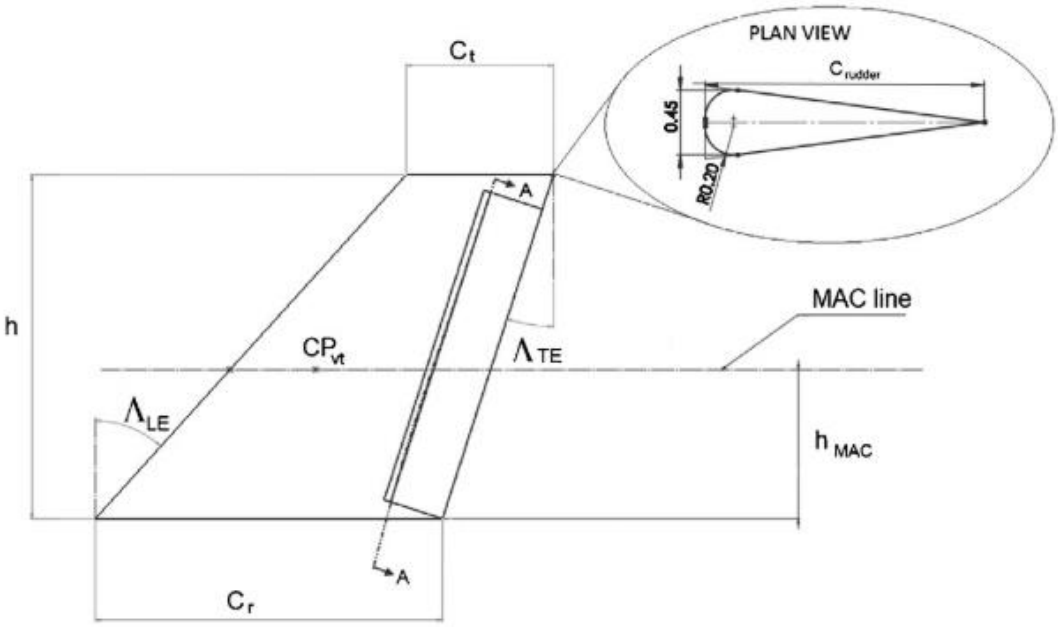

Fig. 2.2: A vertical tailplane design parameters with the stabiliser and rudder (Larkin and Coates 2017).

The vibration and instability of the system are caused by buffeting impact on the vertical tailplane. The vertical tailplane buffeting effect usually occurs at lower sideslip angles, generating a vortex around the vertical surface (Sheta and Huttsell 2003). Meanwhile, Lee (2000) argued that the buffeting effect on the vertical tail plane arises from a higher sideslip angle. Recently, Nguyen et al. (2019) proposed an electric propulsion distribution, which increases the aerodynamic performance by reducing the tail size.

A tail-wing structure was originally designed to provide the optimum control and stability to the aircraft. The appropriate shape and sizing of the vertical tail surface are still debated among researchers regarding which one offers the ideal aerodynamic efficiency (Monner et al. 2009). In a study by Tavakoli and Seif (2016), a mathematical model was created to analyse the

impact of wings on aerodynamics. The outer wing has a relatively minor impact on ground height, while the inner wing has a greater effect on aerodynamic characteristics in the ground effect. The model has been validated and shown to calculate lift and drag coefficients accurately. The impact of edge models and the possible attachment of some shapes are commonly used to improve aerodynamic performance (Sevant et al. 1998). These strategies enhanced the efficiency and overall performance of the aircraft (Rokhsaz 1993). Fig. 2.3 shows the plane's overall parameters with a detailed VTP design parameter.

Cg – Centre of gravity

ac_{wf} – wing-fuselage aerodynamic centre

ac_v – vertical tail aerodynamic centre

I_v – Distance between ac_{wf} and ac_v

I_{vt} – Tail arm

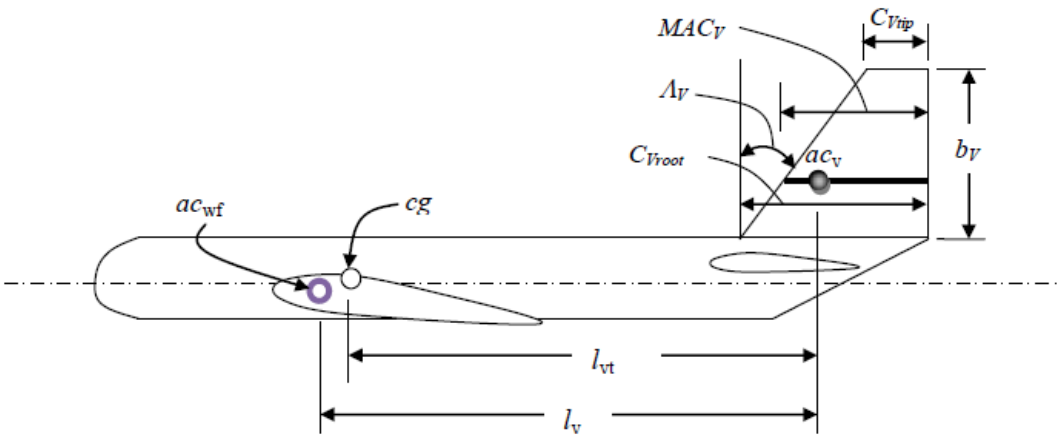

Fig. 2.3: A complete structure of the aircraft with the vertical tailplane parameters (Sadraey 2012).

Based on the parameters described above, the taper ratio of the vertical tailplane is defined as the ratio of the tip chord Cv_{tip} to the root chord Cv_{root}.

$$\lambda_v = \frac{\text{Cvtip}}{\text{Cvroot}}$$

Therefore, the aspect ratio is also based on the bv–span, and MACv – Mean aerodynamic chord.

$$AR = \frac{\text{bv}}{\text{MACv}}$$

Hence, the MACv is describe in terms of the root chord and the taper ratio parameter as follows:

$$\text{MACv} = \frac{2}{3}\ \text{Cvroot}\left(\frac{1 + \lambda_v + {\lambda_v}^2}{1 + \lambda_v}\right)$$

The vertical tailplane planform area is given as: $S_v = b_v \times \text{MACv}$

Various types of vertical tailplanes are utilised based on the aircraft's application. Fig. 2.4 illustrates the aft vertical tail, considered widely used configuration in vertical tailplane design.

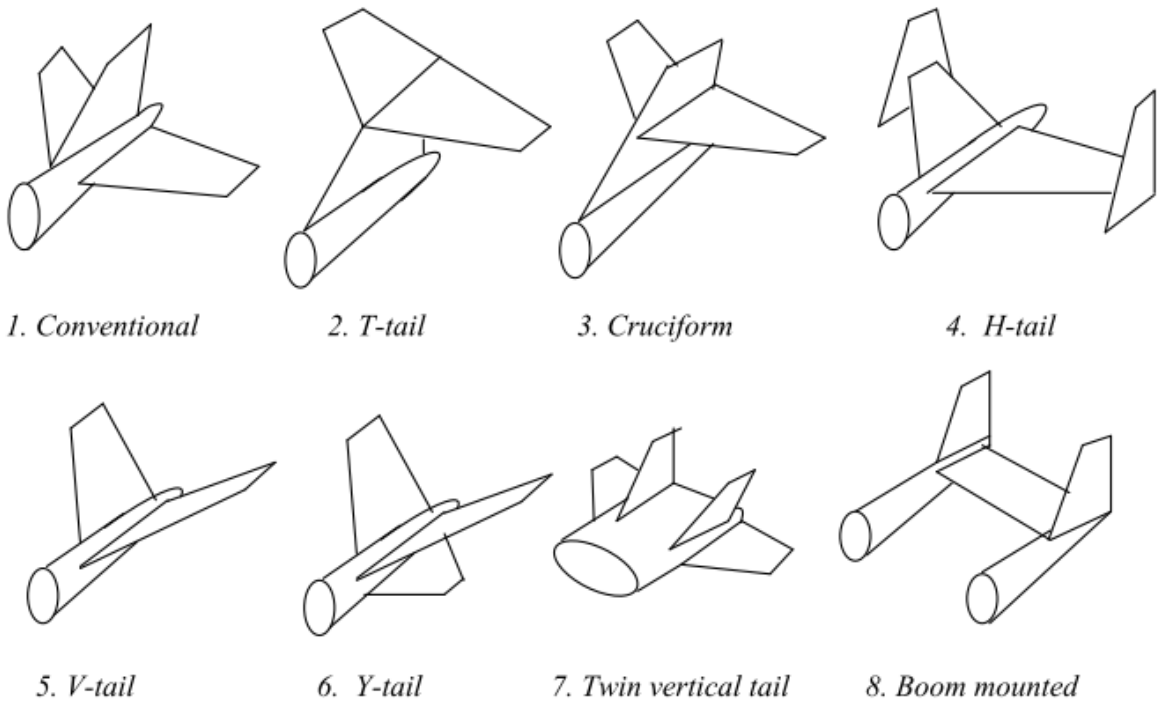

Fig. 2.4: Different configurations used in tail design (Sadraey 2012) .

1. Conventional: In this configuration, one vertical tailplane and one horizontal tailplane are located on both sides of the empennage structure. As earlier mentioned, the vertical tailplane is responsible for the aircraft's directional stability, while the horizontal tailplane

contributes to the longitudinal stability of the aircraft. This type of vertical tailplane is most convenient and easy to design.

2. T-tail: The T-tail vertical tailplane type of configuration consists of a single vertical tailplane and horizontal tailplane on top of the tip side of the vertical tailplane. This configuration's major advantage is that it is out of the wing wake, avoiding the downwash effect. Still, it is also considered a rather dangerous design because it is top heavy and associated with deep stall performance.
3. Cruciform: The cruciform is designed based on the shortcomings of conventional design and the T-tail design of the vertical tailplane. As the name implies, the configuration is a cross-like structure with the horizontal tailplane installed in the middle of the vertical tailplane to avoid the deep stall features and not make the vertical tailplane top heavy.
4. H-Tail: The vertical tailplanes are not positioned on the empennage in this type of vertical tailplane as in the previous designs. Two vertical tailplanes are located on the end of the horizontal tailplanes from left to right of the empennage. This type of tailplane is mostly used in military aircraft, and therefore, the design is complex, and the configuration is heavier than the conventional and the T-tail.
5. V-Tail: The V-Tail is a new design like the H-Tail because there is no vertical tailplane on the empennage. The shape of the V-Tail is purposely proposed for applications where the size of the vertical tailplane is a major concern. The two v-type tailplanes are considered to operate as both vertical and horizontal tailplanes.
6. Y-Tail: The Y-Tail is an improvement of design from the V-Tail, where an extra part is added to serve as the vertical tailplane while the other two V-Tail parts operate as the horizontal tailplane.
7. Twin vertical tail: This configuration consists of two vertical tailplanes mounted on the aircraft's empennage. The twin vertical tailplanes are designed largely to increase the directional stability offered by a single vertical tailplane. The configuration is common in fighter aircraft.
8. Boom-mounted: The boom-mounted configuration is less commonly used than other types. It becomes particularly suitable when a rear

installation of a prop-driven engine is necessary due to the inefficiency of the conventional configuration. A short fuselage structure with vertical tailplanes on both sides is the only viable option. However, this design tends to be heavier, necessitating careful consideration and caution in its implementation.

2.3 Numerical methods

Realising and utilising the computational capabilities is a discovery that improves the design difficulties reported during the engineering design concept (Obayashi 1998; Hoburg and Abbeel 2014). The solution to engineering design problems can be achieved using theoretical, experimental, and numerical methods. Leveraging computational simulation during the initial stages of the design concept allows for the verification of results prior to the final implementation.

The choice of numerical methods is significant in CFD research to solve flow over a VTP. The most common numerical methods include Reynolds-averaged Navier-Stokes (RANS), the large eddy simulation (LES), and the direct numerical simulation (DNS). Here, RANS has some limitations in dealing with flow separations, which is where LES comes in. The LES simulation is designed as a method that outperforms the RANS models while generating results similar to DNS with lower computational resources. Large-scale turbulence eddies are important because they contain high energy and depend on the geometry and boundary conditions employed. In contrast, the small scales are independent of the geometry and the smallest eddies, dissipating all the turbulent energy. LES is recommended in problems that involve vortex shedding and complex separation effects of the laminar boundary layer (Almutairi 2010). The LES is a step ahead of the conventional RANS model in efficiently capturing the turbulent flow structures. The LES method requires a subgrid-scale model to solve the smaller eddies, while in the DNS, all eddies are directly resolved, unlike in RANS, where they are fully modeled.

2.3.1 Reynolds Average Navier-Stokes (RANS) Methods

There are several turbulence models available that can be used in both external and internal flows. No model is considered as the best amongst all the turbulence models (Ansys 2021). The best model always translates into and reflects the true experimental or benchmark data for certain applications. However, some models have shown reliability in giving a good result that agrees with the physical reality aligned to some particular applications. Many studies have numerically investigated aerofoils using various turbulence models (Anil et al. 2018). There is agreement among scholars that the CFD approach using turbulence models has given considerable confidence in aerospace research in terms of verification and validation with experimental data (Bardina et al. 1997; Mereu et al. 2019; Yossri et al. 2021).

Matyushenko et al. (2017) identified that the turbulence model faces major challenges in predicting stall to match experimental data. The study used turbulence models (k-ω SST and SST) and Reynolds numbers Re ≥ 10^6 to analyse discrepancies between experimental data and numerical simulations. The impact of compressibility and the influence of wind tunnel height were extensively examined to identify factors contributing to the observed disagreements. The study attributed the disparities to three-dimensional effects in the experimental results, which the numerical simulation cannot capture accurately. Therefore, it highlights the importance of accounting for these factors to enhance the accuracy of numerical simulations and align them more closely with experimental results. The simulation results were thoroughly compared with experimental results.

The numerical prediction of the stall can be linked to the shape of the aerofoil and Reynolds number; at a higher Reynolds number using the NACA 0015, the Spalart-Allmaras correctly predicted the stall while the other models failed to predict the stall (Bakırcı 2023). In a different study, the stall was well predicted by the k-ω SST compared to other models using NACA 63-215 and NACA 65-421 (Ouchene et al. 2023). Fernandes et al. (2020) studied the S814 aerofoil, where the S-A model shows a small separation region compared to the other models. The effect of separation on the aerofoil's shape changed how

the turbulence models treated the flow around the aerofoil. It is reported that some turbulence models are Reynolds number bounded.

Most RANS models inaccurately predict aerofoil stall angles. Volikas and Nikas (2019) study assessed the turbulence model's performance in predicting aerodynamic forces at various angles of attack using the S809 aerofoil. The four turbulence models investigated are k-ω SST, transition SST, Spalart-Allmaras and realizable k-ε at a Reynolds number of 2×10^6. The investigation confirmed a reliable prediction of the aerodynamic coefficients of all the models at lower angle of attack compared to the experimental data. However, it was observed that the models failed to extend such agreement beyond due to the inability to account for the separation behaviour. The k-ω SST and transition SST models are modified to improve aerodynamic coefficient performance and accuracy. However, the modification's effectiveness was limited to higher angles of attack, with no reasonable impact at lower angles. This study highlights challenges and targeted improvements in turbulence modelling for accurate aerodynamic predictions.

The flow separation is always a major concern in aerofoil investigations. Eleni (2012) compared the performance of different turbulence models with experimental results. Among the three studied turbulence models, Spalart-Allmaras, k-ε, and k-ω SST, the k-ω SST shows a better separation compared to the experimental result. However, at higher angles of attack, these models fail to predict the force coefficients due to the influence of separation caused by the shape of the aerofoil used. This border between lower and higher angles of attack in RANS marks the onset of challenges in predicting the stall angle due to separation effects.

The development of the transition models in computational fluid dynamics has gained popularity due to their ability to provide more accurate results than conventional turbulence models. According to Rahimi et al. (2014), it is recommended that a thorough check in the creation of the mesh be made for transition simulation. Mishra et al. (2019) and Khan et al. (2020) investigated the transition k-kl-ω model's effectiveness over different turbulence models. The results of the transition k-kl-ω show improvement over of the conventional models to predict the stall angle over the NACA 0018 and NACA 0021 aerofoil.

This is due to the model's ability to predict and capture non-equilibrium turbulence along the shear layer. Similarly, Hassan et al. (2022) indicated that out of the five turbulence models studied, including the transition models, all the models were unable to satisfactorily predict the stall angle of NACA 0012 and NACA 2412 at Reynolds number of 50,000.

The transition models are more complex than conventional models because of the additional equation that enhances transition development. Achieving convergence of the model is difficult, particularly at higher angles of attack. Moreover, the advantage comes at a computational cost, as highlighted by Aftab et al. (2016). The computational cost of the model should be considered and balanced based on the requirement between computational efficiency and accuracy in practical applications. A summary of the performance of different turbulence models is given in Table 2.1.

Computational Aerodynamics has seen significant progress thanks to improvements in transition models. These advancements have enhanced our ability to predict and understand the low Reynolds number flows and complex transition and separation phenomena. Transition models have played a critical role in predicting the onset of turbulence and accurately representing laminar bubbles in the boundary layers. Despite these achievements, challenges still remain, and further development is needed to create even more accurate and simplified models for different aerodynamic applications.

Table 2.1: Summary of the performance of different turbulence models.

Author	Turbulence Models	Reynolds Number	Aerofoil Type	Findings
Bakırcı (2023)	Spalart-Allmaras, k-ε, and Standard k-ω	1×10^6	NACA 63-215, NACA 65-421	The SA model predicted the post-stall aerodynamic coefficients while the k-ε and Standard k-ω underpredicted the stall angle.
Ouchene et al. (2023)	k-ω SST, Spalart-Allmaras, and LS k	1.95×10^6	NACA 0015	The assessment of the deep stall by the k-ω SST model shows a better result than the other models.
Wu et al. (2022)	Spalart-Allmaras, SST, k-v, and SPF k-v	1×10^5, 1×10^6	NACA 64A006, NACA 0012	The SPF k-v models performed better in the stall prediction for thin aerofoil.
Liu et al. (2021)	Transition models $R_{e\theta}$-γ, k-kl-ω, γ and LowRe	2.3×10^4 - 2×10^5	NACA 0012, NACA 4415	The k-kl-ω predicted the transition compared to the experiment. At the same time, the $R_{e\theta}$γ and γ model is recommended for higher Reynolds number analysis.
Fernandes et al. (2020)	k-ω SST, Spalart-Allmaras	1.5×10^6	S814	For the S814 aerofoil, the SA model overpredicted the force coefficient, while the k-ω SST shows a more decent prediction close to the experimental data.

2.3.2 Large Eddy Simulation (LES)

The evolution of turbulence modelling in computational fluid dynamics (CFD) has seen significant advancements, particularly in Large Eddy Simulation (LES) and Direct Numerical Simulation (DNS). Reynolds (1990) comprehensively outlined both techniques' advantages and disadvantages. DNS provides complete resolution of all turbulent scales but is computationally expensive due to the need to resolve the smallest eddies. On the other hand, LES, as demonstrated by Boris et al. (1992), filters out smaller scales using subgrid models, therefore, faces challenges in accurately capturing small-scale structures, particularly when comparing results across different grid resolutions. The sensitivity of LES to grid resolution requires prolonged simulations with averaged results to mitigate discrepancies arising from mesh differences. The use of subgrid-scale methods like Smagorinsky helps in filtering unresolved eddies. Lesieur and Métais (1996) established a significant relationship between conventional subgrid-scale models like Smagorinsky and the Scale Similarity (SF) model, with SF performing better in certain wake scenarios.

The subgrid scale is peculiar to LES simulation because of the need to model the unresolved scales around the wall boundary. There is no doubt that the influence of the Reynolds number can affect the function and the choice of the subgrid-scale model (Sarlak 2017). The high-order statistics prediction by the wall adapting local eddy-viscosity (WALE) subgrid-scale model is considered to be better than that observed in the Smagorinsky subgrid model (Kakka and Anupindi 2020).

According to a study conducted by Bazdidi-Tehrani et al. (2019), there is a significant difference between subgrid models regarding flow fields and computer time requirements. The comparison of three different subgrid models has revealed a good agreement between them and the experimental data. However, the WALE subgrid model runs 20% faster in computational time than the other two models. Similarly, research findings by Aubard et al. (2014) point towards the cost of the Smagorinsky model. Depending on the specific application, the subgrid model showed no difference in the flow field compared to the experiment. However, the Smagorinsky models demonstrated

a smaller value than the others (Feng et al. 2021)). It may, however, be noted that the LES relied on the hypothesis on the resolved and unresolved region of the scales to ensure an accurate prediction of the flow. Recent developments in artificial neural networks have suggested a method to replace and improve the subgrid-scale efficiency (Sarghini et al. 2003). As previously reported, there are many developments to enhance the subgrid-scale model for more advanced LES simulations; the following researchers suggested the use of machine learning (Maulik et al. 2019) and similarity concept (Newman et al. 2014) to replace the traditional subgrid-scale models. Nonetheless, the conventional subgrid scales remain the popular and accurate models in most LES studies (Lee and Cant 2017).

The intricacies of turbulence necessitate investigations using state-of-the-art high-performance computing, as Moin and Kim (1997) highlighted, enabling more comprehensive predictions of turbulent flow. Spalart (2000) delves deeper into the intermediate development between Reynolds-averaged Navier-Stokes (RANS) and LES, providing additional insights into the evolutionary trajectory of turbulence modelling. The completeness of LES in resolving turbulent kinetic energy becomes a focal point, determining the extent of resolution required for accurate solutions. Pope (2004) raised pertinent questions regarding the balance between computational cost and solution accuracy, elucidating the controversial discussion surrounding LES criteria based on cost-effectiveness and accuracy.

Furthermore, LES finds applications in complex flows, such as reacting flows in combustion, as Fureby (2008) recommended, demanding methods to verify accuracy. Rizzetta et al. (2008) highlighted the potential of LES in active flow control, employing higher-order implicit finite difference methods for controlling separation using leading-edge vortex control and plasma actuators. In addition, while LES offers distinct advantages over DNS, its implementation in turbulence modelling requires a delicate balance between computational cost, solution accuracy, and verification methods. The evolution and challenges in these techniques underscore the ongoing quest for more efficient and accurate turbulence models in computational fluid dynamics. The general recommendations and the development of LES are reported by Georgiadis et

al. (2010). For a more comprehensive review of LES with a specific focus on transitional flow, the work was reported by Zhiyin (2015). Both reviews highlight inflow boundary conditions as one of the major challenges in LES.

2.3.3 Hybrid RANS/LES Methods

The major goal of turbulence modelling development has been algorithm development with fewer uncertainties. Typically, the RANS models performed extremely well in wall-bounded flows, as mentioned in the previous section. It is widely believed that one of the limitations of the RANS model is the inability to perform well in a separated region with significant instability of the flow feature. Therefore, the LES was employed to improve the limitations of the RANS model in the separated region because of the method's robustness in resolving the large-scale eddies and filtering the smaller eddies using the subgrid-scale methods (Bush et al. 2019). Although the RANS method was considered reliable for industrial applications, it was not always consistent (Corson et al. 2009).

It can be said that the RANS and LES are designed to be performed mostly in attached and separated flows, respectively. The LES is computationally expensive and operated at a range of low Reynolds numbers compared to the RANS due to computational resources. Therefore, Spalart (2000) developed another model that combines the RANS and LES methods to establish a hybrid RANS/LES method that will perform better than RANS regarding numerical accuracy and is less expensive than the LES method. This method is a breakthrough in numerical methodology, especially in applications that require high Reynolds number flow.

The hybrid RANS/LES can be treated as zonal and non-zonal approaches between the RANS and LES interfaces. The non-zonal approaches are commonly employed because the zonal was complex compared to the non-zonal approaches. Spalart and Allmaras (1994) proposed the non-zonal approach called the detached eddy simulation DES that uses the RANS Spalart-Allmaras one-equation. In this approach, the regions of interest, i.e., the attached and separated areas, can be analysed using the combined RANS and LES. This method is somehow difficult because of the physics of the

transition between the zones; it is known that the RANS method is a product of the ensemble averaging of the Reynolds stress, which modelled all the eddies, while the LES zone, in this case, is treated with the SGS models that filtered the unresolved eddies. The eddy-viscosity switch between the hybrid zone is a complex feature that should be treated cautiously.

The difficulty associated with the interface between the inner RANS and outer LES is hindered by the loss of appropriate connections between the regions. Hybrid coupling techniques like blending and scale grid modification have been suggested to tackle this issue. However, these methods still face limitations, as the transformation of the scale length tends to underpredict the LES outer region, resulting in the logarithmic law mismatch and potentially impeding seamless interaction between the inner and outer areas. To mitigate this issue, careful consideration of filters is necessary for smooth coupling. Although there are suggestions for overcoming such errors, such as the stochastic forcing, its reliability is limited to specific applications.

In the original DES, the outer flow region is treated by the LES while the inner flow region is treated by the RANS models. It was found that the DES is limited to highly separated flow near the wall region. An improved version of the DES models, known as the delayed detached eddy viscosity DDES, was proposed by Spalart et al. (2006) to improve the blend between the RANS and LES using the subgrid models in the near wall region. That also helps the model to recover the length scale in terms of the eddy viscosity and the grid size.

Depending on the subgrid scale employed, the RANS and LES methods can be integrated into three ways: interfacing, blending, and segregation. In the interfacing method, the LES and RANS methods depend on the time variation caused by the transition. The hybrid blending methods ensure the concurrent run of the RANS and LES, while the segregated method separates the LES and RANS zones in the domain.

Zhou et al. (2019) explored the efficacy of a blended approach involving delayed detached eddy simulation DDES and $\gamma - Re\theta t$ to enhance the transitional separated flow over A-Aerofoil and DBLN-526 at Reynolds number of 2.1×10^{6}. The investigation focused on decreased inflow turbulence

intensity in the freestream region where the LES operates. Also, the decrease in inflow turbulence intensity is characterized by a transition delay. The new methodology, incorporating the combination of DDES and γ – Reθt, demonstrated notable improvements in the freestream region. Specifically, the blend effectively eliminated low turbulence intensity. Meanwhile, the LES was selectively activated in the wake region, enhancing the overall performance of the transitional separated region.

In another study, a combination of the γ – Reθt and improved delayed eddy simulation IDDES models has demonstrated significant improvements in capturing the flow features of the laminar-turbulent transition, compared to each model used separately. The results obtained from testing the ONERA M6 wing have shown a notable enhancement in capturing the flow structure in the wake region of the wing (Kim and Kwon 2021)

2.4 Laminar Separation Bubble

The laminar to turbulent flow separation transition is typically linked to the laminar boundary layer separation known as the laminar separation bubble (LSB). This phenomenon arises due to the instability and unsteadiness in the boundary layer, which usually occurs within a certain range of Reynolds numbers. The LSB can take the form of a short and long bubble along the surface of the aerofoil.

Gaster (1967) conducted a comprehensive study investigating the laminar separation bubble (LSB) phenomenon, which arises when the boundary layer transitions from laminar to turbulence. The primary focus was the short and long bubbles over the aerofoil, based on pressure distribution formation and Reynolds number effect. The study revealed that the Reynolds number significantly influences the LSB. An increase in the Reynolds number causes a contraction of the bubble length, while a decrease in the Reynolds number results in an expansion along the aerofoil's surface. Additionally, the mean and fluctuating velocities provided valuable insight into the LSB presence. In a different study, the influence of Reynolds number on the formation of LSB was investigated at a range of Reynolds number 50,000 – 200,000 using NACA 66_3-018 aerofoil (O'Meara and Mueller 1987). It was discovered that the

bubble length and thickness increased as the Reynolds number and incidence angle increased from 10°- 12°.

The details and criteria that distinguish between the short and long bubbles were described further by Horton (1968). A bubble formation can be distinguished based on the bubble length obtained from the separation ratio to the reattachment point. However, this method was considered insufficient because the formation based on the bubble length is inconsistent with most flows. The influence of the short and long bubbles is highlighted based on the pressure distribution. It was observed that short bubbles exhibit a high-pressure peak, which undergoes changes and behaves similarly to an inviscid flow, exerting minimal influence on the overall surface of the aerofoil. In addition, the long bubble over the pressure distribution occupied a long distance over the aerofoil surface, with a high-pressure peak collapsing and floating downstream.

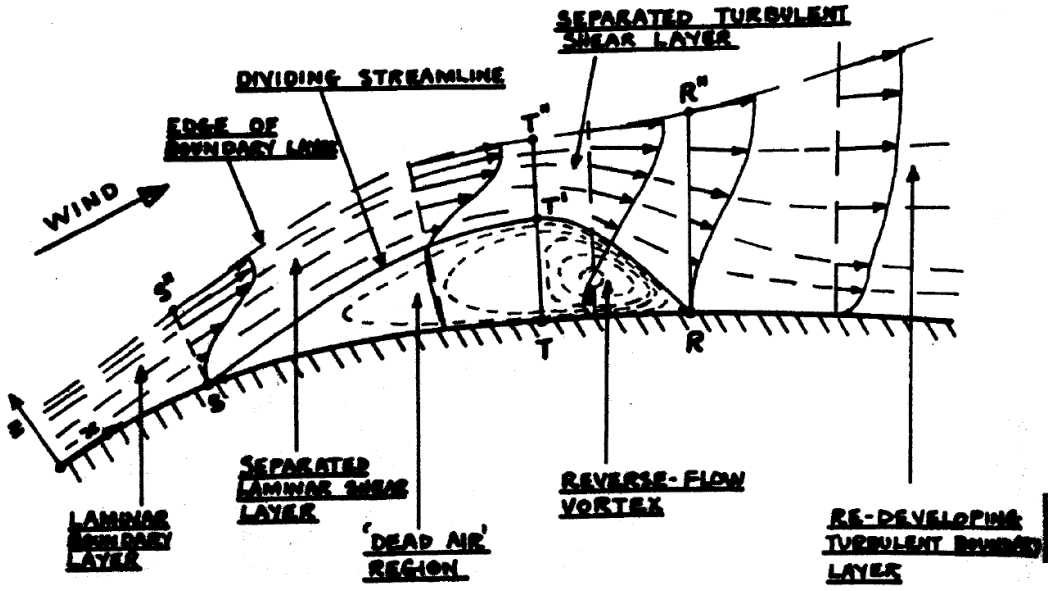

Fig. 2.5: A detailed view of the formation of the laminar separation bubble over a surface (Horton 1968).

The LSB is caused by an unfavourable pressure gradient originating from the stagnation point. This pressure gradient affects the laminar boundary layer, causing it to separate. In Fig. 2.5, the separation point is represented by S, the transition by T, and the reattachment point by R. Between the transition point by T and the surface, a recirculation bubble forms due to the flow exchange between the surface and dividing streamline. It can be observed that

the bubble enclosed in the dividing streamline is concentrated towards the turbulence region because of the reverse flow vortex. In contrast, the laminar region is referred to as the dead-air region. The reattachment point occurs because turbulent flows have a greater momentum to overcome the unfavourable pressure gradient.

The formation of the LSB is strongly influenced by the angle of attack and the Reynolds number, as discussed. Therefore, the phenomenon is common at lower angles of attack associated with the high-pressure gradient along the laminar separation boundary. A numerical study of the cambered wing with a low Reynolds number of 60,000 and a small incidence of 6° was thoroughly investigated (Chen et al. 2013). The presence of LSB can be computed using transition models that account for the transition and ability to capture the bubbles. Also, Chen et al. (2013) found that the 2D and 3D geometries investigated showed good agreement in predicting the presence of laminar separation bubbles along the suction surface. However, at incidences below 5°, a recirculation was observed at the trailing edge, which intensified upstream from 5°-10° to form a leading-edge bubble and trailing-edge recirculation. The turbulent kinetic energy is unphysically produced near the stagnation point, causing the conventional RANS models to fail in predicting the LSB.

In the context of the vertical tailplane aerofoil, the RANS models found it difficult to accurately predict the laminar separation around the vertical tailplane structure (Wokoeck et al. 2006). Modifying the models to add a transition effect improved the ability of the conventional RANS models to account for the accurate prediction of the LSB and transition along the suction surface of the aerofoil. The development of transition models, such as the γ-model and $R_{e\theta}$-γ model has shown a successful transition and the formation of the laminar separation bubbles. The $R_{e\theta}$-γ model solves turbulence fluctuations based on Reynolds number while the γ-model only calculate the turbulence intermittency as a one-equation model.

The development of the laminar separation bubble is a crucial aerodynamic phenomenon marked by airflow separation. Choudhry et al. (2015) highlight the complexity of these bubbles, which is influenced by significant flow parameters such as Reynolds number, turbulence intensity,

and angle of attack. The investigation was performed using NACA 0012 aerofoil at a Reynolds number of 120,000. Comparing the performance of the transition models, the k-kl-ω models demonstrated superior predictive accuracy compared to the $R_{e\theta}$-γ model. Notably, the k-kl-ω models predicted the reattachment point in closer agreement with experimental observations, while the $R_{e\theta}$-γ model indicated an earlier reattachment point. Fig. 2.6 illustrates the intricate interplay between the short and long bubbles, showcasing the evolution of laminar separation bubbles in a complex aerodynamic context. The research findings showed how the long bubble affected stall and lift-to-drag ratio efficiency. The author assessed the long bubble's impact on the aerofoil's aerodynamic performance and suggested the need to control and reduce the bubble to improve the aerodynamic performance.

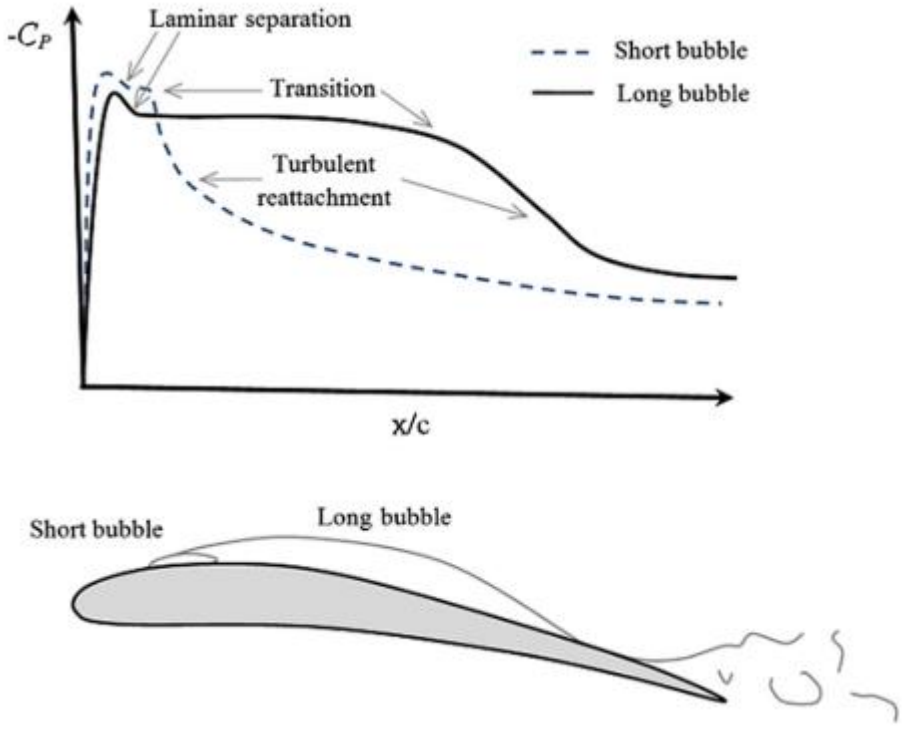

Fig. 2.6: Pressure coefficient plot showing the evolution of short and long bubbles (Choudhry et al. 2015)**.**

Liu et al. (2021) studied the effect of three different transition turbulence models $R_{e\theta}$-γ, k-kl-ω and γ-model. The numerical work used two different aerofoils NACA 0012 and NACA 4415, at a range of Reynolds numbers of 23,000 to 200,000. The $R_{e\theta}$-γ and γ-model demonstrated a smooth prediction from the laminar separation bubble to the reattachment at the trailing edge. On the other hand, the k-kl-ω model showed a proper prediction of the leading-edge separation bubble but failed to show the turbulence reattachment compared to other models at a low Reynolds number. The results are further compared with the experimental and DNS data. These findings could help develop a better understanding of the laminar separation bubble at low Reynolds numbers.

Elgammi et al. (2022) further investigated the influence of the LSB using the transition k-kl-ω model over the NACA 0015, NACA 6415, and NACA 6421 aerofoil. The numerical simulation was carried out at a low Reynolds number of 300,000 and angles of attack of 4° and 6°. The results indicated the long bubble increased the drag coefficient and lowered the lift-to-drag ratio. Further observations revealed the influence of the angle of attack on the formation of the LSB, which reduced the bubble length by 5%, from 4° to 6°.

Various transition models yield distinct predictions of LSB in contrast to experimental data. This discrepancy highlights a notable area for enhancement within the model. Salimipour (2019) proposes the modified k-kl-ω transition model to predict the long bubbles in the transition region accurately. The study conducted simulations using NACA 0012 and Eppler 387 aerofoils at Reynolds numbers of 30,000 and 130,000. The modifications yielded improved predictions of the LSB that align more closely with experimental and DNS results for both NACA 0012 and Eppler 387 aerofoil. These findings highlight the potential for refining transition models to enhance their predictive capabilities and better capture the complex aerodynamic phenomenon observed in LSBs. These modifications can be utilised for low Reynolds numbers and different aerofoil configurations.

The formation of the LSB can be controlled using different approaches to ensure a more attached flow. The utilization of the leading-edge tubercles was tested experimentally to eliminate the LSB along a NACA 4415 aerofoil at a Reynolds number of 120,000 (Sudhakar et al. 2019). The flow over the aerofoil was carried out using three angles of attacks of 6°,12°, and 18°; the baseline results of the pressure distribution at the lower incidence of 6° demonstrated a high peak of surface pressure with the formation of the LSB. At this incidence angle, where the presence of the LSB is observed, the tubercles eliminated the LSB and collapsed the high-pressure peak. Fig. 2.7 illustrates the streamlines of the baseline and control case using the tubercles at an incidence angle of 6°. The effect of the peak location of the tubercles reduced the LSB on the suction side of the aerofoil. It was also observed that even at a post-stall incidence of 18°, the tubercle's presence significantly reduced the separation region along the surface by almost 50% compared to the baseline case.

A numerical study was conducted on the E216 aerofoil, focusing on the LSB using the transition model, with the Reynolds number of 100,000 (Sreejith and Sathyabhama 2018). The investigation extended to exploring a strategy aimed at minimising the impact of LSB on the aerofoil's aerodynamic performance. This involved implementing a boundary layer trip method at various chord locations and heights. The trip boundary layer method significantly enhanced the lift-to-drag ratio, particularly at an angle of 6°. The study found that increasing the trip height proved more effective in eliminating the laminar separation bubble.

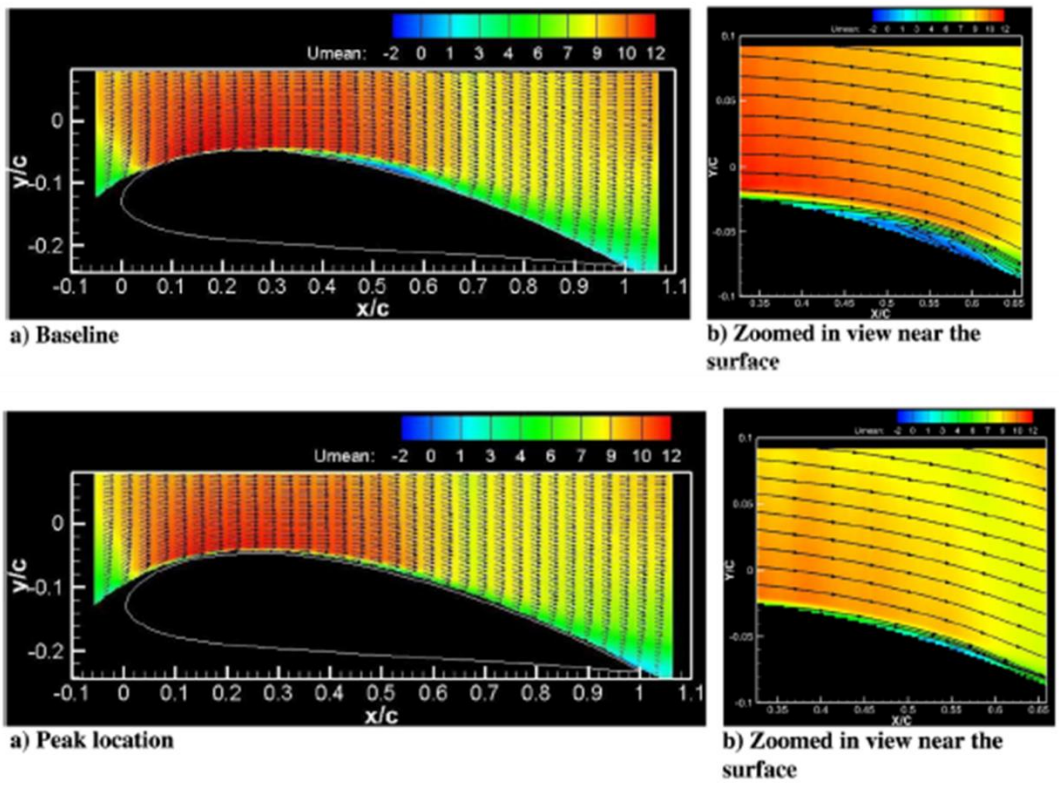

Fig. 2.7: Velocity field of the baseline and tubercle's peak location (Sudhakar et al. 2019).

As mentioned above, laminar separation bubbles reattach to the surface downstream as turbulent flow. The details of the turbulence inside the bubble from the separation point to the reattachment point are reported for the short bubble (Rinoie and Hata 2004). The bursting phenomenon is contingent upon the nose shape of the aerofoil, and when the short bubble fails to reattach due to an increase in the incidence angle, the outcome is termed a short bubble burst. The turbulent energy balance was carried out using NACA 0012 with an incidence angle of 10° at the Reynolds number of 130,000. The results of the energy balance of the short bubble revealed that the major parameter influencing the turbulent kinetic energy growth is the turbulent production term.

2.5 Fundamentals of Flow Control on Aircraft

The idea of flow control on aircraft started several decades ago. In 1964, the challenges of a fighter jet aircraft's interference, stability, and control were thoroughly investigated by McKinney et al. (1964). Several factors contributed to jet and commercial aeroplanes' instability and interference. When designing a control device, it is important to keep it economical and easy to handle and maintain. Aerodynamic flow control aims to modify the flow behaviour to improve the aircraft performance. This can be achieved using active or passive control techniques such as vortex generators and plasma actuators. For example, vortex generators are common passive flow control devices that require no energy.

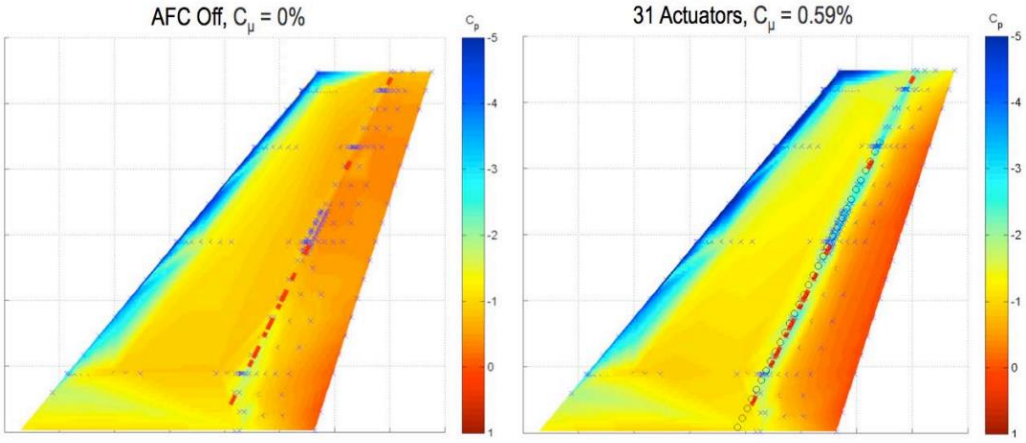

Fig. 2.8: A pressure coefficient contour of sweeping jet actuator on VTP (Lin et al. 2016).

As an active flow control device, the sweeping jet actuators were used to improve the performance of the vertical tailplane from an aerodynamic perspective (Lin et al. 2016). The pressure coefficient at a negative sideslip angle of β = -7.5°with a rudder deflection angle of δ = 30° is shown in Fig. 2.8. When the sweeping jet actuators are turned on, an increase in the pressure coefficient is observed at the leading edge of the vertical tailplane as compared to the baseline. This effect is also present at the rudder's leading edge, a hinge line divided between the rudder and stabiliser. The flow control strategies used to manipulate the airflow around the aircraft play a vital role in enhancing the aerodynamic performance of the vertical tailplane at higher side slip and rudder deflections. The results suggest that sweeping jet actuators can improve

aircraft efficiency, particularly when operating in challenging conditions such as take-off and landing or when flying in turbulent weather.

The causes of separation over an aerofoil have been widely investigated experimentally (Hu and Yang 2008; Katz 2019) and numerically (Azim et al. 2015), and the control to remedy the effects has been suggested by Jones et al. (2018). Various passive and active control techniques have been identified to regulate separation effects around aerofoils. For instance, incorporating a simple microcylinder positioned at a specific distance from the leading edge has enhanced aerofoil performance and mitigated downstream separation effects (Luo et al. 2017).

Recent studies conducted by Zhang et al. (2023) and Guoqiang and Shihe (2020) have examined the application of plasma actuators for active flow control on an aerofoil, as shown in Fig 2.9, where the larger structures were broken down when the plasma is turned on. The findings indicate that implementing dynamic stall treatment can improve the overall aerodynamic performance, accompanied by a significant reduction in separation. Another approach to controlling separation over an aerofoil involves utilising travelling waves. Interestingly, varying the amplitude of travelling waves can yield different degrees of enhancement in separation control (Akbarzadeh and Borazjani 2020); notably, increasing the amplitude of the waves results in a decrease in aerodynamic coefficient performance, whereas employing low amplitude waves demonstrates a marked improvement in coefficient performance with slight delay in separation effects. The use of different strategies contributed to the reduction and control of the separation effects over an aerofoil.

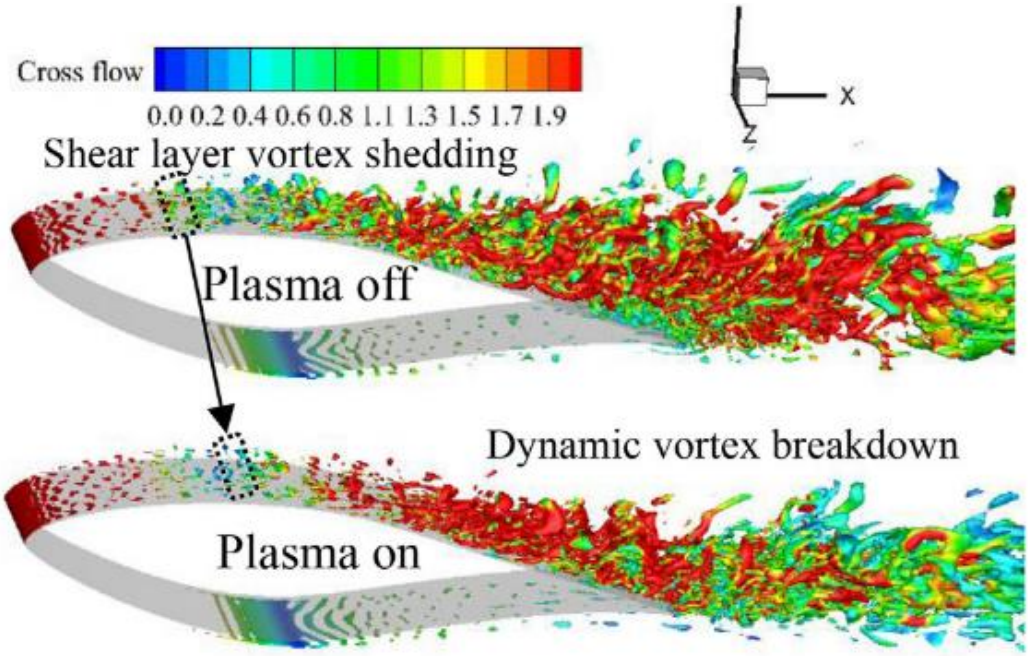

Fig. 2.9: The effect of plasma active control on vortex shedding over a wing (Guoqiang and Shihe 2020).

One of the significant ongoing discussions pertains to the regulation of turbulent flow using flow control devices. However, the main challenge associated with this type of application lies in that such flows can only be evaluated through high-fidelity simulations, such as LES and DNS, which necessitate substantial computational resources. LES has been employed in examining passive flow control devices on an aerofoil. Heffron et al. (2016) demonstrated the effectiveness of micro vortex generators in suppressing separation on an Eppler E387 aerofoil, utilising LES as the methodology. Shi et al. (2019) employed LES to simulate and explore the flow around an S809 aerofoil equipped with a microcylinder as a passive flow control device. These results revealed enhancements in the aerodynamic performance of the stalled aerofoil. Mishra and De (2021) conducted a numerical investigation on a NACA 0021 aerofoil featuring leading-edge undulation, demonstrating a reduction in separation and improvement in the prediction of aerodynamic coefficients after the stall.

The adoption of new flow control methodologies is leading to significant advancements in aerodynamic applications. Rahmani and Wang (2023), in a

recent study, utilised an equilateral triangular trip method on an E423 aerofoil. The obtained LES data demonstrated a noteworthy decrease in wing suction separation compared to the uncontrolled case; this can be seen in Fig. 2.10. Here, the primary objective of flow control is related to the laminar separation bubble at the leading edge of an aerofoil and the turbulent separation near the trailing edge. By combining passive control devices with high-fidelity simulation, it is possible to find a solution for the impact of separation on the aerofoil surface. Implementing novel techniques such as flexible aerofoil surface has significantly enhanced the aerodynamic coefficient and reduced laminar and turbulent separation effects at low Reynolds numbers (Genc et al. 2020).

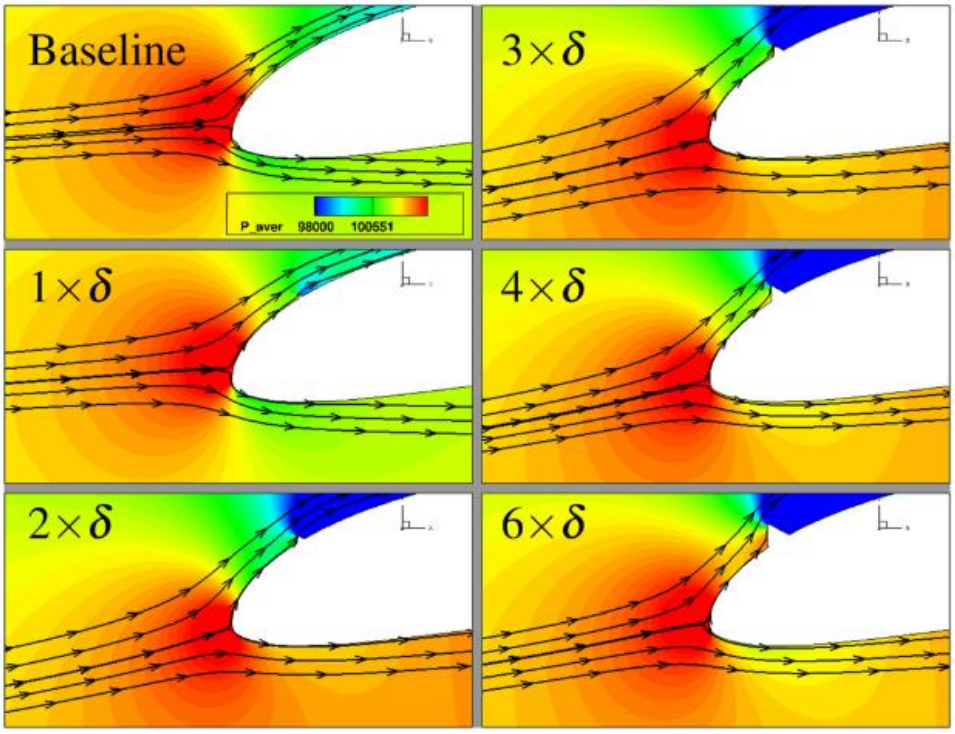

Fig. 2.10: A pressure contour showing LES result of triangular trip passive flow (Rahmani and Wang 2023).

2.5.1 Leading Edge Slat

Flow control techniques have been developed to improve aircraft performances in recent years, primarily focusing on the leading and trailing edges of the wing, where slats and flaps can be deployed to optimise the pressure distributions over an aerofoil (Chacksfield 1980). Jacob (1974) investigated the multi-element aerofoils to improve pressure and lift coefficients. These investigations were followed by a study to optimise the position of the leading-edge slat to maximise the lift of multi-element aerofoil (Olson et al. 1979).

Savory et al. (1992) investigated experimentally the aerodynamic performance of multi-element aerofoil with a slat angle of 25° and flap angle of 20° at a Reynolds number of 1.26×10^6. The cove region of a multi-element aerofoil which is a gap between the slat and the main element aerofoil provides details of flow parameters, such as the mean velocity, turbulence intensity, and pressure distributions. The influence of the turbulence intensity and the mean velocity was used to assess the accuracy of the results around the cove region. The leading-edge slat improved the overall performance at incidence angles of 8°-20° when a turbulence level of 0.20% is used.

Chin et al. (1993) studied the effect of the Reynolds number and the flap gap on the aerodynamic performance of a supercritical aerofoil with a leading-edge slat and a single-element trailing-edge flap. McGinley et al. (1998) discovered that flap deflection angle influenced the Reynolds stress in the slat and flap wake regions, while the change strongly influenced the pressure distribution around these elements in the slat and flap gaps.

Small vortex generators were incorporated into a three-element aerofoil with a single slat and flap (Lin et al. 1994). In this case, the small vortex generator was mounted on the flap to reduce the flap separation effect. The findings revealed that the flap-mounted vortex generators of at least 0.18% of the total flap chord reduced the flap's separation region, increasing the aerodynamic performance. However, the effect was inconsistent at a lower incidence angle where the flow is attached. Meunier and Brunet (2008) studied micro-electromechanical flow control using slats, flaps, and two

actuators, including air jet vortex generators. The numerical findings confirmed a significant correlation between the pressure and skin friction coefficient observed in the experiments. Incorporating an active, internally blowing flap and a precisely positioned leading edge slat can significantly improve the performance of pressure and overall force coefficients (Burnazzi and Radespiel 2014).

The location of slotted slats and flaps significantly impacts the aerodynamic characteristics of the high-lift aerofoil, as shown in Fig. 2.11. The slat and flap respond differently with an increased angle of attack. The flap influences the lift coefficient curve, while the slat influences the stall angle compared to the baseline case (Kanazaki et al. 2007). Further studies numerically investigated the significance of the gap and location of the flap on aerodynamic performance (Velkova and Todorov 2015; Jo et al. 2016).

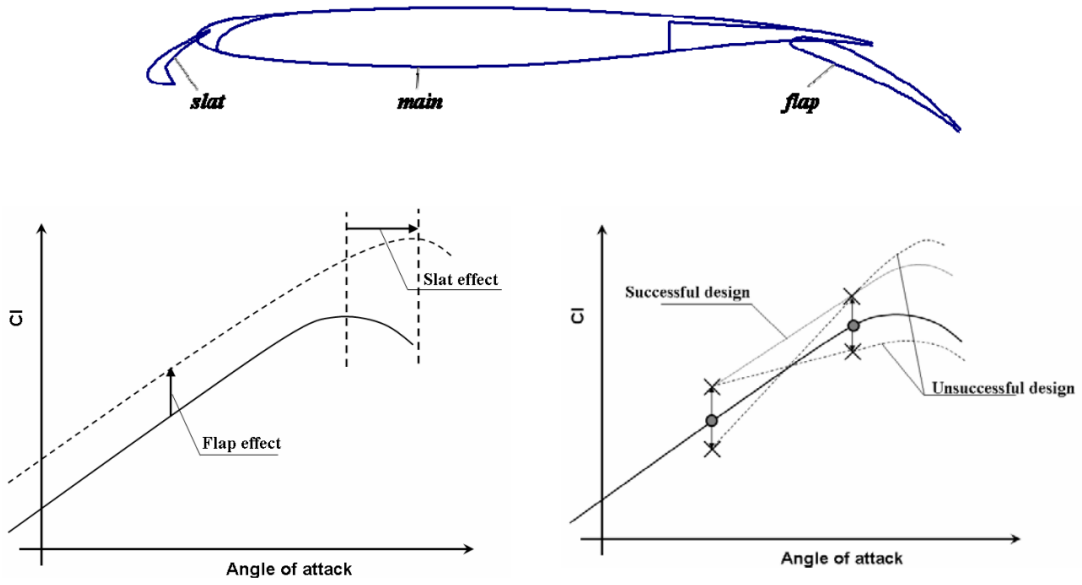

Fig. 2.11: The effect of slat and flap on the performance of the lift coefficient (Kanazaki et al. 2007).

The effect of slat performance for high Reynolds numbers (Steiner et al. 2020) and low Reynolds numbers (Traub and Kaula 2016; Zaki et al. 2022) are investigated regarding the parametric slat design. It was shown that the lift and drag coefficient of the multi-element aerofoil are independent of the Reynolds number. Three different Reynolds numbers (4.2×10^6, 9×10^6 and 16×10^6) were investigated (Lin and Dominik 1997), and the influence of the Reynolds numbers on the slat and the flap was carefully analysed. They showed that increasing the Reynolds number decreases the maximum lift coefficient.

In a study by Mandadzhiev et al. (2017), the performance of bio-inspired leading-edge slats was tested using the cambered aerofoil s1223. Inspired by the alula effect observed in birds, the study experimentally examined a bird-like alula slat at various angles of attack and alula deflection angles. They revealed that increasing the alula deflection angle significantly improved aerodynamic performance, enhancing the lift coefficient. The research sheds light on the potential benefits of incorporating bird-inspired features, such as alula-like slats, to enhance the aerodynamic performance of aircraft wings. Further study by Raj Mohamed et al. (2023) focuses on optimising the bio-inspired slat effect at different slat chords and gaps using the Clark Y aerofoil. It was concluded that the lift coefficient increases up to the stall angle at a minimum slat chord. An increase in the slat's chord size and forward distance shows an increase in the lift coefficient beyond the stall angle due to the slat effect. Implementing slats can also delay stall occurrence and improve efficiency by controlling flow separation.

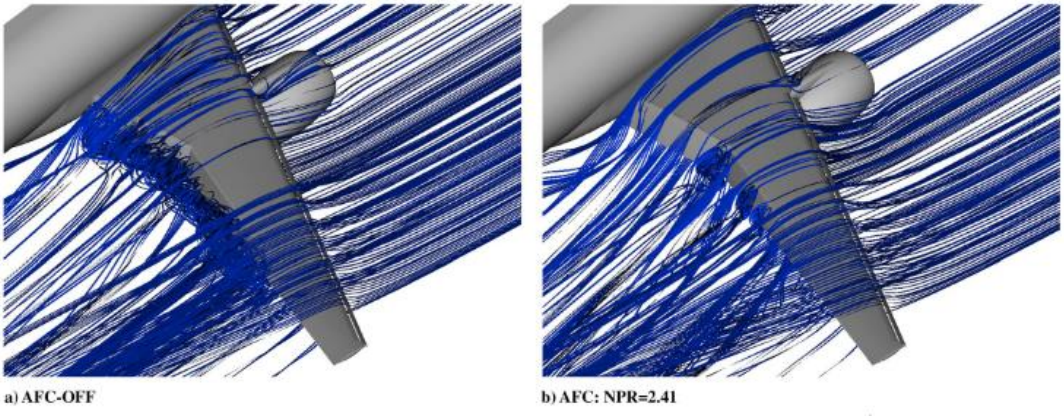

Fig. 2.12: The effect of hybrid active and passive control on wing section (Vatsa et al. 2021).

Gupta et al. (2020) investigated the effect of slat and flap position on the performance of two different aerofoils of NACA 4412 and MDA 30P-30N. The results indicated that the baseline single aerofoil of NACA 4412 stall angle was increased from 16° to 20° using multi-element aerofoils. However, the influence of the slat and flap gap on aerodynamic performance was higher in MDA 30P-30N compared to NACA 4412.

Consideration of the slats gap and flap positions are thoroughly investigated, influencing the aerodynamic performance of wing. Finding appropriate slat positions and gap fillers on the wing can improve their performance by enhancing lift and drag coefficients (Van Dam 2002; Zhi et al. 2021). Adjusting the slot positions and flap trailing edge can further enhance lift and drag coefficients (Anitha et al. 2018).

Vatsa et al. (2021) conducted a numerical analysis to compare the performance of conventional and active flow control strategies in high-lift development. The simulation, utilising the powerFLOW code, incorporated the wing, fuselage, slats, and flaps. Numerical results aligned closely with experimental findings, particularly regarding aerodynamic force coefficients and pressure coefficients. Fig. 2.12 depicts the noticeable impact of sweep jet actuators. Streamlines with the actuator turned off indicated strong separation regions and vortices in both inboard and outboard directions. Conversely, activating the actuators led to a substantial reduction in the separated region and minimised the generation of wing-tip vortices. This highlights the efficacy

of active flow control in mitigating separation and enhancing overall aerodynamic performance.

Similarly, control devices influence the impact of vortices generated on the wing's surface. At a low angle of attack, there is less to show on how the effect is on the wing. The impact of the leading edge slat on the vortex structures is shown in Fig. 2.13. It can be seen that the leading-edge slat disintegrated the larger structures compared to the baseline wing, thereby resulting in a reduction of separation on the slat (Xiao et al. 2020). With an increased angle of attack, the control devices show more vortex behaviour on the top part of the wing surface (Li and Hearst 2021).

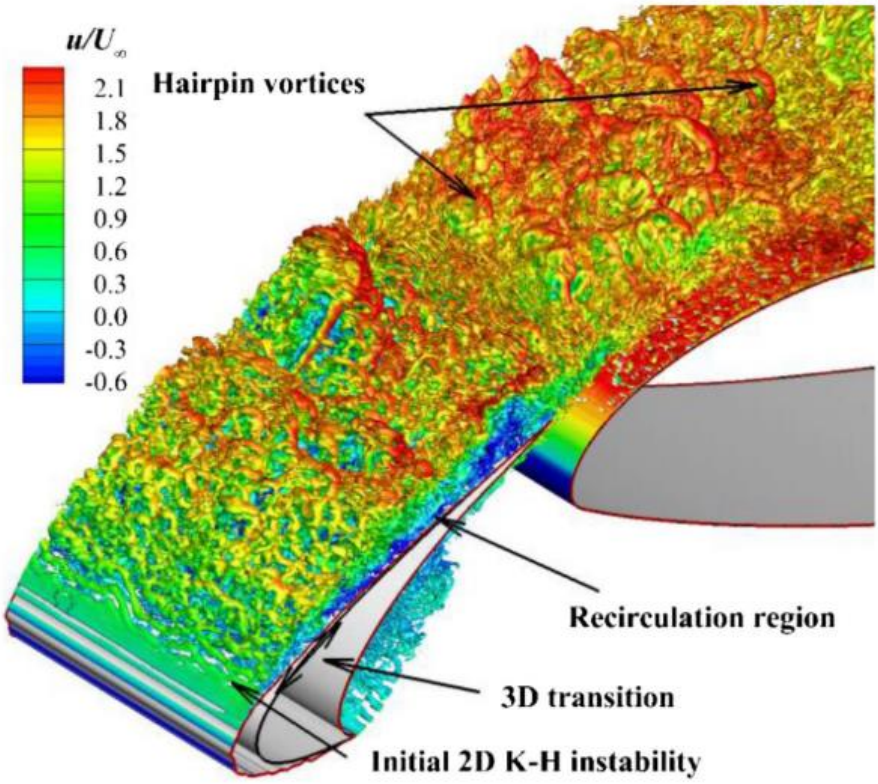

Fig. 2.13: The effect of the leading-edge slat on the vortex structures (Xiao et al. 2020).

2.5.2 Leading Edge Undulation

Leading-edge undulation is currently one of the most active areas of flow control research and has been extensively studied in the past two decades. Humpback whale flipper bumps enhance its movement (Fig. 2.14). They have the advantage of delaying the angle of attack until the stall (Miklosovic et al. 2004), the potential for bio-inspired design in wing-like structures (Fish and Battle 1995) and passive flow control with numerous benefits for lifting bodies in the air (Fish and Lauder 2006) have been studied. The main advantages of a bump are increased lift and reduced drag (Fish et al. 2011). These bumps can be applied to artificial hearts (Abe et al. 1997), power turbines (Shyam et al. 2015), and aircraft propellers (Asghar et al. 2020), making them suitable for many applications.

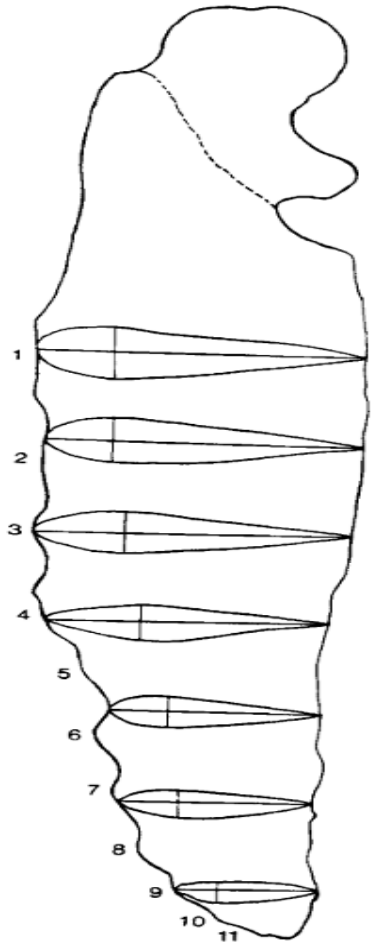

Fig. 2.14: The Humpback whale Flipper planform with the chord and the thickness represented by the horizontal and vertical lines (Fish and Battle 1995) .

Inspired by the humpback whale flipper, the incorporation of tubercles on the aerofoil's leading edge has been investigated for its effects on lift and drag performance. Hansen et al. (2011) experimentally investigated the impact of leading-edge tubercles using two different aerofoil profiles of NACA 65-021 and NACA 0021. The work was performed at two different Reynolds numbers 4370 and 5250. It has been found that tubercles can improve lift performance in the post-stall regime for both aerofoil profiles, but NACA 0021 indicated reduced lift performance in the pre-stall regime. Fernandes et al. (2013) also observed that the effect of the tubercles was not noticed in the pre-stall region using NACA 2412 at the Reynolds number 2.185×10^6. The numerical simulation shows evidence that the tubercles benefit the lift coefficient by 5.33% and reduce the drag coefficient by 2.72% in the post-stall region.

The wavy wing of NACA 0020 at a low Reynolds number of 800 and deep stall angle of 20° was found to reduce the streamwise structures compared to the smooth wing without the wavy design (Favier et al. 2012). Wei et al. (2018) experimented with different tubercle shapes of a tapered wing using an SD 7032 aerofoil profile. The work was performed for Reynolds numbers 5.5×10^4 and 8.2×10^4, and the results indicated that of the performance of tubercles are not sensitive to the Reynolds number. The results of different angles of attacks have been thoroughly analysed based on the skin-friction coefficients. The effect of the LSB was observed at a lower angle of attacks of 0° and 9° in the baseline case. It was found that the tubercles effect modified the LSB, therefore, this enhancement is believed to be the reason for the increase in the lift coefficient.

Additionally, some tubercle designs can reduce the aerodynamic coefficients. The study by Bolzon et al. (2014) indicated that the tapered wing of NACA 0012 of the tubercles at the Reynolds number of 2.2×10^5 shows a decrease in the lift and drag coefficients by 4-6% and 7-9.5%, respectively.

The tubercles of the wing showed notable improvements under post-stall conditions (Bolzon et al. 2016). Kim et al. (2018) reported that tubercles on a wing delay stall by 7° and increase the maximum lift coefficient by 22%, as shown in Fig. 2.15, but at higher angles of attack, the tubercle's effect on drag coefficient remains unchanged. The experiment was conducted using the

NACA 0020 aerofoil profile for the design of the tapered wing, and the chord Reynolds number is given by 1.8×10^5. Incorporating tubercles on the aerofoil wing designed by NACA 4415 improves the aerodynamic performance and delay stalls at a Reynolds number of 1.2×10^5 (Aftab and Ahmad 2019). Sudhakar et al. (2020) conducted an extensive experiment to examine the effect of leading-edge tubercles on S1223 and NACA 4415 aerofoil at three different low Reynolds numbers of 1×10^5, 1.5×10^5 and 2×10^5. The finding revealed that the greatest benefit of the aerodynamic performance is observed in the S1223 aerofoil compared to the NACA 4415 aerofoil. The S1223 aerofoil shows remarkable improvement in the aerodynamic performance and delays in the stall angle.

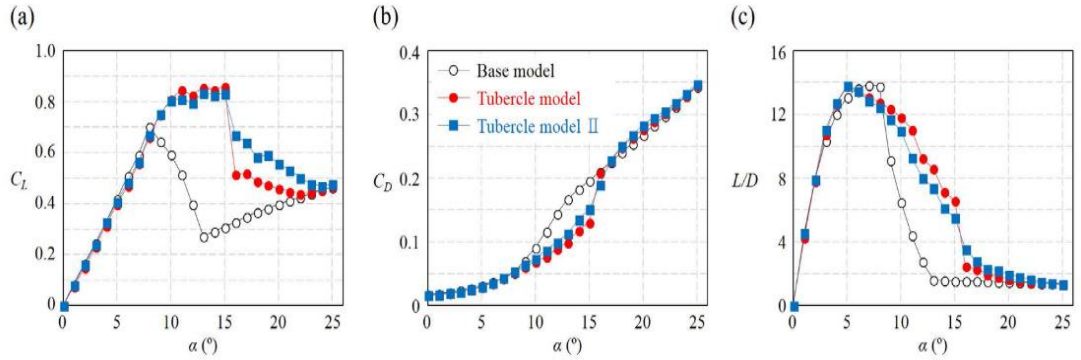

Fig. 2.15: Tubercle effect on the lift and drag coefficient (a) lift coefficient,(b) drag coefficient and (c) lift-drag ratio (Kim et al. 2018).

Skillen et al. (2013) performed large-eddy simulation (LES) using different geometrical shapes. The leading-edge undulation reduced the separation and significantly increased the aerodynamic performance as shown in Fig. 2.16. The reduction in the separation region is as a result of the influence of the trough and the decrease in the production term in the peaks of the leading-edge undulation. The simulation was carried out using NACA 0021 profile at a Reynolds number of 1.2×10^5 and an angle of attack of 20°.

In addition, the tubercles considerably reduce the size of the recirculating zone downstream of the separation (Kumar et al. 2018) using the NACA 0012 aerofoil profile. By adding leading-edge tubercles to NACA 4415 at a low Reynolds number of 1.2×10^5, the modified aerofoil maintained an attached flow of up to 50% of the chord. At the same time, the unmodified case suffered

complete separation starting from the leading edge (Sudhakar et al. 2019). Undulated NACA 0012 wing cases were found to reduce the circulation of the wingtip vortex by 25% (Loughnane et al. 2021).

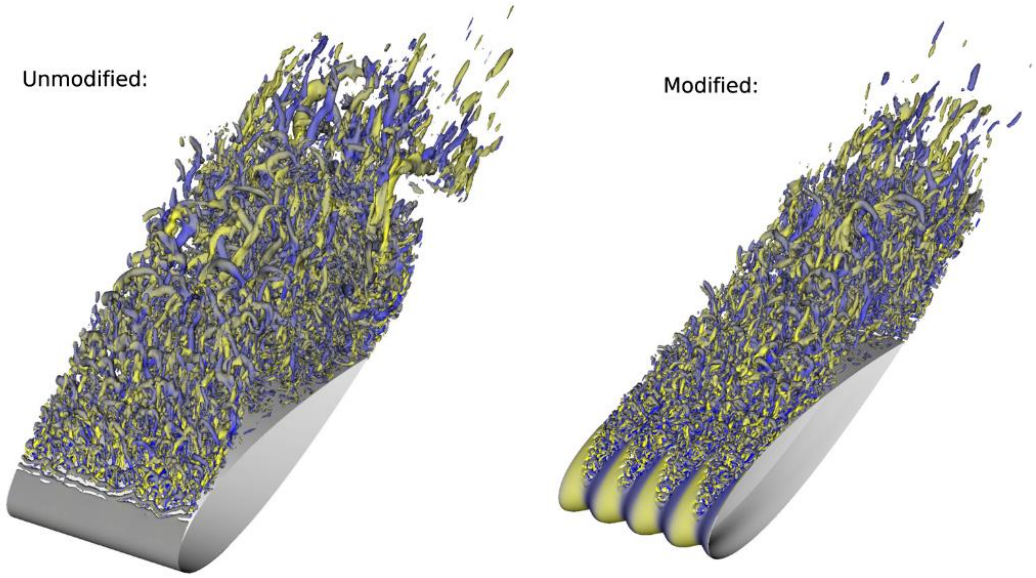

Fig. 2.16: The disintegration of the vortex structure by the leading-edge undulation effect (Skillen et al. 2013).

According to the investigation by Johari et al. (2007), the magnitude of the protrusions of the NACA 63_4-021 wing negatively impacted the aerofoil's efficiency, see Fig. 2.17. The modified wing demonstrated a degraded lift and drag coefficient in the pre-stall region identified from the unmodified aerofoil. After the post-stall of the unmodified wing, however, the modified undulation case indicated an increase in the lift coefficient, with the drag coefficient remaining unchanged. The NACA63_4-021 aerofoil modified with leading-edge protrusion at the Reynolds number of 2×10^5 demonstrated enhanced performance, especially at the post-stall angles, compared to the unmodified configuration (Zhang et al. 2013). However, by optimising the amplitude and wavelength of the tubercles using the NACA 63_4-421 aerofoil profile, the pre-stall lift performance can approach the values of an unmodified aerofoil (Lobo et al. 2020).

An experiment by Van Nierop et al. (2008) found that the delay in the stall was independent of the undulation wavelength, see Fig. 2.17. Jack Fish's study reveals that the swimmer's performance can be enhanced through undulation

with larger wavelengths, resulting in improved thrust production by the caudal fin, reduced drag production and power consumption by the trunk (Khalid et al. 2021). Su et al. (2021) demonstrated that an oscillating blade at the right wavelength could boost diffusion and reduce pressure loss by 12.9% at an 8° angle after stall. The undulation frequency and the Reynolds number affect the aerodynamics of the snake-like model. Increasing the undulation frequency stabilises the vortex, whereas increasing the Reynolds number intensifies lift production (Gong et al. 2022). A recent study conducted by Kim et al. (2022) revealed that the most effective way to achieve optimal leading-edge undulation (LEU) using NACA 65(12)-10 aerofoil is through a combination of 30% wavelength (λ/c) and 6% amplitude (h/c). This approach considers the aerodynamic performance and noise reduction, resulting in the best possible outcome.

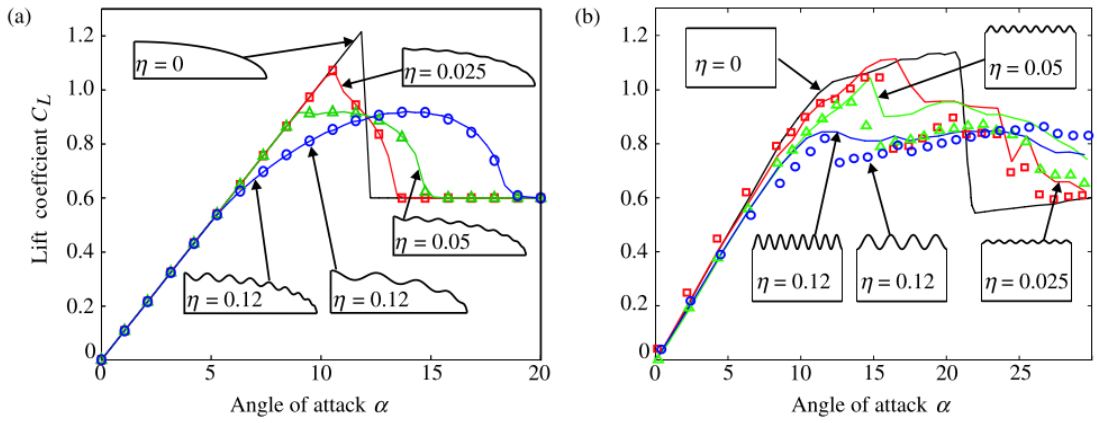

Fig. 2.17: The effect of different undulation magnitudes on the lift and drag performance (a) Van Nierop et al. (2008), (b) Johari et al. (2007).

2.6 Chapter Summary

The literature examines the latest developments of flow around the vertical tailplane. The major concern related to the flow over the VTP is associated with widespread separation effects from the laminar separation bubbles to the turbulent separation at the trailing edge. The design of the VTP consists of the vertical stabiliser and the rudder separated by the hinge line. The rudder deflection makes the flow complex because, at low side slip angles, the flow will experience separation due to rudder deflection.

The causes of the separation around the leading and trailing edges have been investigated based on the RANS and LES models. The numerical attempt does not seem different in analysing the effect of separation on the surface of the vertical tailplane. The focus of the RANS simulation was mostly based on preliminary findings because the models are unsuitable for high-fidelity investigation of the separation effect around the vertical tailplane. However, the recent development of the RANS transition models has changed the story of the inability of the RANS models to predict the earlier transition and laminar separation bubbles. Several transition models were found worthy of predicting the laminar separation bubble compared to the experimental data, LES and DNS simulation.

The high-fidelity simulation using the hybrid RANS/LES to utilise the pure LES simulation has been reported compared to the RANS models. Furthermore, the superiority of the LES models over the RANS models in predicting the separation models has been thoroughly investigated. There is no argument about the ability of the high-fidelity simulation to produce better predictions of the boundary layer separation and reattachment of the turbulent separation. The impact of these parameters was observed to contribute negatively to the performance of the VTP.

This study aims to investigate the impacts of separation around the vertical tailplane at low Reynolds numbers and explore strategies for mitigating these effects using various passive flow controls.

3. Chapter three

NUMERICAL METHODS

3.1 Introduction

This chapter provides an overview of the general CFD methodology employed in the analysis of fluid flows. CFD is a powerful tool for researchers, offering insights into the behaviour of fluids. The initial stage of the CFD process involves pre-processing, where the emphasis is on design considerations and mesh generation. Design considerations include defining the system's geometry under study, and mesh generation. The computational domain was discretised into grid elements, with careful attention to refining the mesh areas of particular interest, such as regions where flow separation is expected. Specifying boundary conditions, and selecting appropriate models for turbulence and other physical phenomena

The processing stage is the second stage of the CFD methodology, and it involves crucial aspects of the solver setup. The solver numerical algorithm is configured to solve the governing equations of the fluid flow. The spatial and temporal discretisation are also determined. Spatial discretisation involves dividing the computational domain into finite volumes, while temporal discretisation addresses the time-stepping approach for simulating transient flows. The careful selection of these parameters is vital to achieving computational efficiency and accurate results.

The Navier-Stokes equation is expressed in terms of the mass and momentum conservation over time and space. It is fundamental in most fluid flow problems, including turbulence modelling simulation. Therefore, the equations' inherent complexity necessitates additional modelling for turbulent flows. The Reynolds-average Navier-Stokes equation RANS are restricted to averaging the Navier-Stokes equation over time. This leads to the decomposition of the Navier-Stokes equation, which provides the basis of the RANS and LES equations. RANS offers a time-averaged representation of turbulent flows, while LES captures large and filtered small turbulent scales. Understanding these equations is important for selecting an appropriate turbulence model in CFD simulations.

The final stage of CFD methodology focuses on the geometry description, offering insights into the design parameters governing the vertical tailplane structure. This stage provides a detailed examination of the physical characteristics and specifications influencing the aerodynamic performance and structure of the vertical tailplane. Each stage, from pre-processing to the intricate details of turbulence modelling and geometry description, contributes to understanding fluid flow simulations.

3.2 Simulation Design

In this project, the Ansys Fluent Finite volume software package is used to test against the baseline and flow control concepts results obtained from the wind tunnel experimental data. The vertical tailplane model is employed as a test case; it is essential to accurately estimate and resolve the complex airflow around the vertical tailplane. The Fluent software utilises the Reynolds-averaged Navier-Stokes Equation and Large Eddy simulation to compute the airflow field over the tailplane structure. The CFD approach using turbulence modelling has significantly increased confidence in aerospace studies, particularly regarding verification and validation with experimental data (Bardina et al. 1997; Mereu et al. 2019; Yossri et al. 2021).

The mesh for the RANS simulation was generated around the vertical tailplane. Five different meshes were generated for the sensitivity study, highlighted in section 4.2. In this stage, the results obtained from the meshes are compared with the experimental data. A different mesh was generated for the LES part, and the simulation results are compared to the experimental data and the RANS results for the force coefficients, as shown in Fig 4.12.

3.3 Solver Selection

Solving fluid flow problems in computational fluid dynamics (CFD) requires the selection of an appropriate solver that can accurately and efficiently simulate fluid behaviour within the Fluent code. One of the most used solvers is the pressure-based solver. However, this solver has two variants: the segregated solver and the coupled solver.

Here, we focus on the coupled solver and how it differs from the segregated solver. The coupled solver is a pressure-based solver that simultaneously solves both the momentum and continuity equations. This solver does not

require a pressure correction equation, a significant advantage over the segregated solver (Riella et al. 2019). By not requiring a pressure correction equation, the coupled solver can accelerate the convergence process, leading to faster and more efficient simulations (Pascau et al. 1996). Therefore, the coupled solver requires less computational time to achieve convergence than the segregated solver. This is because the coupled solver solves both the momentum and continuity equations simultaneously, which leads to faster convergence. Moreover, the coupled solver is more effective than the segregated solver on structured grids.

However, there are some drawbacks to using the coupled solver. One of the most significant disadvantages is that it requires additional memory compared to the segregated solver (Guo et al. 2022). This is because the coupled solver simultaneously solves the momentum and continuity equations requiring additional memory. Additionally, the energy and turbulence equations are independently solved, which can lead to inaccuracies in some simulations. Despite these drawbacks, the coupled solver is widely used in CFD simulations, particularly in cases where faster convergence is needed.

The coupled solver has been the subject of numerous studies, and researchers have proposed several modifications to improve its performance and reduce its memory requirements. Falk and Schäfer (2013) developed a modified version of the coupled solver that reduces memory requirements while maintaining accuracy. Their modification uses a multi-grid approach to decrease the number of iterations required to achieve convergence. This approach reduces solver memory requirements while maintaining accuracy, making the coupled solver a powerful tool for CFD fluid flow simulations.

3.4 Governing Equations

The Navier-Stokes equation serves as a foundational expression for the conservation of momentum in fluid flow, applicable across a range of problems, including those involving turbulence modelling simulations. However, the inherent complexity of turbulent flows prompts the need for modelling.

Reynolds-averaged Navier-Stokes equations (RANS) address this complexity by averaging the Navier-Stokes equation over time. RANS provides a time-averaged representation of turbulent flows, while LES resolve the larger and modelled the smaller turbulent scales. Understanding this equation becomes crucial in selecting an appropriate turbulence model for CFD simulations.

The continuity equation and the Navier-stokes equation is given as follows:

$$\frac{\partial \rho}{\partial t} + \frac{\partial}{\partial x_i}(\rho u_i) = 0 \tag{3.1}$$

$$\frac{\partial}{\partial t}(\rho u_i) + \frac{\partial}{\partial x_j}\left(\rho u_i u_j\right) = -\frac{\partial p}{\partial x_i} + \mu \frac{\partial^2 u_i}{\partial x_j \partial x_j} \tag{3.2}$$

3.4.1 RANS Method equations

The RANS equations are derived from the decomposition of Eq. (3.1) and (3.2) This decomposition process is termed as the Reynolds decomposition and that makes the RANS equation time-averaged over the fluid flow.

$$\varphi = \bar{\varphi} + \varphi' \tag{3.3}$$

Equation (3.3) shows the decomposition of the instantaneous components φ in terms of the average $\bar{\varphi}$ and fluctuating components φ'. The quantities here are presented in a scalar and vector form where φ can be velocity, pressure, or other flow variables. The Navier-Stokes equations are differential equations describing the motion of fluids. After the substitution of the decomposed components, the time average of the continuity and momentum equations with the mean overbar is given in Eq. (3.4) and Eq. (3.5), respectively. These

equations are the outcome of the Reynolds decomposition where the mean fluctuation components are zero.

$$\frac{\partial \rho}{\partial t} + \frac{\partial}{\partial x_i}(\rho \overline{u_i}) = 0 \tag{3.4}$$

$$\frac{\partial}{\partial t}(\rho \overline{u_i}) + \frac{\partial}{\partial x_j}\left(\rho \overline{u_i}\overline{u_j}\right) = -\frac{\partial \bar{p}}{\partial x_i} + \frac{\partial}{\partial x_j}\left[\mu\left(\frac{\partial \overline{u_i}}{\partial x_j} + \frac{\partial \overline{u_i}}{\partial x_j} - \frac{2}{3}\delta_{ij}\frac{\partial \overline{u_i}}{\partial x_i}\right)\right] + \frac{\partial}{\partial x_j}\left(-\rho\overline{u_i u_j}\right) \tag{3.5}$$

Equation (3.5) shows that there is a term $-\overline{\rho u_i' u_j'}$, which accounts for the effect of non-linearity due to turbulence known as the Reynolds stress. The Reynolds stress must be modelled to close the equation.

3.4.2 LES Simulation

In the LES simulation, the average quantities in the Navier-Stokes filtered the small scale. In other words, the large scales are resolved while the small scales less than the filter are filtered using the subgrid scales (SGS). The filtering is vital in this aspect as it ensures that the resolution of the large scales is accurately resolved, denoting the filtered quantities by hat (^), the residual stress τ_{ij} and the filtered Navier-Stokes equation are given by the following equation.

$$\tau_{ij} \equiv \rho\widehat{u_i u_j} - \rho\widehat{u_i}\widehat{u_j} \tag{3.6}$$

$$\frac{\partial}{\partial t}(\rho\widehat{u_i}) + \frac{\partial}{\partial x_j}\left(\rho\widehat{u_i}\widehat{u_j}\right) = -\frac{\partial \hat{p}}{\partial x_i} + \frac{\partial}{\partial x_j}\left[\mu\left(\frac{\partial \widehat{u_i}}{\partial x_j} + \frac{\partial \widehat{u_i}}{\partial x_j} - \frac{2}{3}\delta_{ij}\frac{\partial \widehat{u_i}}{\partial x_i}\right)\right] + \frac{\partial}{\partial x_j}\left(\rho\widehat{u_i u_j} - \rho\widehat{u_i}\widehat{u_j}\right) \tag{3.7}$$

3.5 Subgrid Scale Models

In LES, the subgrid models are employed to account for the unresolved scales. There are different methods used in the implementation of the subgrid models. However, the popular among the methods deals primarily with the eddy viscosity in the filtering processes of the unresolved scales. The approach is based on the Boussinesq assumption that the the subgrid eddy viscosity μ_t is given in terms of the subgrid stress tensor τ_{ij} and strain rate tensor $\hat{S}_{ij}$ as given in Eq. (3.8)

$$\tau_{ij} - \frac{1}{3}\tau_{kk}\delta_{ij} = -2\mu_t \hat{S}_{ij} \tag{3.8}$$

The strain rate tensor $\hat{S}_{ij}$ can be expanded in terms of the velocity components as follows:

$$\hat{S}_{ij} = \frac{1}{2}\left(\frac{\partial \widehat{u_i}}{\partial x_j} + \frac{\partial \widehat{u_j}}{\partial x_i}\right) \tag{3.9}$$

3.5.1 Smagorinsky Model

One of the widely used subgrid models was proposed by Smagorinsky (1963).The model is also based on the eddy viscosity introduced as a subgrid model to solve the unresolved scales of the LES. In this model the subgrid eddy viscosity is related to the subgrid strain rate and the mixing length.

$$\mu_t = (C_s\Delta)^2 \left|\hat{S}\right| \tag{3.10}$$

Where the C_s and Δ are the Smagorinsky constant and the filter width while $\left|\hat{S}\right| = \sqrt{2\hat{S}_{ij}\hat{S}_{ij}}$. The Smagoronsky constant can be adjusted depending on the application to ensure appropriate damping of the flow region. The constant initially derived by Smagorinsky is 0.23, and recent research has shown that a range of 0.05 to 0.5 can be suitable. However, in the Fluent LES set-up, it is believe that the 0.1 is good for most of the flows. The filter width given as the cube root of the volumes in three directions as $\Delta = \left(\Delta_x \Delta_y \Delta_z\right)^{1/3}$. Now, the subgrid eddy viscosity of the Smagorinsky model is given by:

$$\mu_t = (C_s\Delta)^2 \sqrt{2\hat{S}_{ij}\hat{S}_{ij}} \tag{3.11}$$

3.5.2 Dynamic Smagorinsky Model

The subgrid modelling is an approach used in fluid dynamics to estimate the effects of small-scale turbulent motion on larger scales. Germano et al. (1991) proposed a modification to this model, known as the dynamic Smagorinsky model, in which the constant used in the original model is allowed to vary with time during the simulation. One of the main issues with the original model is that the constant cannot account for significant dissipation in the flow. The dynamic Smagorinsky model addresses this problem by allowing the constant to change dynamically. In the modification, a second filter width was introduced which is called the test filter. The test filter should always be greater than the grid filter. In the Fluent solver is assumed to be twice the grid filter.

3.5.3 Wall-Adapting Eddy Viscosity (WALE) Model

The Smagorinsky model has been widely used, but there still exist some shortcomings associated to the model accuracy in different applications. However, this model finds it difficult to accurately predict smaller eddy viscosities, which can cause disturbances during transitions. Studies conducted by Kim et al. (2020) strengthened this concern. On the other hand, the Wall-Adapting Local Eddy-viscosity (WALE) model has proven to be particularly good at capturing the boundary and transition behaviour in the near-wall region (Weickert et al. 2010). This is primarily because of its unique ability to correct laminar zones and generate zero turbulent viscosity in the boundary layer region, which makes it a valuable approach. As highlighted by Arya and De (2019), the precision of the WALE model in these areas is unmatched, making it an essential tool for researchers and professionals in the field of fluid dynamics. The WALE model is effective with structured and unstructured meshes and is commonly used in complex geometries because it detects rotation and strain rates. The WALE sub-grid scale model proposed by Nicoud and Ducros (1999), compared to the Smagorinsky model, provides a higher production of subgrid turbulent kinetic energy and turbulent stresses in the near-wall region (Ren et al.2013).

The WALE model utilises a different velocity scale to overcome the limitation of the Smagorinsky model for calculating eddy viscosity as follows:

$$\mu_t=(C_w\Delta)^2\frac{\left(S_{ij}^dS_{ij}^d\right)^{3/2}}{\left(\hat{S}_{ij}\,\hat{S}_{ij}\right)^{5/2}+\left(S_{ij}^dS_{ij}^d\right)^{5/4}} \tag{3.12}$$

The S_{ij}^d is traceless tensor based on the velocity gradient tensor as:

$$S_{ij}^d=\frac{1}{2}\left(\widehat{g_{ij}}^2+\widehat{g_{ji}}^2\right)-{}^1\!/_3\left(\delta_{ij}\widehat{g_{kk}}^2\right),\ \text{where}\ \widehat{g_{ij}}=\frac{\partial\widehat{u_i}}{\partial x_j} \tag{3.13}$$

The WALE model coefficient constant is set to be $C_w = 0.325$

3.6 Discretisation Schemes

The relationship between the spatial discretisation schemes and the time discretisation schemes used in the Fluent code is fundamental in understanding how CFD simulations are conducted and how the numerical solutions to governing equations are obtained. The governing equations are solved using the Fluent code's finite volume method (FVM). The FVM discretises the computational volume into discrete control volumes, allowing the conservation of mass, momentum within each volume. The numerical results depend on the synergy between the spatial and time discretisation schemes where the spatial part ensures the accurate representation of the equations within the control volume. Meanwhile, the temporal part is ensuring the evolution of the flow over a time.

The finite volume method is a technique that uses divergence operators to solve conservation equations expressed as partial differential equations. This method involves applying the Gauss theorem and to convert volume integrals into surface integrals within the control volume. To achieve this, the computational domain that contains the cell elements is divided into finite cells within the control volume. Then, the variable values are assigned to the cell faces or volume centers after domain decomposition.

3.6.1 Spatial Discretisation Schemes

Different spatial discretisation schemes are available in the Fluent code. These schemes are usually represented using an upwind schemes interpolation of the cell centre values. The discretisation of the computational domain into smaller cells significantly influences the accuracy of the numerical solution. However, the choice of the discretisation scheme such as the first order upwind schemes and the central differencing schemes determines how the values at cell faces are interpolated. The selection of the schemes influences the continuity and momentum equations; therefore, a careful selection will minimise the numerical errors and ensure accurate discretisation of the flow physics.

Since the mesh adopted in this study is structured, the face gradients can be easily obtained using either the least square cell or the Green-Gauss node cells method. In the RANS simulation the least square method was used while in the LES simulation the Green-Gauss approach was employed to calculate the face gradients at the face centre of the cells.

The momentum equations for the pressure-based coupled solver were discretised using the bounded central differencing (BCD) scheme. This scheme is known for providing accurate results while being computationally efficient (Zhu and Rodi 1991). The BCD scheme represents a hybrid approach, where the features of the pure central differencing and upwind schemes are dynamically alternating. This approach effectively mitigates the disruptive oscillations exhibited by the pure central differencing. The strategic combination of central differencing and upwind elements and oscillation stabilising mechanism makes it vital in predicting turbulent structures.

3.6.2 Time Discretisation Schemes

This study employs distinct temporal discretisation techniques for Reynolds Averaged Navier-Stokes (RANS) and Large Eddy Simulation (LES), modifying the approaches to the inherent characteristics of each simulation. The implicit time step is used in the pressure-based solver utilised in this study, where the dual time stepping technique is often employed. Like the spatial discretisation schemes the temporal aspect is divided into discrete intervals,

where the choice of the time discretisation scheme affects the accuracy and stability of the simulation.

The steady-state pseudo-transient time discretisation method is implemented in RANS simulations, utilising the incomplete lower-upper factorisation (ILU). The pseudo-transient technique treats the RANS simulation as transient, employing a control time formulation to achieve comprehensive convergence toward a steady-state solution. The pseudo-transient steps applied through the ILU method contribute to robustly representing steady-state conditions in the RANS simulation.

The implicit and explicit schemes are two numerical methods with distinct features and advantages. The explicit scheme uses data from the previous time level only, making it simpler but less stable. In contrast, the implicit scheme uses data from the previous and the next time levels, leading to increased stability and the ability to use larger time steps, reducing simulation time. The explicit scheme's stability depends on constraints related to the smaller time step size and the courant number.

Conversely, the nature of the LES simulations being inherently transient calls for the application of implicit dual time stepping as a temporal discretisation strategy. The time discretisation accuracy used is the bounded second-order implicit time integration. This method involves a sequence of iterations within each time step, characterised by its dual nature. The flexibility of conducting numerous iterations per time step, using a defined time-step size (Δt), aligns with LES simulations' dynamic and transient nature, ensuring accurate depiction of the evolving flow conditions. The technique is highly recommended particularly in capturing transitional flow behaviour without compromising the computational stability and accuracy.

In the context of steady-state simulation, an implicit formulation of the linearised equation utilises a combination of the Euler implicit discretisation and the Newton linearised equation for time discretisation. This steady-state time discretisation approach effectively achieves the governing equations' convergence.

The temporal discretisation process is accomplished when the system reaches a steady state. The governing equations no longer exhibit significant changes in this scenario, indicating a stable and unchanging pattern. This achievement signifies the completion of the simulation process. The pseudo-transient method is employed to regulate the pseudo-time step behaviour of the flow in steady-state simulations. This method acts as a control mechanism, influencing the convergence behaviour by adjusting the pseudo-time step. By implementing the pseudo-transient method, the simulation ensures stability and accuracy in capturing the steady-state conditions, contributing to the reliability of the overall numerical solution.

Implicit-time stepping denotes a simulation technique featuring dual time stepping for unsteady conditions. This approach finds its application primarily in scenarios characterised by unsteady turbulence behaviour, especially in the context of flows exhibiting low Mach numbers.

3.7 Turbulence Models

An incompressible steady-state simulation is performed using RANS models. The RANS models used throughout this study include the one-equation Spalart-Allmaras model, two-equation models k-ω SST and k-ε and the transition three-equation model k-kl-ω. All the models are available in the Fluent flow solver. Here, the details of the model's transport equations and constants utilisation in the solver are given in detail. From Eq.3.2 of the RANS equation, the Boussinesq hypothesis is used to relate the Reynolds stress and the mean velocity gradients as follows:

$$-\rho\overline{u_i' u_j'} = \mu_t \left(\frac{\partial \overline{u_i}}{\partial x_j} + \frac{\partial \overline{u_j}}{\partial x_i} \right) - \frac{2}{3} \left(\rho k + \mu_t \frac{\partial \overline{u_k}}{\partial x_k} \right) \delta_{ij} \tag{3.14}$$

3.7.1 Spalart-Allmaras Model

The Spalart-Allmaras equation is one of the eddy-viscosity models specifically designed for aerodynamic flow at a low Reynolds number. Spalart and Allmaras (1994) developed the model, and the transport equation in terms of the turbulent kinematic viscosity is given in Eq. (3.15).

$$\frac{\partial}{\partial t}(\rho\nu_t)+\frac{\partial}{\partial x_i}(\rho\nu_t u_i)= G_v+\frac{1}{\sigma_v}\left[\frac{\partial}{\partial x_j}\left\{(\mu+\rho\nu_t)\frac{\partial \nu_t}{\partial x_j}\right\}+C_{b^2}\rho\left(\frac{\partial \nu_t}{\partial x_j}\right)^2\right]-Y_v+S_{\nu_t} \quad (3.15)$$

σ_v and C_{b^2} are constants while S_{ν_t} is a user-defined function. The turbulent viscosity value is given by G_v and Y_v. Where the G_v and Y_v represents the production and destruction of the turbulent viscosity. The turbulent viscosity is given using of the viscous damping function f_{v1} in Eq. (3.16) while the details of terms in Eq. (3.15) and Eq. (3.16) are detailed in Diskin and Galbraith (2023). The viscous damping function is given in Eq. (3.17).

$$\mu_t=\rho\nu_t f_{v1} \quad (3.16)$$

$$f_{v1}=\frac{\chi^2}{\chi^3+C_{v1}^3} \quad (3.17)$$

$$\chi \equiv \frac{\nu_t}{\nu}$$

3.7.2 Realizable k- ε model

The realisable k-ε is a two-equation eddy viscosity turbulence model proposed by Shih et al. (1995). The model was proposed to address the general shortcomings of the k-ε models in the dissipation rate modelling. The transport equations that have been modelled for the variables, namely k and ε in the realisable model, are as follows:

$$\frac{\partial}{\partial t}(\rho k)+\frac{\partial}{\partial x_j}(\rho k\bar{u_j})=\frac{\partial}{\partial x_j}\left[\left(\mu+\frac{\mu_t}{\sigma_k}\right)\frac{\partial k}{\partial x_j}\right]+G_k+G_b-\rho\varepsilon-Y_M+S_k \quad (3.18)$$

$$\frac{\partial}{\partial t}(\rho\varepsilon)+\frac{\partial}{\partial x_j}(\rho\varepsilon\bar{u_j}) = \frac{\partial}{\partial x_j}\left[\left(\mu+\frac{\mu_t}{\sigma_\varepsilon}\right)\frac{\partial \varepsilon}{\partial x_j}\right] +\rho C_1 S\varepsilon-\rho C_2\frac{\varepsilon^2}{k+\sqrt{\nu\varepsilon}}+C_{1\varepsilon}\frac{\varepsilon}{k}C_{3\varepsilon}G_b+S_\varepsilon \quad (3.19)$$

$$C_1 = max\left[0.43,\frac{\eta}{\eta+5}\right], \eta = S\frac{k}{\varepsilon}, S=\sqrt{2\bar{S}_{ij}\bar{S}_{ij}}$$

The turbulence model parameters include: G_k and G_b are the turbulence kinetic energies due to mean velocity gradients and buoyancy. Y_M represents the contribution of fluctuation in compressible turbulence to the overall dissipation rate. Constants C_2 and $C_{1\varepsilon}$ are integral, and σ_k and σ_ε indicate turbulent Prandtl numbers for k and ε. Additionally, user-defined source terms S_k and S_ε are incorporated in the model to account for external influences on the turbulence characteristics.

3.7.3 Shear Stress transport k-ω Model

The k-ω SST model is a two-equation model derived by Menter (1994) from combining the original k-ω model and standard k-ε model to enhance the flow on the wall surface. The k-ω SST model is a two-equation eddy viscosity model, proven robust and accurate in aerofoil research by Kandula and Wilcox (1995), was affirmed by earlier studies by Whitlock Mentor and Jones (1995) for multi-element aerofoils. In a recent numerical investigation by Fatahian et al. (2020) using Fluent software, the k-ω SST model demonstrated reliability, showcasing substantial agreement with experimental data in studying a three-element aerofoil. The transport equation for the k-ω SST developed by Menter is given as:

$$\frac{\partial}{\partial t}(\rho k)+\frac{\partial}{\partial x_i}(\rho k\bar{u}_i)=\frac{\partial}{\partial x_j}\left(\Gamma_k\frac{\partial k}{\partial x_j}\right)+G_k-Y_k+S_k \tag{3.20}$$

$$\frac{\partial}{\partial t}(\rho \omega)+\frac{\partial}{\partial x_i}(\rho \omega\bar{u}_i)=\frac{\partial}{\partial x_j}\left(\Gamma_w\frac{\partial \omega}{\partial x_j}\right)+G_w-Y_w+D_w+S_w \tag{3.21}$$

The generation of turbulent kinetic energy due the mean velocity is represented by G_k while the specific dissipation rate is given by G_w. Also, the effective diffusivity in terms of k and ω is given by Γ_k and Γ_w, D_w represents the cross-diffusion, which blends the k-ω model and standard k-ε model. S_k and S_w are user-defined functions.

$$D_\omega=2(1-F_1)\rho\sigma_{\omega,2}\frac{1}{\omega}\frac{\partial k}{\partial x_j}\frac{\partial \omega}{\partial x_j} \tag{3.22}$$

3.7.4 k-kl-ω Model

The transition k-kl-ω is developed purposely to improve the transition capture of the boundary layer development. It is considered a three-equation eddy viscosity turbulence model where the turbulent kinetic energy and laminar kinetic energy equations are given as K_T and K_L, respectively. The third equation of ω is considered as the inverse turbulent time scales. The transition k-kl-ω models are more complex than conventional models because of the additional equation that enhances transition onset development. The model was developed by Walters and Cokljat (2008), and the model was tested for a variety of applications, including aerofoils. The aerofoil results show improvement in the prediction of the transition onset compared to the conventional turbulence models. The equations of the turbulent kinetic energy K_T, the laminar kinetic energy K_L, and the inverse turbulent time scale are given as follows:

$$\frac{Dk_T}{Dt} = P_{K_T} + R + R_{NAT} - \omega k_T - D_T + \frac{\partial}{\partial x_j}\left[\left(\nu + \frac{\alpha_T}{\alpha_k}\right)\frac{\partial k_T}{\partial x_j}\right] \tag{3.23}$$

$$\frac{Dk_L}{Dt} = P_{K_L} - R - R_{NAT} - D_L + \frac{\partial}{\partial x_j}\left[\nu \frac{\partial k_L}{\partial x_j}\right] \tag{3.24}$$

(3.25)

$$\frac{D\omega}{Dt} = C_{\omega 1}\frac{\omega t}{k_T}P_{k_T} + \left(\frac{C_{\omega F}}{f_W} - 1\right)\frac{\omega}{k_T}(R + R_{NAT}) - C_{\omega 2^2}\langle\omega^2$$
$$+ C_{\omega 3} f_\omega \alpha_T f_W^2 \frac{\sqrt{k_T}}{d^2} + \frac{\partial}{\partial x_j}\left[\left(\upsilon + \frac{\alpha_T}{\alpha_{wj}}\right)\frac{\partial \omega_j}{\partial x_j}\right]$$

3.8 Geometry Model Design.

This study uses the 3D VTP geometry, modified for the flow control cases involving a leading-edge slat and undulation. The same geometry is used for experimental wind tunnel tests and numerical simulations. The scaled model from the experiment is adopted throughout the study to compare numerical simulation with experimental data easily. The test model is selected to fit in the wind tunnel facility, with a span of 0.4m, essentially the height of the VTP in the spanwise direction, as highlighted in Fig. 3.1 (a).

A symmetrical aerofoil is required for the vertical tailplane structures, which makes the rudder and stabiliser symmetrical. Although the stabiliser will be fixed while the rudder is deflected, the symmetrical behaviour is translated to both ends. The rudder chord is 30% of the overall chord, and the largest rudder deflection of 30° was considered in this study to investigate the separation behaviour of the VTP further. The NACA 6410 aerofoil shape used in this study is a symmetrical aerofoil that produces no lift at an angle attack of zero. Fig. 3.1 (c) indicated a 2D symmetrical aerofoil profile of the VTP with a sharp trailing edge. For reference and traceability of the airfoil geometry, please see Appendix A.

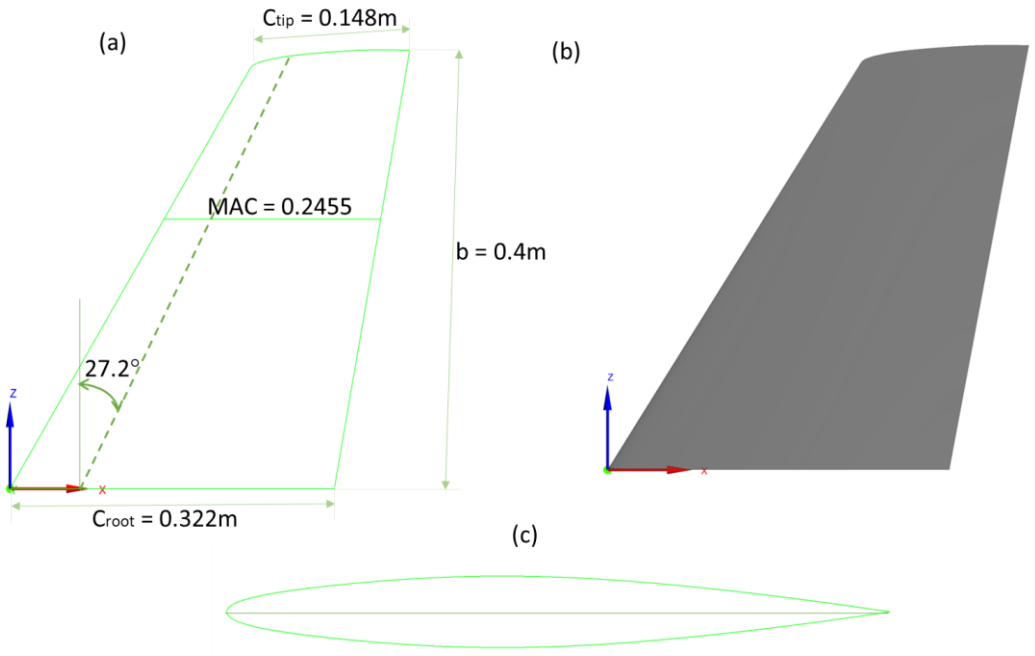

Fig. 3.1: (a)Planform, (b) 3D Geometry and (c) Symmetrical aerofoil profile of the VTP with sharp trailing edge.

Table 3.1: VTP parameters.

Trapezoidal dimensional parameters	
Span (b) [m]	0.4
Root chord [m]	0.322
Tip chord [m]	0.148
Sweep (1/4) [°]	27.2
Dihedral [°]	0
Surface [m]	0.375
Aspect Ratio	0.425
Taper Ratio	0.46
Trapezoidal MAC [m]	0.2455

3.9 Mesh Generator

In computational fluid dynamics (CFD), mesh generation is crucial for accurate simulations, particularly in capturing intricate flow phenomena. This study utilized the Gambit meshing tool to create a structured mesh focused on the VTP region. Gambit provided a comprehensive platform for mesh development, ensuring the integrity and completeness of the VTP CAD model.

A notable advantage of Gambit is its control over meshing, particularly in clustering hexahedral elements around the VTP surface, essential for turbulence modelling. This practice adhered to the best practices in LES mesh generation, aiming for high-quality meshes. Special emphasis was placed on LES mesh refinement around the VTP, strategically applied in streamwise, wall-normal and wake regions.

Understanding the pivotal role of mesh quality in CFD studies, this investigation prioritised mesh refinement along the leading and trailing edges of the tail as shown in Fig. 3.2 (a,b). The Gambit tool, central to this study offered flexibility, control, and precision in creating structured meshes. The hexahedral mesh, though time-consuming, was recommended for LES due to its advantages in reducing simulation time and providing high resolution.

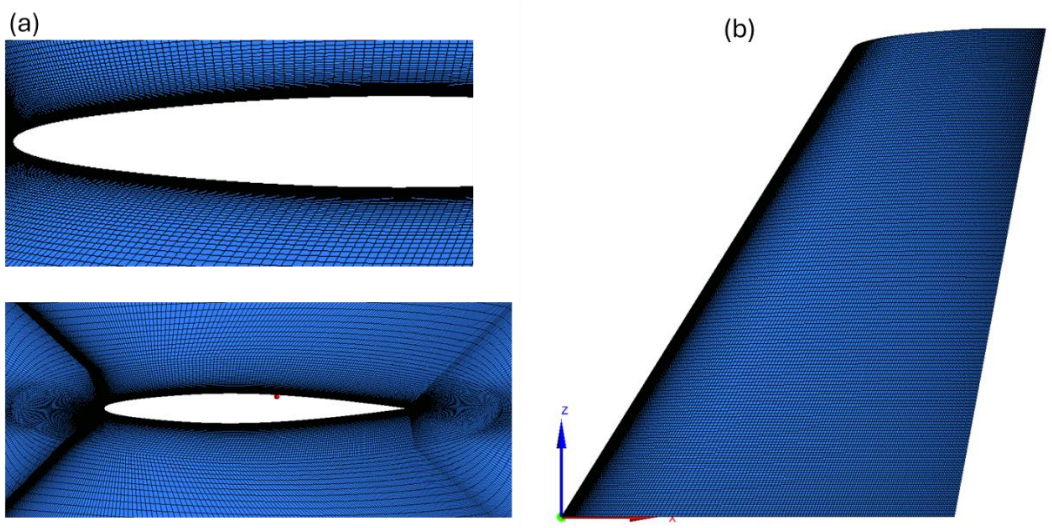

Fig. 3.2: (a) Symmetrical aerofoil Profile of the VTP with the zoom leading edge mesh refinement, (b) 3D view of the mesh Geometry.

Despite the advantages of hexahedral mesh, such as reduced simulation time, it lacks the flexibility to easily adapt to mesh elements and geometry changes compared to the tetrahedron mesh approach. However, the consistent arrangement of elements and internal angles in the hexahedral mesh proved beneficial for achieving high resolution in scale-resolving simulations (see Fig 3.3(a).

The VTP is enclosed in a domain-like rectangular shape representing the wind tunnel set-up (see Fig 3.3 (b). In this study, the wind tunnel size was found to be smaller to be reflected in the numerical domain. Therefore, the domain was extended in both directions to ensure a stable simulation run with better accuracy. The wind tunnel size results in an unstable simulation with a reverse flow generated due to insufficient wake region size.

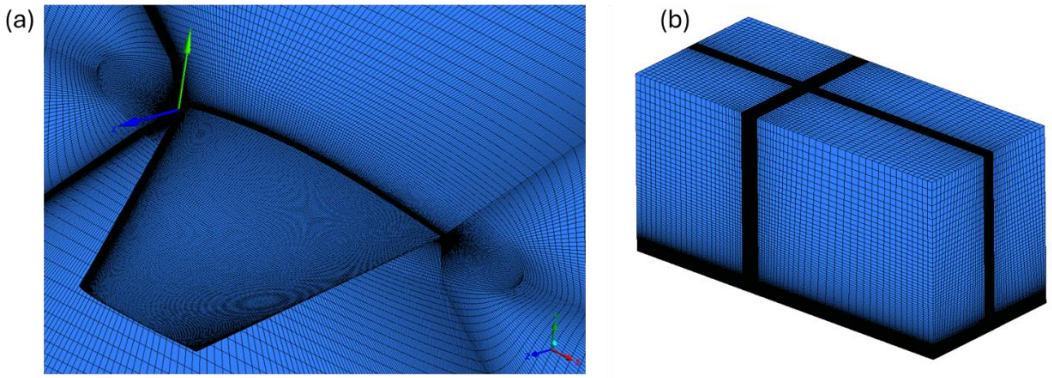

Fig. 3.3: The VTP with the zoom mesh refinement in the computational domain (a), 3D view of the domain mesh (b).

The computational domain is assigned a boundary condition to facilitate the simulation run. In this large computational domain, the inlet is assigned a boundary condition of velocity inlet where the turbulence level and other parameters are entered. A pressure outlet was assigned conditions similar to the velocity inlet conditions on the outlet side. For the computational domain, one wall was assigned with a slip condition close to the root of the VTP to ensure an effect on the boundary layer. The VTP is assigned as a no-slip condition while the other walls are all assigned to freestream conditions because the computational domain is large enough to reflect any impact.

3.10 Computing Cluster

The simulation process for the VTP was conducted using the high-performance computing (HPC) facility at the University of Nottingham. The Augusta HPC facility is equipped with both cloud and on-premise computing capabilities. It comprises 4,700 cores, 31 TB of RAM, and 6 GPUs with 750 TB of storage dedicated to GPU users. All RANS and LES simulations were performed using the Augusta HPC facility at the University of Nottingham. The suitable partitions utilised during the simulation process are presented in Table 3 below.

Table 3.2: Augusta HPC partitions.

Partition Name	Number of Nodes Available
defq	Each compute node has 40 cores. There are 90 nodes available in this partition with usable memory of 179 GB. A job can run for a maximum of 168 hours.
mmemq	There are 12 nodes in this partition with usable memory of 755 GB. A job can run for 168 hours
hmemq	This is a high memory compute node with only 1 node of 80 cores. A job can run for 168 hours with a usable memory of 1476 GB
Shortq	This partition can run only for 12 hours with a usable memory of 179 GB. The partition contains 12 nodes of each 40 cores.

High-Performance Computing (HPC) performance is crucial for simulations involving many nodes. This study's typical LES study with approximately 22 million cells is computed using 96 cores. On average, it takes two weeks to complete the simulation, excluding waiting time or IT maintenance. However, each job can only run for 7 days before exiting automatically. Consequently, jobs must be resubmitted to achieve solution convergence.

3.11 Chapter Summary

This chapter explores the numerical methods used to implement the simulation processes. The numerical methodology is based on the Ansys Fluent code in solving flow fields over the VTP using different turbulence modelling and scale-resolving techniques.

The design of a simulation is critical to the simulation process. It involves preparing various stages, from pre-processing to post-processing, to ensuring the replicability of wind tunnel experimental data results. Each stage is considered carefully to achieve accurate results.

In the simulation process, selecting the right solver should be based on the designed parameters. Since the flow is incompressible, a pressure-based coupled solver should suffice to investigate the flow field around the VTP.

The Navier-Stokes governing equations are solved for both the RANS and LES models. In the RANS model, extra equations of the turbulence models are solved along with the continuity and momentum equation. In LES, the selection and implementation of the subgrid model are critical to account for the unresolved scales. A thorough analysis of the modes was conducted, and the WALE was selected due to its advantages in returning the asymptotic viscosity to zero compared to the existing models.

The simulation can only run with the combination of the spatial and temporal discretisation schemes. Both schemes were carefully selected for a better solution method and stability of the simulation.

A detailed overview of the geometry model and mesh generation methods was given. Mesh generation is the most crucial part of the pre-processing process, particularly in the case of scale-resolving LES simulation. The hexahedral mesh was implemented throughout for better resolution and faster running time compared to the tetrahedron approach.

4. Chapter four

BASELINE RANS AND LES SIMULATION WITHOUT RUDDER DEFLECTION

4.1 Introduction

This chapter investigates the Reynolds-averaged Navier-Stokes equation RANS using various turbulence models, which are crucial for assessing the flow performance over the VTP. The RANS is commonly employed when the goal is to determine aerodynamic coefficients (Catalano and Amato 2003), as outlined in Chapter 2 of the literature.

The consideration of the RANS is also valid for industrial applications, where the aim is to solve the side force and drag force coefficients (Corson et al.2009; Bush et al. 2019). Four turbulence models were utilised to analyse the flow over the VTP, and their performance was thoroughly investigated. The one-equation model (S-A), two-equation models k-ω SST and k-ε, and transition model k-kl-ω were selected to ensure a thorough investigation of the aerodynamic predictions and characteristics of the flow physics. All the turbulence models were tested for different sideslip angles from the lower to the higher sideslip angles (-10° to 30°). The performance of these turbulence models was compared with the wind tunnel experimental results based on the force coefficient at different sideslip angles. The comparison shows how all models predicted the side and drag force coefficients. The one-equation Spalart-Allmaras (S-A) model, two-equation models k-ω SST and k-ε, and transition k-kl-ω model used in this study have proven to be effective in evaluating aerodynamic performance, particularly in the pre-stall condition, where the separation effect is not prevalent (Hassan et al. 2022).

This chapter is a prerequisite to the present study's main objective, which is to use a high-fidelity simulation to capture the separation and utilisation of strategies to reduce their effects on the performance of the VTP. The expectation is always preliminary in this study, as the objective was far from the capabilities of the turbulence models using RANS. However, as expected, all turbulence models demonstrated a good prediction of the aerodynamic coefficients in the attached flow. The transition models performed better in terms of aerodynamic prediction and showed the presence of a laminar separation bubble at the leading edge of the VTP. At rudder deflection angle δ

= 0°, the flow separation effect cannot be fully understood, as the flow remains attached at even large sideslip angles.

One of the main objectives of this study was to utilize strategies to understand the complex flow phenomena around the VTP. Since the RANS computation is not accurate enough to compute the global flow separation phenomenon and velocity fluctuations (Wokoeck et al. 2006), a LES simulation was also used. A baseline LES simulation was conducted without rudder deflection and was compared with RANS and experimental data to verify and validate the simulation. Additionally, three different sideslip angles were considered for the LES to show the impact of separation at a lower sideslip angle, medium sideslip angle, and higher sideslip angle, which is the stall angle. These analyses demonstrated the effect of separation and how it can be controlled using slat and leading-edge undulation flow control devices in Chapters 5 and 6, respectively. In general, this chapter is prepared to achieve a preliminary flow study over the VTP using different turbulence models and LES to be utilised in the flow control study to investigate the flow structures and fluctuations thoroughly.

This chapter also discusses the mesh sensitivity analysis of the RANS computation to ensure accurate results. Five meshes with refinement in the streamwise, spanwise, and wall-normal directions were used for the analysis. However, comparing the side-force Cs, drag-force coefficients Cd, and surface pressure coefficient for different meshes highlights the importance of mesh refinement (Ahmed et al.1998). Therefore, systematic mesh refinement is crucial for obtaining precise simulation results (Lu et al.2021).

4.2 Mesh Sensitivity Analysis

Performing a mesh sensitivity analysis is an integral part of the simulation process, as it helps evaluate the accuracy of the results (Siddharth et al.2016). This analysis involved testing various meshes to ensure that the simulation outcomes were independent of the grid size. The objective was to verify that the results remained consistent regardless of the number of grid points. A fully structured mesh was employed, which usually provides a closer comparison to the experiment than an unstructured mesh, as Karkoulias et al. (2022) recently observed.

This study employed five distinct meshes with refinements in the streamwise, spanwise, and wall-normal directions. The initial cell height was determined based on the flow parameters specified by the boundary conditions. Table 4.1 provides detailed information on the five meshes used, such as the number of cells generated, growth rate factor, wall y^+, first cell height. The y^+ is the dimensionless wall distance of the grid spacing. At the same time, the growth factor is a parameter used to control the grid refinement from the region of interest where the fine mesh is desirable to the area where global coarsening of the mesh is enough.

It is worth noting that a consistent growth rate was maintained when the wall y^+, was varied in all cases. This allowed us to obtain detailed information on the sensitivity of the results to mesh parameters. The results of this study provide a comprehensive understanding of the influence of mesh parameters on simulation results. These can be used to optimise the mesh size for future simulations.

To analyse the aerodynamic forces and transition behaviour associated with turbulence for the VTP, we conducted a comprehensive grid study using the k-kl-ω transition, known for its robustness (Rahimi et al. 2014). The model can predict the laminar separation bubble by considering the natural and bypass transition mechanisms and accounting for the production and dissipation terms (Mishra et al.2019). The results of our study show that a finer mesh contains nearly four times more cells than a coarser mesh. Different meshes are summarised in Fig. 4.1 to indicate the resolution of the mesh refinement. Similarly, the surface y^+ of the meshes shown in Fig. 4.1 are illustrated in Fig. 4 .2.

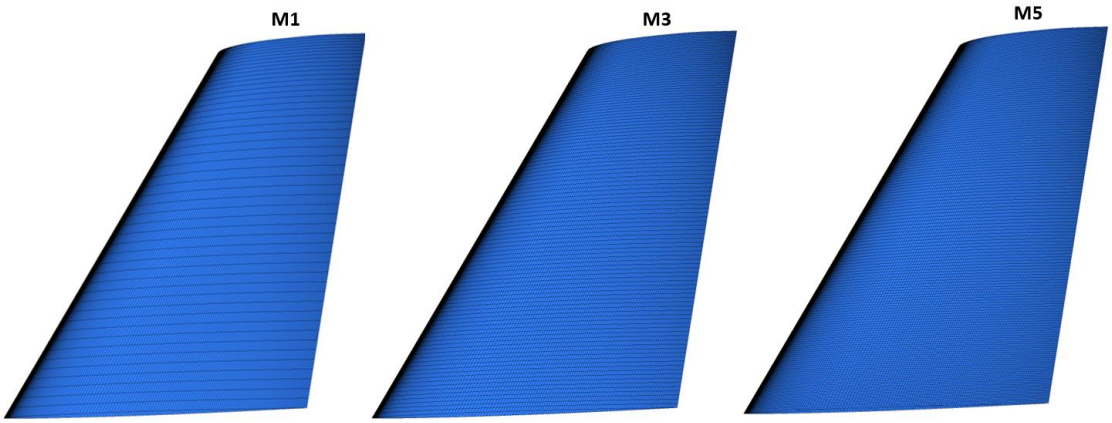

Fig. 4.1: Mesh refinement of three different meshes on the VTP.

Table 4.1: Details of meshes used for sensitivity analysis.

Mesh	Number of cells	Growth Factor	Height of the First cell	Corresponding y^+
M1	5,870,000	1.08	1.27×10^{-4}	7.3
M2	8,610,000	1.08	4.96×10^{-5}	3.5
M3	12,800,000	1.08	1.43×10^{-5}	1.14
M4	16,307,000	1.08	1.41×10^{-5}	1.15
M5	20,800,00	1.08	2.92×10^{-6}	0.25

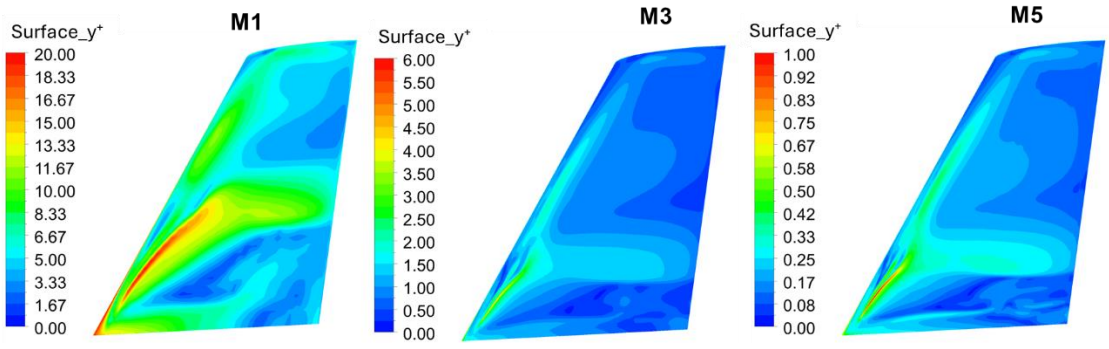

Fig. 4.2: Corresponding Surface $\mathbf{y^+}$ of three different meshes on the VTP.

This study aimed to assess the effectiveness of five distinct meshes by analysing the side force and drag force coefficients at a sideslip angle of β = 10°. The results of this analysis are shown in Fig. 4.3. This finding demonstrated that coarse mesh M1 overestimated the side force and drag force coefficients owing to fewer nodes associated with streamwise and spanwise directions. However, M2 and M3 demonstrated enhanced Cs values, with M3 predicting Cd values similar to the refined meshes of M4 and M5. This indicated that after M3, all meshes became grid-independent with respect to the Cs and Cd values. The impact of mesh refinement in the spanwise direction can be observed in M4, where additional refinement in the wall-normal direction did not alter the force coefficient values. It is concluded that mesh refinement must be systematically executed to ensure that the grid refinement in the streamwise, spanwise, and wall-normal directions does not impact the solution. It was also observed that the side force and drag force coefficients did not depend on the mesh density from M3, which was also reported in a different study by Rogowski et al. (2021), where the lift and drag coefficient behaviour was consistent when the mesh density satisfied the governing equations.

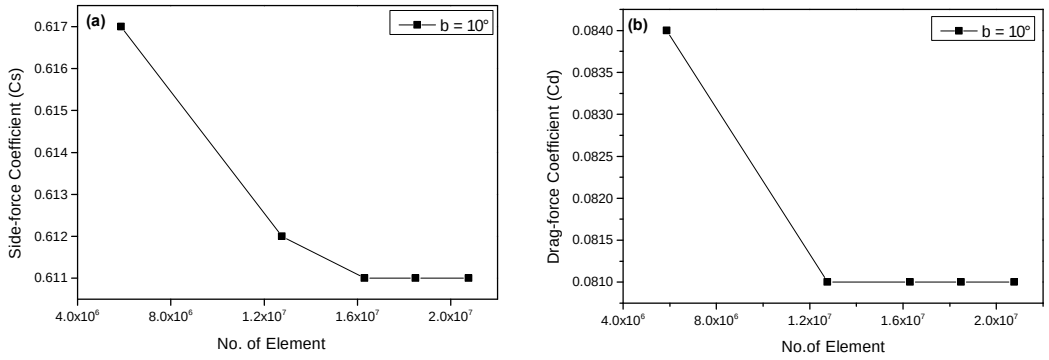

Fig. 4.3: Comparison of side-force Cs (a) and drag force Cd (b) coefficients of five different meshes.

Figure 4.4 details the surface pressure coefficients of four distinct meshes. Compared to the other three meshes, the M1 coarse mesh displays an overshoot pressure coefficient along the mid-span on the stabiliser leading edge. This is because of the low node count in both directions; there is not enough streamwise and spanwise node count, so there is a higher prediction of

Cs and Cd. The spanwise cut sections for η = 0.15 and η = 0.75 in Fig. 4.5 display (-Cp) was under-predicted, as shown in Fig. 4.5 (b), particularly in the area closer to the tip.

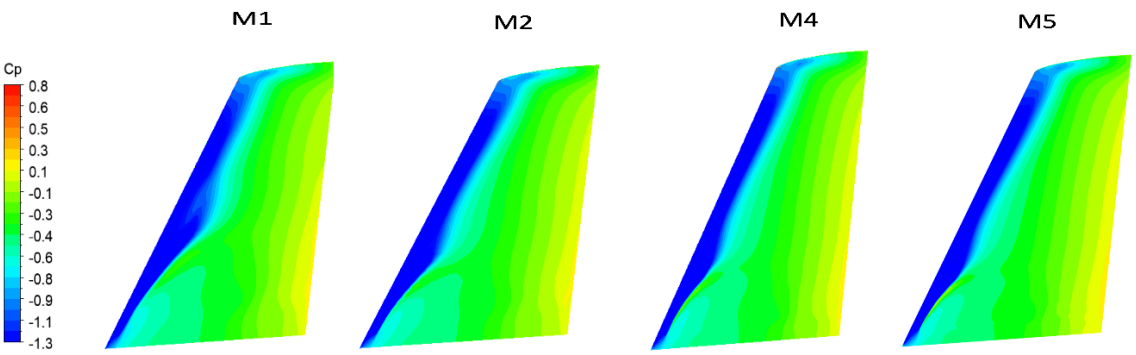

Fig. 4.4: Comparison of surface pressure coefficients for four different meshes.

Figure 4.4 compares the surface pressure coefficient of all the meshes at the spanwise section of η = 0.15 in Fig.4.4 (a). The high-pressure peak observed at the leading edge of the suction side of the coarse to finer meshes indicated the importance of mesh refinement. The finer mesh displayed superiority over the coarse mesh due to enough node distribution across the span. This is the reason for considering the mesh resolution before the simulation. The mesh's accuracy would give the study confidence that further refinement will not affect the solution regarding the aerodynamic coefficients and transition effect. M3, M4, and M5 showed good conversion at the suction side of the outboard region, as shown in Fig. 4.4 (b) for η = 0.75. All the meshes can be utilised in this study, except for the M1 and M2 meshes. Even without experimental pressure coefficient data, an independent study provided the required confidence in the outcome of the numerical solution.

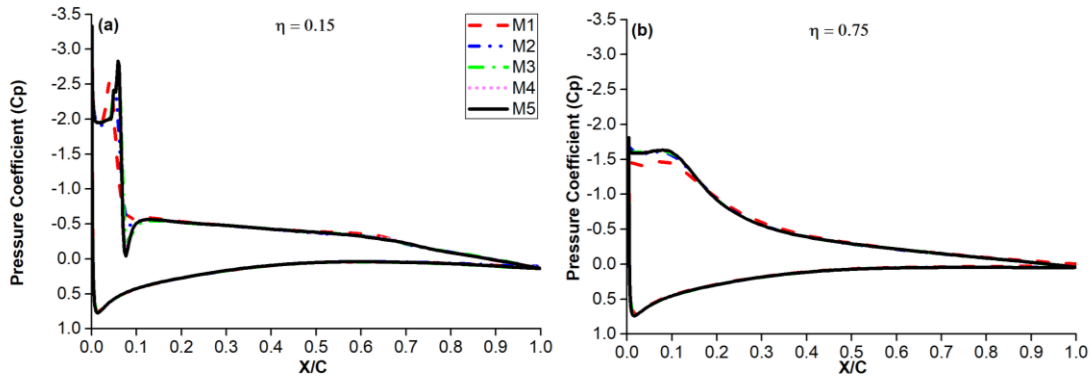

Fig. 4.5: Surface pressure coefficients of five different meshes (a) η = 0.15, (b) η = 0.75.

Figure 4.6 illustrates the behaviour of the surface friction coefficients for the four selected meshes, similar to the surface pressure coefficients in Fig.4.4. The skin friction coefficient is presented alongside the skin friction lines on the suction side of the VTP. The M1 mesh decreases skin friction compared to the other three meshes (M2, M3, and M5). However, the skin friction lines and coefficients exhibit similar behaviour as the number of cells increases.

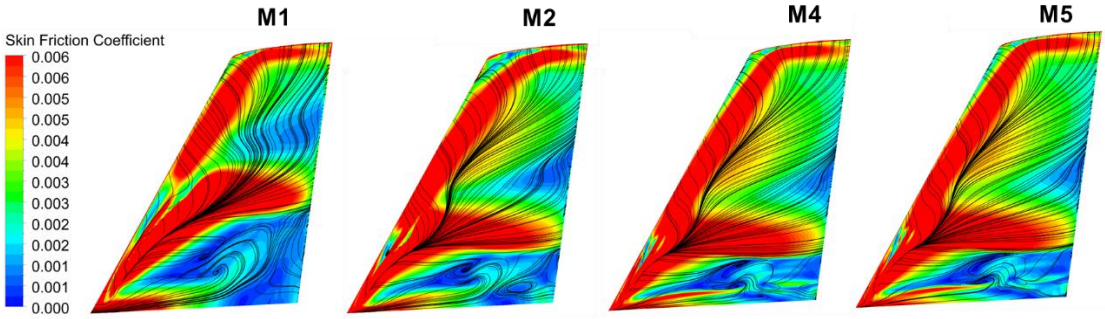

Fig. 4.6: Comparison of Skin friction coefficients for four different meshes.

Similarly, the skin friction coefficient plot in Fig. 4.7 captures the flow separation and reattachment, similar to the surface pressure coefficient plot in Fig. 4.4. The skin friction coefficient increased with the grid size. Pressure and skin friction coefficients are widely used for detailed grid refinement around aerofoils (Diskin et al.2015).

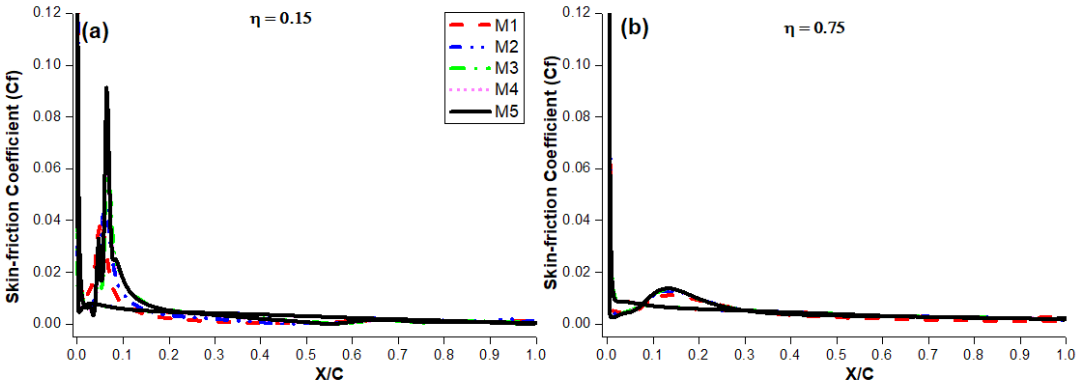

Fig. 4.7: Skin-friction coefficient of five different meshes: (a) η = 0.15, (b) η = 0.75.

4.3 Effect of Turbulence level

The influence of turbulence intensity on aerodynamics cannot be overestimated, as it directly impacts crucial parameters, such as lift and drag coefficients, pressure coefficient, and Reynolds number (Damiola et al.2023). The lift and drag coefficients are the primary indicators of an object's aerodynamic performance, and the turbulence intensity can be altered by changing the airflow around the object (Li et al.2011). These parameters play a fundamental role in determining aerodynamic performance, where the turbulence intensity increases the force coefficient by delaying the stall (Abdullah et al.2001). It was also found that an increase in turbulence intensity can reduce the lift coefficient at a lower angle of attack in CFD computation of NACA 0012 aerofoil (Zhang et al. 2020). The Reynolds number and turbulence intensity were found to have a significant impact in predicting the formation of laminar separation bubbles and the subsequent reattachment of the flow.

Table 4.2. Summarises the side force and drag force coefficients for five turbulence levels investigated in this study.

Table 4.2: Side and drag force coefficients at different turbulence intensities.

Tu (%)	Cs	Cd
0.1	0.999	0.332
0.2	0.993	0.331
1	0.996	0.331
2	0.997	0.332
4	0.999	0.332

The pressure coefficient is also crucial because the turbulence intensity can modify the pressure distribution around the VTP. According to Fig. 4.8, the primary effect of turbulence level can be seen on the transition point close to the leading edge. A high turbulence intensity typically decreases the suction negative pressure coefficient (Orcid 2021), by promoting boundary layer transition to turbulence.

The effect of the turbulence level was only studied at higher side slip angles of $\beta = 20°$, which is the stall angle according to experimental results. However, the turbulence model used is the transition k-kl-ω. Similarly, the skin friction plot (Fig. 4.9) for $\eta = 0.15$ and $\eta = 0.75$ indicated the turbulence effect where Tu-2% shows a higher rise in the skin-friction closer to the leading edge compared to the others.

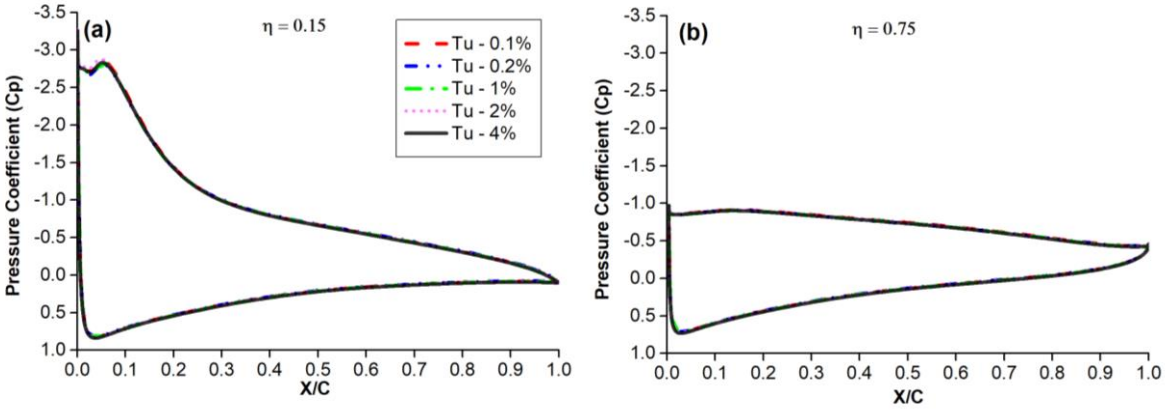

Fig. 4.8: Effect of turbulence intensity on Pressure coefficient at spanwise cut sections of $\eta = 0.15$ (a) and $\eta = 0.75$ (b).

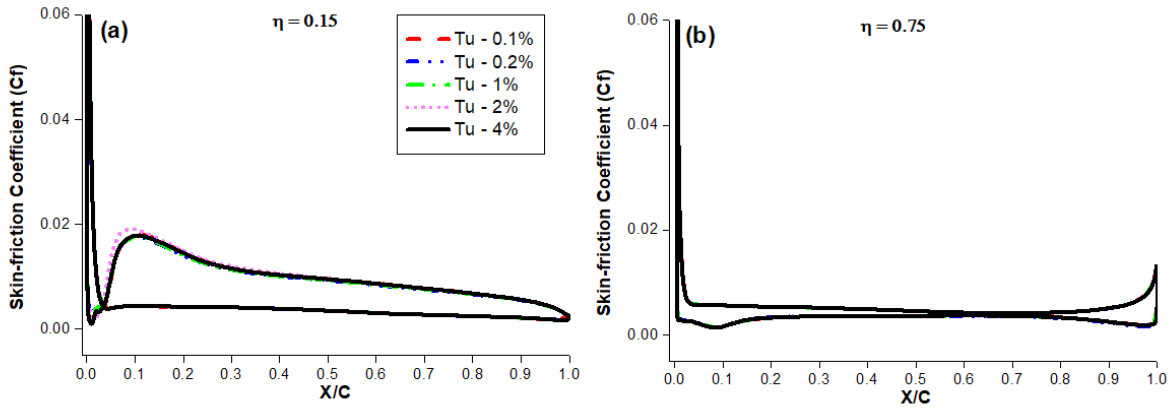

Fig. 4.9: Effect of turbulence intensity on Skin-friction coefficient at spanwise cut sections of η = 0.15 (a) and η = 0.75 (b).

4.4 Convergence in Numerical Simulation

This section investigates the convergence of RANS computation and the LES simulation. All the turbulence models converged to a steady-state solution after an iterative process. The one-equation model (S-A) models show the fastest convergence, followed by the two-equation models (k-ω SST and k-ε). The transition model k-kl-ω, however, leads to unsteady-like fluctuations at higher sideslip angle and the residuals stagnate without decreasing to a certain level. Therefore, it is recommended that both the residual and integral values be checked to assess the quality of the simulation.

Nevertheless, with the adjustment of the numerical schemes and pseudo-transient time step, all sideslip angles converged to a steady-state solution, as shown in Fig. 4.10. The turbulence model residuals were considered satisfactory if the imbalances were below the specified criterion of 10^{-3}. Each solution showed a notable decrease in residuals, although the convergence assessment primarily relied on the force coefficients obtained. During the iterative process, a pressure residual of 10^{-4} and below was achieved for all turbulence models.

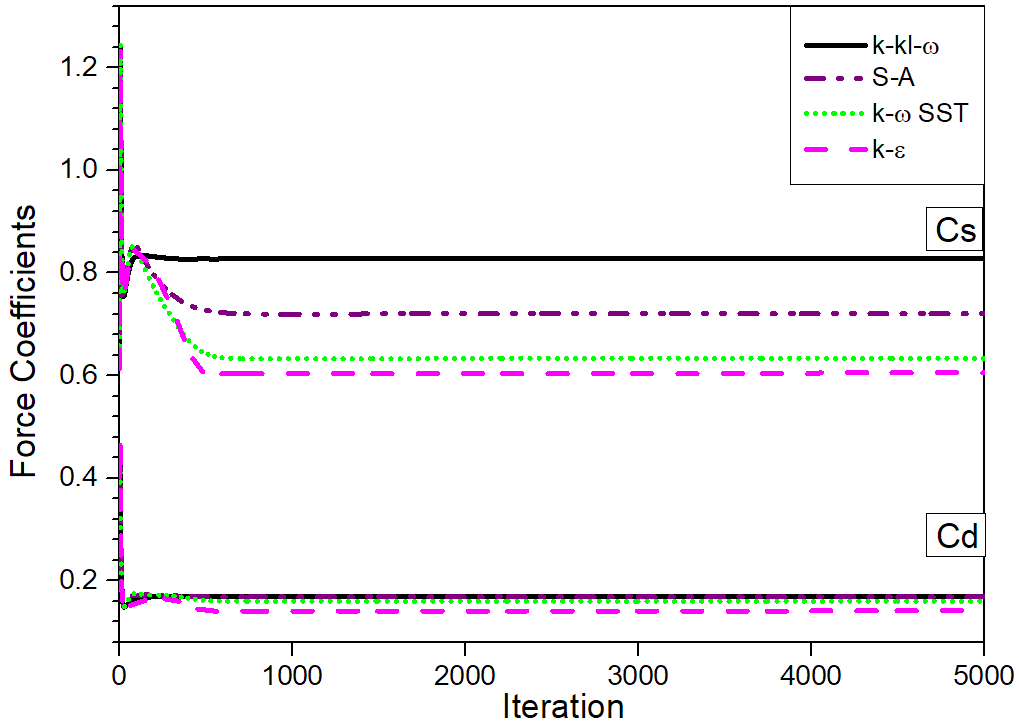

Fig. 4.10: Steady-state variations of Cs and Cd during the numerical simulation of different turbulence to models to show convergence for δ = 0° and β = 14°.

In the case of LES simulation, the solution is derived by averaging fluctuations over time, as shown in Fig 4.11. Here, the non-dimensional convection time is defined by $t^* = t \cdot U_\infty / c$. A different mesh was generated for the LES case with 22 million cells.

The convergence results for β = 8° and β = 14° show that all sideslip angles reached a stable solution based on the average values (Fig. 4.11). However, the convergence was determined by meeting the residual criteria, with the continuity equation settling below the 10^{-4} threshold. Attempting stricter convergence by reducing the continuity equation to 10^{-6} yielded a solution similar to the previous state. The tighter the residual convergence criterion, the slower the simulation time.

The first grid point of y^+ was checked after the simulation and is presented in Fig. 4.12, where y+ was found to be $y^+<1$. The plots were obtained at β = 8° and β = 14°.

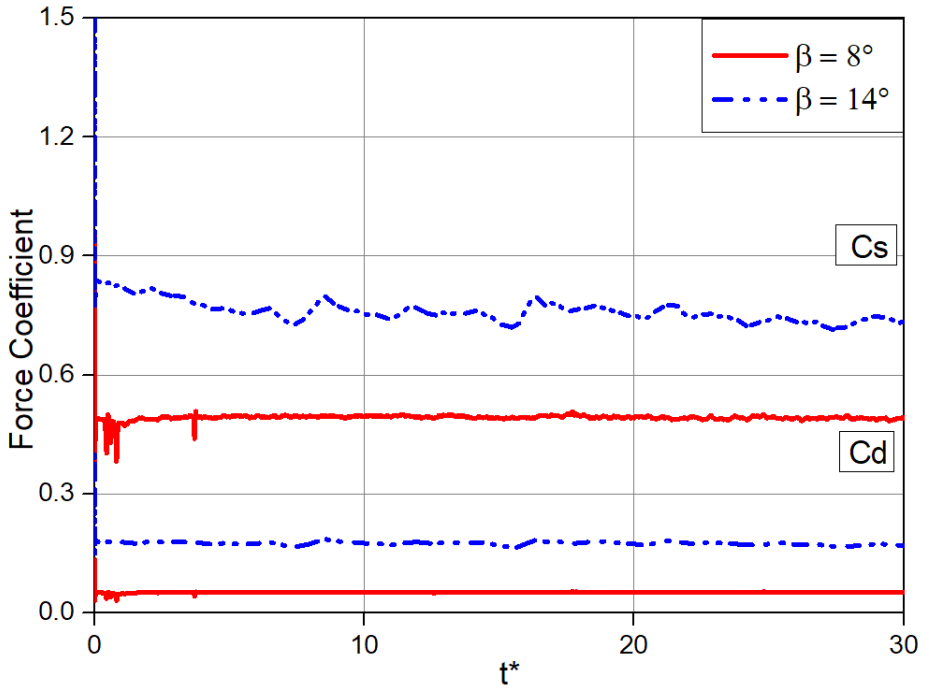

Fig. 4.11: Variation in Cs and Cd with dimensionless time during the numerical simulation to show convergence for β = 8° and β = 14°.

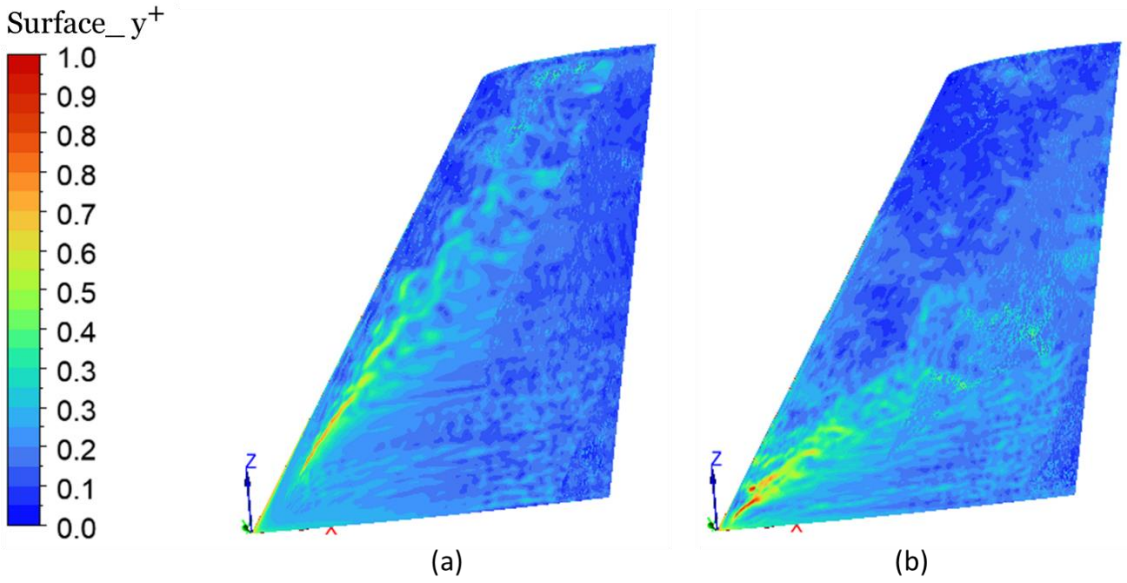

Fig. 4.12: LES Surface y^+ around the vertical tailplane surface for δ = 0° (a) β = 8°, (b) β = 14°.

4.5 CFD simulation validation of the Wind tunnel experiment

In this section, the numerical simulation of the VTP was performed using the LES simulation method with rudder deflection $\delta = 0°$ at a side slip angle of $\beta = 14°$. The simulations were carried out with and without the wind tunnel walls to establish the CFD correction factor of the wind tunnel wall interference. The numerical simulation of the wind tunnel model (with wall) and the freestream simulation were conducted without a gap between the root of the VTP and the floor. This allows for a direct comparison of the two cases, as they share a similar computational domain of the floor surface with slip boundary conditions. The virtual CFD wind tunnel utilised the exact dimensions of the physical wind tunnel with walls. In contrast, the freestream case used a large computational domain.

4.5.1 Description of Experimental Set-up

An experimental study was conducted at the University of Nottingham using a vertical stabiliser model with a rudder in a low-speed, open-return wind tunnel. The test section measured 1.5 m × 0.9 m × 0.9 m (length, height, and width), with a freestream velocity of 10 m/s (see Fig. 4.13). The wind tunnel experimental model details are described by Dong et al. (2022) and Kim et al. (2022), in different studies. In this study, the experiment was conducted in-house by group member Yaxing Wang who also contributed to the article detailing the wind tunnel setup by Dong et al. (2022). At an angle of attack of 15°, the blockage of the test model in the wind tunnel test section was less than 3%. Therefore, the leading edge of the test model is 1.5 MAC from the wind tunnel side walls, making the wall's effect on the load measurement negligible. The dimensions of the VTP model are described in section 3.8, which indicates the full geometry used in the wind tunnel and the numerical simulation.

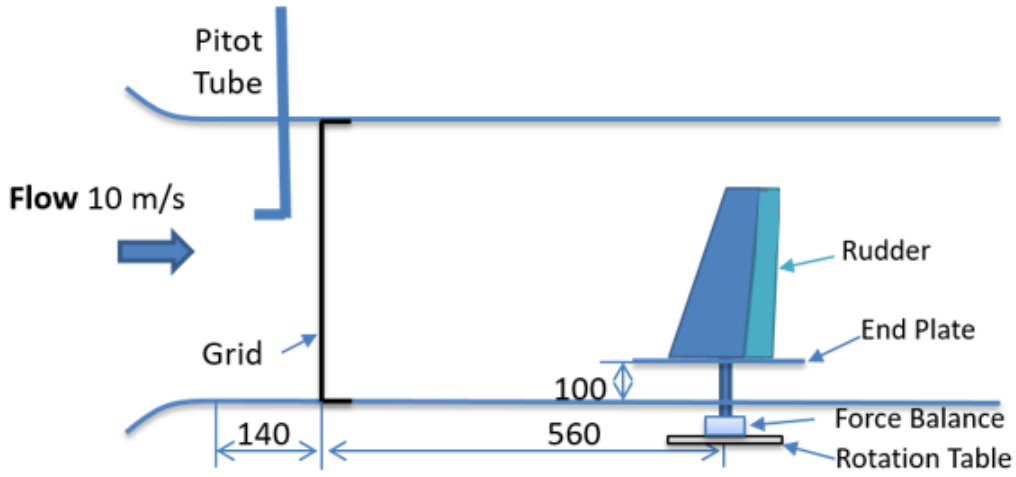

Fig. 4.13: Wind tunnel configuration and the test model. All dimensions are in mm.

4.5.2 Numerical Virtual Wind Tunnel

The computational domain and mesh are illustrated in Fig. 4.14 for the virtual wind tunnel numerical simulation. A structured mesh was generated across the computational domain, and the VTP had 19 million cells with a $y^+<1$. A dense mesh cluster is visible around the VTP root and tip sides, as shown in Fig. 4.14(b). The number of mesh points is coarser away from the VTP, with a higher concentration of mesh points clustered around the vicinity of the VTP, as clearly shown in Fig. 4.14 (b). The outer domain of the virtual wind tunnel case accurately represents the wind tunnel model dimensions with an upstream length like the physical wind tunnel model. The boundary conditions used for the virtual wind tunnel case are velocity inlet at the inlet, the outlet's pressure outlet, and the root base is assigned symmetry condition. At the same time, in the VTP model, the side walls and the top wall are categorised as walls with no-slip condition.

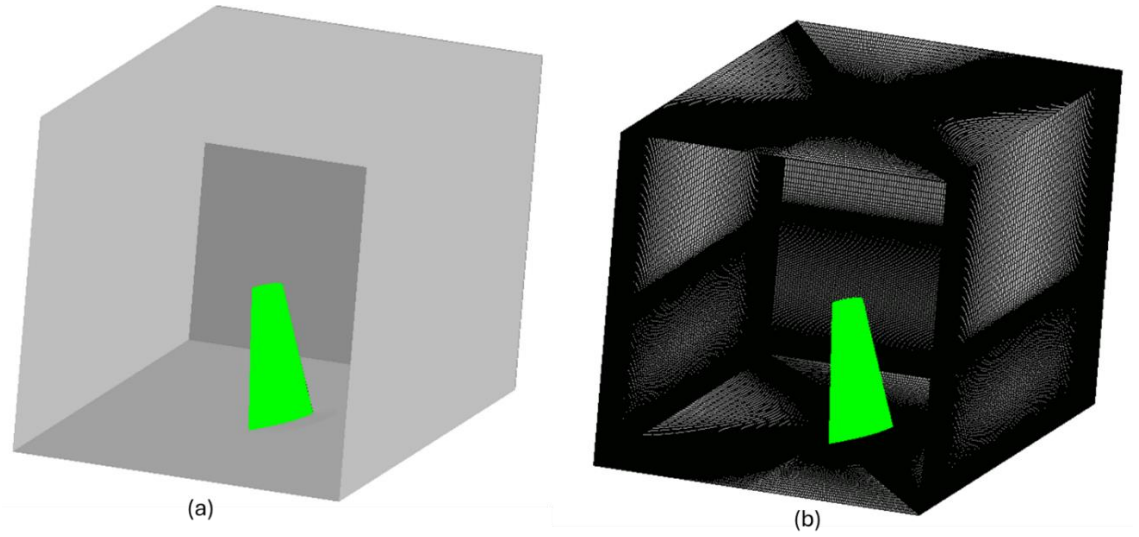

Fig. 4.14: The computational domain of the CFD wind tunnel model (a) and the mesh of the computational model (b).

4.5.3 Numerical Freestream conditions

The freestream case utilised a larger computational domain than the numerical virtual wind tunnel case. The computational domain of this case extends 30 chords upstream from the VTP leading edge and 21 chords to the top wall, while the side walls are 18 chords from the test model. In this case, the computational domain and VTP geometry are shown in Fig. 4.15(a). In contrast, the computational domain mesh is illustrated in Fig. (4.15b). A different mesh is generated differently from the numerical virtual wind tunnel case; the total number of mesh cells in this case is around 22 million. The mesh refinement is clustered mainly close to the test model, with over 85% of the mesh cells. Therefore, the grid points are maintained coarse in the far-field domain and along the tunnel's side walls. Additionally, this setup utilises a velocity inlet and a pressure outlet at the inlet and outlet, respectively. The second-order upwind accuracy and bounded central differencing schemes were used to evaluate the continuity and momentum equations for both cases of the CFD wind tunnel and CFD freestream condition.

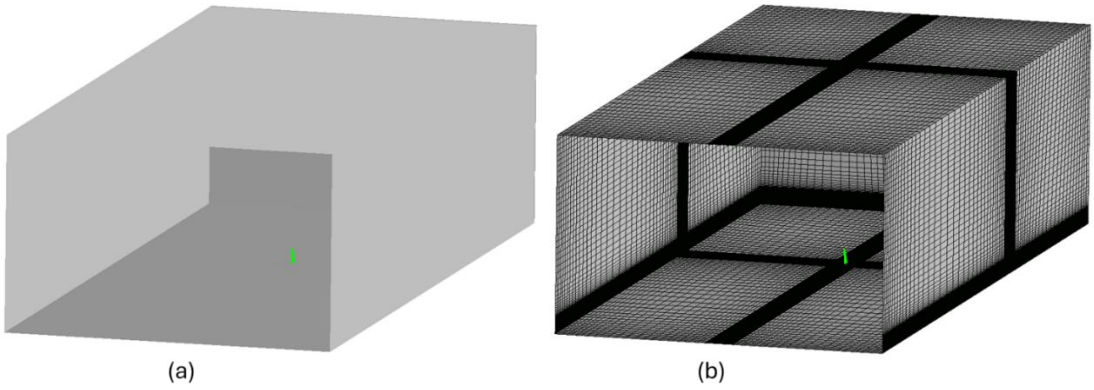

Fig. 4.15: The computational domain of the freestream model (a) and the mesh of the computational model (b).

4.5.4 Numerical CFD Result Comparison

Based on the parameters in Table 1 below, the force coefficient results from the CFD freestream and CFD wind tunnel simulations were analysed. The CFD wind tunnel simulation indicated increased side force and drag coefficients due to the entrapped air in the small domain. Therefore, the blockage due to the wall effect contributed to the increase in the Cs and Cd. There is a negligible difference in the change in value of the drag coefficient $\Delta Cd = 0.00078$ at the side slip angle of $\beta = 14°$, while a small difference is observed for the side force coefficient $\Delta Cs = 0.031$. The LES result captured the flow interaction with the CFD wind tunnel and the CFD freestream case with a larger computational domain, showing no major differences in the force coefficient's performance. The change in the force coefficients is calculated by subtracting the CFD wind tunnel case from the CFD freestream case.

Change in Force Coefficients = CFD Wind tunnel – CFD Freestream

Table 1: Comparison of the CFD virtual wind tunnel and the CFD Freestream.

Force Coefficients	Experiment	CFD-LES Freestream	CFD-LES Wind tunnel	ΔCFD
Cs	0.76343	0.75023	0.78154	0.031
Cd	0.20945	0.17486	0.18271	0.0078

Qin (2003) established the best practice for assessing real freestream conditions in physical wind tunnels by relating CFD freestream and CFD wind tunnel cases. A similar study used this approach to calculate changes in CFD between far-field conditions and virtual wind tunnel conditions with solid walls (Haque et al. 2016). This method effectively evaluates the accuracy and differences in aerodynamic simulations under various boundary conditions, ensuring reliable results in wind tunnel testing and computational fluid dynamics analysis.

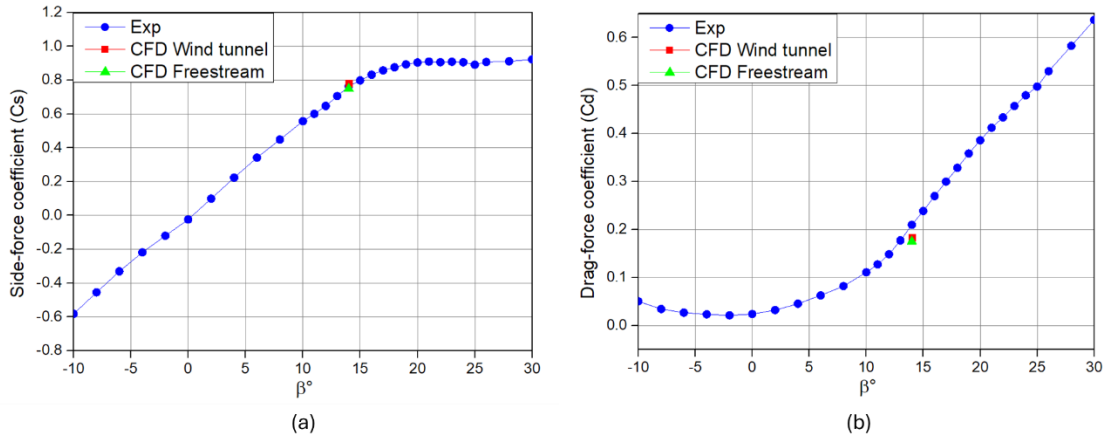

Fig. 4.16: Comparison of the side force coefficient (a) and drag coefficient (b) between the experiment, CFD wind tunnel, and the CFD Freestream case.

The simulation of rudder deflection $\delta = 0°$ at a side slip angle of $\beta = 14°$ can be considered as a near -stall angle where the flow is partially separated on the surface of the VTP, as shown from the experimental data in Fig. 4.16. Therefore, the comparison of the force coefficients between the experimental data, the CFD wind tunnel, and the CFD freestream case shows a good agreement, as shown in Fig. 4.16(a) for the side force coefficient and Fig. 4.16(b) for the drag coefficient. The side force coefficient compared better with the experimental data than the drag coefficient. This is due to the sensitivity of the drag coefficient to other attached structures that are not modelled in the numerical simulation. Overall, the comparison between the CFD wind tunnel and CFD freestream conditions shows no major differences, as both sets of coefficients nearly overlap from Fig. 4.16. It can be deduced that even at medium side slip angles of $\beta = 14°$, where strong flow interaction with tunnel walls occurs, the wall interference effect remains important.

This study employs a large computational domain to easily model different side slip angles, eliminating the need for remeshing each angle for simulation. This approach ensures the flow is fully developed upstream before reaching the test model, providing stability during the simulation. Although the sensitivity of different turbulence models to the domain extent was not studied, the large computational domain proved sufficient and stable for all turbulence models examined. This method simplifies the process while maintaining the accuracy and reliability of the simulation results. Additionally, verification of the numerical virtual wind tunnel with solid walls indicated that correcting for wall effects in the physical wind tunnel is crucial. This condition accounts for wall interference, ensuring the simulation accurately reflects the physical free air conditions.

4.6 Result and Discussion

4.6.1 Aerodynamic force coefficients δ = 0°

This study compared only the three sideslip angles of the LES results against the experiment data: for β = 8° considered as a medium, β = 14° considered the pre-stall angle, and β = 20° as the stall period. RANS results are shown for sideslip angles from -10° to 30°. Fig. 4.17 compares the wind tunnel experimental data, four turbulence models, and LES data for the side and drag force coefficients. The turbulence models used in this study included the S-A model, the k-kl-ω model, the k ω-SST model, and the k-ε models.

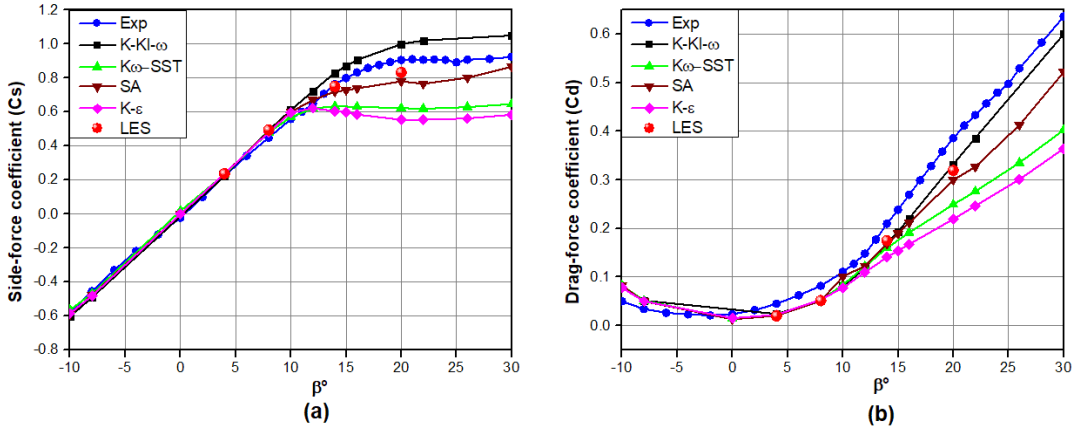

Fig. 4.17: Turbulence model comparison and validation: (a) side force coefficient and (b) drag force coefficient.

It is clear from the comparison that even the less expensive turbulence model, the one equation S-A model, predicted both Cs and Cd quite well for the sideslip angle of up to $\beta = 10°$. This model can predict the aerodynamic coefficient with faster solution convergence (Rumsey and Vatsa 1995). As Carmichael (1982) reported, the model was found to be more reliable at low Reynolds numbers with good capability in predicting the aerodynamic coefficient, but not certainly good in capturing the flow physics.

At $\beta = 14°$, k-kl-ω overpredicted Cs and underpredicted Cd. In contrast, the S-A value for Cs was found to be close to the corresponding experimental value, meanwhile Cs predicted by k-ω SST and k-ε was far below the experimental value. The original k-kl-ω is widely used in the prediction of force coefficients, transition flow, and the boundary layer development (Aftab et al. 2016).

In addition, for $\beta = 20°$, which is close to the stall angle, the conversion of the force coefficients was slow but, the four turbulence models continued to show the same pattern, where only k-kl-ω overpredicts the values of the side force coefficient. It is common for different turbulence models to disagree and agree on the qualitative and quantitative predictions of aerodynamic coefficients, particularly after the stall angle. Srinivasan et al.(1995) evaluated several turbulence models using the NACA 0015 aerofoil; their study concluded that all the turbulence models performed well in the attached flow compared to the established experimental data. However, it was found that none of the turbulence models have shown a good comparison beyond the aerofoil stall angle because most of the models either overpredicted or underpredicted the separation and reattachment as identified as the causes of the inconsistency.

This study shows that all turbulence models can accurately predict the side force and drag force coefficients as long as the flow is attached at lower sideslip angles. However, these models underpredict the side and drag force coefficients near the stall angle, as shown in Figs. 4.17(a) and 4.17(b). Furthermore, the turbulence models predict different stall angle when compared to the experimental stall angle of $\beta = 20°$. For example, the k–ε model predicted early stall angle at about $\beta = 12°$, while the k -ω SST model predicted about $\beta = 14°$ and the S-A model, obtained $\beta = 16°$. The k-kl-ω and

LES show a similar stall angle to the experimental data; the only difference between the two is the value of the side force coefficient at the stall angle of $\beta = 20^{\circ}$.

In addition, the S-A turbulence model performed better than all the turbulence models except for the transition k-kl-ω model in predicting the force coefficients. Boughou et al. (2022) recently conducted a study on various turbulence models and compared their results with experimental data. The S-A model performed exceptionally well, with its lift and drag coefficients matching closely with the XFoil and experimental data at the pre-stall angle. However, the model's inability to handle the transition and separation effects of the aerofoil was noted after the stall angle. Diskin and Galbraith (2023) conducted a workshop to evaluate the improvement of the S-A model. They investigated various wing-body configurations using NACA 0012 aerofoil profile. They concluded that it is possible to improve the model's linear eddy viscosity to account for generating eddy viscosity within the vortices.

At higher sideslip angles, there is global flow separation, resulting in complex aerodynamic behaviours. This scenario challenges traditional CFD methods, such as RANS, owing to their limitations in capturing the turbulent flow intricacies and separation effects.

It can be said that the k-ε and k-ω SST provided a result far below the experimental data. Therefore, their prediction cannot be used to establish a baseline to develop strategies to control the separation phenomena. However, the S-A, k-kl-ω, and LES can be used to predict the side-force and drag-force coefficients as indicated in Fig. 4.17. The k-kl-ω transition prediction is believed to be more robust in aerodynamic coefficient prediction than the S-A model. The prediction of the force coefficients is not enough evidence to decide on the performance of the turbulence models. The pressure contours indicate the actual physics of the flow around the surface of the VTP. These findings provide valuable insights into the flow behaviour over the VTP surface using different turbulence models and highlight the complex interplay between flow separation as the effect for the conventional RANS models to predict the side force and drag force coefficient at higher sideslip angles.

In contrast, the LES stands out in such scenarios. LES resolves larger turbulent structures while modelling smaller ones, allowing it to manage unsteady, transitional flow, and separation effects more accurately. This capability enhances its performance, particularly when conventional RANS models fail, owing to their inherent limitations in resolving unsteady and transitional turbulence. But the transition k-kl-ω model among the RANS model is like the LES regarding the transitional turbulence predictions. The transitional performance displayed by the LES makes it a preferred choice for aerodynamic simulations at high sideslip angles. LES's ability to capture the dynamic behaviour of turbulence and its interaction with separated flows provides a better understanding of the aerodynamic performance under these conditions.

4.6.2 Flow Field Analysis

The discussion on the flow field analysis in this section is centred around data for $\beta = 8°$, $\beta = 14°$ and $\beta = 20°$ sideslip angles. In Fig. 4.18, at a lower sideslip angle, all the turbulence models exhibit a consistent pattern in the velocity around the VTP at the spanwise location of $\eta = 0.15$. In this location, the earlier prediction of separation near the leading edge resulted in the formation of a laminar separation bubble. Only the LES and the transition k-kl-ω model demonstrate the presence of this laminar separation bubble, as indicated in Fig. 4.18 (b).

Figure 4.14 shows the velocity contour plot with streamlines for $\beta = 14°$. In this location, the laminar separation for k-kl-ω and LES increases with the sideslip angle compared to Fig. 4.18. The bubble develops slowly along the surface until it reaches a point where turbulent reattachment occurs. After this critical point, the flow reattaches to the VTP surface, resulting in a turbulent boundary layer. As the sideslip angle increases, flow separation reoccurs, which is identified as turbulent separation towards the trailing edge. This turbulent separation around the VTP reduces the aerodynamic coefficients and gives rise to significant pressure fluctuations, attributed to the intense flow activities in the specific region.

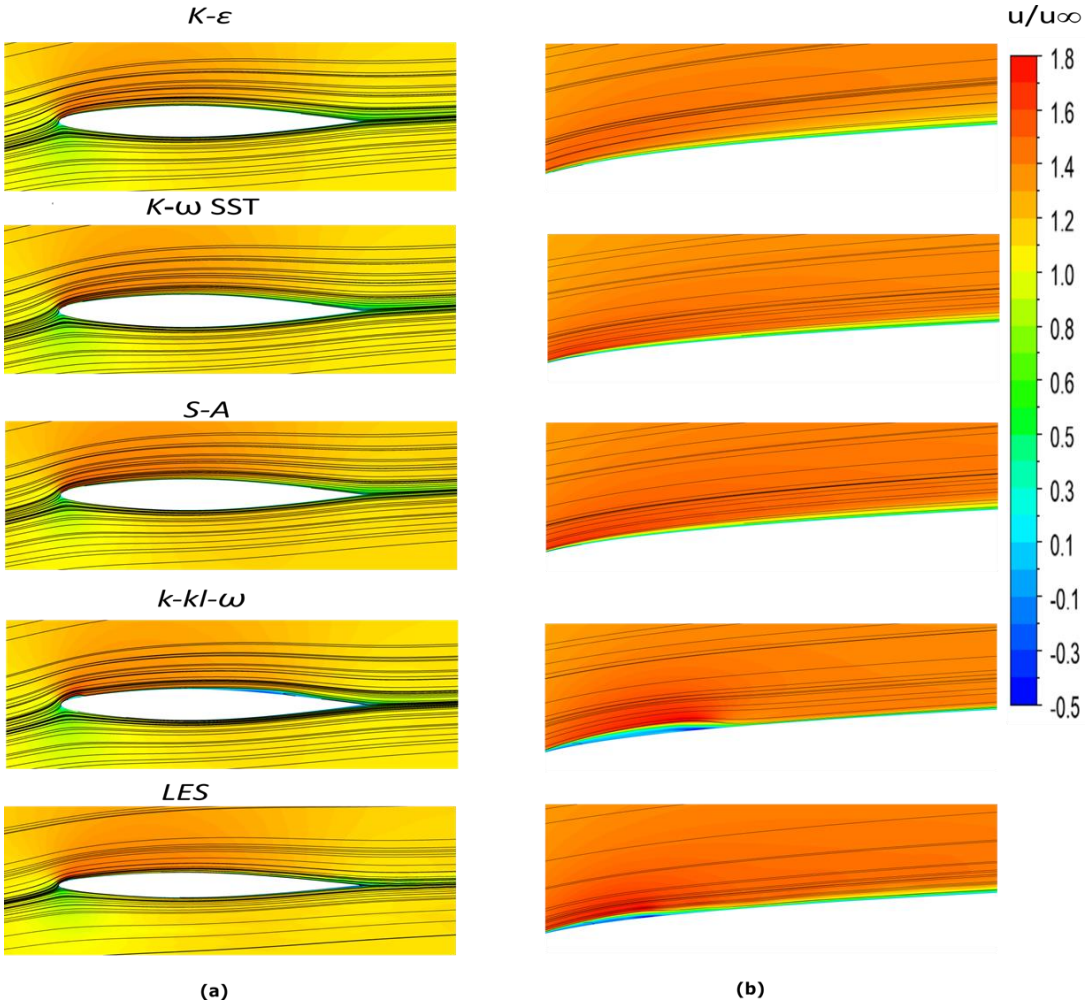

Fig. 4.18: Velocity contour from different turbulence models for β = 8° at η = 0.15.

Among the models studied, the *k*-ε shows a different representation of the velocity distribution over the VTP at β = 14°, especially at the leading edge, where all other models show at least a small size of the leading-edge laminar separation bubble, which is entirely not observed in the k-ε model. No evidence of such a feature was predicted by the k-ε model for the entire surface of the suction, and the turbulent separation diminishes.

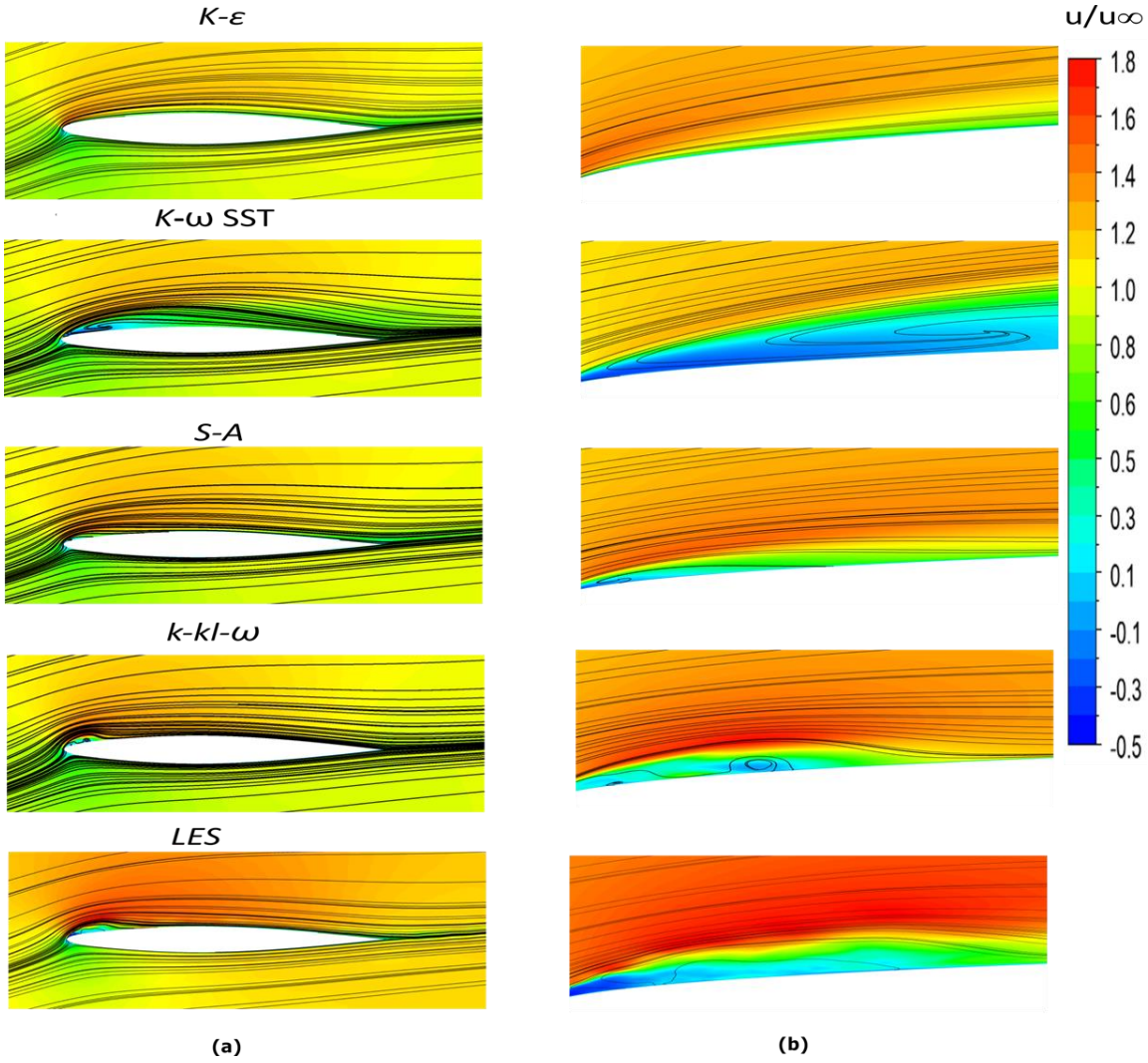

Fig. 4.19: Velocity contour from different turbulence models for β = 14° at η = 0.15.

In their study, Sadikin et al.(2018) insisted that the ability of the k–ε to delay separation at a lower angle of attack made the model exceptional among others. The study also highlighted that the k–ε does not predict the separation bubble at the leading edge compared to S-A and k -ω SST models, as shown in Fig. 4.19. Similarly, in Fig. 4.17, the S-A model has been found to provide results that are reasonably close to experimental data compared to other conventional RANS models, such as k-ω SST and k-ε. It is evident that among the conventional models, the S-A model prediction shows a partial improvement when compared to LES. This is also shown in a study by Weber and Ducros (2000) that compares the LES and different turbulence models and found that the LES and S-A are better aligned than others. The study compared the velocity profiles of the models and LES around the A-Aerofoil.

The k -ε and k -ω SST models often face challenges in accurately predicting the laminar separation bubble (LSB) due to their tendency to predict unphysical turbulence kinetic energy near the stagnation point to be shown in Fig. 4.33 in the turbulent kinetic energy analysis. On the other hand, The S-A turbulence model is better than the k-ε and k-ω SST models in predicting the LSB.

However, the LES method differentiates its characteristics from other turbulence modes. It can be established from the lower β = 8° to higher β = 20° that the LES method consistently predicted the transition from laminar to turbulent where they exist on the suction surface, as shown in 4.18 and 4.19. The LES is expected to prove the limitations of the RANS model in a complex flow where the transition to turbulence is not captured appropriately. Still, the transition model has shown remarkable results related to the leading-edge laminar separation bubble capture and the flow reattachment to the surface. None of the turbulence models fully capture the dynamic activities, as they all miss some aspects of predicting laminar separation and turbulent reattachment. Nevertheless, the k-kl-ω and S-A models predicted the leading-edge LSB well and showed insufficient reattachment. For the behaviour of the turbulence models and LES at the larger side slip angle β = 20°, see Fig. 4.20. It can be observed that the overall flow field around the VTP varies with the turbulence models due to different techniques employed by the models.

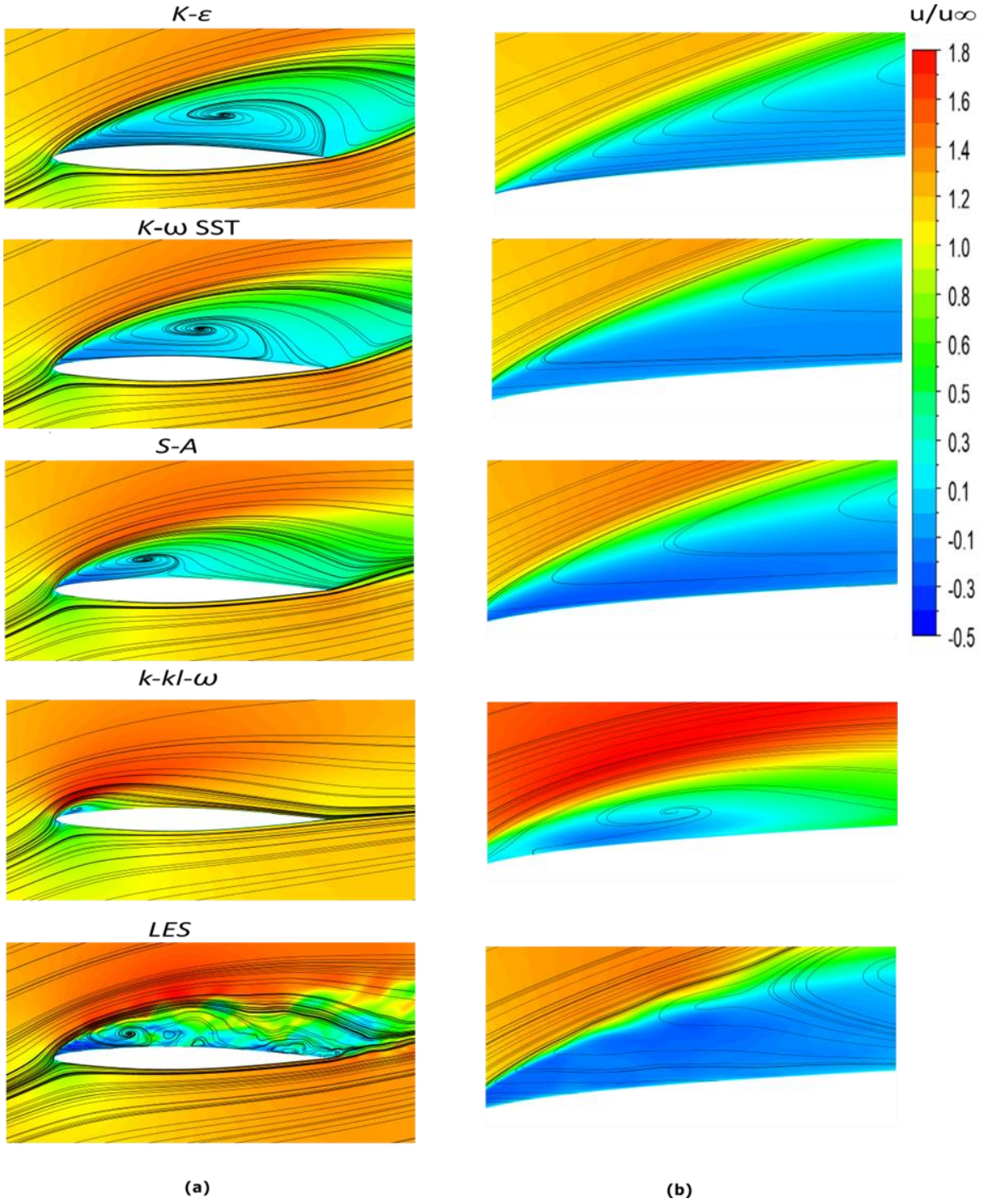

Fig. 4.20: Velocity contour from different turbulence models for β = 20° at η = 0.15.

Figure 4.21 shows the velocity and streamline at the spanwise location of η = 0.5 for β = 8°. The location is close to the mean aerodynamic chord of the entire VTP surface. It can be observed that the presence of flow separation is seen to increase chordwise, where the surface plot indicated that the separation moves upstream to the leading edge compared to the spanwise location of η = 0.15, which is close to the root side. The LES demonstrates a high-fidelity flow prediction where the turbulent reattachment was clearly captured after the formation of the laminar separation bubble compared to other models. All the turbulence models and LES are in close agreement even with the RANS limitations.

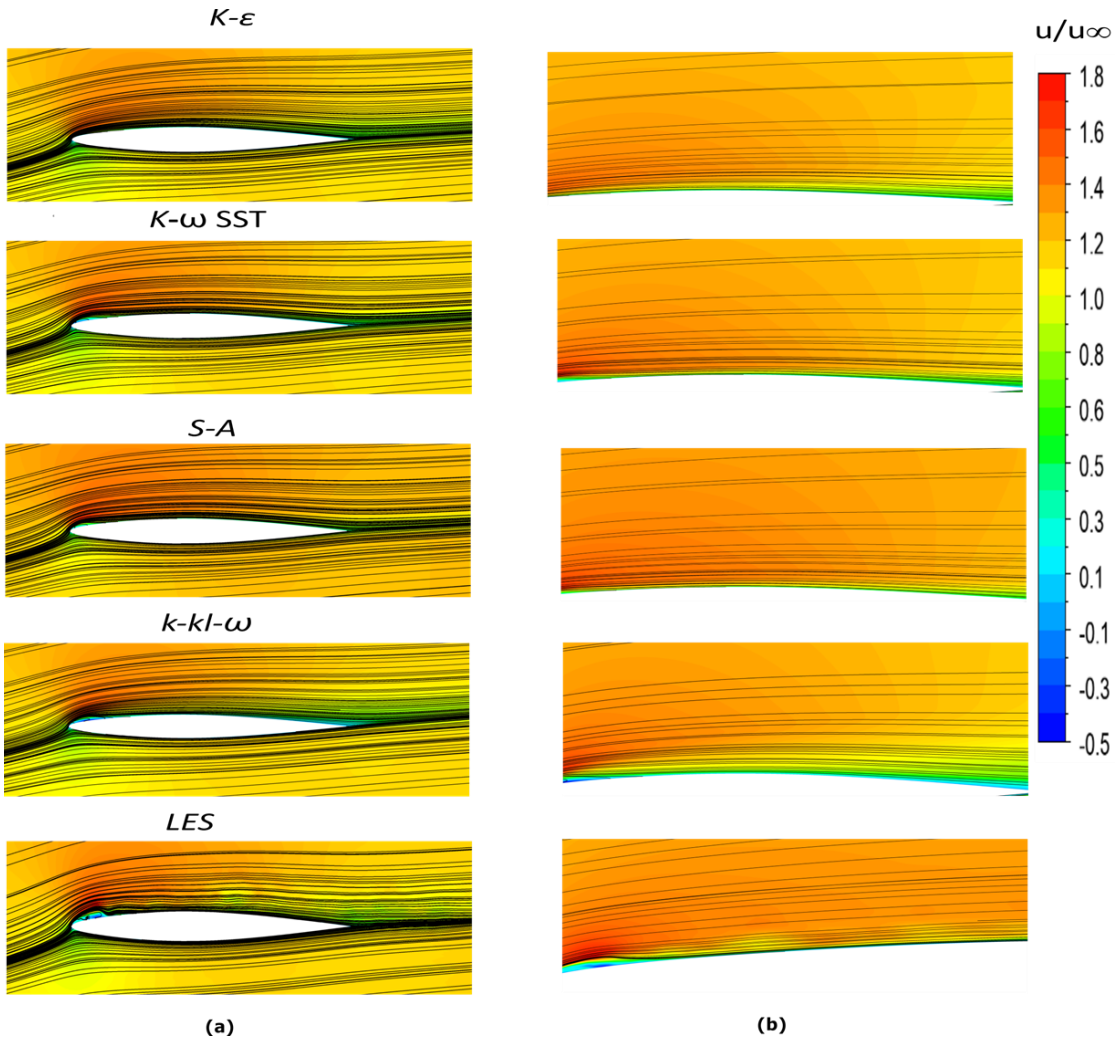

Fig. 4.21: Velocity contour from different turbulence models for β = 8° at η = 0.50.

The streamline is plotted on top of the streamwise velocity contour in Fig. 4.22 for $\eta = 0.50$ at $\beta = 14°$ for the results by four turbulence models and the LES. The flow becomes complex because of the fluid dynamic's intricacies related to flow features; the flow around the VTP is naturally complicated. As the chordwise distance increases from the root side, the leading-edge laminar separation bubble observed in Fig. 4.19 (a-b) diminishes in Fig. 4.22 (a-b) for k-ω SST, k-ε and S-A. At this sideslip angle, all three turbulence models (k-ω SST, k -ε, and S-A) are closely aligned regarding velocity characteristics, except for the transition model. All the models experienced severe adverse pressure gradients from sideslip angles of 12° -16°, and the stall occurred, decreasing the side force coefficient drastically compared to the experimental data.

A similar result at a higher sideslip angle for $\beta = 20°$ at $\eta = 0.50$ is shown in Fig. 4.18. The flow is separated from the leading edge as the sideslip angle and chordwise distance increase. This leads to a more severe adverse pressure gradient on the suction side of the VTP as the sideslip angles increase. The bursting effect of the short bubble indicates a large scale of separation that almost covers the entire surface of the suction. Therefore, a large recirculation region is developed, as seen in Fig. 4.23, where all the turbulence models and LES have shown the presence of the large recirculation. It's evident that the wake velocity increased due to the large recirculation region, which increased the drag coefficient.

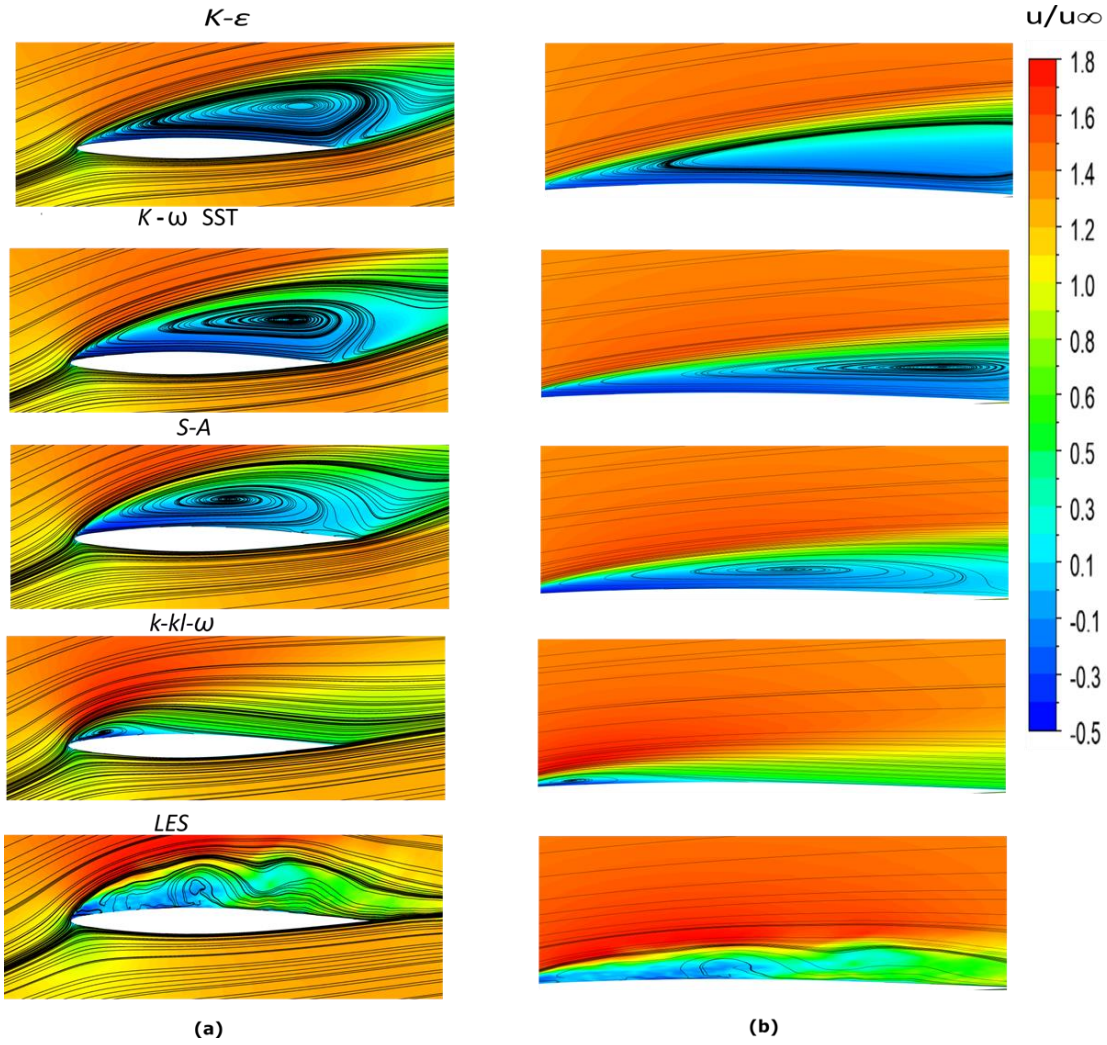

Fig. 4.22: Velocity contour from different turbulence models for β = 14° at η = 0.50.

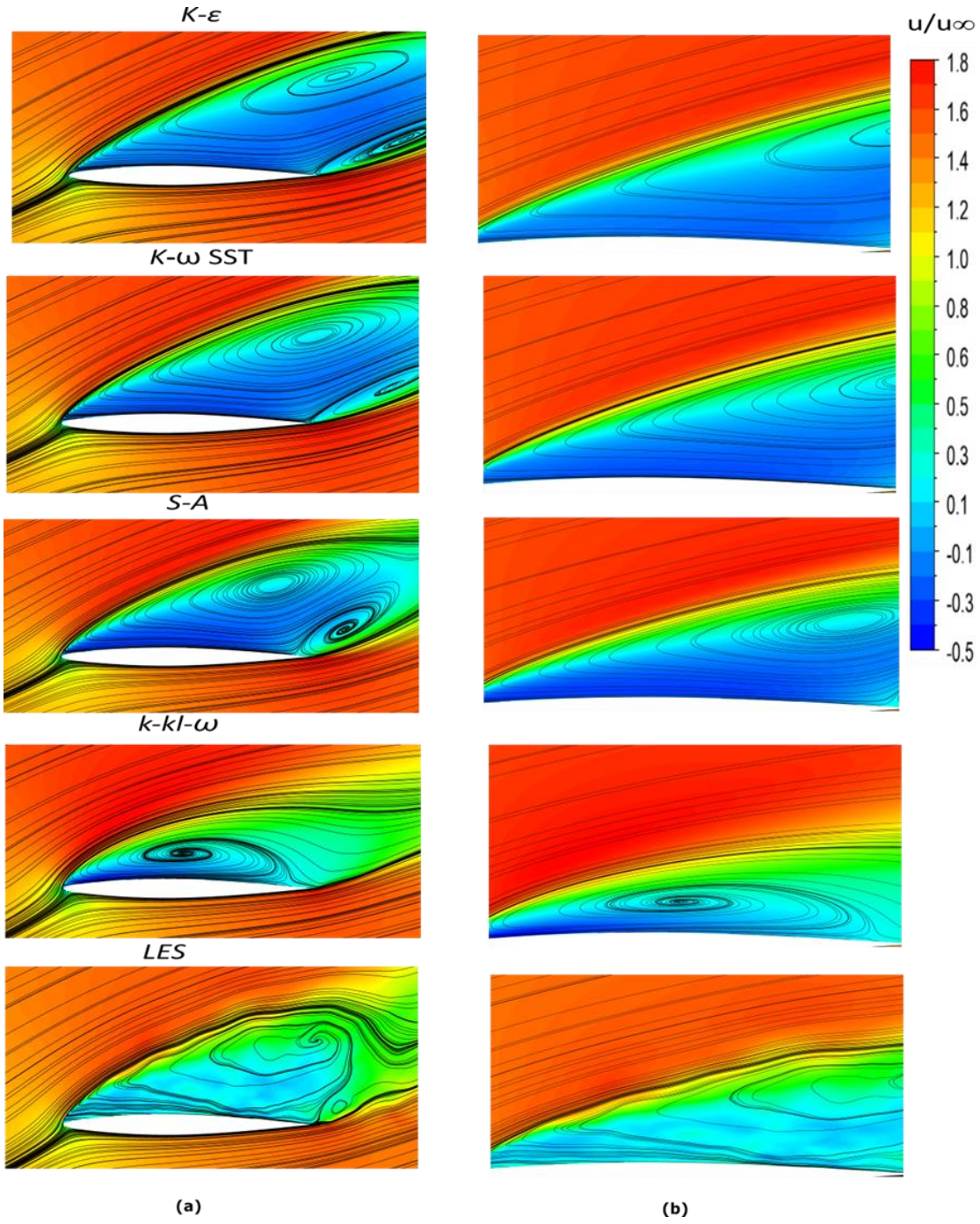

Fig. 4.23: Velocity contour from different turbulence models for β = 20° at η = 0.50.

It is important to note that the streamwise velocity profile predicted by the turbulence models and LES remains consistent with an increase in the sideslip angle. For example, at a lower sideslip angle of β = 8° (Fig. 4.24), the k-kl-ω model predicted a similar velocity profile on the suction side compared to the other three models, k-ω SST, S-A, and k-ε. However, as observed earlier, the LES results mostly balance the three models k-ω SST, S-A, and k-ε and the transition k-kl-ω model.

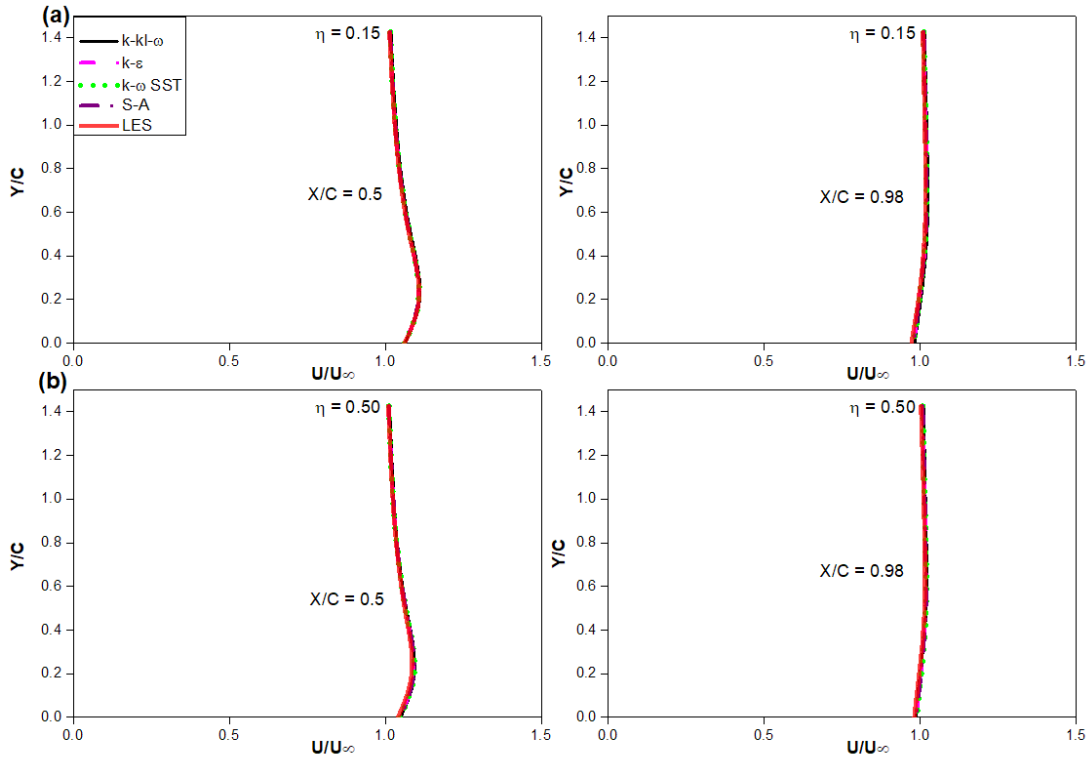

Fig. 4.24: Velocity profile from different turbulence models and LES at β = 8° (a) η = 0.15, (b) η = 0.5.

The details of the velocity profile at β = 14° are investigated in Fig. 4.25 using the boundary layer plot. The analysis is based on the spanwise cut sections of η = 0.15 and η = 0.50 at the chord mid-point and the trailing edge. The chordwise locations of the two spanwise cut sections correspond to the x/c = 0.5 at the chordwise midpoint and x/c = 0.98 at the exit of the trailing edge. In Fig 4.25 (a), where η = 0.15 at x/c = 0.5, all the turbulence models agree well except the k-ω SST, which shows a different characteristic of the relationship between the leading-edge separation and the trailing-edge separation features.

Figure 4.25 (b) highlights the effect of the velocity profile at $\eta = 0.50$, where the flow is partially separated. In this scenario, the turbulence models, namely of k-ω SST, S-A, and k-ε, exhibit an overestimation of the separation size compared to the predictions made by the transition k-kl-ω model and the LES. In contrast, the LES and k-kl-ω display an overprediction of the velocity profile compared to the other three turbulence models k-ω SST, S-A, and k-ε. The LES and k-kl-ω exhibit similar characteristics in estimating the velocity and the separation size at $x/c = 0.5$ and at the trailing edge where $x/c = 0.98$. Therefore, the transition model k-kl-ω and LES matched well in the flow field compared to the other turbulence models. It is indeed realistic to believe that the LES and k-kl-ω should be considered in this study even without the experimental data to compare the flow physics. Fig. 4.26 shows the velocity profiles at a higher sideslip angle of $\beta = 20°$. In addition, as the sideslip angle increases, the k-kl-ω model displays a faster drop in velocity, but still higher than the other three models.

The S-A and k-kl-ω models consistently show improved force coefficient performance as the sideslip angle increases. At higher sideslip angles, the S-A, k-kl-ω models, and LES provide more accurate predictions of force coefficients (Fig. 4.17). Still, the k-ε and k-ω SST models could not predict the side force and drag force coefficient at higher sideslip angles. The turbulence models utilised in this study effectively acknowledge the importance of flow separation around the VTP surface. The findings from the velocity contour analysis suggest that all turbulence models successfully estimate and capture the flow separation differently. It has been observed that only the k-ε turbulence model did not show evidence of capturing the leading edge LSB. As a result, it is evident that the LSB at the leading-edge decreases as the sideslip angle increases, as demonstrated in the DNS method (Balakumar 2017).

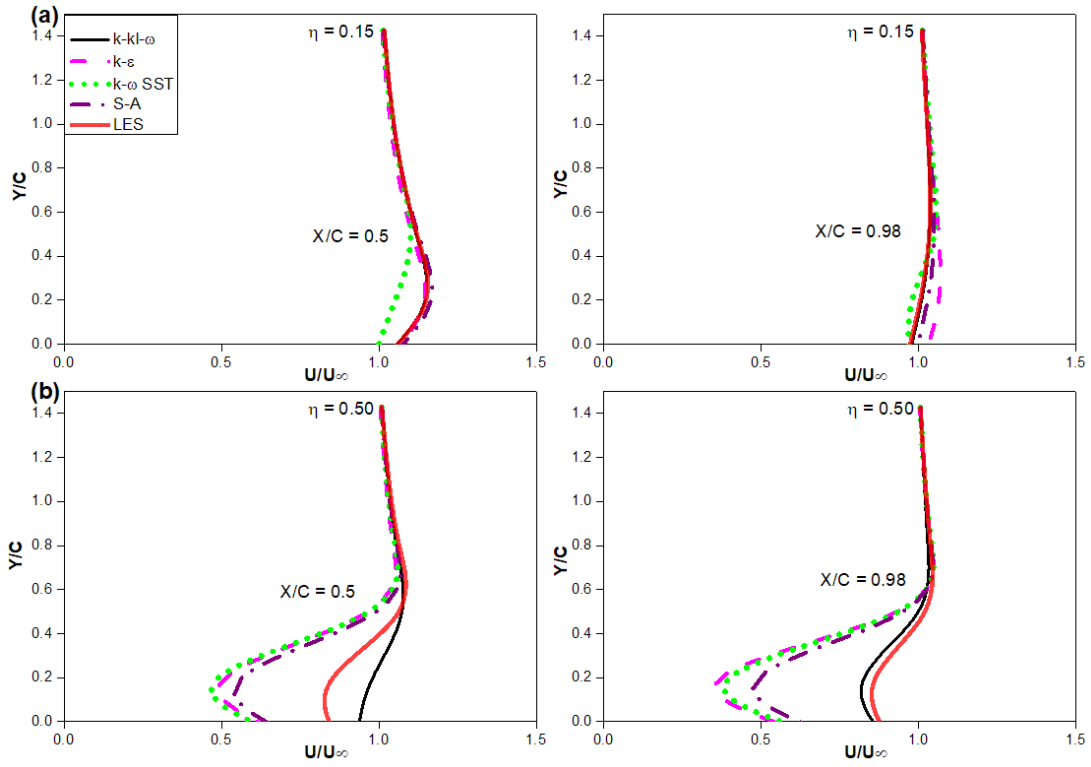

Fig. 4.25: Velocity profile from different turbulence models and LES at β = 14° (a) η = 0.15, (b) η = 0.5.

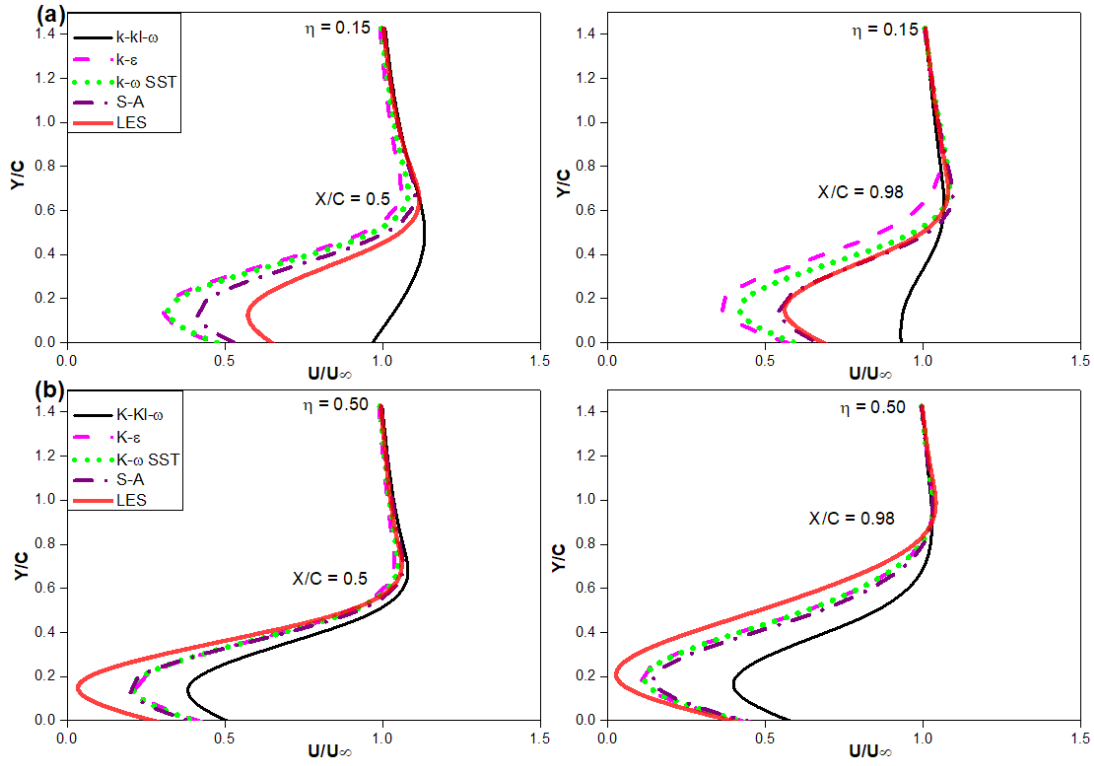

Fig. 4.26: Velocity profile from different turbulence models and LES at β = 20° (a) η = 0.15, (b) η = 0.5.

4.6.3 Pressure Coefficient Analysis for β = 8°, β = 14° and β = 20°

Figure 4.27 compares the surface pressure coefficients derived from the LES results and four turbulence models. Aerodynamic force analysis indicated that the flow remained attached for δ = 0° and β = 8°. Interestingly, all four turbulence models and LES aligned closely when examining the suction pressure coefficient plot Fig. 4.28 (a).

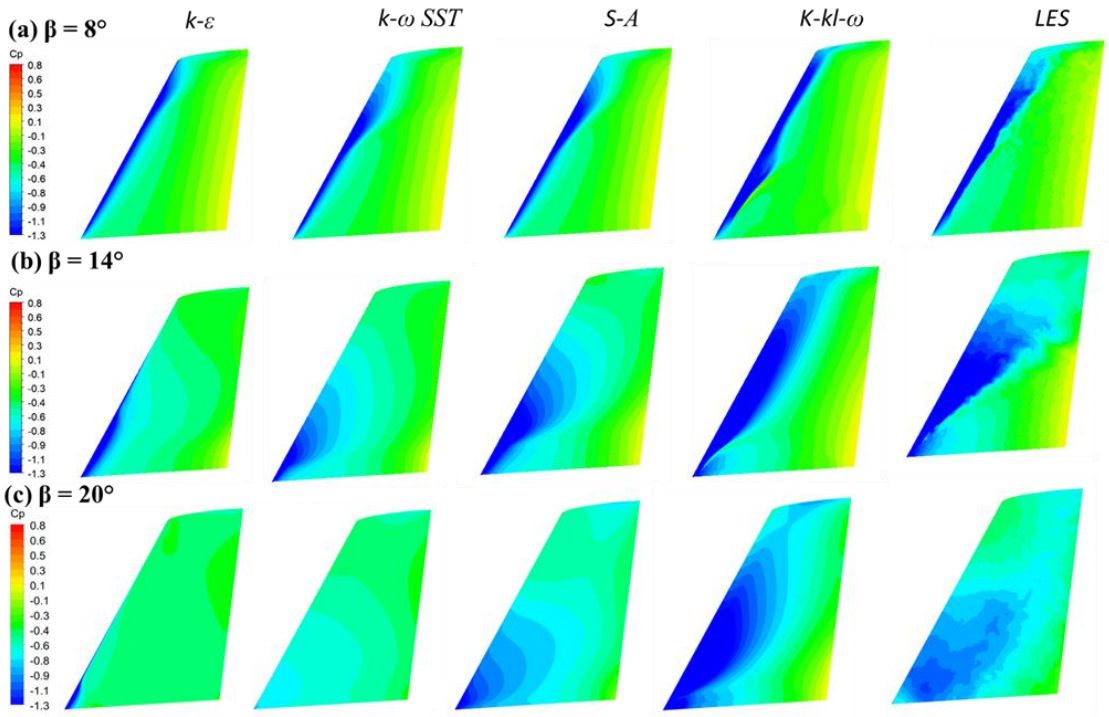

Fig. 4.27: Comparison of surface Pressure Coefficient plot for δ = 0° and β = 8° (a), 14° (b), and 20° (c) with four turbulence models and LES method.

The findings in Fig. 4.27 (b) highlight the pressure distribution over the VTP surface at a sideslip angle of β = 14°. Notably, the results indicate that the flow is not fully separated, as evidenced by the spanwise cut sections shown in Fig. 4.19 and 4.22 of the velocity contours. Interestingly, partial separation is only predicted in the three turbulence models and LES simulations, while it is missing in the k-kl-ω transition model because of the negative pressure coefficient along the leading edge. The surface pressure coefficient plot in Fig. 4.27 (c) which is at higher sideslip angle of β = 20° is similar to with the turbulence model performance shown at the lower sideslip angles.

Figure 4.28 shows the results obtained for $\delta = 0°$ and $\beta = 8°,14°$ and $20°$ for the cut sections $\eta = 0.15$. The LES and all four turbulence models showed good agreement on the pressure side, as indicated in Fig. 4.28 (a-b). It was discovered that for section $\eta = 0.15$, all turbulence models converge to the same pressure gradient as highlighted in Fig. 4.28 (a-b). Because of the high negative pressure peaks prediction at the leading edge, obtaining a good agreement of all the turbulence models in this section for $0 < x/c < 0.2$ is difficult.

The performance of the individual models in predicting the pressure coefficient at the spanwise cut sections was evaluated in the absence of experimental data. The results presented in Fig. 4.28 demonstrate that the transition model and LES could predict the presence of a laminar separation bubble at $\eta = 0.15$ and $\eta = 0.5$. In addition, the LES model captured a longer separation bubble than the transition model at lower sideslip angle of $\beta = 8°$ in Fig. 4.28 (a). Similar results were observed and confirmed in the velocity analysis in Fig. 4.18 where the bubble was captured at similar cut sections of the $\eta = 0.15$. In contrast as the chordwise distance increase $\eta = 0.50$ in Fig. 4.29 (a) the indication of the LSB was also observed from the LES and transition k-kl-ω, but in this case the bubble length predicted by the LES seems to be a long bubble as compared to the transition k-kl-ω. The velocity analysis result in Fig. 4.21 indicated that the height and the length of the bubble of the LES is greater than the transition k-kl-ω result.

In Fig. 4.28 (b) at $\beta = 14°$, all the turbulence models and LES disagree at the suction side of the cut section $\eta = 0.15$. The discrepancy between the turbulence models and LES is seen for $x/c < 0.2$. For $x/c > 0.2$, all the models conform to reattachment at the trailing edge apart from the transition k-kl-ω. The LSB is observed in the velocity analysis in Fig. 4.19 for all the turbulence models and LES except the k -ε. At this point, it can be observed that in Fig. 4.28 (b) the k-kl-ω and LES show similar behaviour of the leading-edge LSB, except that the k-kl-ω seems to indicate a different transition. The Fig. 4.29 (b) shows the influence of the chordwise and sideslip increase, the LSB is reduced with increase in sideslip angle and chordwise location.

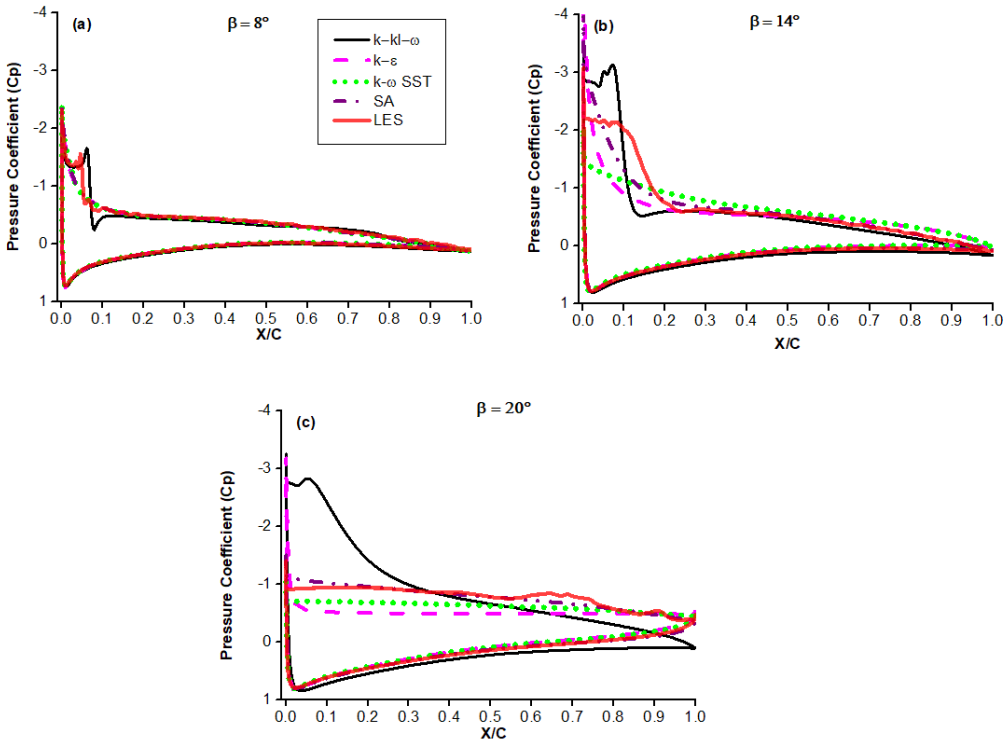

Fig. 4.28: Pressure Coefficient plot for δ = 0° at different sideslip angles for η = 0.15.

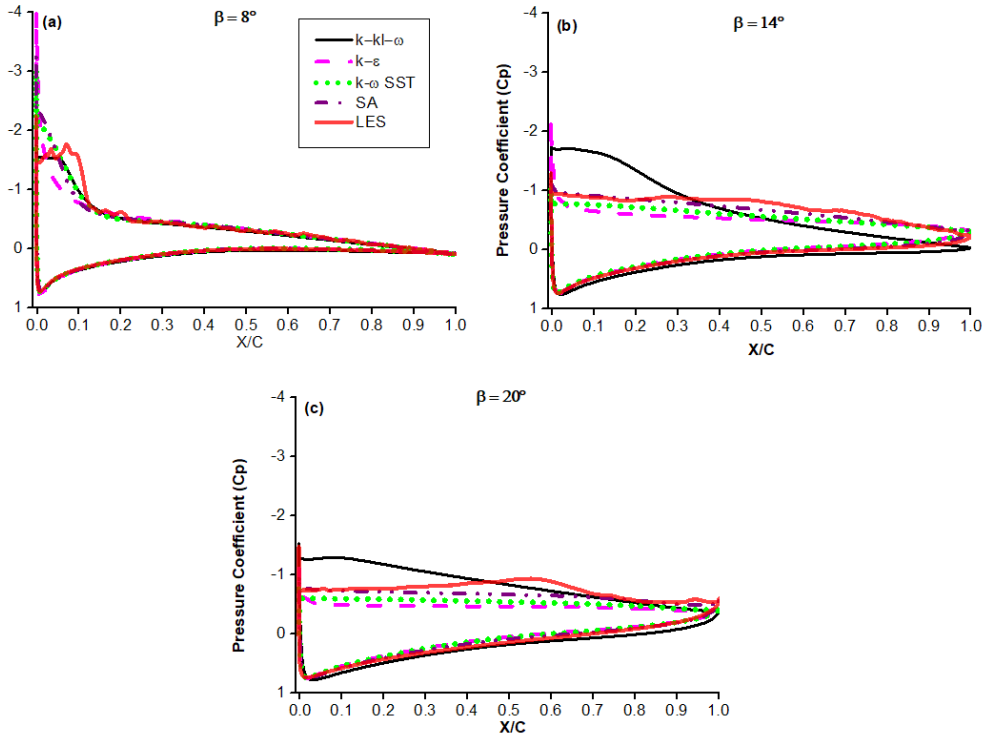

Fig. 4.29: Pressure Coefficient plot for δ = 0° at different sideslip angles for η = 0.50 .

However, at higher sideslip angle of β = 20°in Fig. 4.28 (c) the pressure side of the k-kl-ω is different from the other models, specifically close to the trailing edge, and this is inability to correctly predict the flow separation. This is clearly shown in the velocity analysis in Fig. 4.20 where the model indicated a small laminar separation at the leading edge while all other turbulence models demonstrated a large-scale recirculation that almost covered the suction surface. The different incorporation of the pressure in the transition k-kl-ω allows the model to generate a better side force and drag force coefficient compared to the other models.

The pressure distribution plotted at the higher sideslip angle of β = 20° is presented in Fig. 4.29 (c). It can be said that all three turbulence models, *k* -ω SST, S-A, *k* -ε, and LES, show a globally separated flow feature as shown in Fig. 4.23 (a)-(b). However, as observed in the previous results, the transition model k-kl-ω seems to show a separation delay. The model disagrees with the other three models and LES on both the suction and pressure side for η = 0.15, while it starts to agree on the suction side for x/c = 0.65 for η = 0.5. The pressure coefficient of the LES results indicated a reattachment in Fig. 4.28 (c) for 0.6 < x/c < 0.75. Similarly, except for k-kl-ω, all three turbulence models and LES agree with the flow features qualitatively. When the flow is separated at a larger sideslip angle, the separation points on the suction side shift upstream, which eliminates the presence of the LSB generated at the leading edge (Brunner et al. 2021).

4.6.4 Skin-Friction Coefficient Analysis for β = 8°, β = 14° and β = 20°

The surface skin friction coefficient superimposed by the skin friction lines is investigated at different sideslip angles and numerical schemes as shown in Fig. 4.30. The reattachment line, originating from the root side of the VTP, is observable in all models, with a general alignment to LES, except for the *k* -ε model, which positions slightly higher closer to the tip as shown in Fig. 4.30 (a). Specifically, the *k* -ε model displays the least accuracy in predicting the leading-edge laminar separation bubble as highlighted in the velocity analysis in Fig. 4.18 and 4.21. Despite this, it is important to note that all

models, including LES, demonstrate proficient predictions of trailing edge separation.

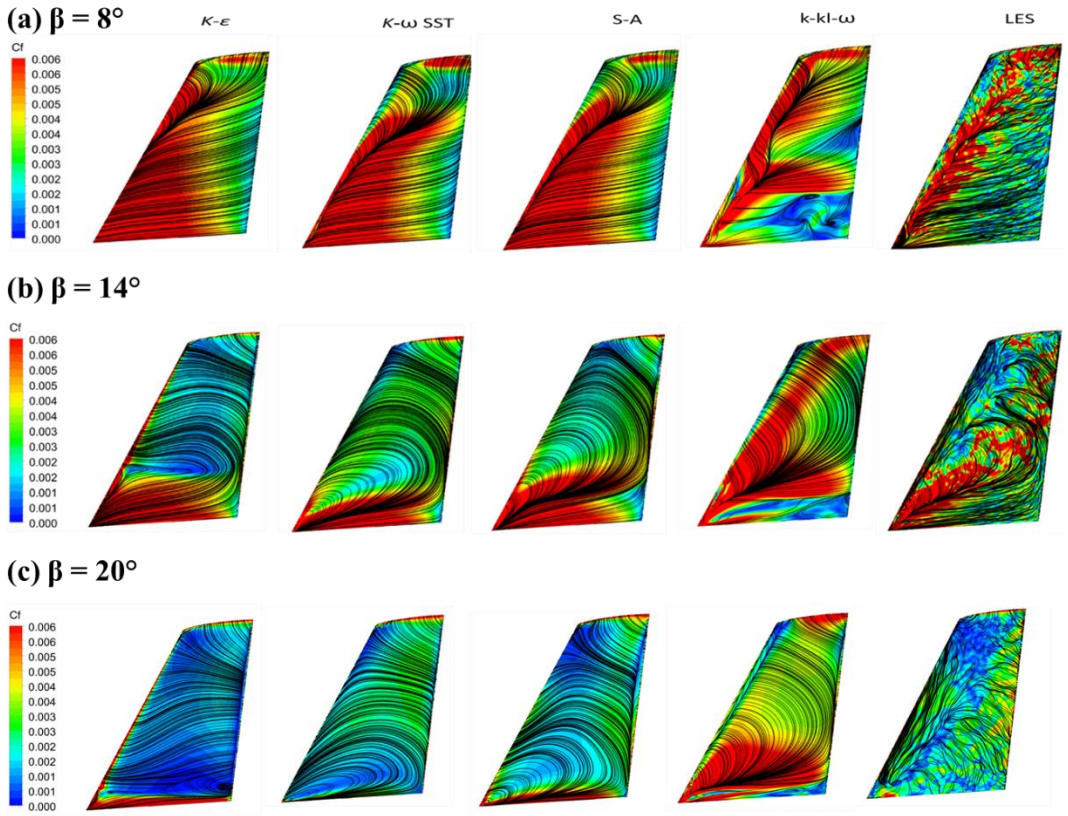

Fig. 4.30: Comparison of skin friction coefficient plot for δ = 0° and β = 8° (a), 14° (b), and 20° (c) with four turbulence models and the LES method.

The skin-friction contour in Fig. 4.30 (b) presented the results of four turbulence models and LES for a sideslip angle of β = 14°. A large separation area is present in the *k* -ε plot, which occupies almost the entire span of the VTP. It seems that the presence and overestimation of the separation by the *k* -ω SST and *k* -ε leads to underestimation of side force and drag force coefficient, respectively. The skin friction comparison of the four turbulence models and LES with superimposed skin friction line for δ = 0° and β = 20° is given in Fig. 4.30 (c).

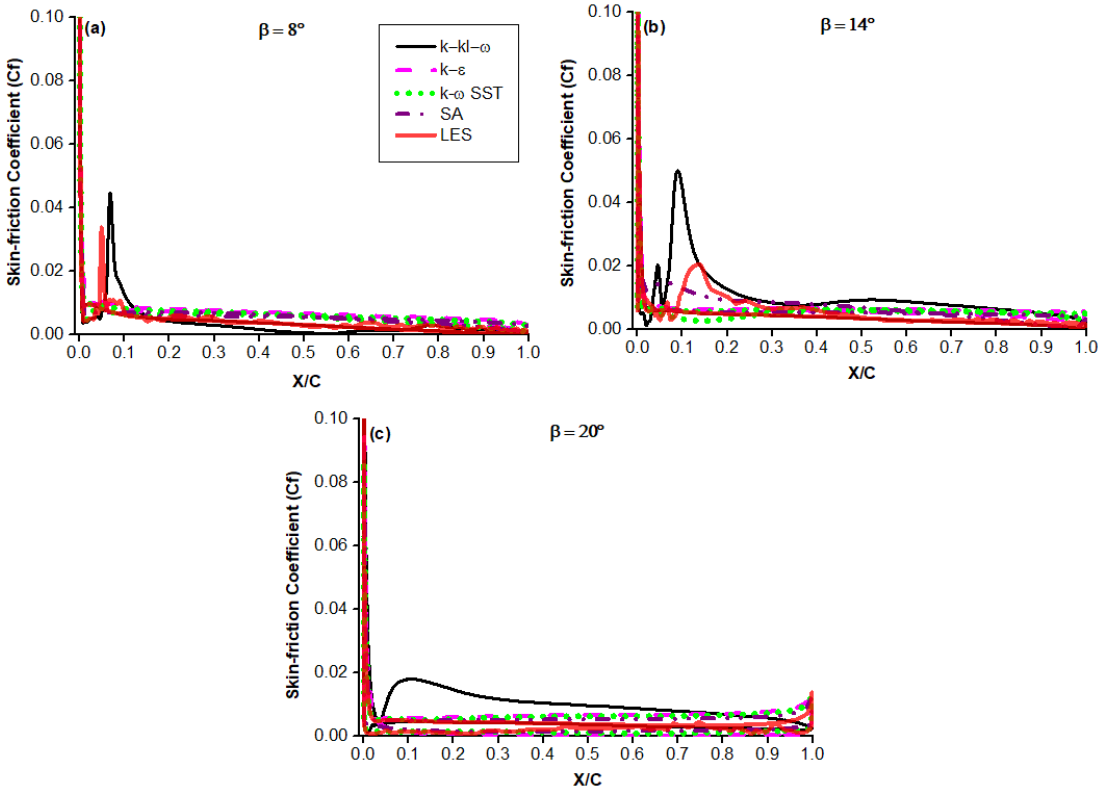

Fig. 4.31: Skin friction coefficient plot for δ = 0° at different sideslip angles for η = 0.15.

An illustration of the skin-friction coefficient for four different turbulence models and LES at slices at spanwise cut section of η = 0.15 and η = 0.50 at δ = 0° is presented in Fig. 4.31. The skin-friction curves in Fig. 4.26 (a) for all turbulence models display an irregular shape at the leading edge, which gradually settles chordwise toward the trailing edge. This peculiar behaviour is typically associated with the LSB, transition onset and turbulent reattachment as described in Fig. 4.18 and 4.21 in the velocity contour analysis. Moreover, upon analysing the pressure coefficient plot, it becomes apparent that the RANS and LES models exhibit a strikingly similar pattern for all four sections, particularly as seen in the case of the pressure coefficient plot. RANS models show better consistency with LES at lower sideslip angles due to reduced flow dynamics, but we acknowledge that capturing transitional and unsteady flows can be challenging. At this sideslip angle, the increase in the chordwise in Fig. 4.32 (a) also indicated the presence of LSB earlier confirmed in Fig. 4.20, in this case the k-kl-ω, S-A, *k* -ω SST and LES demonstrated the onset of transition and turbulent reattachment.

However, as shown earlier at a lower sideslip angle, the skin-friction coefficient indicated a rise close to the leading edge for the LES and transition k-kl-ω as shown in Fig. 4.31 (b). The skin-friction distributions at spanwise locations η = 0.15 indicated that the skin-friction levels of the turbulence models and LES were not constant at η = 0.15 as depicted in Fig. 4.31 (b) for β = 14°. However, as the chordwise location increased η = 0.5 as highlighted in Fig. 4.32 (b) all the turbulence models showed an almost constant value of the skin-friction coefficient except the transition model k-kl-ω, which exhibits an upstream flow separation. This means that the small and constant value of Cf downstream reflects flow separation.

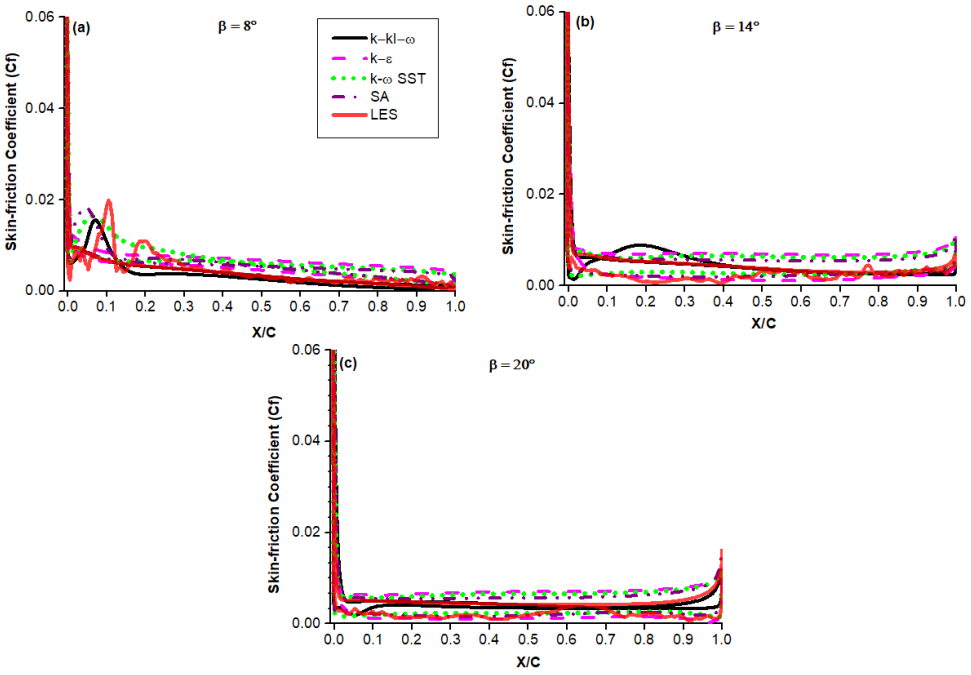

Fig. 4.32: Skin friction coefficient plot for δ = 0° at different sideslip angles for η = 0.50.

Figures 4.31 (c) and 4.32 (c) demonstrated the skin friction at a higher sideslip angle of $\beta = 20°$. The flow around the VTP surface is completely separated, as the three turbulence models predicted, except for the transition models, which show a delay in the separation close to the root. This prediction for a delay in separation can significantly impact the side-force and drag-force characteristics of the VTP and should be carefully considered in the design process.

Furthermore, the turbulence models qualitatively show different behaviours from each other's models as the chordwise increase. This is important information because it suggests that the simulations accurately capture the behaviour of the flow around the VTP at different chordwise locations, which is useful for the optimisation of the aerodynamic performance of the VTP.

4.6.5 Turbulent Kinetic energy

Figure 4.33 for $\beta = 8°$ presents the turbulent kinetic energy (TKE) of three turbulence models and the LES. The figure shows that the TKE highlights the turbulence around the VTP based on the turbulence models studied. The effect of the TKE is observed based on the spanwise cut sections at $\eta = 0.15$ and $\eta = 0.50$. From Fig. 4.33 (a), it can be seen that the flow separation increases the TKE near the trailing edge for all the models and LES. As the chordwise increases in Fig. 4.33 (b), the k-ω SST differs from other models.

In Fig. 4.34 (a) at $\beta = 14°$, as the sideslip angle increases, a further of the TKE shifts upstream toward the leading edge. In contrast, at lower sideslip angles, the TKE is predominantly captured near the trailing edge. This phenomenon is commonly observed in aerofoils, as Shah et al. (2015) noted at a comparable Reynolds number of 10^5. In Fig. 4.34 (b) at $\eta = 0.50$, all the k-ω SST and k-ε turbulence models agreed well as the chordwise increase compared to the transition k-kl-ω model and LES.

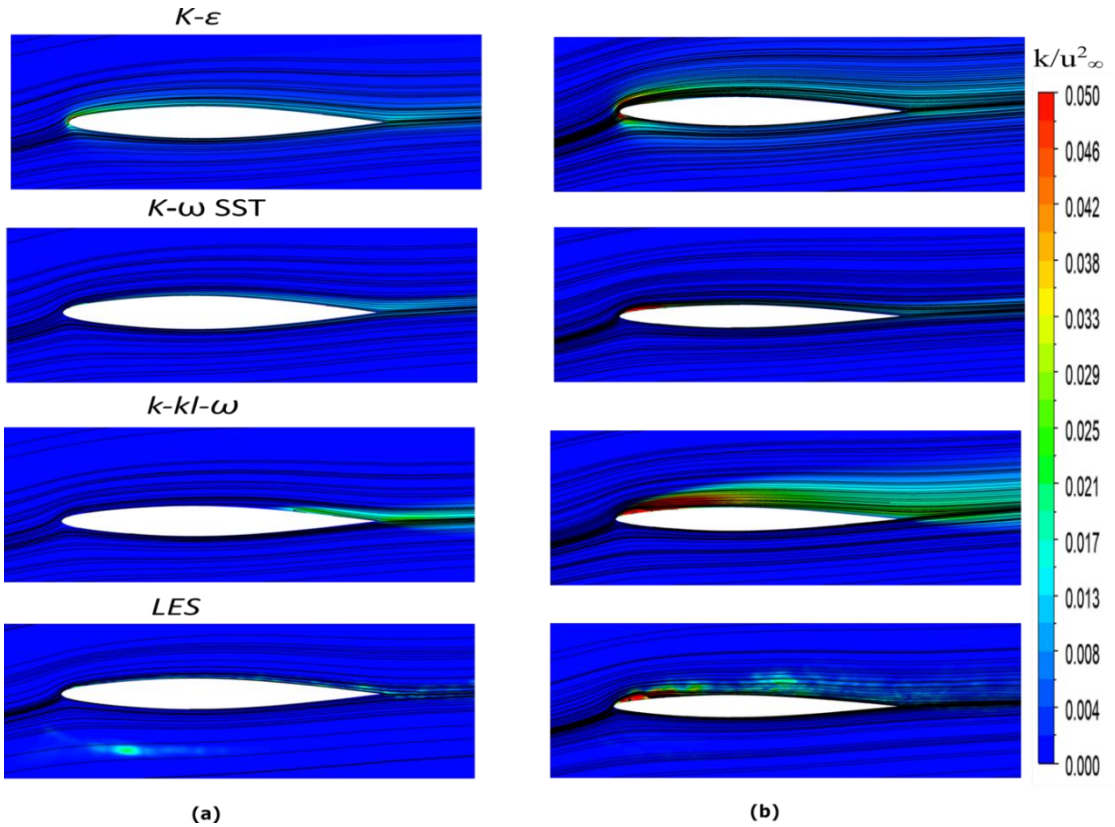

Fig. 4.33: Turbulence kinetic energy from different turbulence models at β = 8° (a) η = 0.15, (b) η = 0.50**.**

Low TKE resolution was observed at the leading edge for k-ε compared to the three turbulence models and the LES at η = 0.15 in Fig. 4.34 (a). Moreover, the results were contradictory for lower side slip angle β = 8° (Fig. 4.33), where the k-ε shows a higher TKE resolution than the other models. The performance of the models decreased with increasing sideslip angle due to its inability to withstand the separation phenomenon exhibited around the VTP.

The increase in the side slip angle resulted in a rise in TKE for all angles. Also, the spanwise cut section of η = 0.50 shows an increase in the TKE compared to the η = 0.15. Therefore, the TKE increases chordwise close to the root where η = 0.15 to η = 0.50 which is far away from the root side of the VTP. In Fig. 4.35 (b), the k-kl-ω model had a significantly higher TKE than the k-ω SST, k-ε, and LES models due to the high-velocity magnitude demonstrated by the model as highlighted in the velocity profile plots.

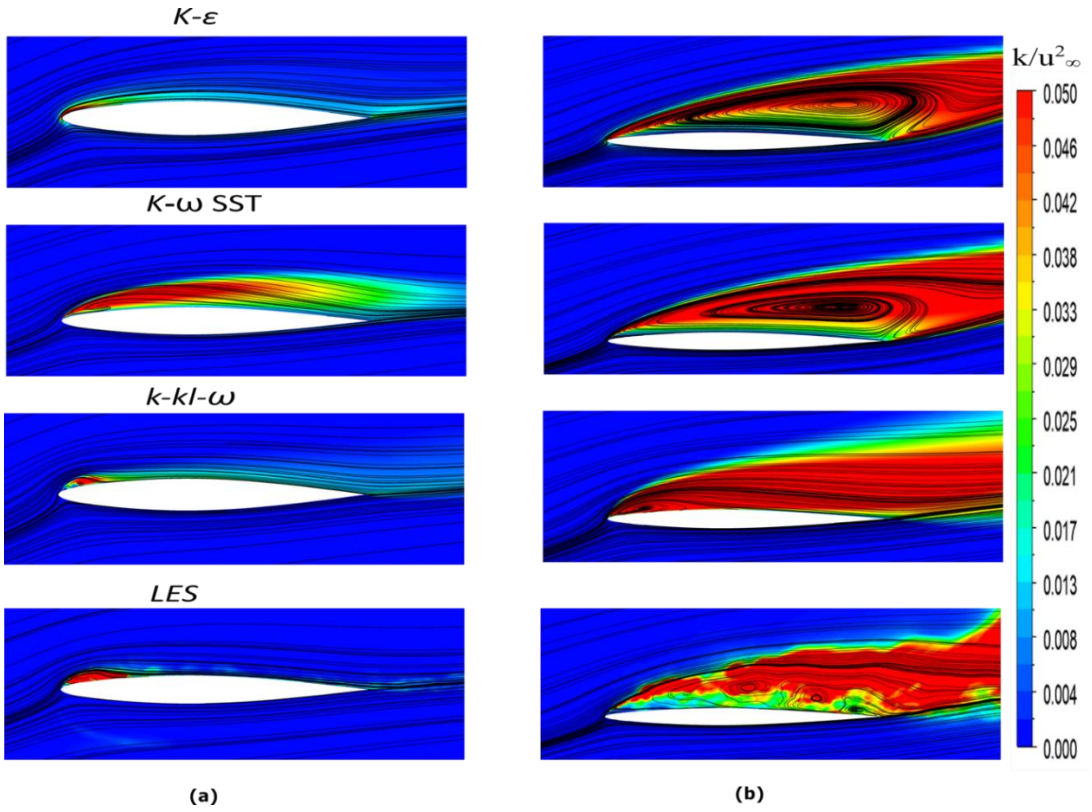

Fig. 4.34: Turbulence kinetic energy from different turbulence models at β = 14° (a) η = 0.15, (b) η = 0.50.

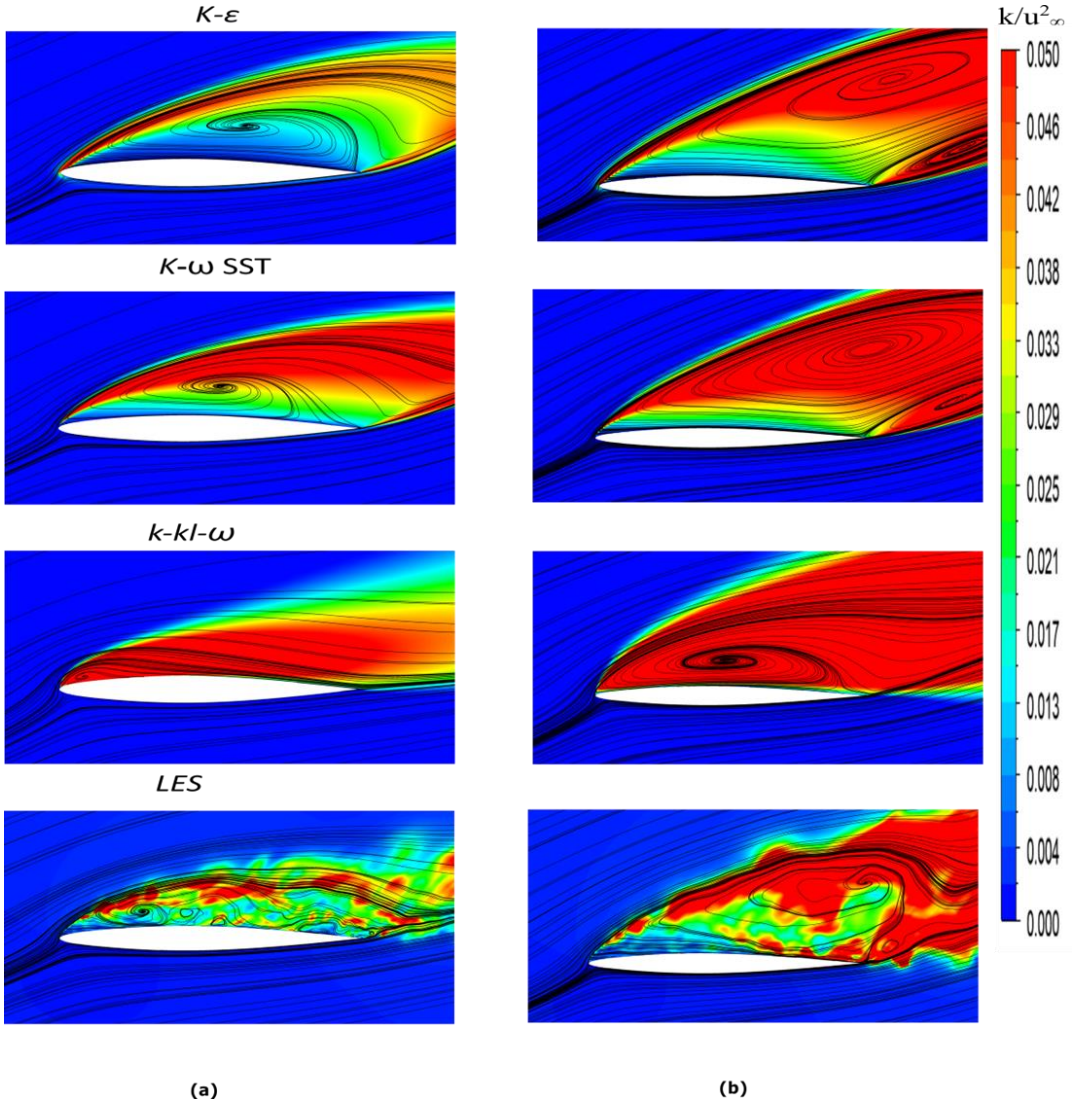

Fig. 4.35: Turbulence kinetic energy from different turbulence models (a) η = 0.15, (b) η = 0.50 at β = 20°.

4.7 Chapter Summary

This chapter thoroughly investigates the RANS model's performances for flow over VTP. These models were compared with the wind tunnel experimental data and the high-fidelity LES. The limitations and advantages of using the RANS models were noticed based on the investigation.

Additionally, three different sideslip angles were considered for comparison with the RANS and experimental data for the LES case to observe the separation effect. The analysis of the angles demonstrated the effect of separation and the changes that occurred from the leading edge to the trailing edge. The subsequent chapters will thoroughly investigate the separation effect using flow control devices. The pure RANS is unsuitable for the flow of the VTP in this study due to the inability to represent the actual flow field parameters. The early loss of the side-force and drag-force coefficient shows the lack of reliability in predicting the separation region because the phenomenon occurred on the surface of the VTP. Introducing the transition model among the RANS turbulence models highlighted improvement, especially around the leading edge where the laminar separation bubble was captured.

The analysis comparing the LES with RANS and experimental data reveals a notable agreement in predicting force coefficients, especially at low sideslip angles. Surface pressure coefficients at the lower sideslip angle remain well predicted by all the turbulence models compared to the LES result. The difference was observed as the sideslip angle increased. At the stall angle, most of the turbulence models underpredicted the flow fields due to the evolution of the separation around the VTP. The transition turbulence model and LES produced a better prediction even at higher sideslip angle and stall angle, and this is evidence to say that the transition model is robust in predicting flow related to transition with the complex region of laminar to turbulent separation. The LES more accurately captured the reattachment point, which the RANS turbulence models either overpredicted or did not predict.

Lastly, the influence of the TKE shows a remarkable result amongst the RANS turbulence models and LES. The TKE increases with an increase in the sideslip angles, and the chordwise representation of the TKE decreases inboard. It was observed that all the turbulence models and time-averaged LES

agreed well in the prediction of the TKE in the observed chordwise locations studied.

5. Chapter five

FLOW SEPARATION CONTROL OF A VERTICAL STABILISER USING A RUDDER-MOUNTED SLAT

5.1 Introduction

This chapter presents a detailed analysis of a study that uses LES to examine flow separation control around a vertical stabiliser with a rudder-mounted slat. The study includes an assessment of the aerodynamic force coefficients based on results obtained from LES and compared with wind tunnel tests. The chapter aims to thoroughly investigate the effect of a rudder-mounted slat as a flow control strategy for the separation effect around the vertical tailplane.

Adding the slat at the rudder leading edge at a rudder deflection of $\delta = 30°$ changes the pressure coefficient distribution over the suction side of the vertical stabiliser. The effect of the rudder-mounted slat was thoroughly investigated based on the pressure and skin friction coefficient distribution on the suction side of the vertical stabiliser. The performance of the slat was evaluated based on the LES results at three different sideslip angles of $\beta = 8°$, $\beta = 14°$, and $\beta = 20°$. At low sideslip angles, the slat significantly improved by attaching the flow and reducing the separation effect on the suction side.

The study also examines the flow's vorticity distribution and vortical structure over the vertical stabiliser with and without the slat. The flow field with a slat attachment is modified compared to the baseline, which is believed to be due to the circulation added by the slat. This is evident from the change in the streamlines around the trailing edge of the rudder. The streamline on the vorticity field indicated how the slat benefits the performance of the vertical stabiliser by attaching the flow and reducing the separation.

In the last part of this chapter, the study delves into the investigation of mean and turbulent velocity profile for two cases: one without the slat and the other with the slat attached. The analysis also assesses the impact of the mounted slat on the turbulence kinetic energy and the Reynolds stress. Overall, the findings highlight the potential benefits of using slats to improve the efficiency and safety of various engineering systems.

5.2 The Slat on the Rudder

The rudder of the test model has been modified by attaching a specially designed slat; an additional element incorporated to improve airflow control over the rudder's surface. Its primary purpose is to prevent flow separation, which can occur when the airflow separates from the surface of the rudder, causing a loss of control and instability. The modification has been designed with precision, considering the principles of aerodynamics.

The slat has been strategically placed at the rudder leading edge, 30% of the model's width, and 20% of the local rudder chord in width. The upper surface of the slat has been shaped using the NACA 6410 aerofoil, which is a common type of aerofoil used in aircraft design. The aerofoil has a maximum thickness of 2mm, optimised to provide maximum performance while minimising drag.

To ensure optimal installation of the slat, the bottom surface of the slat has been flattened. The slat has been securely attached to the rudder using five streamlined struts, and the gap between the slat and the rudder has been set at 4mm, considering the estimated thickness of the local boundary layer. The vertical tailplane has a tapered trapezoidal shape with a 0.4m span dimension, a 0.322m root chord, and a 0.148m tip chord. The full 3D section of the VTP, which includes the stabiliser, rudder, and slat aerofoil, is depicted in Fig. 5.1.

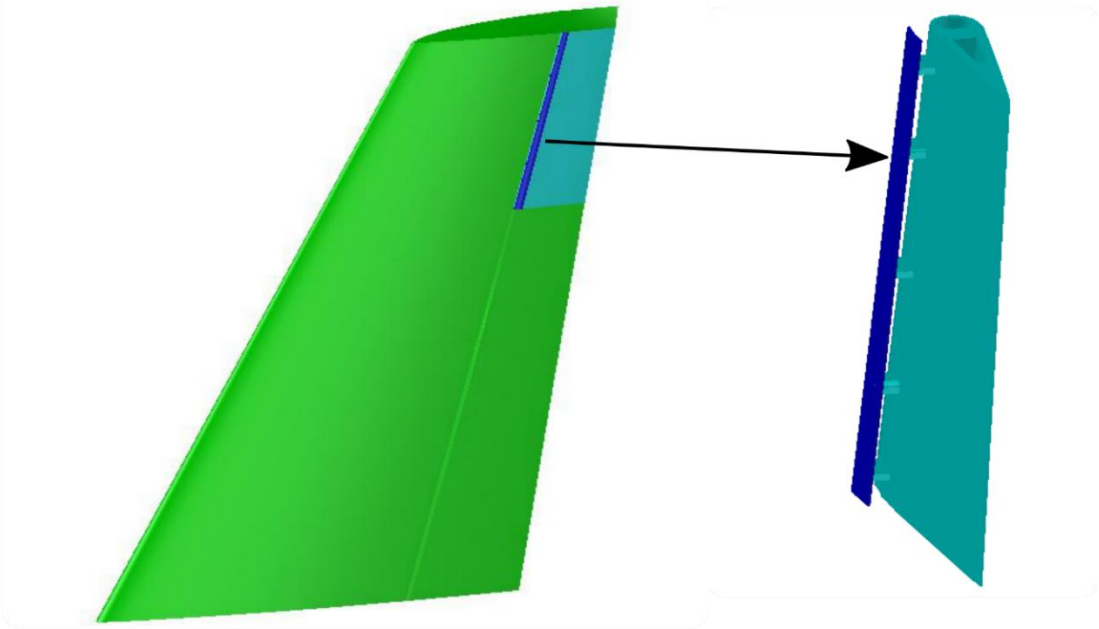

Fig. 5.1: Vertical Stabiliser model and slat attachment on the rudder.

5.2.1 Simulation Set-up and Boundary Conditions

The large-eddy simulation (LES) was carried out using Fluent's finite volume software by solving the time-dependent incompressible Navier-Stokes equations. The wall-adapting local eddy-viscosity (WALE) scheme was employed to model the subgrid eddy viscosity (Qin et al. 2018). The pressure-based coupled solver was selected, and the momentum equations were discretised using the bounded central differencing (BDC) scheme (Zhu and Rodi 1991). Here, the pressure-based coupled algorithm solves a coupled, non-linear system of equations comprising the momentum and pressure equations. This approach accelerates the convergence process (Pascau et al. 1996) but requires additional memory (Guo et al. 2022) compared to the pressure-based segregated algorithm. For the time discretisation, the bounded central differencing scheme was used with the time-step size of $\Delta t = 1 \times 10^{-4}$ s (Mereu et al. 2019). The dimensions of the computational domain are 20m × 8.4m × 5.2m in the streamwise (x), wall-normal (y) and spanwise direction (z), see Fig. 5.2(a). The velocity-inlet and pressure-outlet boundary conditions were employed, and the freestream turbulence level was set to 4%. The no-slip boundary condition was set over the model surfaces, placing 30 chords from the inlet. At the same time, the no-slip boundary condition was specified over the top wall of the computational domain. Here, the slip boundary condition was set on the floor to avoid the boundary layer growth affecting the model. A similar consideration was made in the experimental wind tunnel study, where the test model was placed away from the floor wall to avoid the boundary-layer effect on the aerodynamic force measurements.

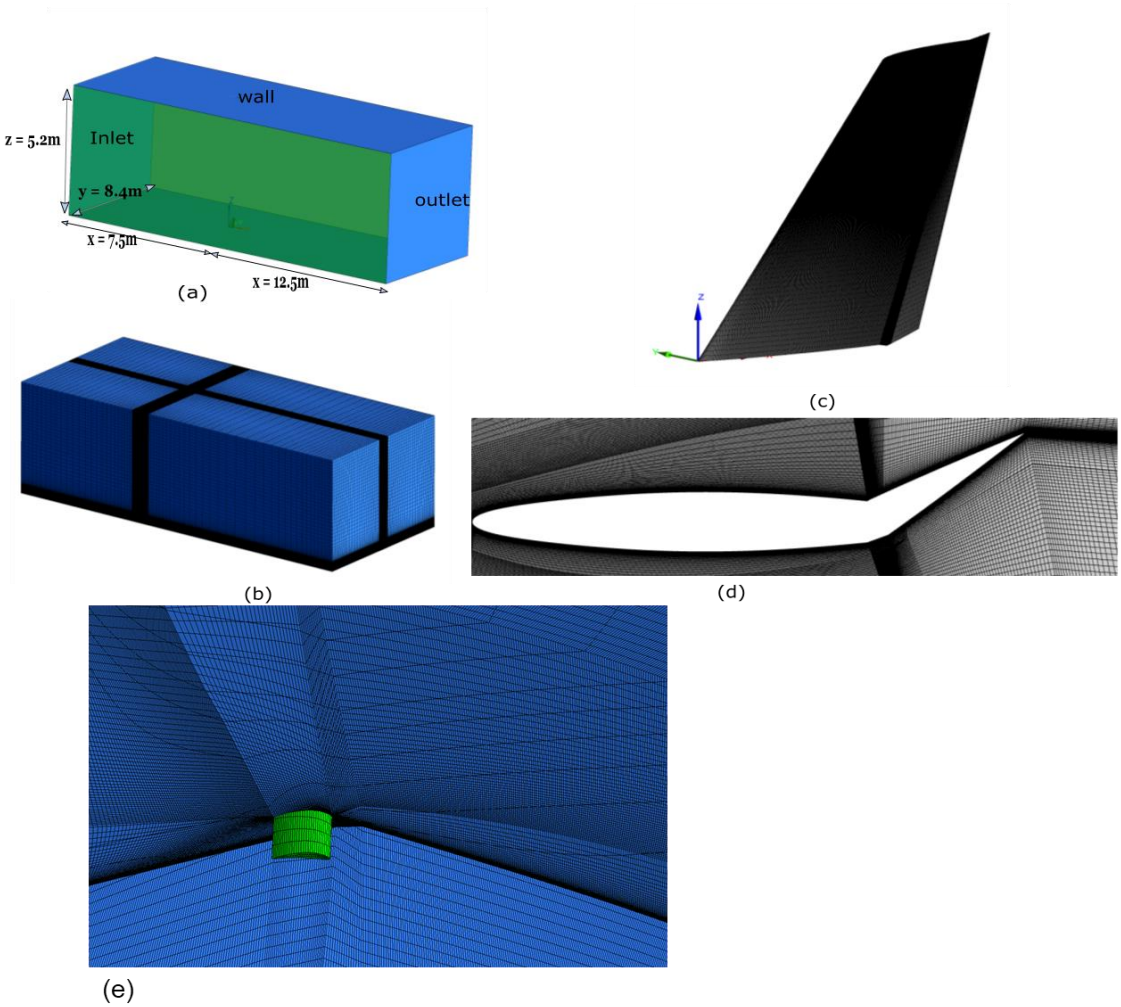

Fig. 5.2: The computational domain size. (a) The domain enclosure, (b) the domain mesh, (c) the structured mesh over the vertical stabiliser and (d) the cut section to show the mesh refinement (e) Slat mesh refinement.

5.2.2 Computational Domain and Mesh Details

The computational mesh size is 680 × 155 × 110 spread in x, y and z coordinates, as shown in Fig. 5.2(b). The mesh surrounding the vertical stabiliser model is refined to 520 × 80 × 60 meshes in streamwise, wall-normal, and streamwise directions. The mesh in the near wake of the trailing edge is also increased. The mesh clustering and control were achieved using a structured mesh adopted in this study. As shown in Fig. 5.2(c) and (d), the node distribution is non-uniform in the streamwise and wall-normal directions, making the vertical stabiliser's vicinity denser. The initial wall distance was set at $y^+ = 1$ and the mesh size in the wall-normal direction was increased by a factor of 1.12, where y^+ is the non-dimensional viscous height.

For the mesh near the slat in Fig. 5.2 (e), the gap between the slat and the rudder surface contains 50 nodes where the nodes are carefully clustered and denser on the walls of the slat and the rudder surface. At this point equal growth rate of 1.09 was used to ensure enough refinement of the node distribution on the pressure side of the slat and the suction side surface of the rudder.

The y^+ value of the first wall-normal grid point over the vertical stabiliser model remained $y^+ < 1$ after the numerical simulation. A visual representation of y^+ distribution over the VTP surface is given in Fig. 5.4, which shows a surface where $y^+<1$, with an average of $y^+<0.2$. This condition is vital in various engineering applications (Yang and Griffin 2021), and it is important to check the wall y-plus after the simulation to confirm if it meets the required value.

In addition, the C-type mesh pattern was used around the vertical stabiliser to capture the leading edge curvature, enhancing the grid line performance along the shear layer region. The computed force coefficients against the non-dimensional time are given in Fig. 5.3, which shows that the side-force coefficient Cs and the drag coefficient Cd converge within $t^* = 20$ of numerical simulation, which lasted up to $t^* = 50$. Here, the non-dimensional time is defined by $t^* = t \cdot U_\infty / c$ where c is 0.2455 m and $U_\infty = 10 m/s$.

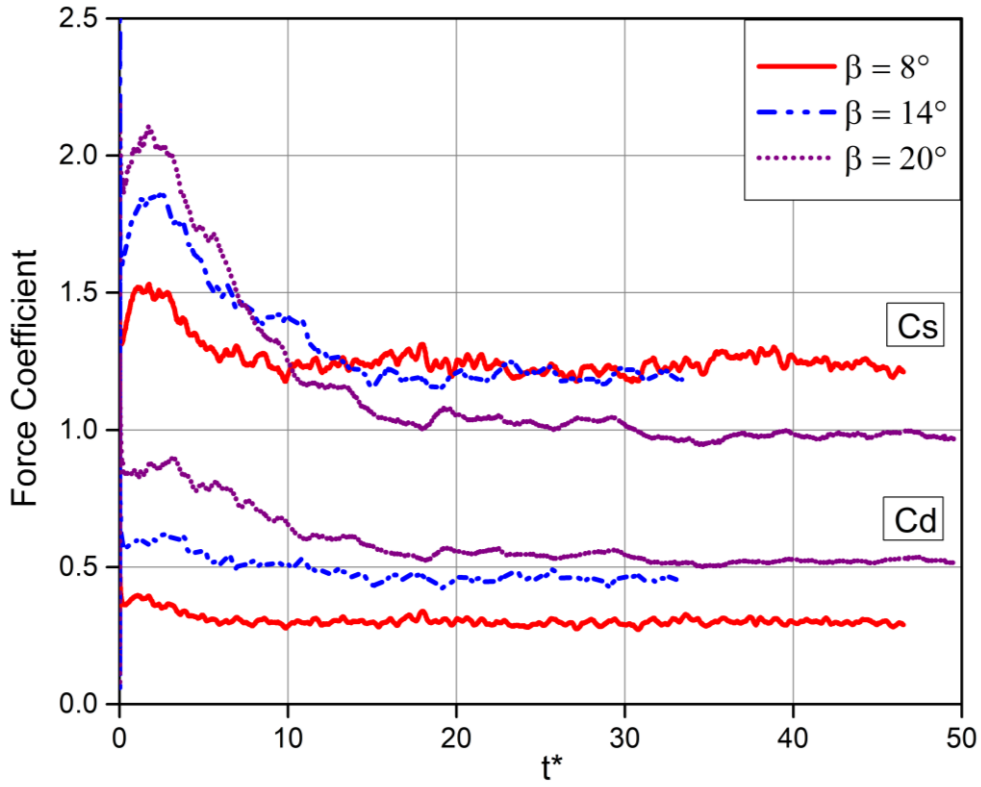

Fig. 5.3: Variation of Cs and Cd during the numerical simulation to show convergence.

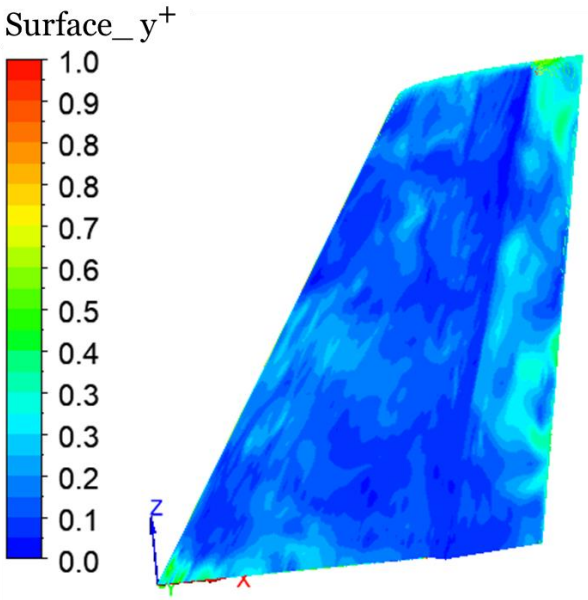

Fig. 5.4: Surface y^+ around the vertical tailplane.

5.2.3 Assessment of LES Mesh Quality

To ensure accurate large eddy simulation (LES) results, we evaluated the mesh using criteria established by (Pope 2004) and (Celik et al. 2005). Prior research has shown that obtaining mesh independence in LES is difficult due to the subgrid viscosity's reliance on mesh size. Consequently, each mesh iteration will produce distinct outcomes. Therefore, each mesh solves different equations. However, the best practice for LES mesh resolution and turbulence assessment is to ensure that 80% of the ratio of the resolved turbulent kinetic energy to the total kinetic energy is well resolved, as suggested by (Celik et al. 2005). The proposed equation by Celik et al. (2005) was used to obtain the LES_IQ in terms of the subgrid eddy viscosity and the molecular viscosity, as shown below:

$$LES\_IQ_v = \frac{1}{1+0.05\left[\frac{(\mu+\mu_t)}{\mu}\right]^{0.53}}$$

A large-eddy simulation quality index (LES_IQ) was conducted for the mesh resolution in several planes in the domain, as shown in Fig 5.5. The LES_IQ value ranged from 0 to 1, the higher the value, the better. It is recommended to aim for a LES_IQ of 75%–85% for LES simulation (Celik et al. 2005). LES_IQ can be visualised in Fig 5.5 in planes in the fluid domain. This confirms that the grid resolution in LES is sufficient to fully resolve the large eddies, except in the near-wall region of the VTP. It is apparent that more than 93% of the turbulent kinetic energy is resolved, particularly around the region of interest.

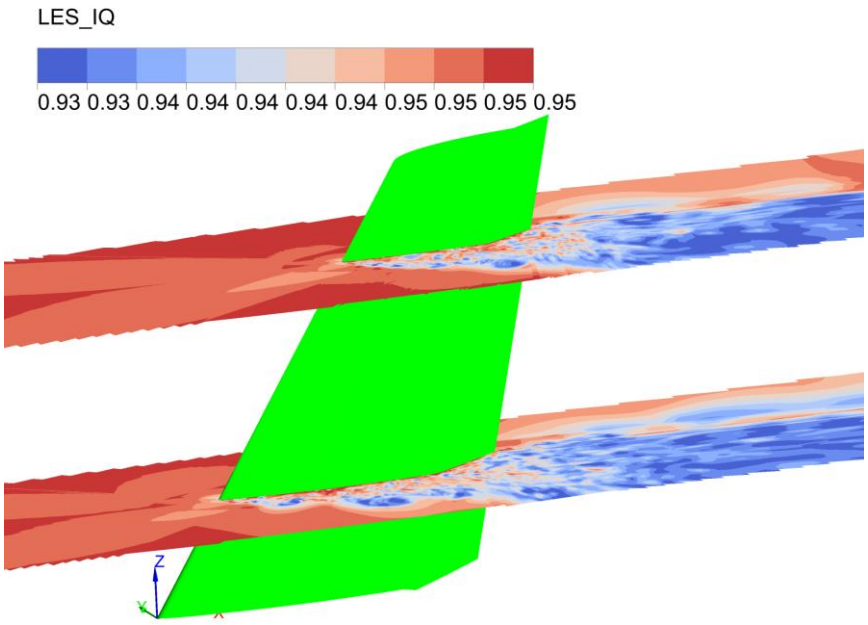

Fig. 5.5: Resolution of mesh quality using LES_IQ 3D domain zoom section of vertical tailplane.

5.2.4 Spectral Analysis

The spectral analysis of the spanwise velocity fluctuation was carried out in the wake region of the vertical stabiliser at two locations, (x/c, y/c, z/c) = (2.04, -0.114, 1.29) and (x/c, y/c, z/c) = (2.04, -0.151, 0.724) as shown in Fig. 5.6(a) and Fig. 5.6(b), respectively. Here, the sideslip angle was set at $\beta = 14°$ with the rudder angle of $\delta = 30°$. These wake locations correspond to the non-dimensional spanwise distance $\eta = 0.79$ and $\eta = 0.45$ from the root of the vertical stabiliser. Although the spectral peaks are not very sharp due to the unsteady nature of the flow separation from the vertical stabiliser with a swept wing shape, they correspond to the expected shedding frequencies of between 16 Hz and 35Hz based on the Strouhal number of St = 0.2. Figure 5.6(a) is of particular interest as it displays the distribution of turbulent kinetic energy of spanwise velocity fluctuations across their frequencies immediately downstream of the slat. Indeed, it is clearly seen that the higher frequency energy is increased by the slat, suggesting that the wake region is narrowed as a result of flow separation control. The power spectrum at $\eta = 0.45$ as shown in Fig. 5.6(b) does not seem to be much different from that of the baseline, as it was obtained closer to the root of the vertical stabiliser.

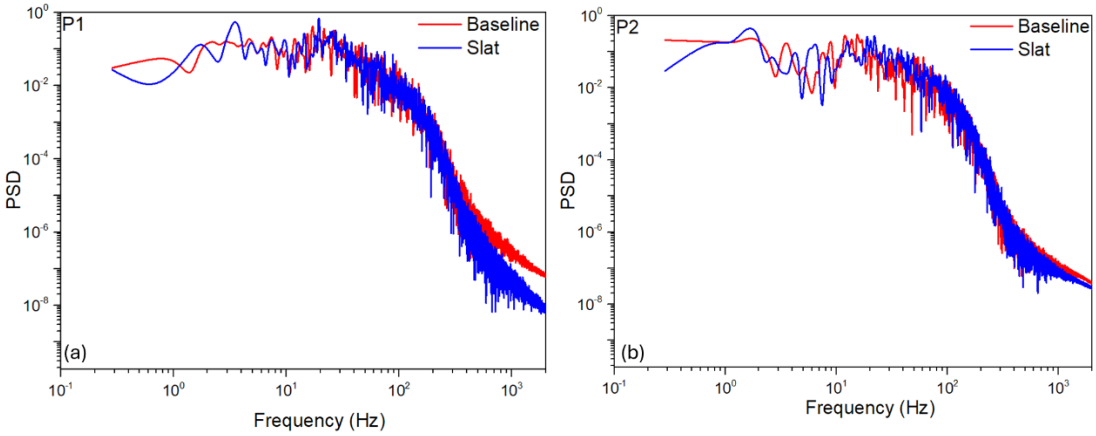

Fig. 5.6: Power spectra of spanwise velocity fluctuation in the wake region of the vertical stabiliser (a) at P1 (x/c, y/c, z/c) = (-2.04, -0.114, 1.29); and (b) at P2 (x/c, y/c, z/c) = (2.04,-0.151,0.724), corresponding to η= 0.79 and η = 0.45, respectively at the sideslip angle β = 20° with the rudder angle δ = 30°.

5.3 Results and Discussion

5.3.1 Aerodynamic Force Coefficients

The experimental results of aerodynamic force coefficients are shown in Fig. 5.7 for three rudder deflection angles of δ = 0°and 30° (TailSurf 2019). When there is no rudder deflection (δ = 0°), the rudder-mounted slat increases the side force coefficient Cs at the sideslip angle range of 10° – 20°, where the flow over the rudder is partially or fully separated. The drag coefficient Cd in the corresponding sideslip angle range increases very slightly. Here, the slat effects on the Cd are hardly noticeable. The most significant impact of the slat is found for the largest rudder deflection angle of δ = 30° tested, where the maximum difference in Cs is about 4% at a sideslip angle of β = 14° as shown in Table 5.1. At a sideslip angle of β = 14°, the experimental and numerical data from Table 5.1 indicated an improvement due to slat attachment, with enhancements of 3.1% in the experimental data and 3.2% in the numerical simulation data. Additionally, at a sideslip angle of β = 20°, the slat attachment enhanced by almost 2% in the experimental and the numerical simulation data for the side force coefficients. It is noted that there is a small increase in Cd with an increase in Cs by the slat. These results clearly indicate that the slat has beneficial effects

in flow separation control when the flow around the rudder surface is partially or fully separated.

The baseline LES results (without slat) for the deflection angle of δ = 0° are also shown in Fig. 5.7, which are compared with the experimental data at the sideslip angles of β = 20°. Both the side-force coefficient Cs and drag-force coefficient Cd agree well with the experiment. The agreement of the LES data with the experimental data with a slat at β = 20° shows an increase in Cs by the rudder-mounted slat. A high-fidelity LES study is also performed at the deflection angle of δ = 30°, where the maximum slat effect is observed from the wind tunnel tests. Here, the agreement of the side-force coefficient Cs and the drag-force coefficient Cd between the LES and experiments is good, clearly showing an increase in the Cs at β = 14°. In comparison, β = 8° and β = 20° indicated a reasonable agreement with the experiment.

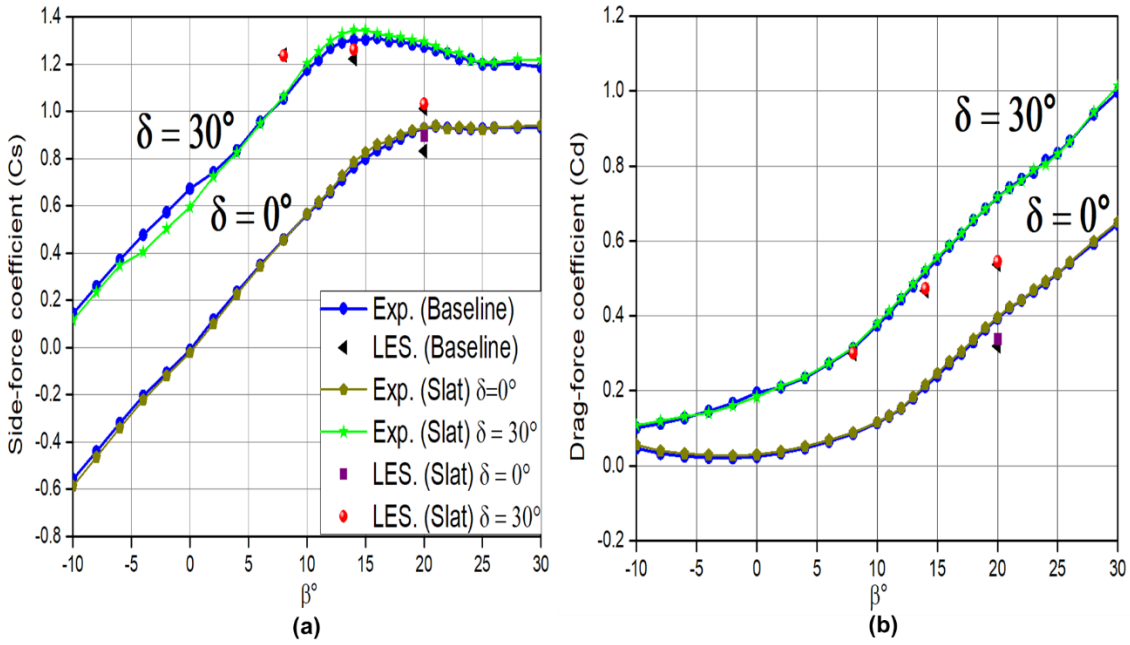

Fig. 5.7: Experiment results to show the side-force coefficient Cs (a) and the drag-force coefficient Cd (b) for the baseline case and with slat at the rudder deflection angles of δ = 0°and 30°. LES data are also shown for comparison.

Table 5.1: Force coefficient enhancement due to the slat effect for δ = 30°

Method	β	Baseline		With slat		Changes	
		Cs	Cd	Cs	Cd	ΔCs	ΔCd
Exp.	8°	1.054	0.312	1.064	0.316	0.9%	1.3%
LES		1.238	0.299	1.237	0.301	-0.1%	0.7%
Exp.	14°	1.303	0.517	1.344	0.523	3.1%	1.2%
LES		1.223	0.467	1.262	0.473	3.2%	1.3%
Exp.	20°	1.274	0.717	1.295	0.717	1.6%	0.0%
LES		1.012	0.537	1.032	0.545	2.0%	1.5%

5.3.2 Surface Pressure and Skin Friction Coefficients

Figure 5.8 shows the distribution of the surface pressure coefficient Cp over the suction side of the vertical stabiliser for the baseline case (a) and with slat (b) for the sideslip angle of β = 8° at the rudder angle of δ = 30°. At this condition, the rudder-mounted slat increases the negative surface pressure coefficient (-Cp). This is clearly seen in Fig. 5.9(a) that the negative surface pressure coefficient (-Cp) along η = 0.75 is increased at the slat position as well as over the rudder. Here, η is the non-dimensional spanwise distance from the root. At η = 0.90, a greater change in the surface pressure coefficient is seen over the rudder surface, which suggests that the slat is helping reattach the separated flow, see Fig. 5.9(b). For a sideslip angle of β = 14° at the rudder angle of δ = 30°, see Fig. 5.10, the slat effect on the surface pressure coefficient is only seen closer to the root of the vertical stabiliser. This is shown by the Cp curve along the spanwise location of η = 0.75 in Fig. 5.11(a) compared to that at η = 0.90 in Fig. 5.11(b). Here, we can see little change in Cp over the rudder surface due to the slat. For a larger sideslip angle of β = 20° at the rudder angle of δ = 30°, see Fig. 5.12, the slat effect on the surface pressure coefficient is seen closer to the root of the vertical stabiliser and spread over the trailing edge of the rudder. This is surprising since the slat is located closer to the tip of the vertical stabiliser, yet it has an effect on pressure distribution closer to the root. This will be explained in the following sections by comparing the flow field around the vertical stabiliser with and without slat. The Cp curves along the

spanwise location of η = 0.75 and η = 0.90 are shown in Fig. 5.13(a), where (-Cp) is seen to increase only at the slat.

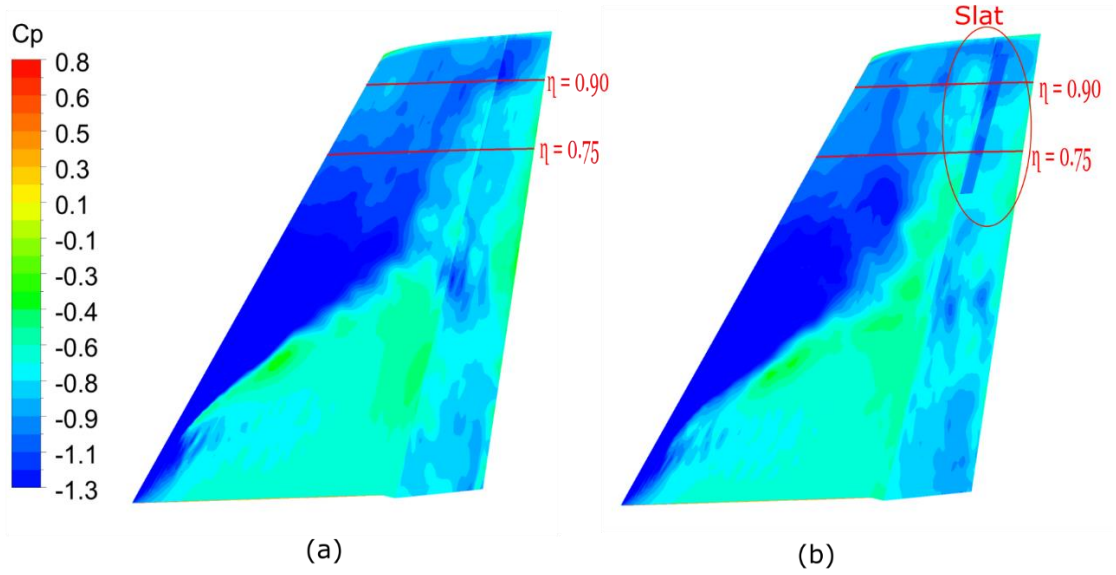

Fig. 5.8: Surface pressure coefficient by LES for the baseline (a) and with slat (b) for β = 8° at δ = 30°.

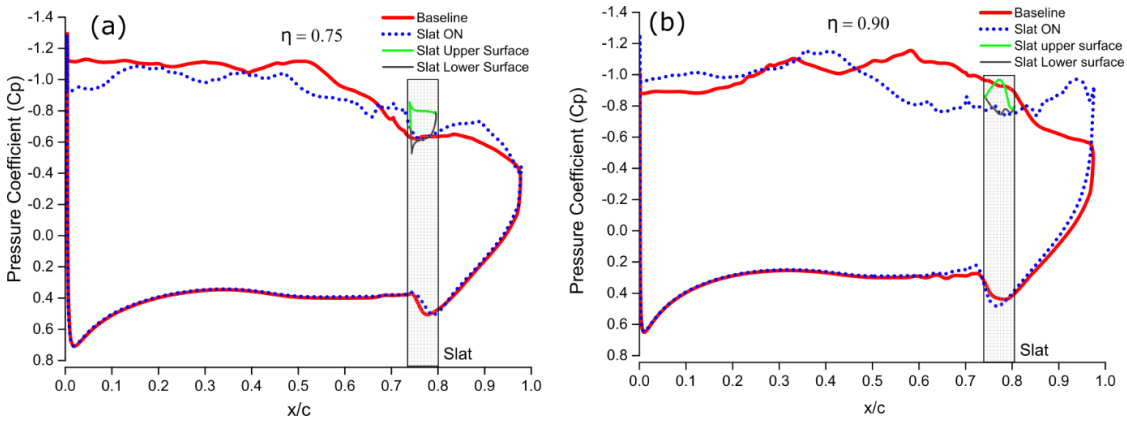

Fig. 5.9: Surface pressure coefficient by LES (a) at η = 0.75 and (b) at η = 0.90 for β = 8° at δ = 30°.

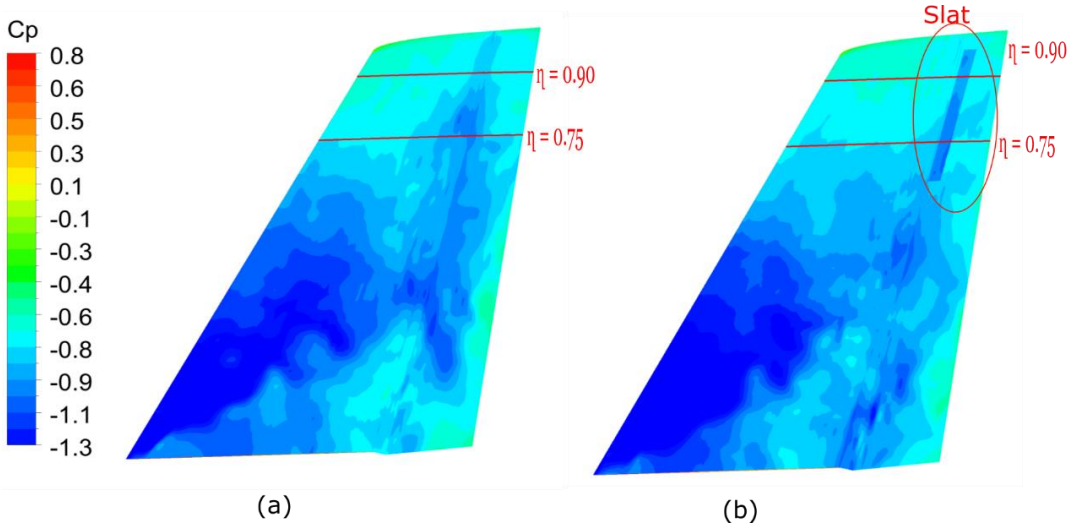

Fig. 5.10: Surface pressure coefficient by LES for the baseline (a) and with slat (b) for β = 14° at δ = 30°.

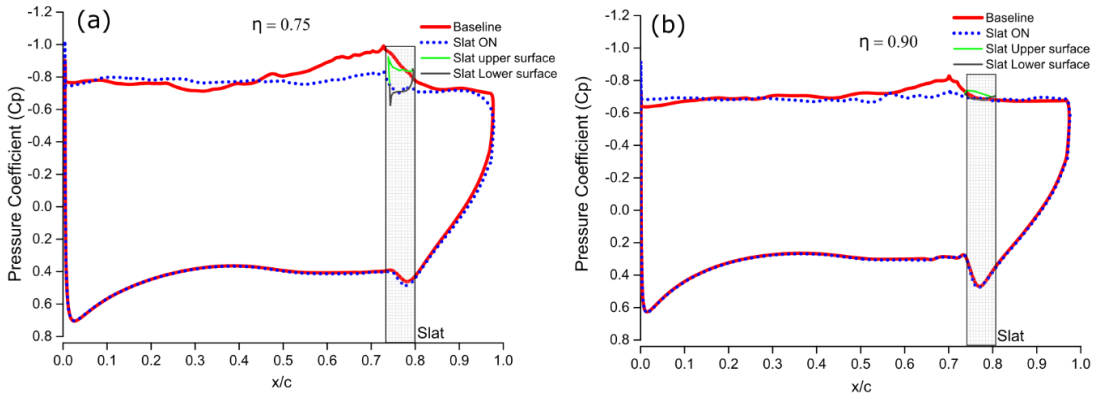

Fig. 5.11: Surface pressure coefficient by LES (a) at η = 0.75 and (b) η = 0.90 for β = 14° at δ = 30°.

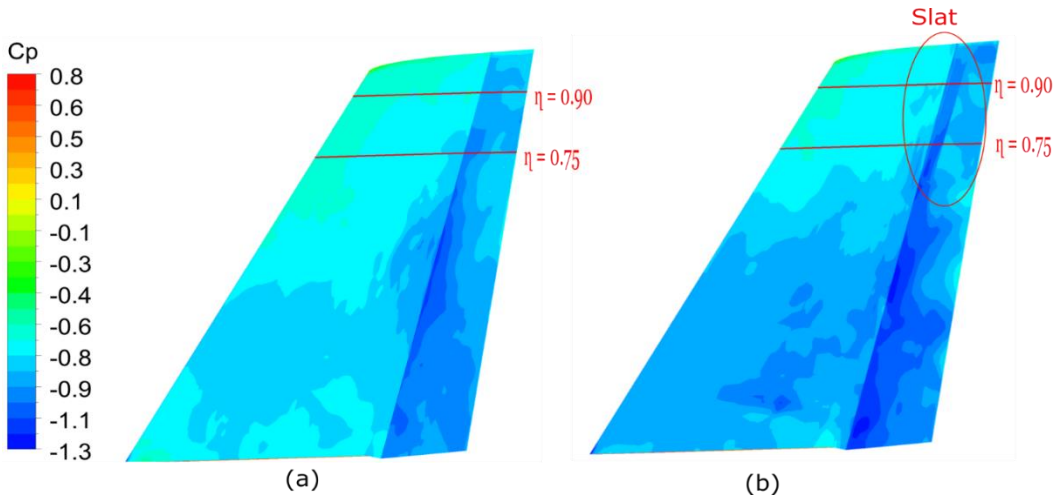

Fig. 5.12: Surface pressure coefficient by LES for the baseline (a) and with slat (b) for β = 20° at δ = 30°.

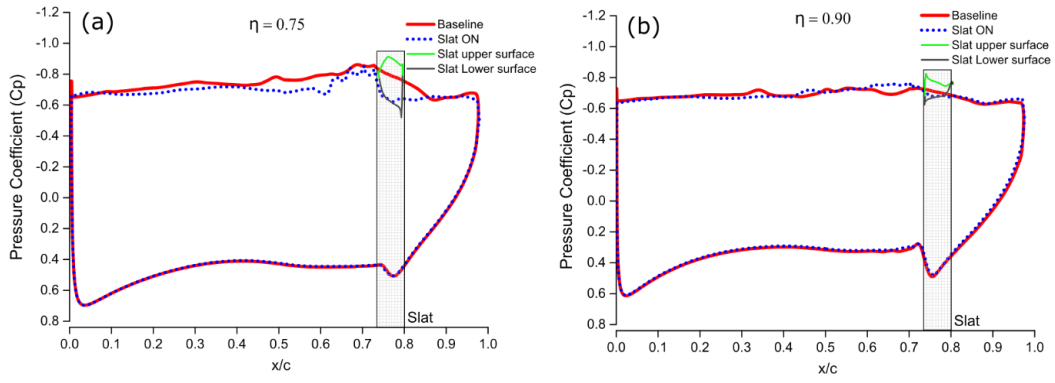

Fig. 5.13: Surface pressure coefficient by LES (a) at η = 0.75 and (b) η = 0.90 for β = 20° at δ = 30°.

The distribution of the total skin-friction coefficient C_f over the suction side of the vertical stabiliser is shown in Fig. 5.14, together with the wall-shear stress lines for the baseline case (a) and with slat (b) for the sideslip angle of β = 8° at the rudder angle of δ = 30°. It is interesting to observe the wall-shear stress lines of this figure, which show a reattachment line coming off the root of the leading edge at about 45° angle. After the reattachment, the wall-shear stress lines are seen nearly parallel to the freestream. The reversed wall-shear stress lines (towards the leading edge) from the reattachment line indicate the existence of a recirculating zone there. The total skin friction coefficient is high (shown in dark red in Fig. 5.14) along the reattachment line as the separated flow impinges on the surface. The flow over the deflected rudder downstream

of this attachment line seems to be separated again as the wall-shear stress lines end at the rudder's leading edge. For a sideslip angle of $\beta = 14°$ at the rudder angle of $\delta = 30°$, the slat seems to help reattach the flow near the root between $\eta = 0.25$ and $\eta = 0.50$ by extending the reattachment line further downstream; see Fig. 5.15. For a larger sideslip angle of $\beta = 20°$ at the rudder angle of $\delta = 30°$, the slat helps reduce the total skin-friction over the rudder surface near the root, see Fig. 5.16.

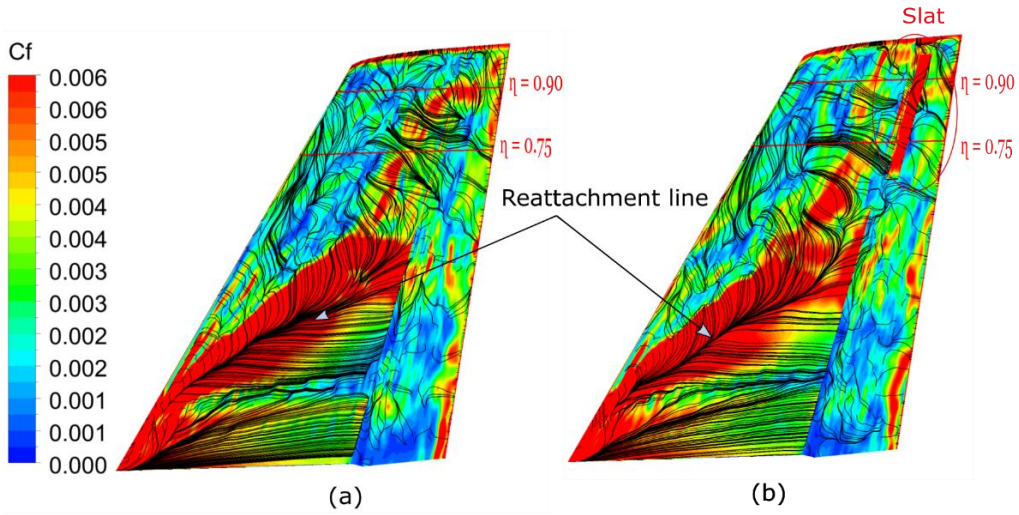

Fig. 5.14: Skin-friction coefficient and wall-shear stress lines by LES for the baseline (a) and with slat (b) for $\beta = 8°$ at $\delta = 30°$.

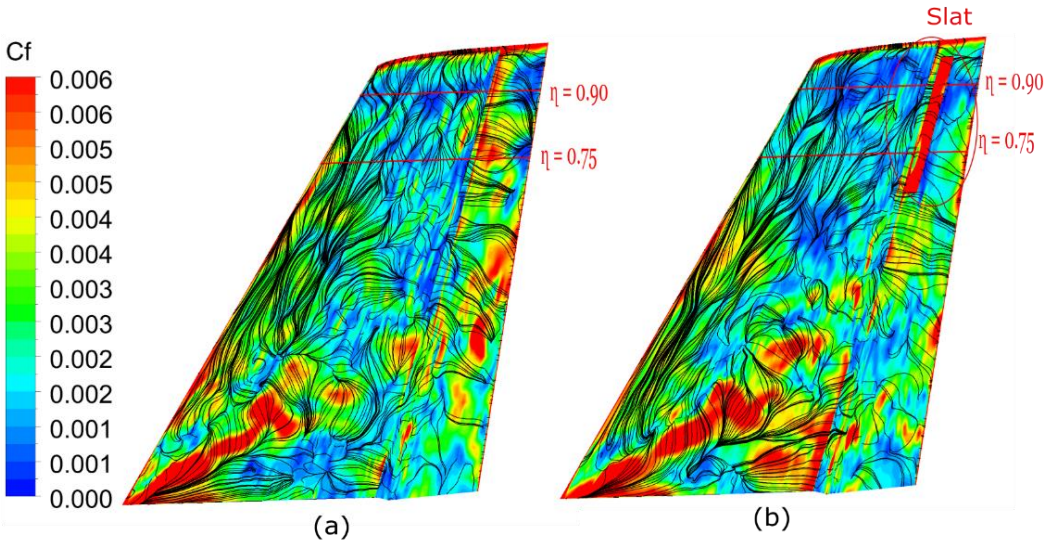

Fig. 5.15: Skin-friction coefficient and wall-shear stress lines by LES for the baseline (a) and with slat (b) for $\beta = 14°$ at $\delta = 30°$.

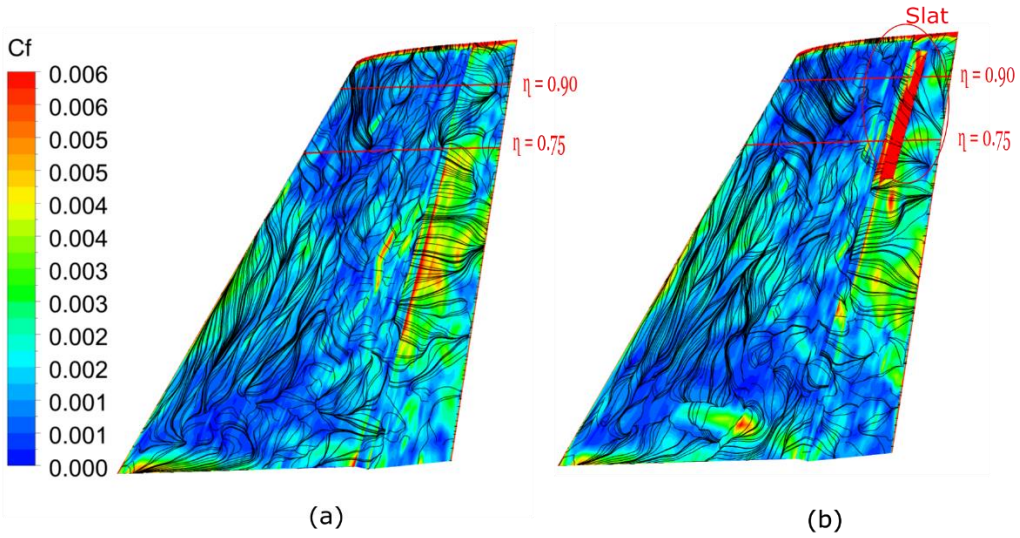

Fig. 5.16: Skin-friction coefficient and wall-shear stress lines by LES for the baseline (a) and with slat (b) for $\beta = 20°$ at $\delta = 30°$.

5.3.3 Vorticity Distribution and Vortical Structure

Figure 5.17 shows the streamlines with the spanwise vorticity around the vertical stabiliser at the cut sections of $\eta = 0.75$ and $\eta = 0.9$ for $\beta = 8°$ at the rudder angle of $\delta = 30°$, where the corresponding zoomed-in views are shown in Fig. 5.18. Without slat, see Figs. 5.13(a) and (c) and Figs. 5.14(a) and (c) for zoom-in views, there is a large wake region behind the rudder. With a rudder-mounted slat, this wake region is pushed downstream, see Figs. 5.17 (b), (d) and Figs. 5.18(b), (d) for zoom-in views, where the reattached flow of the vertical stabiliser is directed smoothly over the rudder surface. For an increased sideslip angle of $\beta = 14°$, see Figs. 5.19 (b), (d) and Figs. 5.20(b), (d) (zoom-in views), there is no reattached flow over the main part of the vertical stabiliser, see Fig. 5.15. Here, the slat draws the flow from the recirculating regions immediately upstream and directs it over the rudder surface. It is confirmed that this flow field change is brought by the circulation added by the slat, which is evident from the change in the streamlines around the trailing edge of the rudder.

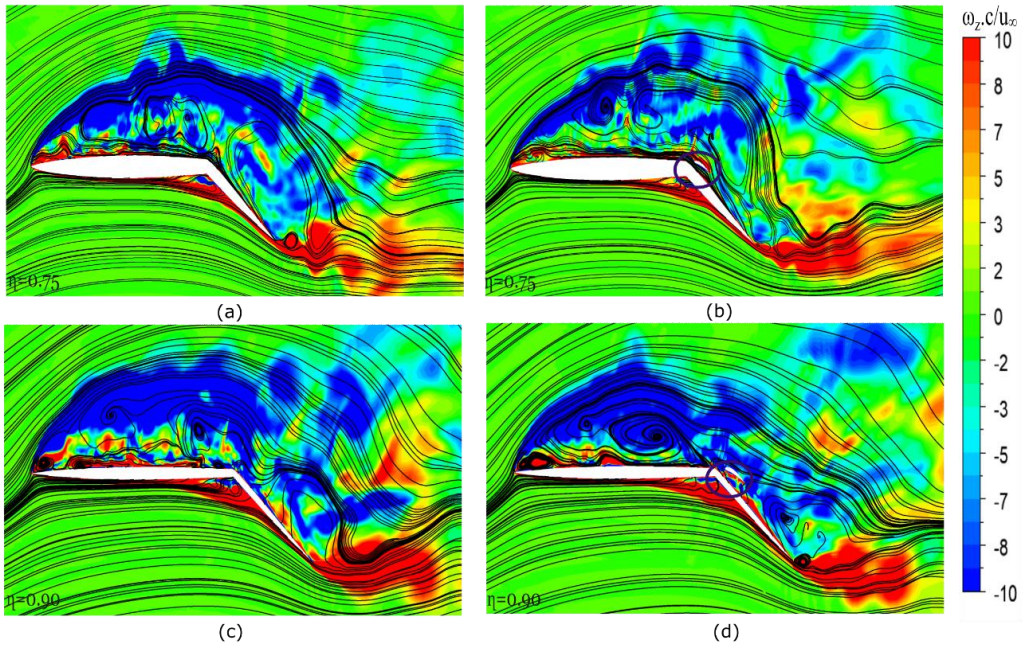

Fig. 5.17: Time-averaged spanwise vorticity ω_z and the streamlines by LES for $\beta = 8°$ at $\delta = 30°$. Baseline results (a) at $\eta = 0.75$ and (c) at $\eta = 0.90$, with slat (b) at $\eta = 0.75$ and (d) at $\eta = 0.90$.

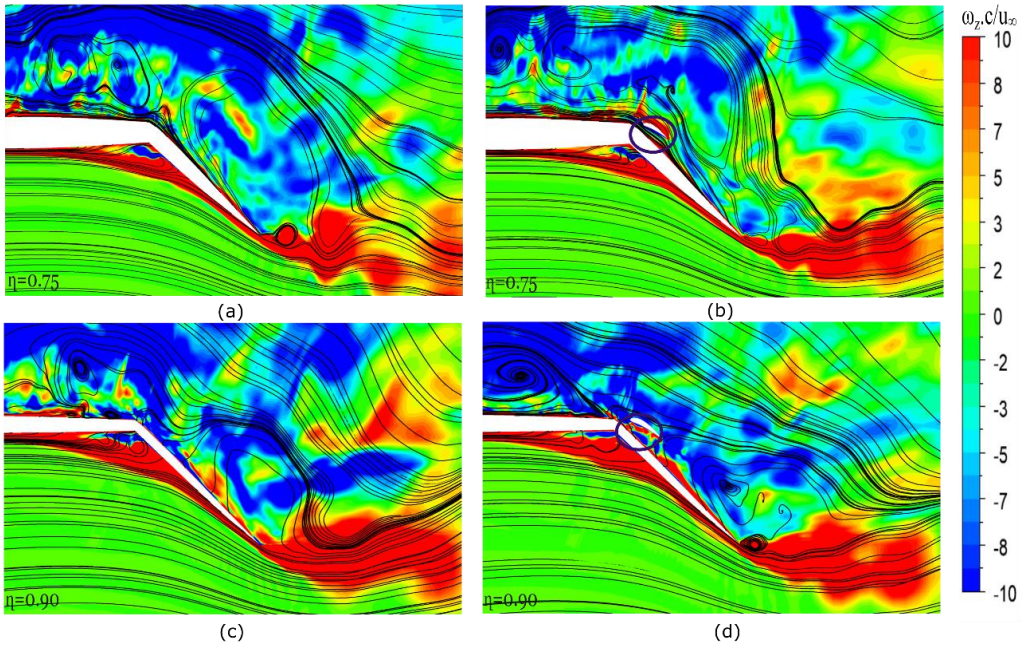

Fig. 5.18: Time-averaged spanwise vorticity ω_z and the streamlines (zoom-in view) by LES for $\beta = 8°$ at $\delta = 30°$. Baseline results (a) at $\eta = 0.75$ and (c) at $\eta = 0.90$, with slat (b) at $\eta = 0.75$ and (d) at $\eta = 0.90$.

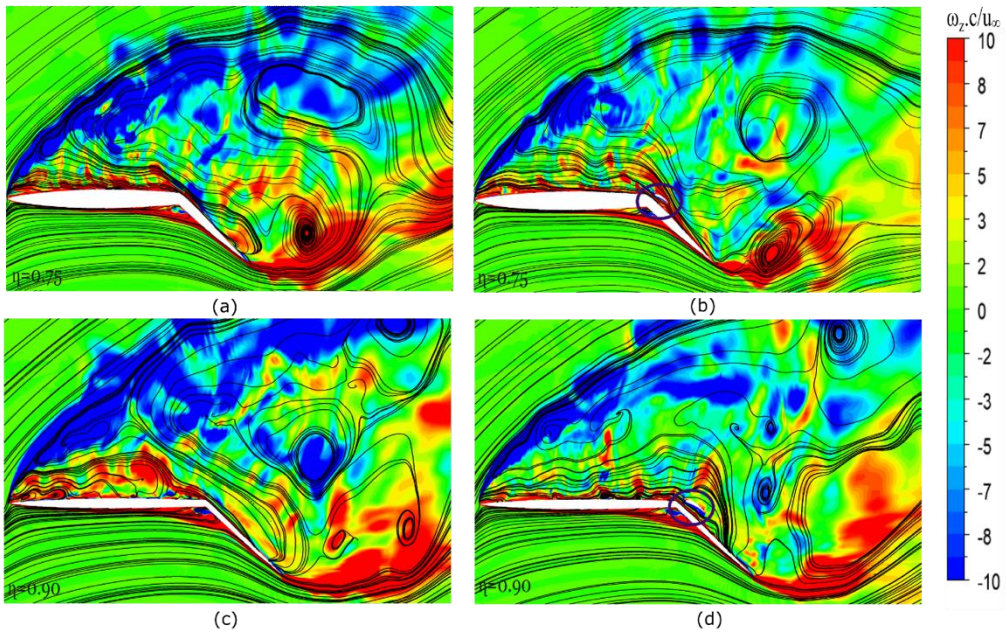

Fig. 5.19: Time-averaged spanwise vorticity ω_z and the streamlines by LES for $\beta = 14°$ at $\delta = 30°$. Baseline results (a) at $\eta = 0.75$ and (c) at $\eta = 0.90$, with slat (b) at $\eta = 0.75$ and (d) at $\eta = 0.90$.

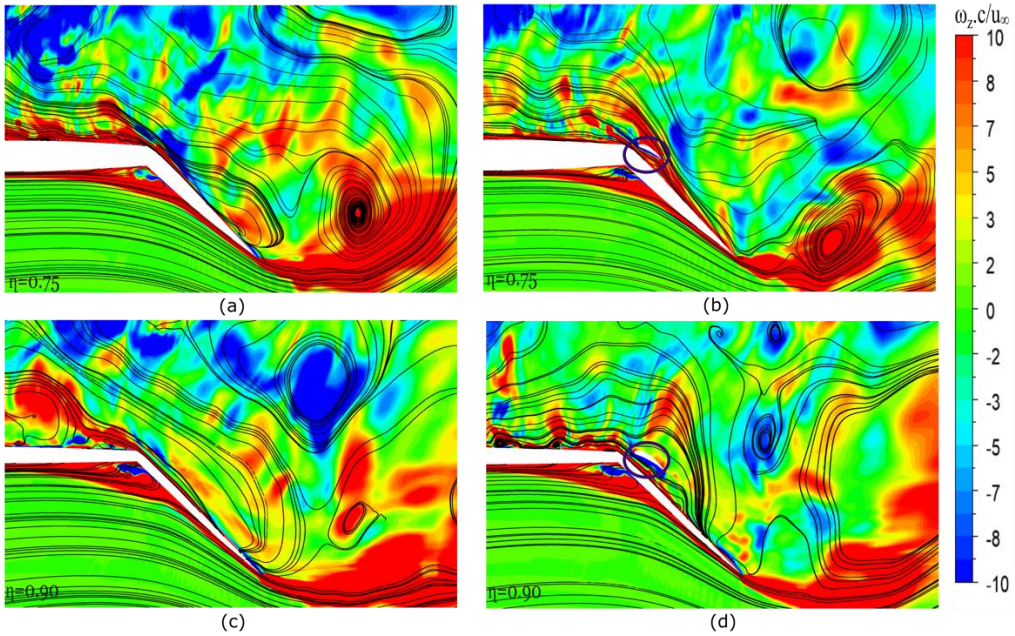

Fig. 5.20: Time-averaged spanwise vorticity ω_z and the streamlines (zoom-in view) by LES for $\beta = 14°$ at $\delta = 30°$. Baseline results (a) at $\eta = 0.75$ and (c) at $\eta = 0.90$, with slat (b) at $\eta = 0.75$ and (d) at $\eta = 0.90$.

Figures 5.21 (a) and (c) show the snapshot of the vortical structure without a slat over the suction side of the vertical stabiliser for $\beta = 8°$ at $\delta = 30°$, which was identified by the λ_2 method (Chen et al. 2015). Here, the spanwise vortices in the separated shear layer due to the Kelvin-Helmholz (K-H) instability develop from the leading edge, which becomes hairpin vortices in a downstream wake region, see Figs. 5.17 and 5.18. With slat, these hairpin vortices are weakened in a smaller wake region, see Figs. 5.21(b) and (d). Here, we can also observe regular spanwise vortices near the root of the vertical stabiliser, although their wavelength is much smaller due to the thinner shear layer. Similar vortical changes due to a rudder-mounded slat are seen in Fig. 5.22 at a greater sideslip angle of $\beta = 14°$.

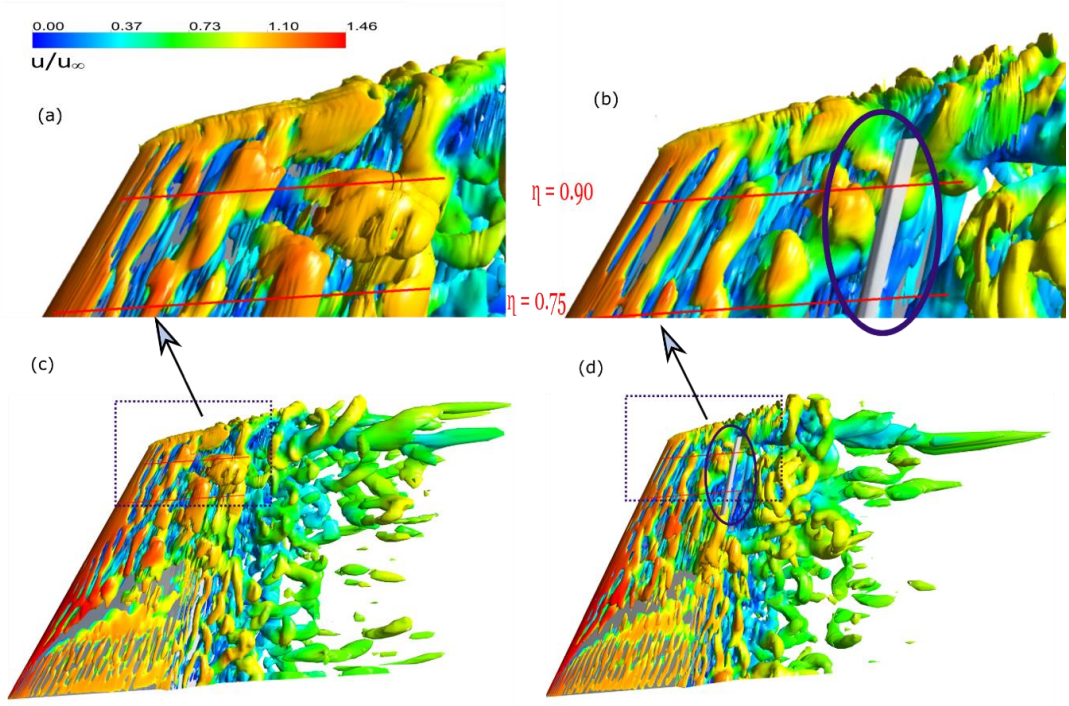

Fig. 5.21: Vortical structures identified by the λ_2 criterion and the total velocity by LES for $\beta = 8°$ at $\delta = 30°$. Baseline results (c) and their zoom-in view (a); Results with slat (d) and their zoom-in view (b).

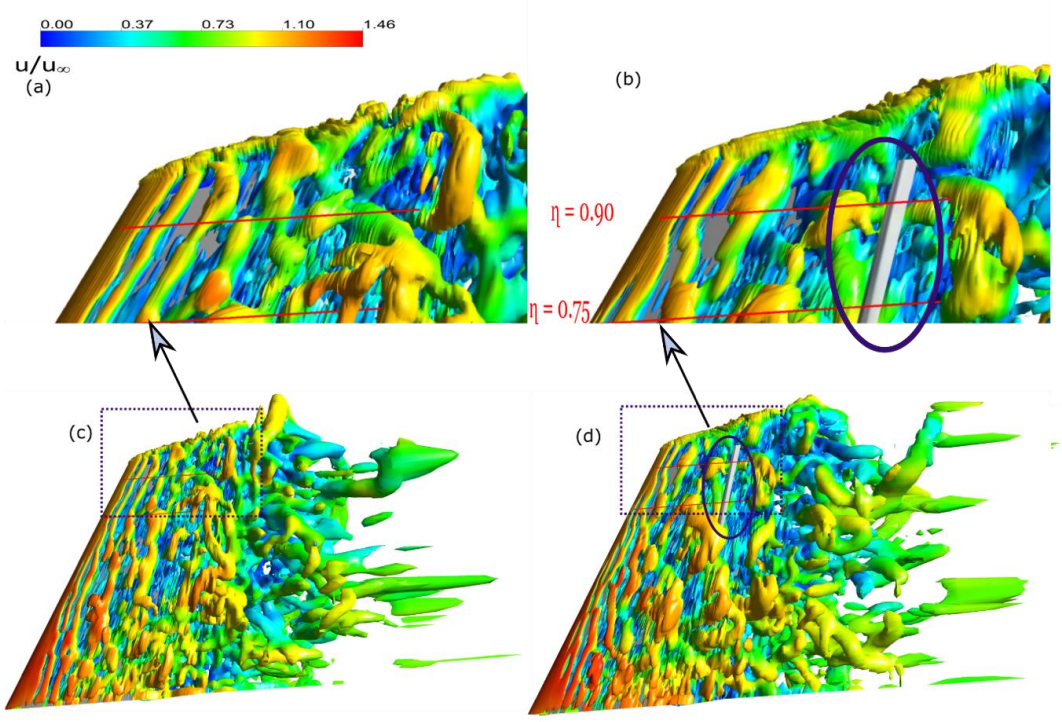

Fig. 5.22: Vortical structures identified by the λ_2 criterion and the total velocity by LES for $\beta = 14°$ at $\delta = 30°$. Baseline results (c) and their zoom-in view (a); Results with slat (d) and their zoom-in view (b).

5.3.4 Mean velocity and Turbulence

Figure 5.23 shows the total mean velocity contours around the vertical stabiliser at the cut sections of $\eta = 0.75$ and $\eta = 0.9$ for $\beta = 8°$ at the rudder angle of $\delta = 30°$. Here, the non-dimensional velocity in each cut section is shown in the colour scale in Figs. 5.23(a) and (c) without slat, compared with the results with a slat in Figs. 5.23(b) and (d). The zoom-in views for the flow around the slat are shown in Fig. 5.24. The streamlines are also shown together in each figure. The corresponding results for the sideslip angle of $\beta = 14°$ are shown in Figs. 5.25 and 5.26. The general observation of these results on the total mean velocity distribution is that the recirculating flow over the suction side of the vertical stabiliser (shown in dark blue colour) is drawn over and along the deflected rudder surface by the slat. The wake region downstream of the slat is reduced in size because of this.

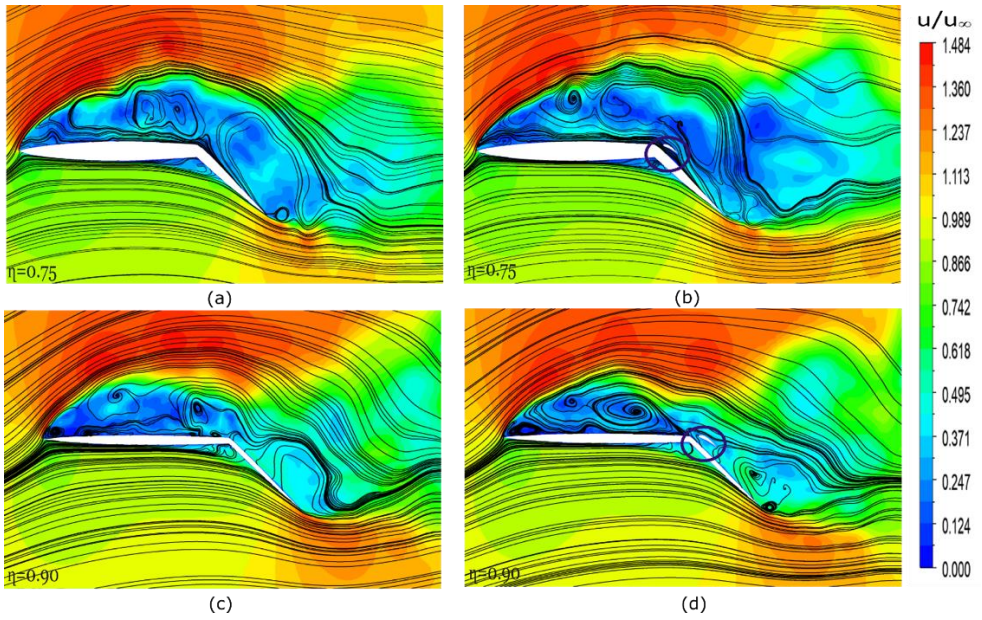

Fig. 5.23: Time-averaged velocity magnitude and the streamlines by LES for β = 8° at δ = 30°. Baseline results (a) at η = 0.75 and (c) at η = 0.90, with slat (b) at η = 0.75 and (d) at η = 0.90.

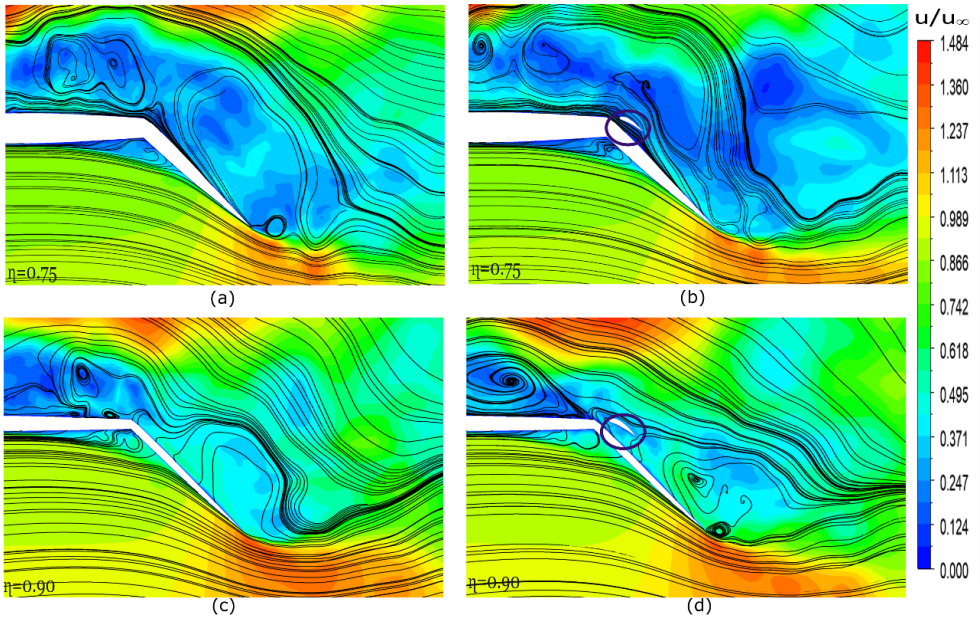

Fig. 5.24: Time-averaged velocity magnitude and the streamlines (zoom-in view) by LES for β = 8° at δ = 30°. Baseline results (a) at η = 0.75 and (c) at η = 0.90, with slat (b) at η = 0.75 and (d) at η = 0.90.

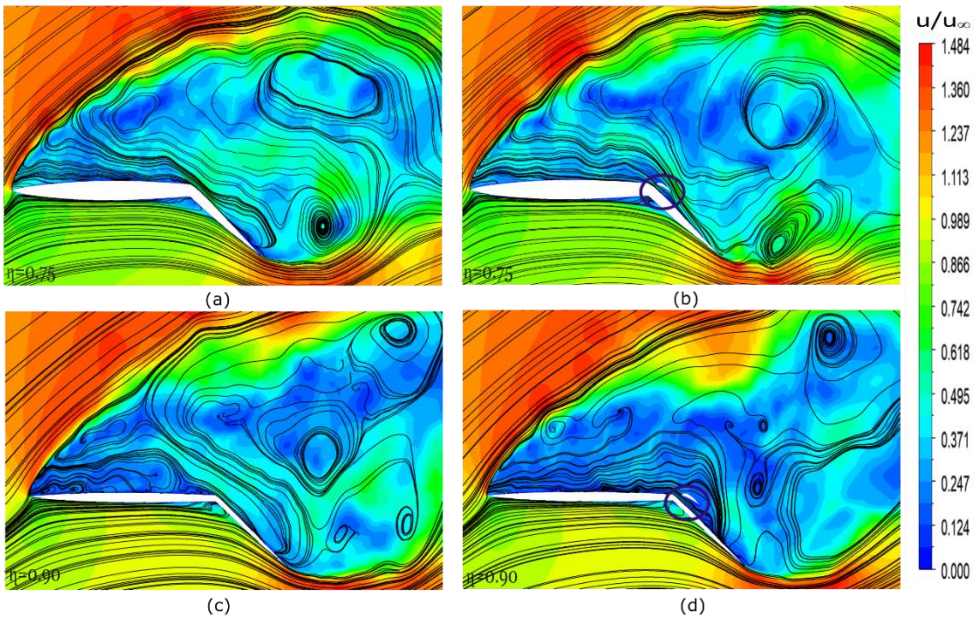

Fig. 5.25: Time-averaged velocity magnitude and the streamlines by LES for $\beta = 14°$ at $\delta = 30°$. Baseline results (a) at $\eta = 0.75$ and (c) at $\eta = 0.90$, with slat (b) at $\eta = 0.75$ and (d) at $\eta = 0.90$.

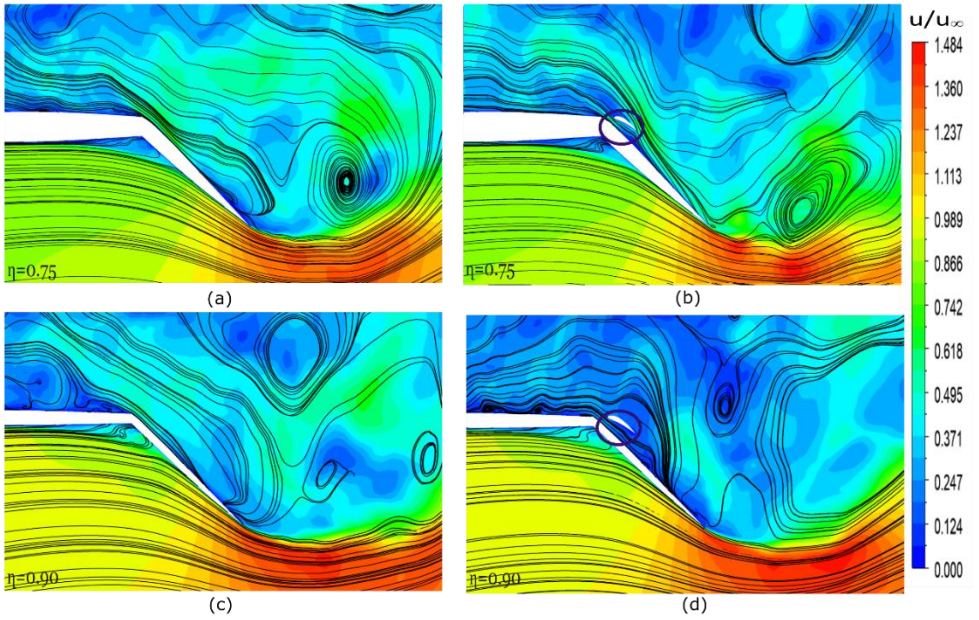

Fig. 5.26: Time-averaged velocity magnitude and the streamlines (zoom-in view) by LES for $\beta = 14°$ at $\delta = 30°$. Baseline results (a) at $\eta = 0.75$ and (c) at $\eta = 0.90$, with slat (b) at $\eta = 0.75$ and (d) at $\eta = 0.90$.

Figure 5.27 shows the time-averaged turbulent kinetic energy (TKE) around the vertical stabiliser at the cut sections of $\eta = 0.75$ and $\eta = 0.9$ for $\beta = 8°$ at the rudder angle of $\delta = 30°$. The corresponding zoom-in views are given in Figure 5.28. These figures indicate that the TKE is mainly generated from the separating share layer from the leading edge and from the shedding vortices downstream. With slat, see Figs. 5.27(b) and (d) and Figs. 5.28(b) and (d), a high TKE region moves closer to the slat as it draws the separated flow towards the deflected rudder surface. With the increase in the sideslip angle to $\beta = 14°$, the leading-edge flow separation region is enlarged, see Figs. 5.29 and 5.30. Here, the TKE over the vertical stabiliser becomes lower, which is further reduced with slat as shown in Figs. 5.27(b) and (d).

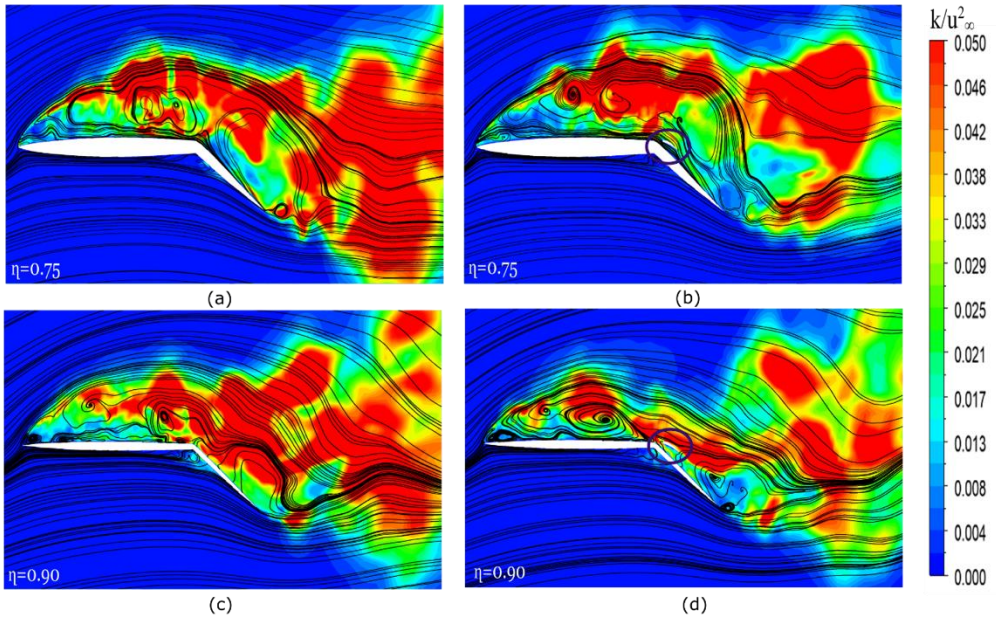

Fig. 5.27 : Turbulent kinetic energy and the streamlines by LES for $\beta = 8°$ at $\delta = 30°$. Baseline results (a) at $\eta = 0.75$ and (c) at $\eta = 0.90$, with slat (b) at $\eta = 0.75$ and (d) at $\eta = 0.90$.

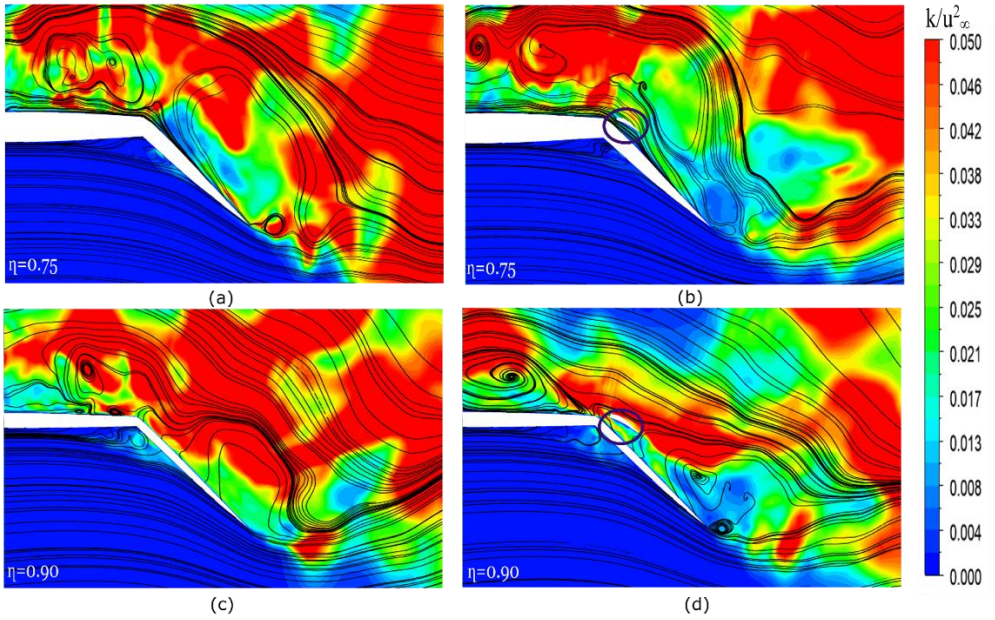

Fig. 5.28 : Turbulent kinetic energy and the streamlines (zoom-in view) by LES for β = 8° at δ = 30°. Baseline results (a) at η = 0.75 and (c) at η = 0.90, with slat (b) at η = 0.75 and (d) at η = 0.90.

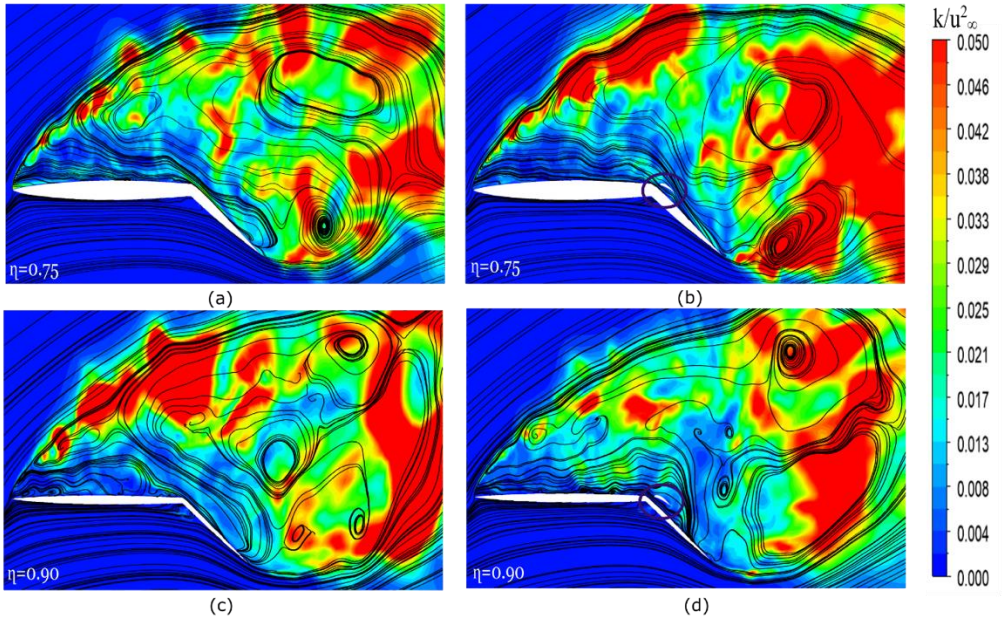

Fig. 5.29: Turbulent kinetic energy and the streamlines by LES for β = 14° at δ = 30°. Baseline results (a) at η = 0.75 and (c) at η = 0.90, with slat (b) at η = 0.75 and (d) at η = 0.90.

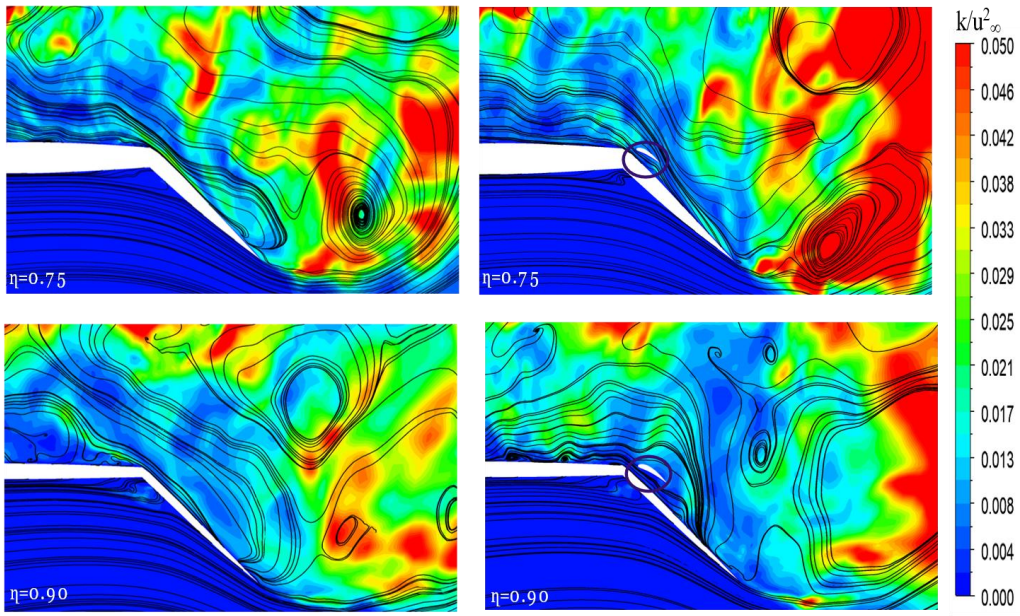

Fig. 5.30: Turbulent kinetic energy and the streamlines (zoom-in view) by LES for $\beta = 14°$ at $\delta = 30°$. Baseline results (a) at $\eta = 0.75$ and (c) at $\eta = 0.90$, with slat (b) at $\eta = 0.75$ and (d) at $\eta = 0.90$.

Figures 5.31 and 5.32 show the distribution of the Reynolds stress around the vertical stabiliser at the cut sections of $\eta = 0.75$ and $\eta = 0.9$ for $\beta = 8°$ at the rudder angle of $\delta = 30°$. The corresponding results for $\beta = 14°$ are given in Figs. 5.33 and 34. Like the TKE distribution as shown in Figs. 5.27 and 5.28 for $\beta = 8°$ and Figs. 5.29 and 30 for $\beta = 14°$, respectively, a high Reynolds stress region is found along the separated shear layer from the leading edge and around the shedding vortices. Here, a negative Reynolds stress region (shown in blue) is generated from the shear layer from the trailing edge. Otherwise, the distribution of the Reynolds stress is similar to the TKE with or without a slat. An alternating sequence of positive and negative Reynolds stresses in the shear layer is due to spanwise vortices resulting from the K-H instability; see Fig. 5.21 for $\beta = 8°$ and Fig. 5.22 for $\beta = 14°$.

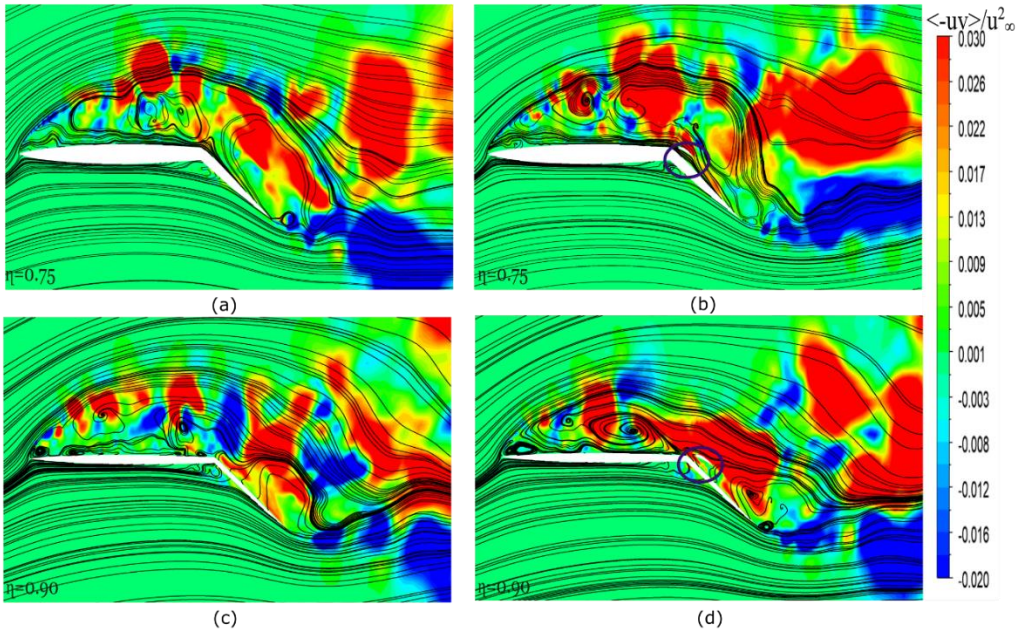

Fig. 5.31: The Reynolds stress and the streamlines by LES for β = 8° at δ = 30°. Baseline results (a) at η = 0.75 and (c) at η = 0.90, with slat (b) at η = 0.75 and (d) at η = 0.90.

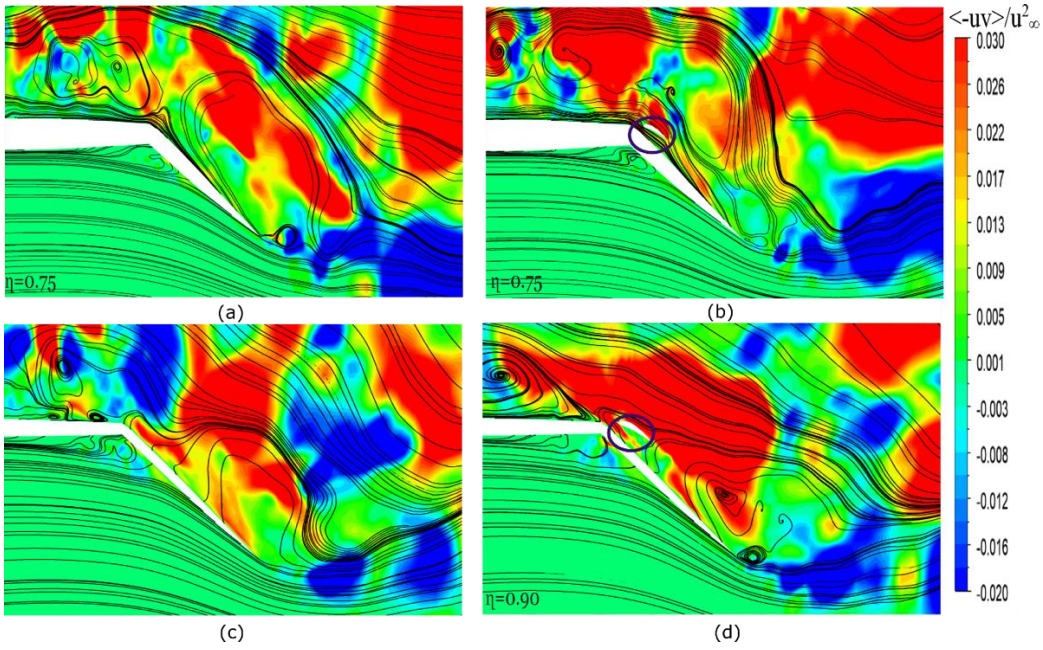

Fig. 5.32: The Reynolds stress and the streamlines (zoom-in view) by LES for β = 8° at δ = 30°. Baseline results (a) at η = 0.75 and (c) at η = 0.90, with slat (b) at η = 0.75 and (d) at η = 0.90.

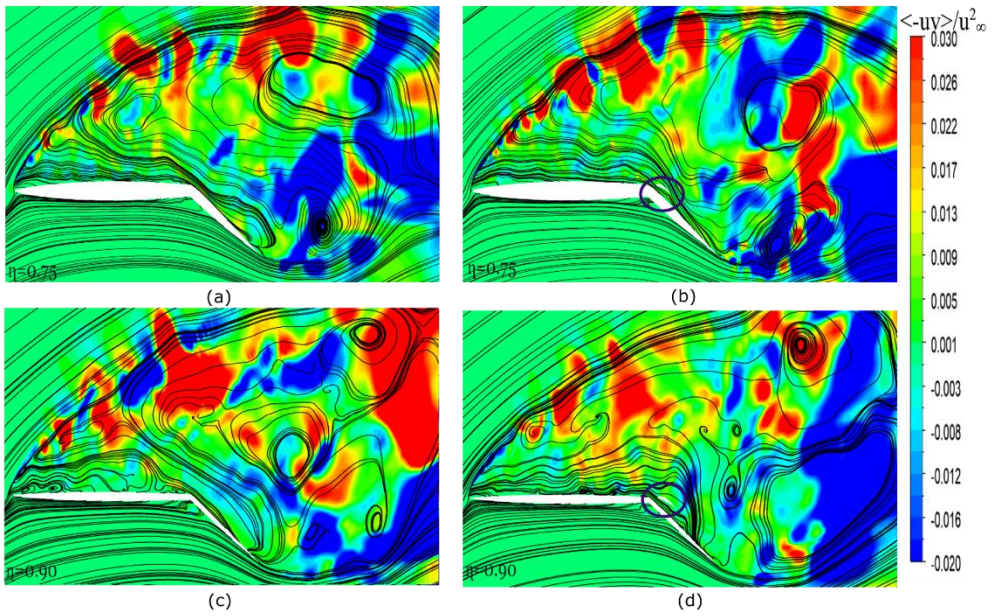

Fig. 5.33: The Reynolds stress and the streamlines by LES for β = 14° at δ = 30°. Baseline results (a) at η = 0.75 and (c) at η = 0.90, with slat (b) at η = 0.75 and (d) at η = 0.90.

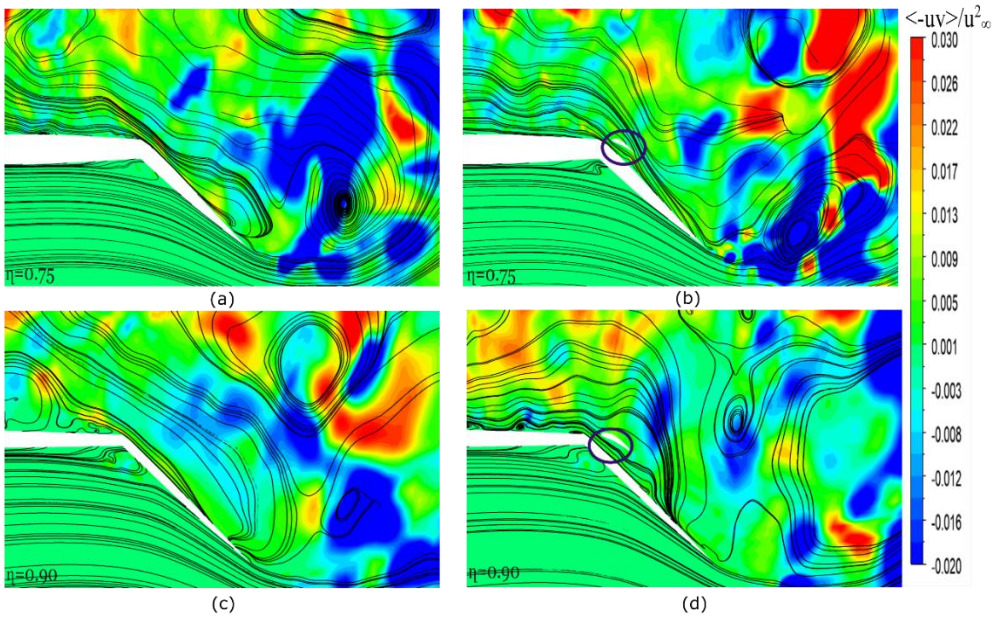

Fig. 5.34: The Reynolds stress and the streamlines (zoom-in view) by LES for β = 14° at δ = 30°. Baseline results (a) at η = 0.75 and (c) at η = 0.90, with slat (b) at η = 0.75 and (d) at η = 0.90.

5.4 Chapter Summary

A numerical test of a vertical stabiliser was carried out at the rudder deflection angle of $\delta = 30°$, where a rudder-mounted slat increased the side force coefficient by up to 3% (Table 5.1). No noticeable increase in the drag coefficient was found at this test condition. This demonstrated that a rudder-mounted slat, which covers only 30% of the span from the tip, is an effective passive device for controlling the flow separation of the rudder when it is partially or fully separated. Here, the LES results agreed well with the experimental force coefficients. The increased performance of the effect of the mounted slat is visible from the lower side slip angle, where the aerodynamic forces start to increase with the increase in the sideslip angles.

Further, the LES study of the model suggests that the slat draws the flow from the recirculating region immediately upstream and directs it over the rudder surface. This phenomenon was also observed closer to the root of the vertical stabiliser by extending the reattachment line further downstream. It is confirmed that these changes were brought by the circulation added by the slat, which is evident from the change in the streamlines around the trailing edge of the rudder.

The spanwise vortices were observed to develop from the leading edge of the vertical stabiliser. This is due to the Kelvin-Helmholtz (K-H) instability of the separated shear layer. The spanwise vortices were the primary source of turbulent kinetic energy (TKE) and the Reynolds stress. Both the TKE and Reynolds stress are important measures of turbulence intensity. As the spanwise vortices moved downstream, they were deformed into a hairpin-like shape. These types of vortices are known to be responsible for the generation of turbulence in fluid flows. However, the hairpin vortices were weakened when the slats were introduced in a smaller wake region. Since the slats were located at the rudder's leading edge and the rudder was deflected, the slats had the additional effect of reducing the strength of the hairpin vortices in the wake region of the rudder.

6. Chapter six

EFFECT OF SINGLE BUMP LEADING-EDGE UNDULATION CONTROL ON THE AERODYNAMIC PERFORMANCE OF VERTICAL TAILPLANE

6.1 Introduction

Leading-edge undulation is an emerging and highly researched flow control domain that has received substantial attention over the past two decades (Aftab et al. 2016). The inspiration drawn from nature, particularly the humpback whale flipper, has fuelled investigations into incorporating undulations on aerofoil leading edges, opening avenues for innovative advancements in lift and drag performance.

According to Hansen et al. (2011), tubercles, which performed like undulation at the leading edge with protrusions to modify the flow, have been shown to enhance lift performance in the post-stall regime, demonstrating their potential for managing aerodynamic forces under challenging conditions. However, this positive effect comes at a cost, as the same study noted a degradation in lift performance in the pre-stall regime when tubercles are employed. The research findings by Hansen et al. (2011) indicate that the dual impact of tubercles on lift and drag performance presents both advantages and drawbacks.

Furthermore, investigations into undulating the wing's leading edge have yielded intriguing results. Skillen et al. (2015) reported that undulating the leading edge can increase lift coefficients. Conversely, Bolzon et al. (2017) found that this modification decreases drag coefficients. This divergence in outcomes suggests the intricate nature of aerodynamic adjustments and emphasises the importance of understanding how different modifications impact the lift and drag coefficients.

It can be observed that the effect of leading-edge modification using undulation was generally believed to be performed after the stall angle with degradation under pre-stall conditions. The single bump protrusion design on the VTP serves as a basis for conventional wing protrusion designs. Conventional undulation in wing design demonstrates superior performance at post-stall angles but lacks enhancement at pre-stall angles. In contrast, the single bump undulation implemented on the VTP in this study demonstrated

improvements in pre- and post-stall conditions. Conversely, certain configurations can decrease the aerodynamic coefficient values compared to their unmodified counterparts. Research conducted by Bolzon et al. (2014) demonstrated that a tapered wing featuring NACA 0012 with tubercles at a Reynolds number of 2.2×10^5 exhibited a reduction in lift and drag coefficients by approximately 4-6% and 7-9.5%, respectively. The model used in this study is a tapered VTP, and the results of the leading-edge modification using a single bump protrusion showed a remarkable increase in both the side force and drag force coefficients without any cost of degradation or the pre-stall condition.

As mentioned earlier, the design parameters, including the protrusion's wavelength, amplitude, and magnitude, play crucial roles in enhancing the aerodynamic coefficients; this has been extensively investigated by Kim et al. (2022). The effectiveness of the single-bump protrusion magnitude selection reveals that reliance on multiple protrusions along the leading edge of the VTP may not always be the optimal choice. Surprisingly, the study indicates that, in certain cases, a single bump protrusion can be crucial, challenging the notion that employing multiple protrusions is universally superior for improving aerodynamic characteristics on the leading edge of the VTP.

Various experimental designs have explored sawtooth-like humpback whale flippers involving different configurations of wavelengths and amplitudes. Fish and Battle (1995) proposed the incorporation of multiple bumps along the wing's leading edge.

To obtain optimum aerodynamic performance, the undulation of the bump enhanced the wing efficiency. Several studies have numerically and experimentally reported the impact of the undulation amplitude and wavelength design. According to Johari et al. (2007), the magnitude of protrusions has negatively impacted the efficiency of aerofoil. The study concluded that the wavelength has a minimal effect on the aerodynamic performance, whereas the amplitude has a greater impact on the aerodynamic performance of the NACA 63_4-021 aerofoil. However, their experimental findings concluded that the lift coefficient was degraded at a lower angle of attack than the unmodified baseline. However, above the stall angle, the effect of undulation on the lift coefficient increased significantly. These findings were

also confirmed by Van Nierop et al. (2008), using a tapered wing, who revealed that the delay in the stall was independent of the bump wavelength. By optimising the amplitude and wavelength of the tubercles, the pre-stall lift performance can approach that of an unmodified aerofoil (Lobo et al. 2020).

A recent experimental study conducted by Kim et al. (2022) revealed that the most effective way to achieve optimal leading-edge undulation (LEU) is through a combination of 30% wavelength (λ/c) and 6% amplitude (h/c) on NACA 65(12)-10 aerofoil. This approach prioritises aerodynamic performance efficiency and noise reduction, resulting in the best possible outcome.

This chapter details the investigation into a single bump on the leading of a vertical tailplane VTP. The single bump has proven transformative in enhancing the aerodynamic force coefficients compared with the unmodified baseline case of the VTP, as indicated by the wind tunnel experimental data of the TailSurf project Deliverable D9 Model 1 test (TailSurf 2019). The performance of the single bump undulation was numerically studied at a sideslip angle of $\beta = 8°$ with a rudder angle of $\delta = 30°$ using the large eddy simulation LES method. The comparison of the experimental and numerical force-coefficient performances was reasonable and in good agreement.

The performance of the leading-edge modification using a single-bump undulation design was thoroughly investigated using turbulence quantities. All quantities demonstrated a different flow pattern in the single-bump undulation configuration compared to the unmodified baseline case. The streamlines over the VTP surface clearly shows how the flow reattached with the introduction of the single bump undulation. In addition, the flow was re-energised beyond the peak and trough of the single bump undulation compared with the baseline case.

6.2 Numerical Methodology

6.2.1 VTP Geometry Design

Previous research has often explored the impact of multiple bumps on wing aerofoils; however, more attention must be paid to the effects of a single bump and other strategies to obtain the desirable design. Therefore, it is important to understand the diverse viewpoints of the leading-edge undulation across various wing sections. This study investigated the significance of a single undulation bump on a vertical tailplane. The primary goal of this study is to gain insight into the aerodynamic and fluid fluctuation performance resulting from a single bump undulation through experimentation and large eddy simulation LES.

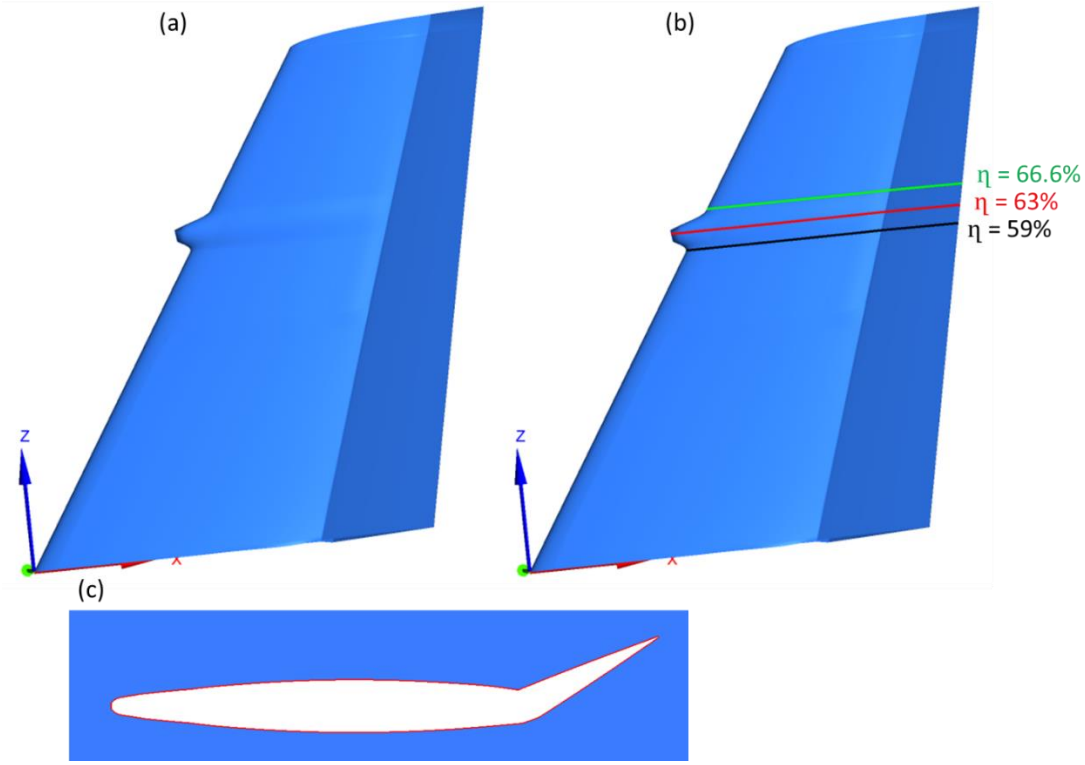

Fig. 6.1: Geometry of the single-bump protrusion design on the VTP in (a) and (b) shows the upper trough (66.6%), peak (63%), and lower trough (59%) of the protrusion and (c) shows the cross-section of the peak region of the bump.

The bump design used in this study is from the TailSurf project (TailSurf 2019) that placed the bump at 66.6% span from the root side, with an amplitude of 12%. According to the experimental data, the optimum side and drag force coefficient performance was found for a span of 66.6 % compared to the other span locations not discussed in this study. This study focuses on the numerical simulation of a single bump with a 66.6% span undulation of the VTP. The single bump geometry is shown in Fig. 6.1. The area of the VTP using the bump is increased by 0.04% compared to the baseline. Therefore, an appropriate area of the bump protrusion was considered.

6.2.2 Numerical Modelling

This study utilised a structured mesh with a higher density surrounding the vertical tailplane area. Both the baseline and undulation mesh volumes were comprised of hexahedral cells. The mesh must be finer because the WALE model requires a more precise mesh than the Smagorinsky model, as was recently discovered by Mikuž and Tiselj (2016). Therefore, the node counts on the surface of the model in the streamwise (x), wall-normal (y), and spanwise (z) directions are given by $N_x \times N_y \times N_z = 670 \times 100 \times 150$. To carry out a wall-resolving LES mesh, it is necessary to ensure a sufficient mesh density in the normal direction of the wall. This means that the mesh was stretched in the direction perpendicular to the wall to ensure sufficient resolution to capture the flow structures, as explained by Cheng et al. (2022). Therefore, the mesh is finer at the VTP wall and becomes coarser away from the model, which helps to maintain a reasonable value of y^+ around the model surface. Node points are clustered at the half span of the VTP to encompass the undulation area extending up to the tip side. This strategy will enable enough resolution to account for the effect of the streamwise vortices anticipated as the mechanism of the undulation. The same mesh type was utilised for the baseline and single bump throughout the LES simulation to ensure the actual flow field changes. Fig. 6.2 highlights the mesh on the surface of the VTP of the single bump case and a cross-section showing the mesh refinement around the leading edge of the VTP.

The non-dimensional, wall-normal distance of the first mesh position y^+ was checked after the simulation to ensure that the value was reasonable for simulation accuracy. In this case, owing to the bump protrusion on the VTP, the average y^+ was maintained at the end of the simulation, with a maximum $y^+ \approx 1.3$ observed around the bump protrusion peak area. However, the enitire VTP adheres to the condition that $y^+ \leq 1$.

The computational domain was designed to be sufficiently large to capture the flow and turbulence around the VTP and minimize its impact on the simulation results. The inlet and outlet were placed 28 chords upstream and 48 chords downstream of the vertical tailplane. The top and bottom walls were placed in 17 chord lenghts, whereas the sidewalls were placed in 20 chords.

A Reynolds number of 1.69×10^5 was based on a mean aerodynamic chord MAC of 0.246m, and a constant freestream velocity of 10 m/s was applied. A velocity inlet boundary condition was imposed at the inlet, and a pressure outlet was applied. A no-slip condition was used for the vertical tailplane.

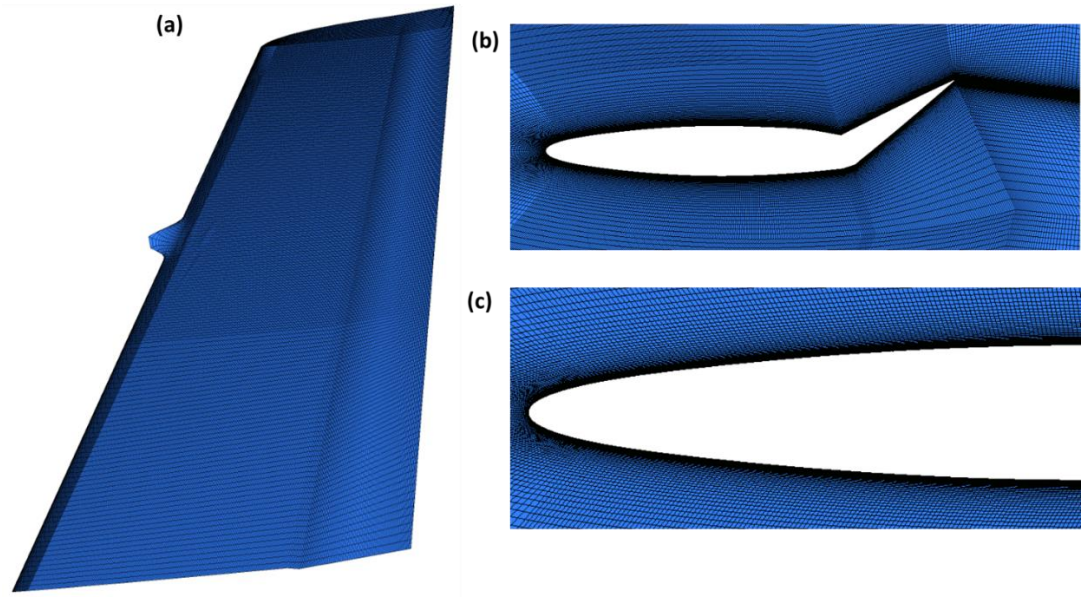

Fig. 6.2: A computational grid around the Vertical tailplane (a) 3D surface mesh distribution (b) 2D cross-section (c) Leading edge refinement.

6.3 Results and Discussion

6.3.1 Aerodynamic coefficient

The aerodynamic coefficient was numerically validated using EU TailSurf project experimental data from the wind tunnel tests conducted at the University of Nottingham (TailSurf 2019). The investigation focused on the VTP, revealing improved aerodynamic performance at a lower rudder deflection angle attributed to a single bump protrusion. As the rudder deflection angle increased to $\delta = 30°$, corresponding enhancements in aerodynamic coefficients were observed. The influence of the single bump, particularly at lower sideslip angles, contributed to the enhanced aerodynamic coefficients at higher deflection angles.

The improvement was more pronounced at higher deflection and sideslip angles, particularly within the baseline stall angle region. A comparison between the LES results at $\delta = 30°$ and $\beta = 8°$ and experimental data (Fig. 6.3) indicated a good agreement for the numerical side force coefficient in the case of the modified single-bump protrusion. However, the numerical baseline case and modified single bump protrusion demonstrated an increased side force coefficient and almost identical drag coefficient values, as shown in Fig. 6.3 (a-b).

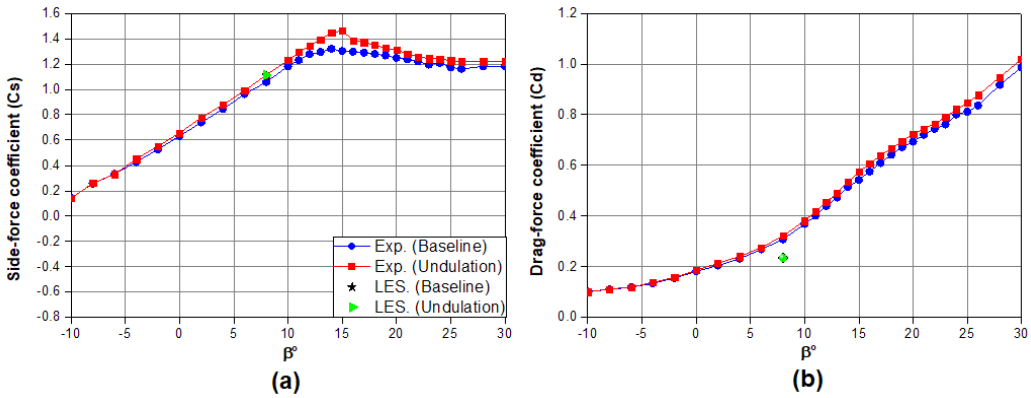

Fig. 6.3: Comparison of the experimental and numerical side force coefficient (a) and drag force coefficient (b) at $\delta = 30°$ and $\beta = 8°$.

As shown in Fig. 6.3, the modification contribution towards the side force coefficients is more pronounced than towards the drag coefficients. Despite enhancing side force coefficients at lower sideslip angles, the drag coefficients remain unaffected and look unchanged, as shown in Fig. 6.3(b). As the VTP side slip angle increases, the side force and drag force coefficients also increase. However, the advantage of the increase in the side force coefficient is much greater than the increase in the drag coefficient at higher side slip angles.

6.3.2 Mean Velocity Analysis

The influence of a single bump on flow separation over the VTP surface was investigated in three different spanwise cross-sections. These cross-sections are considered based on the location of the single bump region to understand the mechanism of the bump region. The spanwise locations are the lower trough on the bump which corresponds to $\eta = 0.59$, the peak region on the bump at to $\eta = 0.63$ and the upper trough region which corresponds to spanwise location of the baseline as $\eta = 0.66$. The streamline and streamwise velocities are presented in Fig.6.4, which illustrate the baseline and undulation single bump cases at the lower trough, peak, and upper trough regions of the VTP.

The influence of the single bump undulation was evaluated using $\delta = 30°$ and $\beta = 8°$. With this high rudder deflection angle, the flow was separated, even at lower sideslip angles. The streamlines over the lower trough of the baseline and the modified single-bump undulation are shown in Fig. 6.4 (a) and (b). At this spanwise location of $\eta = 0.59$, the influence of the single bump is becoming notable compared with the baseline case. The separated flow from the leading edge in the baseline case (Fig. 6.4 a) was modified by a single bump undulation, as shown in Fig. 6.4 (b). It can be observed that the single bump reduces the separation region near the leading edge. The flow in the modified single bump undulation reattaches the flow at $x/c = 0.59$ on the suction side, although the flow is separated downstream at $x/c = 0.73$ again.

At the peak region in Fig. 6.4 (c) and (d), the influence of a single bump is more pronounced than that of the lower trough region. In this region, the baseline case in Fig. 6.4 (a) indicates a large region of suction side separation and downstream recirculation along the deflected rudder. However, Fig.6.4 (d) shows a different flow feature owing to the influence of the single bump undulation peak region. It shows no evidence of the leading-edge separation exhibited by the baseline case in Fig. 6.4 (c). The streamlines indicate that the influence of peak region of the single bump undulation benefit in additional flow attachment along the surface.

The baseline and modified leading-edge single bump undulations are presented in the upper trough region in Fig. 6.4 (e) and (f). Interestingly, the peak region reduces the anticipated separation region, as shown in Fig. 6.4 (c) and (d). In the upper trough region, like the peak region, the flow reattaches well with the leading-edge separation bubble observed in the undulation case which is assumed to help in the aerodynamic performance compared to the baseline case.

Furthermore, modifying the leading edge using a single bump undulation modifies the flow around the VTP. The single bump case exhibited a laminar separation bubble at the leading edge corresponding to the modified model's lower and upper-trough region. A separation bubble was formed in the single bump owing to the excessive separation of the laminar boundary layer at the leading edge of the VTP. The application of single bump undulation suppression of the separation and further mid-chord reattachment shows that the modification potential is beneficial to the design of the VTP. This is because of the energised flow experienced around the peak and trough regions owing to the modification introduced at the leading edge of the VTP.

Recent research by Gopinathan and Ralphin Rose (2023) focused on investigating symmetrical aerofoils such as NACA 0015 and NACA 4415, revealed significant improvements along the suction peak of the leading-edge undulation. Similar to our results, the separation bubble in the symmetrical aerofoil was reduced in the peak region, leading to flow reattachment downstream compared to the baseline case. The noteworthy enhancement

observed can be attributed to the contribution of the peak region to the force-coefficient performance.

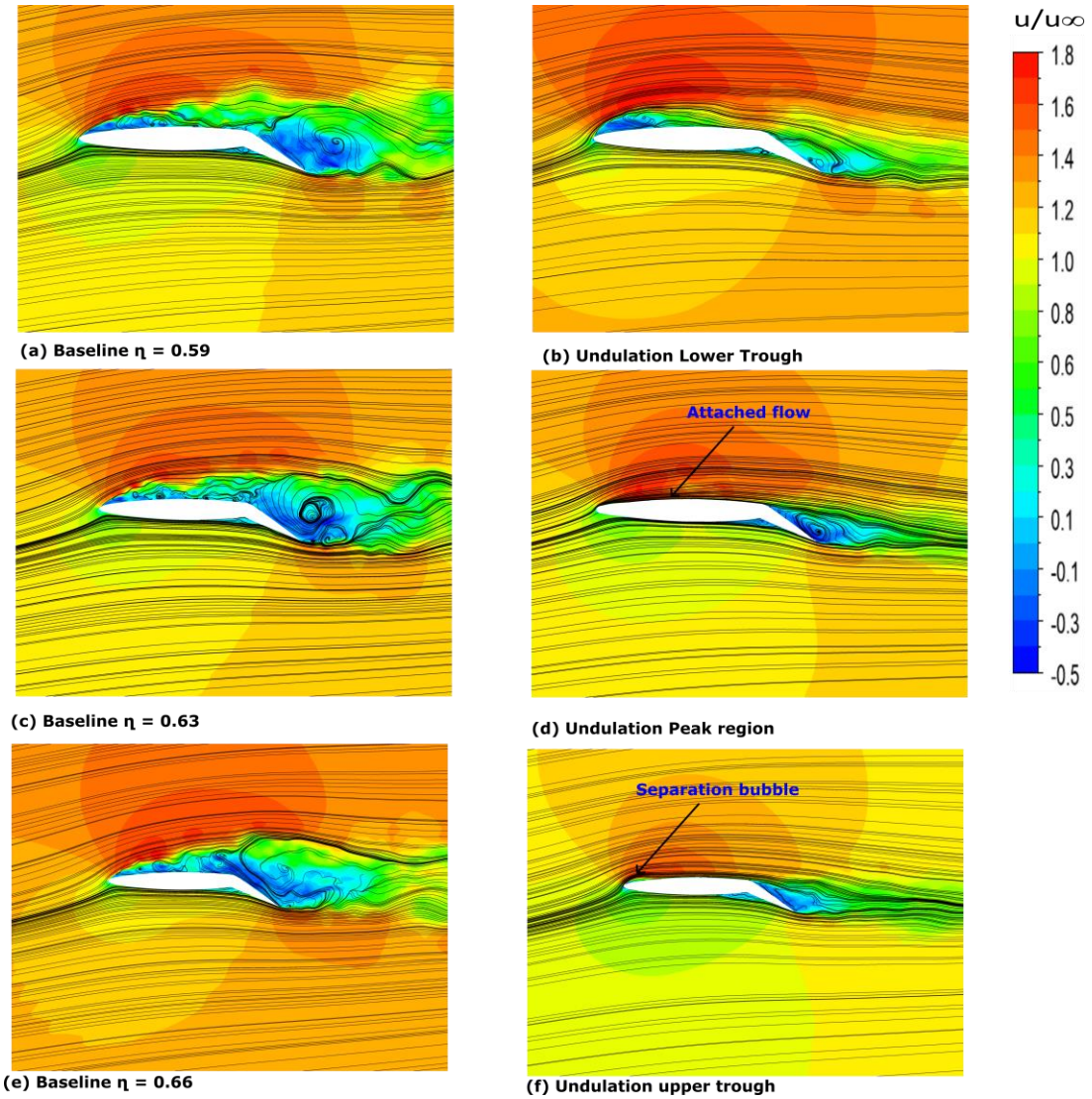

Fig. 6.4: Comparison of streamwise velocity and streamline pattern for baseline (a) η = 0.59, (c) η = 0.63 and (e) η = 0.66 and modified single-bump undulations (b) lower trough, (d) peak region and (f) upper trough at δ = 30° and β = 8°.

The evolution of the laminar separation bubble and its reduction and elimination due to leading-edge modification was also highlighted by Sathyabhama and Sreejith (2022). The leading-edge undulation design found that the amplitude and wavelength contributed to eliminating the laminar separation bubble at the peak region by moving the LSB upstream of the

leading edge. In addition, the undulation design with a smaller amplitude and wavelength resulted in the total elimination of laminar separation bubbles in the peak region. However, it can be established that in this study, the laminar separation bubble is eliminated at the peak region of the modified single bump undulation. The magnitude and the amplitude of the single bump undulation can be considered small because it eliminates the peak region laminar separation bubbles upstream of the peak region, the presence of the laminar separation bubbles benefits the flow on the upper trough region.

The introduction of a single bump undulation at the leading edge of the VTP reduces the large separation region observed in the baseline. This reduction is evident in Fig. 6.4 (f), where the separation region is shortened in the upper-trough region with formation of a leading-edge short bubble, accompanied by a more extensive attachment along the entire surface of the suction side. The comparison demonstrates the ability of the modified single-bump undulation to mitigate and modify the characteristics of the separation in the upper trough region when compared with the baseline configuration. This could be due to increased turbulence level by the bump undulation see Figs. 6.10 and 6.11. In a different study with different wing types, the concept of leading-edge modification showed a similar behaviour whereby the bubble behind the peak region was eliminated and reduced behind the trough region (Sudhakar et al. 2019).

6.3.3 Surface Pressure Coefficient

Figure 6.5 presents the surface pressure coefficients from the VTP surface at three spanwise locations of the single bump's lower, peak, and upper trough regions. The analysis focuses on a sideslip angle of $\beta = 8°$ and a rudder deflection angle of $\delta = 30°$. This provides insights into the pressure distribution across these critical regions, offering a comprehensive understanding of the aerodynamic characteristics influenced by the modified single-bump undulation in the pre-stall region.

At the lower trough region in Fig. 6.5 (a), the baseline pressure coefficient is compared to the lower trough at a spanwise location of $\eta = 0.59$ from the root side. As observed in Fig.6.4 (a) and (b), the leading-edge separation bubble indicates that the modified single bump undulation demonstrated compared to the baseline case. In addition, the reattachment is observed by the modified single bump undulation from $x/c = 0.59$ to $x/c = 0.73$, which is also visible in the streamwise velocity contour in Fig. 6.4 (b).

Cp distribution along the peak region of the modified single bump at a spanwise location of $\eta = 0.63$ is compared with the baseline case in Fig. 6.5 (b). The influence of the peak region is different from that of the trough location; in this location, despite the flow reattachment observed in Fig. 6.4 (d) due to the introduction of the single bump undulation, further reattachment can be further observed from the pressure coefficient plot at $x/c = 0.60$ to $x/c = 0.72$.

In the upper trough region, the modified single bump undulation pressure coefficients, and the baseline at the spanwise location of $\eta = 0.66$ were compared. Concurrently, the laminar separation bubble at the leading edge of the baseline, as shown in the velocity plot in Fig. 6.4 (e), is also illustrated in the pressure coefficient plot in Fig. 6.5 (c).

Notable differences were observed in the modified single bump undulation's lower and upper trough regions, marked by significantly higher negative (– Cp) peaks than the peak region. This observation implies that the rate of increase in (-Cp) near the leading edge helps in increasing the Cs. The distinct pressure characteristics in the trough regions of the modified configuration indicate a potentially improved aerodynamic performance compared with the baseline.

These findings demonstrate the significance of the modified single-bump undulation in enhancing the overall flow characteristics in the trough regions.

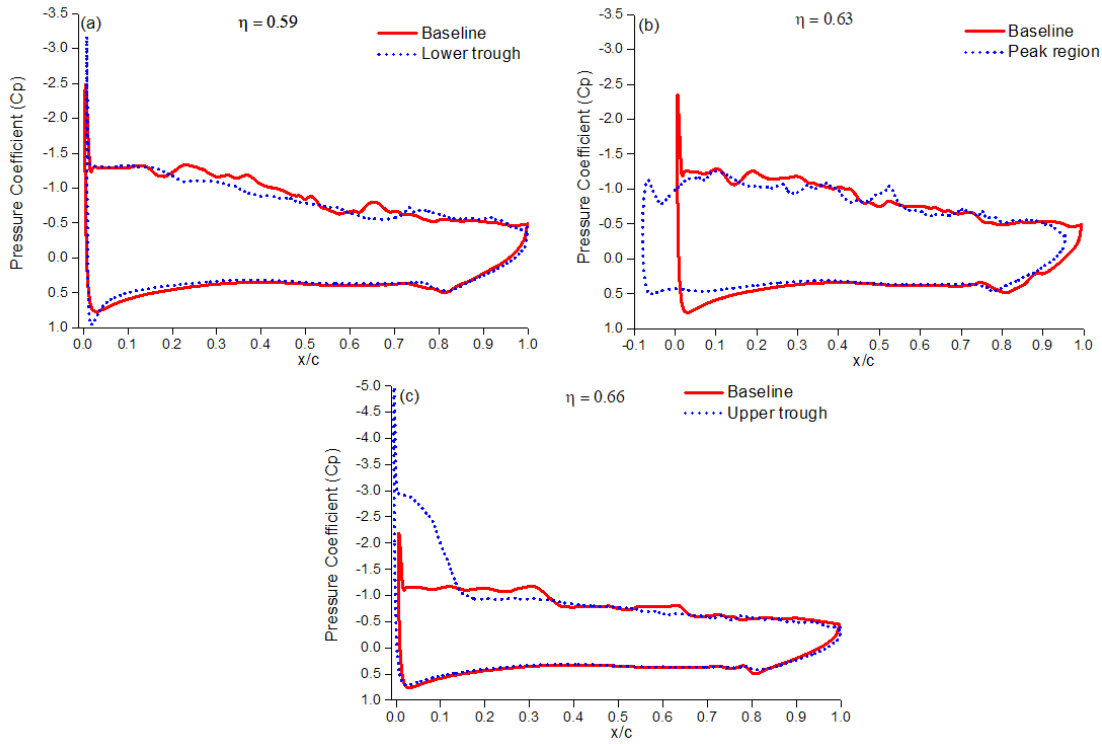

Fig. 6.5: The comparison of surface pressure coefficient of the baseline and (a) lower trough region, (b) peak region, (c) upper trough region at $\delta = 30°$ and $\beta = 8°$.

The effects of the modified single bump undulation are primarily localised to the region where the bump is mounted, as evidenced by the surface pressure coefficient plot in Fig. 6.6. Specifically, the benefits of enhancing the aerodynamic coefficients are attributed to the influence of the single bump undulation's upper trough region, with pressure peak significantly decreased at the peak region while increased at the upper trough region. Conversely, the lower peak region contributes less to the overall aerodynamic enhancement. Consequently, the mechanism of the single bump undulation demonstrates a significant effect of the tip side pressure gradient as indicated in Fig. 6.5 (c) and Fig. 6.6 (b), primarily towards the tip side of the VTP structure.

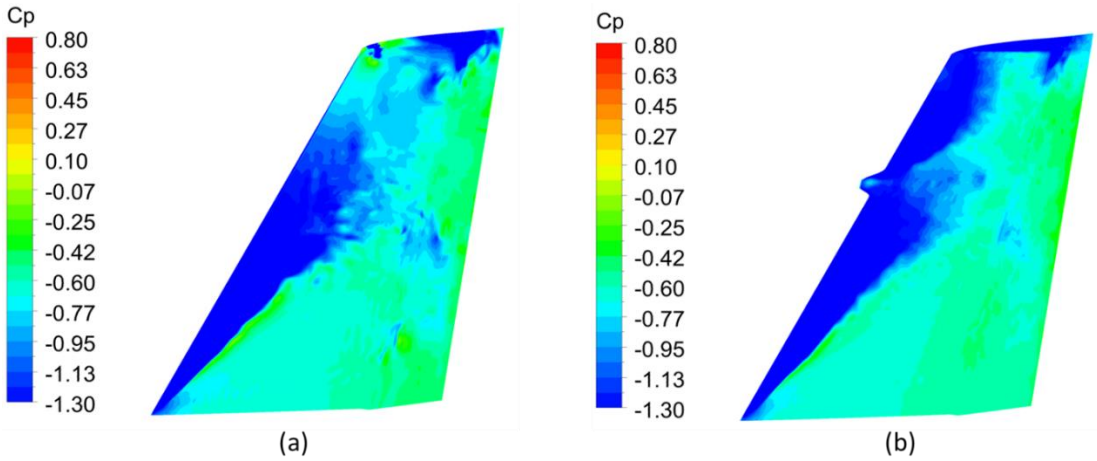

Fig. 6.6: Surface pressure coefficient of the Baseline (a) and Single bump undulation (b) at $\delta = 30°$ and $\beta = 8°$.

6.3.4 Skin friction Coefficient

The skin friction coefficient at the lower trough, peak, and upper trough regions, highlighting the modified single bump undulation's impact compared to the baseline, is presented in Fig. 6.7. As observed in the previous section that the lower trough region shows less effect of the bump compared to the upper trough region as seen in Fig. 6.7 (a). In Fig. 6.7 (b), the peak region is compared with the baseline, revealing that the re-energised boundary layer seen in the velocity plot corresponds to heightened skin friction. As a result of flow separation control, the boundary layer is attached with increased shear stress behind the peak and further downstream. Fig. 6.7 (c) illustrates separation along the mid-chord of the upper trough region, consistent with the earlier observation in this region. These comparisons show the influence of the modified single bump on the skin friction and the boundary layer characteristics. As earlier observed in Fig. 6.4 where the separation bubble was seen in the upper trough regions, a similar separation bubble like pattern is demonstrated in the Fig. 6.7 (c) in the skin friction plot near the leading edge of the single bump undulation.

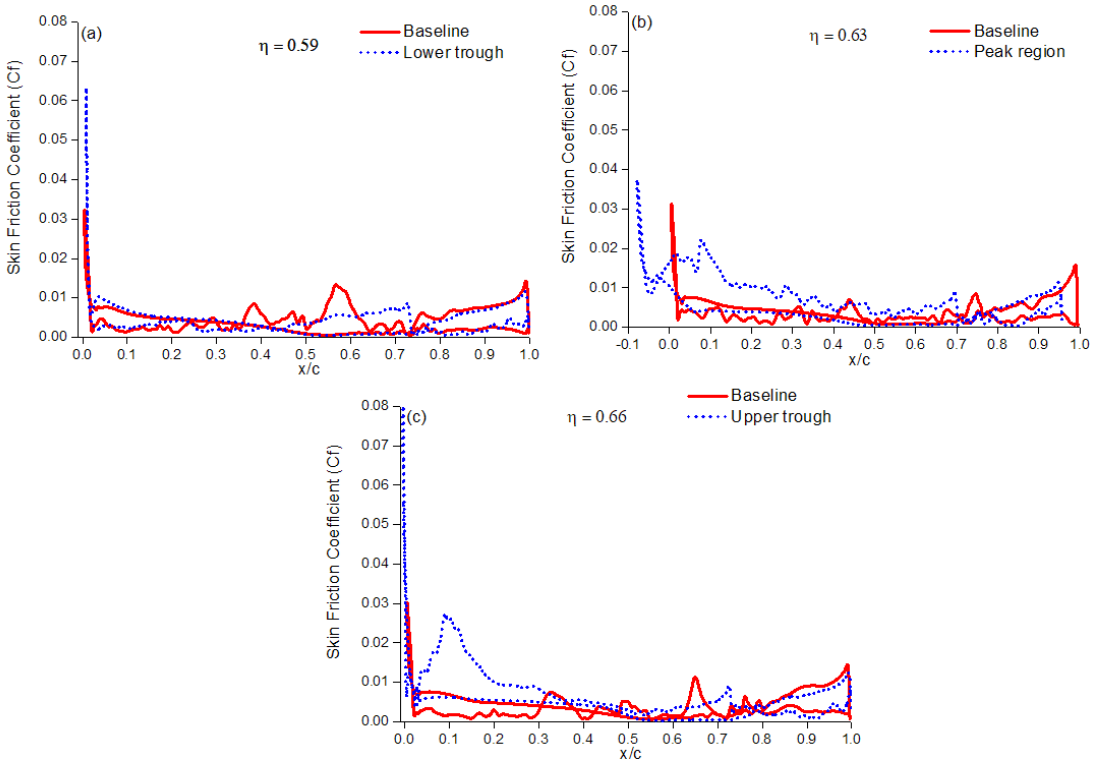

Fig. 6.7: The comparison of skin friction coefficient of the baseline and (a) lower trough region, (b) peak region, (c) upper trough region at δ = 30° and β = 8°.

Figure 6.7 illustrates the skin friction behaviour at spanwise locations of the lower, peak, and upper trough regions for both the baseline and single bump undulation. The effect of the bump is much clearer on the Cf distribution over the VTP surface, as shown in Fig. 6.8. The overall characteristics of the benefit of the single bump undulation are shown in Fig 6.8 using the three-dimensional VTP surface. The skin friction coefficient contour on the suction side of the VTP is superimposed with the skin friction lines. The baseline case exhibited a different pattern than the single bump undulation modification; the effect of the single bump undulation modification is noticeable around the peak and upper trough regions. The skin friction lines surrounding the bump display parallel reattachment, corresponding to the friction lines originating from the root side. The pattern extends upstream towards the tip side, exhibiting heightened shear stress along the path.

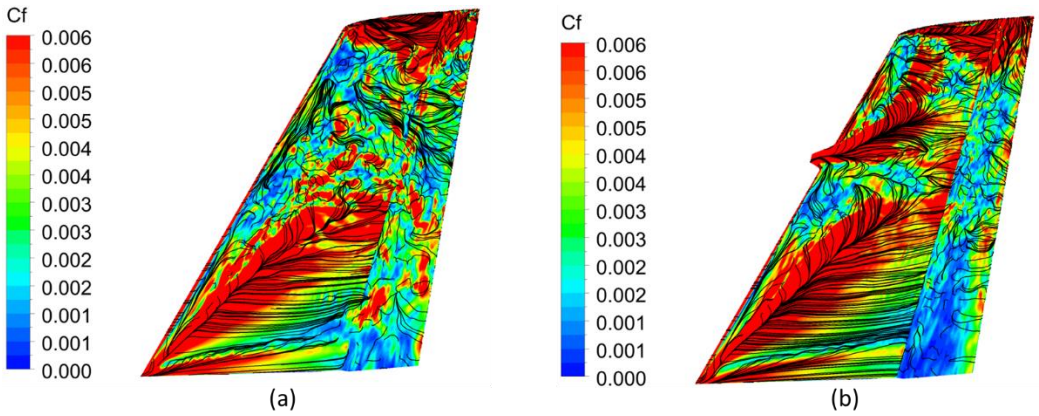

Fig. 6.8: Skin friction coefficient of the Baseline (a) and Single bump undulation (b) at $\delta = 30°$ and $\beta = 8°$.

6.3.5 Vortex Structure and Streamline Vorticity Contours

Figure 6.9 illustrates the three-dimensional coherent vortex structure of the single bump undulation with and without modification. The vortex structures are colour-coded based on the mean streamwise velocity at a sideslip angle of $\beta = 8°$ and rudder deflection angle of $\delta = 30°$. In the zoomed-in region corresponding to the single bump undulation, the baseline case shows a large harpin vortex along the span of the VTP. The region of the lower trough of the single bump undulation case highlights the generation of streamwise vortices due to the bump at the leading edge, which is tilting the spanwise vortices because of the K-H instability at the flow-separated shear layer. At the leading-edge of the single bump undulation, it can be observed that the large structures abruptly change into a 2D structures, and therefore resulting into an extended streamwise vortices.

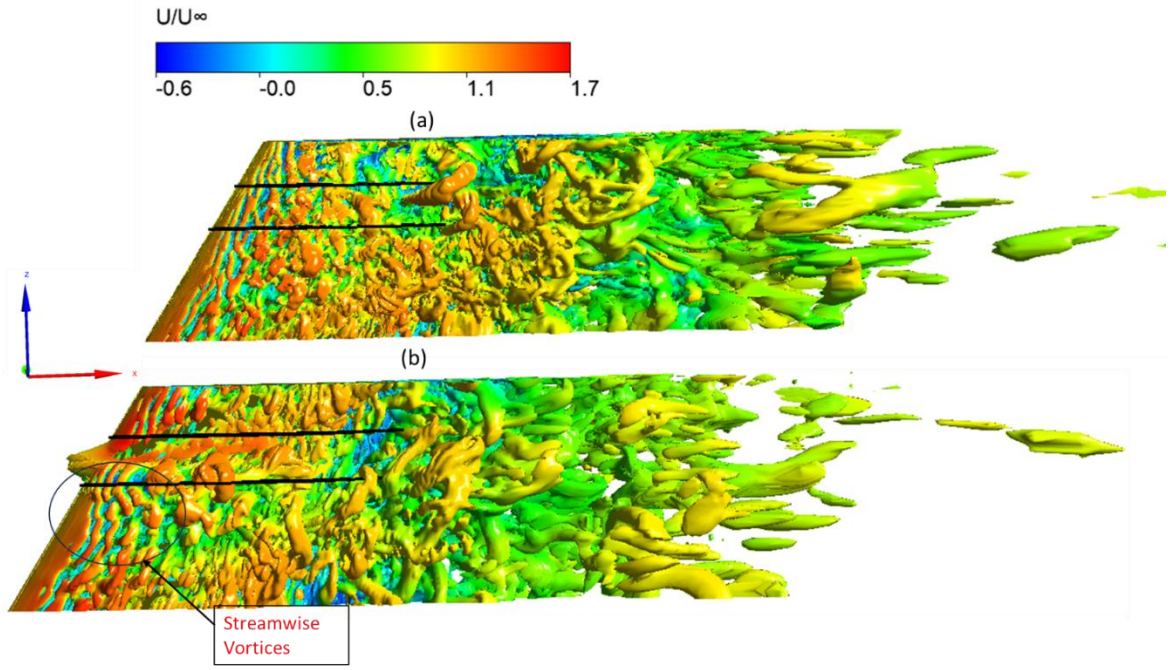

Fig. 6.9: Flow structures visualised using λ-2 criterion with iso-value of -2 × 10^4 and coloured with streamwise velocity for Baseline (a) and Single bump undulation (b) at δ = 30° and β = 8°.

Figure 6.10 describes the streamwise vorticity at three different spanwise locations corresponding to the lower, peak, and upper trough regions. The location behind the lower trough region in Fig. 6.10 (b) corresponds to the baseline location η = 0.59; in the single bump undulation case, there is a higher vortex strength along the surface span, while the wake region shows a reduced effect. This behaviour is clearly demonstrated in the three-dimensional vortex structure in Fig. 6.9. In contrast, the peak region in Fig. 6.10 (c) and (d) highlights how the modified single bump suppresses the surface structures behind the peak region. At a spanwise location η = 0.63, the peak region shows a weaker streamwise vorticity along the suction side compared to the baseline. At the mid-chord behind the peak region, the presence of the coherent large vortex structure observed in Fig. 6.10 (c) is growing weaker. Due to the single bump undulation protrusion at the upper region, the streamwise vorticity in the upper trough decreases (Fig. 6.10 (f)). All this can be attributed to the flow separation region being reduced by the bump. This behaviour was captured by the three-dimensional coherent structures of the baseline and single bump undulation in Fig. 6.9 (a-b).

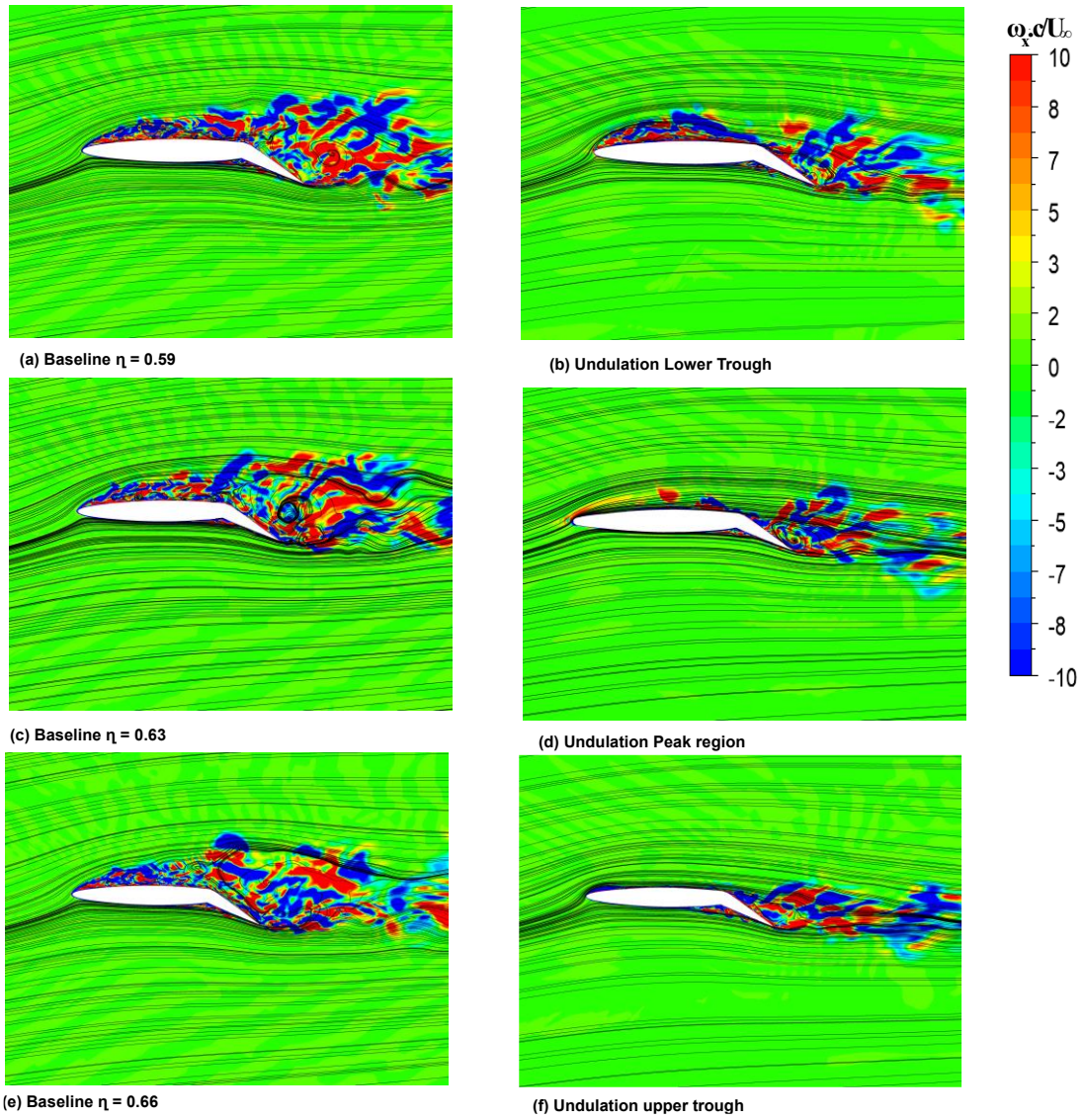

Fig. 6.10: Comparison of streamwise vorticity and streamline pattern for the baseline (a) η = 0.59, (c) η = 0.63 and (e) η = 0.66 and modified single-bump undulations (b) lower trough, (d) peak region and (f) upper trough at δ = 30° and β = 8°.

6.3.6 Streamline Turbulent Kinetic Energy Contours

Figure 6.11 illustrates the baseline and single bump undulation mechanism of the turbulent kinetic energy TKE. The results are presented in Fig. 6.11 (a-b), which indicates the influence of the TKE on the lower trough region along the surface from the leading edge. It can be observed that the TKE increases compared to the baseline case, which would be the reason why the separation bubble is reduced or suppressed by the bump. In Fig. 6.11 (c-d) for

the peak region, it can be observed that behind the peak region, the TKE was reduced and abruptly increased mid-chord, showing a wake downstream increase. In the case of the upper trough region in Fig. 6.11 (e-f), the baseline shows an increase in the TKE along the surface compared to the upper trough region. However, for the upper trough region in Fig. 6.11 (e), it is apparent that the increase in the TKE at the wake region is a result of the enhanced flow structures behind the stabiliser's trough region for the upper trough region.

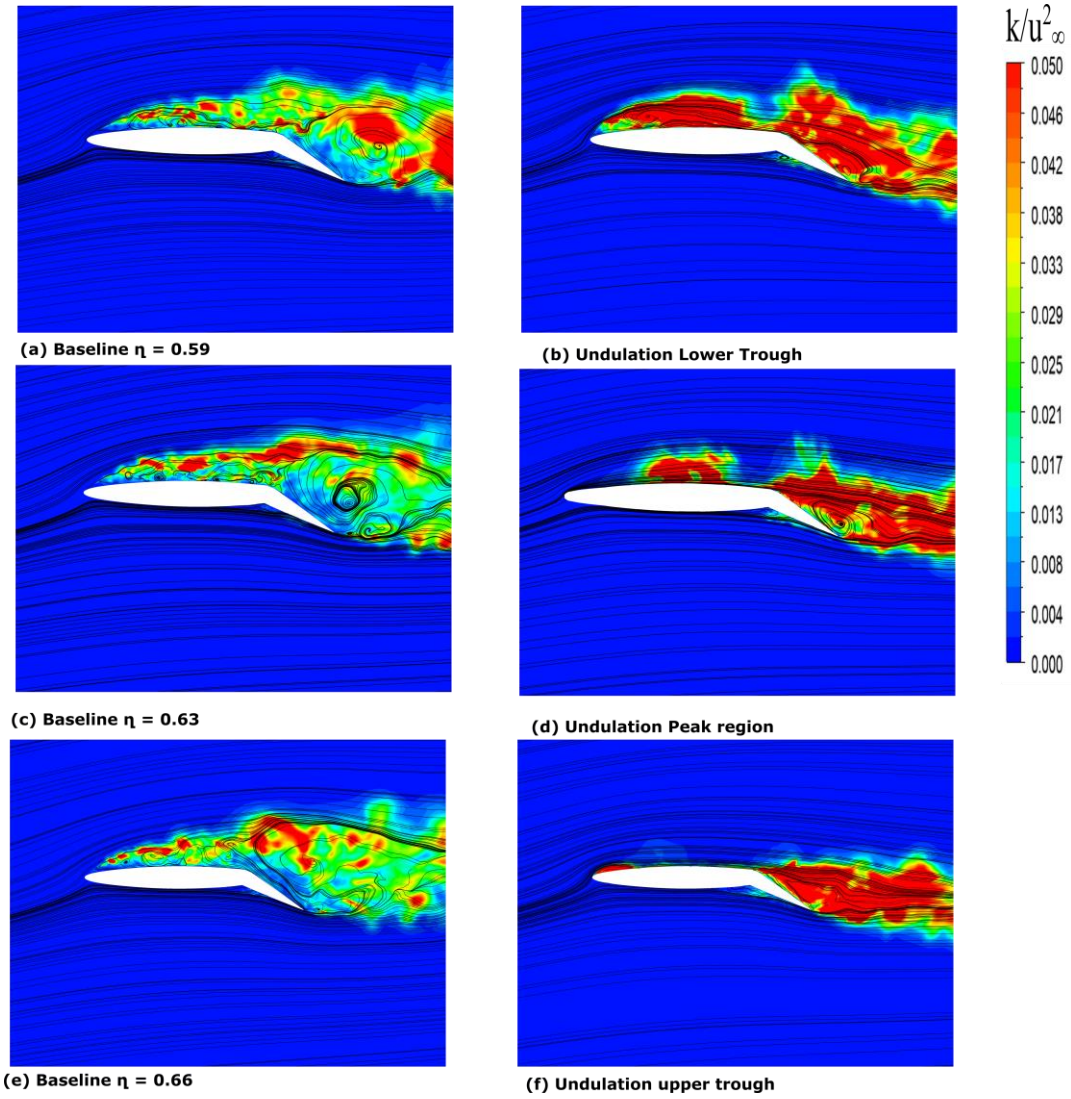

Fig. 6.11: Comparison of Turbulent kinetic energy and streamline pattern for the baseline (a) η = 0.59, (c) η = 0.63 and (e) η = 0.66 and modified single-bump undulations (b) lower trough, (d) peak region and (f) upper trough at δ = 30° and β = 8°.

6.3.7 Streamline Reynolds Stress Contours

The Reynolds stress is important in determining the average fluctuation in turbulence modelling. Fig. 6.12 compares the Reynolds stress of three spanwise locations identified as the modified single bump undulation's lower trough, peak, and upper trough regions with the baseline case. The Reynolds stress distribution of the Reynolds stress behind the lower trough region Fig. 6.12 (b), the peak region Fig. 6.12 (d), and the upper trough region Fig. 6.12 (e) indicated a redistribution of the Reynolds stress and less dispersed. These are closely linked to the distribution of the TKE since the TKE is the result of energy production, which is directly proportional to the Reynolds stress.

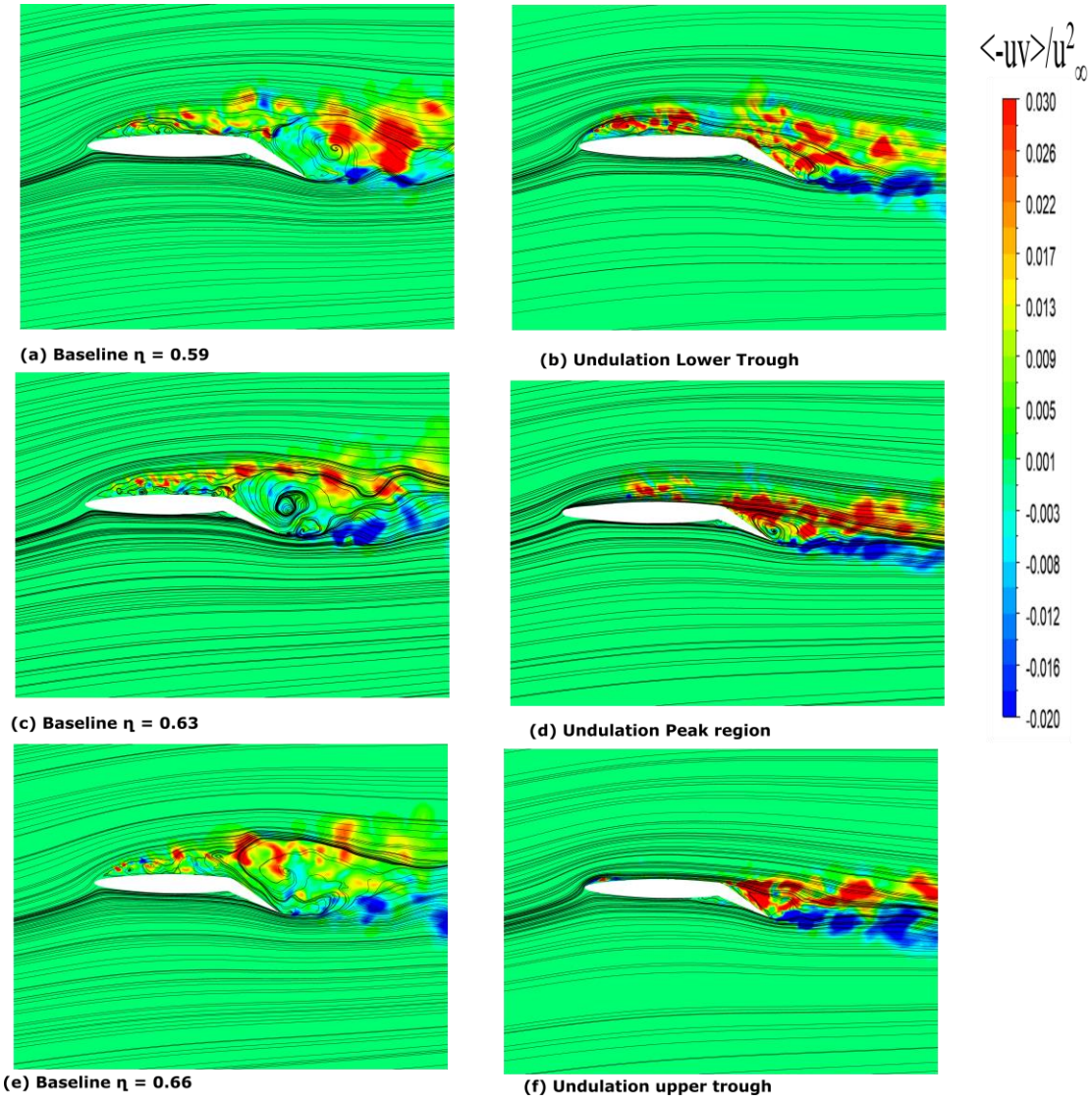

Fig. 6.12: Comparison of Turbulent kinetic energy and streamline pattern for the baseline (a) η = 0.59, (c) η = 0.63 and (e) η = 0.66 and modified

single-bump undulations (b) lower trough, (d) peak region and (f) upper trough at δ = 30° and β = 8°

6.4 Comparison between single bump undulation and side bumps

We assessed the effectiveness of two side bumps derived from the single bump undulation. These side bumps are obtained only by removing the protrusion of the single bump undulation in Fig. 13 (b). Therefore, these side bumps would be positioned on the suction and pressure side surfaces of the vertical tailplane, as illustrated in Fig. 13 (a). Consequently, the leading edge of the side bump is larger than the baseline leading edge, influenced by the presence of the upper and lower bumps as shown in Fig. 13 (c). The side bump is at 66.6% from the root side, maintaining consistency with the placement of the single bump undulation. The side bump exhibits a magnitude of the bump height at 0.2% with a protrusion of 0.04%.

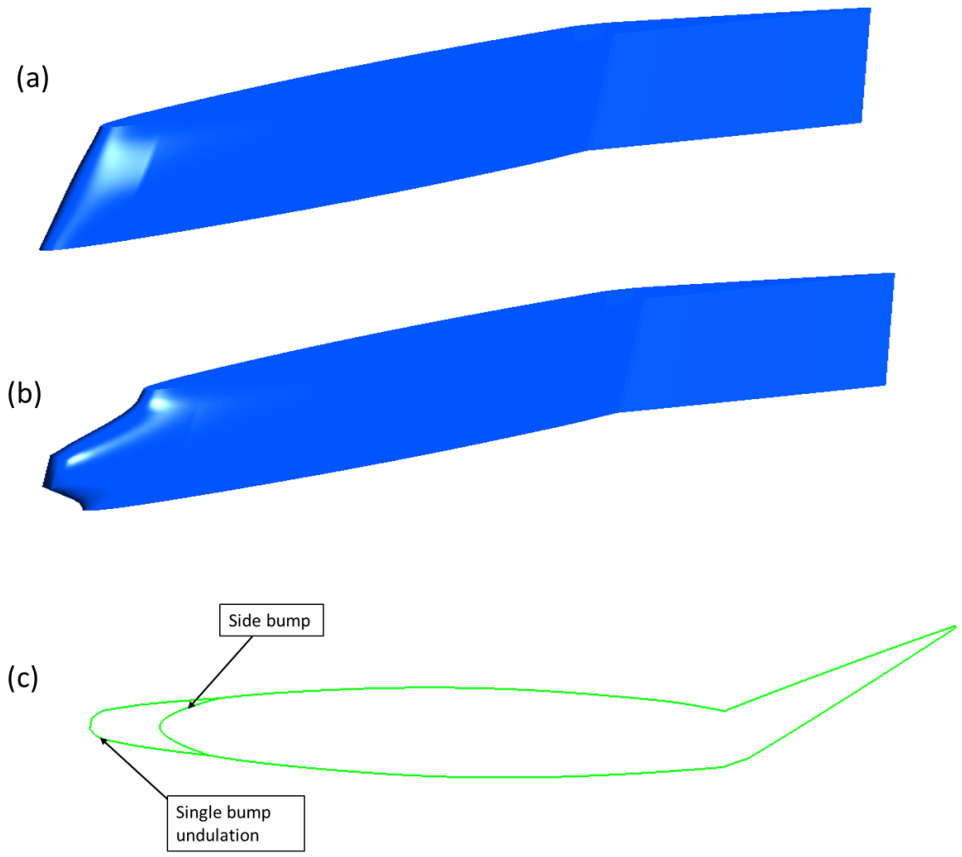

Fig. 6.13: Geometry of the (a) modified side bumps, (b) single-bump undulation design on the VTP, (c) cross-section of the peak region of the bump.

The comparison between the single bump undulation and the two side bumps was conducted numerically due to the absence of experimental data for the latter. The validation of the single bump undulation was established in the preceding section through comparison with the baseline case, where the numerical simulation exhibited good agreement with experimental results concerning the side and drag force coefficients. This validation highlights the reliability of the numerical approach.

The side and drag force coefficient result indicated that the side bumps can be used similarly to the single bump undulation in increasing the overall aerodynamic performance. Evidently, the contribution of the double bump in terms of the aerodynamic coefficients is encouraging from the numerical data. Even without existing experimental data, since the single bump undulation was compared with the experimental data, it is sufficient to further the analysis.

6.4.1 Mean Velocity Analysis

This section presents the streamwise velocity of the baseline, single bump undulation and the modified side bumps in Fig. 6.14. It is evident that the single bump undulation enhanced the flow through reattachment, as shown by the averaged streamlines at the lower, peak, and upper trough regions. However, the investigation of the modified single bump undulation without the leading-edge bump is the side bumps from the suction and pressure side of the VTP. These bumps were found to modify the flow by adding additional flow reattachment compared to the baseline case.

Figure 6.14 (a-c) illustrates the spanwise cut section of the baseline and modified side bumps, which correspond to the lower trough region of the single bump undulation. It was observed previously that the downstream region of the peak region showed less benefit than the upstream region of the peak. In this region, the baseline, the single bump undulation, and the modified side bumps show a long bubble that attaches at a half-chord length. However, the baseline exhibited a large region of the long bubble compared to the single bump undulation.

At the peak region in Fig. 6.14 (d-f), the large separation region demonstrated by the baseline case was found to attach the flow by both the single bump undulation and the modified side bumps. It is clearly shown that the side bumps benefit the flow in further reattachment but not as well as the single bump undulation.

At the upper trough region, this region was observed to influence the flow and benefit the VTP performance through flow reattachment. In addition, the single bump undulation and the modified side bump show the presence of leading-edge laminar separation bubbles, which may also exist to benefit and improve the aerodynamic performance.

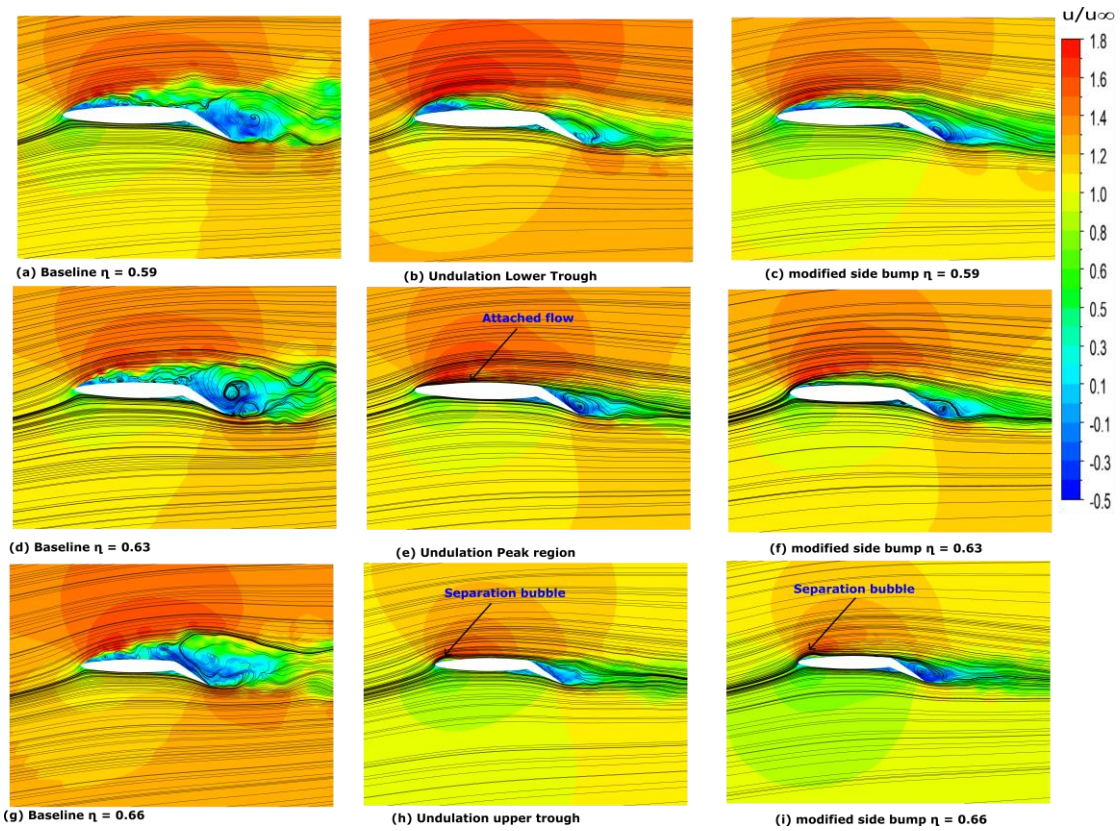

Fig. 6.14: Comparison of streamwise velocity and streamline pattern for baseline (a) $\eta = 0.59$, (d) $\eta = 0.63$ and (g) $\eta = 0.66$, single-bump undulations (b) lower trough, (e) peak region and (h) upper trough, and modified side bumps (c) $\eta = 0.59$, (f) $\eta = 0.63$ and (i) $\eta = 0.66$ at $\delta = 30°$ and $\beta = 8°$.

6.4.2 Streamline Vorticity Analysis

The streamlined vorticity analysis involves the baseline, single bump undulation (see Fig. 6.10) and modified side bumps, as shown in Fig. 6.15. The single bump undulation predominantly manifests its effect at the peak and upper trough regions. The investigation of the lower trough region (Fig. 6.15a-c) reveals a significant reduction in wake recirculation due to both the single bump undulation and the side bump, compared to the baseline. In Fig. 6.15 (d-f), the focus shifts to the peak region, where side bumps are observed to weaken counterclockwise vorticity both along the surface and downstream. However, the impact of the single bump undulation at the peak region is particularly conspicuous, indicating a notable alteration in vortex complexity attributed to the bump attachment and its influence on flow dynamics.

The Fig. 6.15 (g-i) compares the baseline, single bump undulation and side bumps at the trough region. Upon examination of the upper trough region in these Figs. 6.15 (g-i), it becomes apparent that the leading-edge protrusion mechanism is not a primary contributor to the enhancement of the flow field. The upper bump of the modified side bump demonstrates similar results to the single bump undulation, indicating comparable effects with the same magnitude of the upper bump. This suggests that the side bumps can be effectively utilised when the objective is to enhance the flow physics through the generation of streamwise vortices and induced high-momentum fluid that reduces the flow separation. Therefore, the single and side bumps reduce surface vortices and weaken downstream wake vortices.

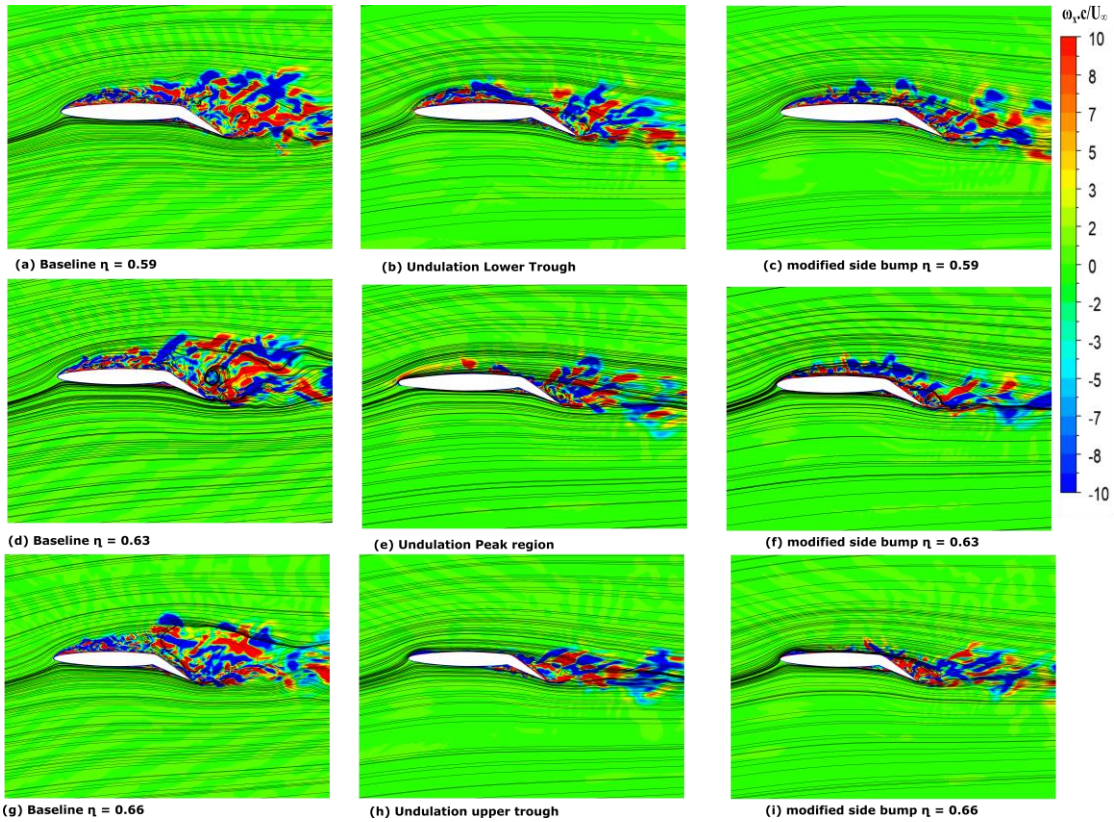

Fig. 6.15: Comparison of streamwise vorticity and streamline pattern for the baseline (a) η = 0.59, (d) η = 0.63 and (g) η = 0.66, single-bump undulations (b) lower trough, (e) peak region and (h) upper trough, and modified side bumps (c) η = 0.59, (f) η = 0.63 and (i) η = 0.66 at δ = 30° and β = 8°.

6.5 Chapter Summary

The design of the undulation protrusion on the leading edge of the VTP was investigated numerically using side slip angle $\beta = 8°$. The conventional design of the undulation protrusion is mostly for multiple protrusions along the leading-edge length of the model. However, several attempts have been made on such a design, and no reasonable enhancements of the aerodynamic performance were observed in the literature. Therefore, an attempt was made to design a single bump undulation at four different spanwise locations of the VTP. The optimum design from the experimental data, which is located at exactly 66.6% from the root side of the VTP, was presented in this chapter.

The single bump undulation was designed to enhance the aerodynamic performance of the VTP and reduce the separation effects that delay the stall angle. The stall angle was delayed, and the separation around the modified region was numerically investigated and compared to the experimental force coefficients. The upper and lower trough regions demonstrated a higher-pressure peak than the baseline case, which enhances the side force coefficient.

The mean fluctuations of the flow around both the modified and the baseline configurations are compared and examined. In the modified case, laminar separation bubbles are observed in the mean streamwise velocity, which contributes to the aerodynamic improvement of the single bump undulation. This effect is particularly noticeable in the upper trough region compared to the lower trough region. The single bump undulation also reduces the large-scale turbulent structures seen in the baseline case. The adverse pressure gradient in the upper trough region enhances the flow structures behind the stabiliser's trough region.

The introduction of a single bump undulation in the leading edge of the baseline VTP has demonstrated notable enhancements in the flow dynamics behind the peaks and troughs of the modified configuration. Lastly, in this study of VTP, a single bump undulation was found to be an effective passive flow control device that indicated modifications in the flow characteristics around the VTP.

7. Chapter seven

CONCLUSIONS AND RECOMMENDATIONS

7.1 Conclusions

The present study was designed to investigate the behaviour of a vertical tailplane with different flow separation control strategies, which was carried out using RANS turbulence models and LES. The flow control devices include the rudder-mounted slat and the single bump undulation at the leading edge. For the control devices, the vertical tailplane was set at a larger deflection angle of $\delta = 30°$; in this deflection angle, the flow is globally separated at zero sideslip angle; therefore, increasing the sideslip angle will increase the separation phenomenon. The main findings can be summarised as follows:

1) The baseline validation of the vertical tailplane with zero rudder deflection $\delta = 0°$, was investigated using various turbulence models. The numerical results were compared with the TailSurf project's experimental data. The turbulence models, high-fidelity LES, and experimental data were comprehensively compared. The analysis thoroughly examined the RANS, LES, and experimental results, considering three different sideslip angles. The conventional RANS models used kω SST, k—, ε and S-A models, which resulted in early loss of the side and drag force coefficient before the experimental data. The transition k-kl-ω model indicated a remarkable improvement in predicting the force coefficients compared to the conventional RANS models. The comparison of the LES and RANS with the experimental data gave a good agreement in predicting force coefficients, especially at low sideslip angles. The transition turbulence model and LES produced better predictions even at higher sideslip angle and stall angle, which proves that the transition model is robust in predicting flow related to transition with the complex region of laminar to turbulent separation. The LES accurately captured the reattachment point, which the turbulence models overpredicted. The transition k-kl-ω model and LES predicted the laminar separation bubble well near the leading edge. The influence of the TKE shows a remarkable result

amongst the turbulence models and LES. The TKE increases with an increase in the sideslip angles. It was observed that all the turbulence models and time-averaged LES agreed well in the prediction of the TKE in the observed chordwise locations studied. In this study, it was observed that the transition k-kl-ω model and LES predicted the laminar separation bubbles better than other turbulence models. As there is no control mechanism used to prevent the formation of the LSB at the laminar boundary layer, it is expected that similar results would be obtained from the experimental data since both methods accurately predicted the force coefficients close to the experimental data.

2) The numerical simulation of a vertical stabiliser was carried out at the rudder deflection angle of angle $\delta = 30°$, where the side force coefficient Cs was increased by up to 4% by a rudder-mounted slat. No noticeable increase in the drag coefficient was found at the test condition. This demonstrated that a rudder-mounted slat, which covers only 30% of the span from the tip, is an effective passive device for controlling the flow separation of the rudder when it is partially or fully separated. It was, however, noted that the Cs is slightly reduced at small sideslip angles, although the Cd remains the same. While the slat mounted at the leading edge of the rudder can help reattach the separated flow at large side-slip angles ($8° < \beta < 25°$), it could disturb the attached flow, thereby reducing Cs at small side-slip angles ($-6° < \beta < 2°$) in certain configurations. It was shown by the LES results for a sideslip angle of $\beta = 8°$ at the rudder angle of $\delta = 30°$ that the negative surface pressure coefficient (-Cp) is increased at the slat position as well as over the rudder, suggesting that the slat is helping reattach the separated flow over the rudder. For a greater sideslip angle of $\beta = 14°$, the slat effect on the surface pressure coefficient is only seen closer to the root of the vertical stabiliser. The wall-shear stress lines over the suction side of the vertical stabiliser for $\beta = 8°$ at $\delta = 30°$ show a reattachment line coming off the root of the leading edge at about 45° angle. The total skin friction coefficient is high along the reattachment line as the separated flow impinges on it. For a sideslip angle of $\beta = 14°$, the slat seems to help

reattach the flow near the root between η = 0.25 and η= 0.50 by extending the reattachment line further downstream. Further LES study of the test model suggested that the slat immediately draws the flow from the recirculating region upstream and directs it over the rudder surface. The slat effect was also observed closer to the root of the vertical stabiliser by extending the reattachment line further downstream. It is believed that these changes were brought by the circulation added by the slat, which is evident from the change in the streamlines around the trailing edge of the rudder. The spanwise vortices were observed developing from the leading edge of the vertical stabiliser due to the Kelvin-Helmholtz (K-H) instability of the separated shear layer. These spanwise vortices were deformed to become hairpin vortices in the wake region of the rudder. With slat, these hairpin vortices were weakened in a smaller wake region.

3) The use of the leading-edge undulation was investigated at a rudder deflection $\delta = 30°$ and sideslip angle of $\beta = 8°$. A single bump undulation on the VTP's leading edge was designed to improve aerodynamic performance by reducing the flow separation. The optimum design of the single bump undulation obtained from the TailSurf project was investigated at 66.6% from the root side of the VTP. The optimum design was numerically examined to compare the force coefficients with experimental data and further the analysis to more detailed physics. The mean fluctuations of the flow around both the modified and the baseline configurations are compared and examined. The single bump undulation reduces the large-scale turbulent structures seen in the baseline case. The adverse pressure gradient in the upper trough region was expected to enhance the flow structures behind the stabiliser's trough region. The introduction of this design demonstrated notable enhancements in flow dynamics behind the peaks and troughs of the modified configuration, resulting in improved aerodynamic performance and favourable modifications in the flow characteristics around the VTP.

7.2 Recommendations

The simulation results confirmed the RANS models' unsuitability for predicting the flow phenomenon, especially at higher sideslip angles and larger rudder deflections. The transition model better-predicted force coefficients and laminar to turbulent transitions. Therefore, it is recommended that more transition models be tested to establish a reliable benchmark for the model. Also, more information on the unsteady transition models with hybrid models may contribute to greater accuracy and less simulation time.

The rudder-mounted geometry was tested for different slat sizes and gaps to ensure optimum force coefficient performance. However, the slat was placed at 30% of the rudder chord from the tip side. Further increasing the slat spanwise coverage is not known. Therefore, since the optimum size and gaps are known, the span of the slat can be tested further from the tip to the root side to investigate if it is sufficient to produce a 4% enhancement at the rudder deflection of $\delta = 30°$.

After analysing the results of the baseline and modified single bump undulation, it was found that the numerical simulation of $\delta = 30°$ and sideslip angle of $\beta = 8°$ are quite different. However, the flow features show that the single bump undulation provides some benefits. Also, it is important to note that the single bump undulation is a new concept. Thus, it is suggested that further investigation be conducted to examine the effect of icing on the leading edge.

APPENDIX A:

The geometry has been generated using the Airbus "Meres" code and exported to Catia. Annex A: TAILSURF_MODEL1_0mm.a_c is the MARES model of the VTP with trailing edge thickness 0mm. Annex B: VTP_TAILSURF_TrailingEdge0mm.arf is the profile used in the MARES model with zero trailing edge thickness. Raul Carlos LLAMAS, the future project office of Airbus, provided the geometry details.

ANNEX A: *TAILSURF_MODEL1_0mm.a_c*

```
AIRCRAFT          A321_ULT
x_ih         40.9392      # [metres]
z_ih         0.665        # [metres]
x_cg         17           # [metres]
x_pitch      21.98        # [metres]
z_pitch      -3.4274      # [metres]
y_roll       3.795        # [metres]
z_roll       -3.943       # [metres]
z_ground     -3.943       # [metres]
visible_ground            0
COMPONENT     LIFTSURF          VTP       VTP_ULT_NLF_0
            Update On Open  1
            Local Symmetry 0
            Locked       0

            span         1.596871     # [m]
            cr           1.286763     # [m]
            ct           0.5919108    # [m]
            sweep        27.2         # [degrees]
            dihedral     0            # [degrees]
            etaINI       0            #
            etaEND       1            # [degrees]

            REAL_PLANFORM_CONTROLS     0
            use_manual_eta           1         #
            manual_eta_str
0,0.0258,0.0516,0.0774,0.1032,0.127,0.1508,0.1746,0.1984,0.2222,0.246,0.2698,0.2936,0.3174,0.
3412,0.365,0.3888,0.4126,0.4364,0.4602,0.484,0.5078,0.5316,0.5554,0.5792,0.6029999,0.626799
9,0.6506,0.6744,0.6982,0.722,0.7458,0.7696,0.7933999,0.8171999,0.841,0.8648,0.8767,0.8886,0.
89455,0.9005,0.90645,0.9124,0.915375,0.91835,0.921325,0.9243,0.9272751,0.93025,0.933225,0.9
362,0.939175,0.94215,0.945125,0.9481,0.951075,0.9540499,0.9555374,0.9570249,0.9585124,0.96,
0.9618182,0.9636363,0.9654545,0.9672727,0.9690909,0.9709091,0.9727272,0.9745454,0.976363
6,0.9781818,0.98,0.9818182,0.9836364,0.9854546,0.9872727,0.9890909,0.9909091,0.9927273,0.
9945455,0.9954545,0.9963636,0.9972727,0.9981818,0.9990909,1
            profile_point_number       80        #

            trailing_thickness         0         # [mm]
            start_squeez  0.5          # [%]

            PROFILES
                        Eta_val      Profile_File  z1 Up       z2 Up       xq Up       zq Up       z1 Down      z2
Down      xq Down      zq Down      M                   p           k           Deformation Type
                        0          VTP_TAILSURF_TrailingEdge0mm.arf        0           0           0           0
0           0           0           0           0           0           0           4

            DELTA_LEADING
                        # eta       x/c         pre_ang      pos_ang      shape_fact
                        0           0           *            *            *
                        0.96        0           *            0            1.5
                        1           -0.7        -90          *            *
                        FUNCTION_CLASS           0
```

```
        DELTA_TRAILING
                # eta     x/c     pre_ang     pos_ang     shape_fact
                0       0       *       *       *
                1       0       *       *       *
                FUNCTION_CLASS          0

        DELTA_THICKNESS/REAL_CHORD
                # eta     t/c_real    pre_ang     pos_ang     shape_fact
                0       0.099       *       *       *
                0.96        0.099       *       0       1.5
                1       0.02        -90     *       1.5
                FUNCTION_CLASS          0

        MANTAIN_PROFILE_CAMBER  0

        CONTROL_SURFACES
                T       0.008   1       0.7     0.7     0       0       0       0.0001
        1       0       0       0       0       0       0       0



        visualization_settings  1;1;1;1;1;9868950;1;0;1
        vis_sides           1;1
        texture_settings        0;;0
```

ANNEX B: *VTP_TAILSURF_TrailingEdgeomm.arf*

```
{
  "arf_nurbs":{
    "MaxTh":0.1069279,
    "MaxTh_X":0.4154772,
    "MaxCb":5.587935e-09,
    "MaxCb_X":0.5702479,
    "MaxLERadius":7.332213e-03,
    "MaxTESlope":1.907349e-06,
    "upper_curve":{
      "Size":2,
      "CPX":[
        0,
        0,
        0.1464466,
        0.5,
        0.8535534,
        1
      ],
      "CPY":[
        0,
        1.891893e-02,
        4.231578e-02,
        6.556184e-02,
        2.160089e-02,
        0
      ],
      "CPW":[
        1,
        1,
        1,
        1,
        1,
        1
      ],
      "K":[
        0,
        0,
        0,
```

```
            0,
            1,
            2,
            3,
            3,
            3,
            3
          ],
          "Degree":3
        },
        "lower_curve":{
          "Size":2,
          "CPX":[
            0,
            0,
            0.1464466,
            0.5,
            0.8535534,
            1
          ],
          "CPY":[
            0,
            -1.891893e-02,
            -0.0423158,
            -6.556182e-02,
            -0.0216009,
            0
          ],
          "CPW":[
            1,
            1,
            1,
            1,
            1,
            1
          ],
          "K":[
            0,
            0,
            0,
            0,
            1,
            2,
            3,
            3,
            3,
            3
          ],
          "Degree":3
        }
      }
}
```

REFERENCES:

Abdullah, M. Z.; Yap, T. C.; Husain, Z.; Ripin, Z. M.; Ahmad, R. The effect of turbulence intensity on the aerodynamic performance of airfoils. 4th International Conference on Mechanical Engineering (ICME). 31–36 (2001)

Abe, Y.; Chinzei, T.; Isoyama, T.; Ono, T.; Mochizuki, S.; Mabuchi, K.; Baba, K.; Matsuura, H.; Sun, Y. P.; Kouno, A.; Atsumi, K.; Fujimasa, I.; Imachi, K. Development of the undulation pump total artificial heart. Artificial Organs. **21** (7) 665–669 (1997)

Aftab, S. M. A.; Ahmad, K. A. Naca 4415 airfoil modification using spherical and sinusoidal tubercle leading edge. AIAA Scitech 2019 Forum. 1–26 (2019)

Aftab, S. M. A.; Rafie, A. S. M.; Razak, N. A.; Ahmad, K. A. Turbulence model selection for low Reynolds number flows. PLoS ONE. **11** (4) 1–15 (2016)

Aftab, S. M. A.; Razak, N. A.; Mohd Rafie, A. S.; Ahmad, K. A. Mimicking the humpback whale: An aerodynamic perspective. Progress in Aerospace Sciences. **84** 48–69 (2016)

Ahmed, N.; Yilbas, B. S.; Budair, M. O. Computational study into the flow field developed around a cascade of NACA 0012 airfoils. Computer Methods in Applied Mechanics and Engineering. **167** (1–2) 17–32 (1998)

Airbus. Airport and Maintenance Planning Code. (2005)

Akbarzadeh, A. M.; Borazjani, I. Controlling flow separation on a thick airfoil using backward traveling waves. AIAA Journal. **58** (9) 3799–3807 (2020)

Alonso, J. J.; LeGresley, P.; Pereyra, V. Aircraft design optimisation. Mathematics and Computers in Simulation. **79** (6) 1948–1958 (2009)

Anil Kumar, B. S.; Ramalingaiah; Manjunath, S.; Ganganna, R. Computational Investigation of Flow Separation over NACA 23024 Airfoil at 6 million Free Stream Reynolds Number Using k-Epsilon Turbulence Model. Materials Today: Proceedings. **5** (5) 12632–12640 (2018)

Anitha, D.; Shamili, G. K.; Ravi Kumar, P.; Sabari Vihar, R. Airfoil shape optimisation using CFD and parametrisation Methods. Materials Today: Proceedings. **5** (2) 5364–5373 (2018)

Ansys, I. Ansys Fluent Theory Guide. Ansys 2021R2. (2021)

Arra, A.; Anekar, N.; Nimbalkar, S. Aerodynamic effects of leading edge (LE) slats and slotted trailing edge (TE) flaps on NACA-2412 airfoil in prospect of optimisation. Materials Today: Proceedings. **44** 587–595 (2021)

Arya, N.; De, A. Effect of grid sensitivity on the performance of wall adapting SGS models for LES of swirling and separating–reattaching flows. Computers and Mathematics with Applications. **78** (6) 2035–2051 (2019)

Asghar, A.; Perez, R. E.; Jansen, P. W.; Allan, W. D. E. Application of leading-edge tubercles to enhance propeller performance. AIAA Journal. **58** (11) 4659–4671 (2020)

Aubard, G.; Volpiani, P. S.; Gloerfelt, X.; Robinet, J.; Aubard, G.; Volpiani, P. S.; Gloerfelt, X. Comparison of Subgrid-scale Viscosity Models and Selective Filtering Strategy for Large-eddy Simulations. Flow, Turbulence and Combustion. **3** (91) 497–518 (2013)

Azim, R.; Hasan, M. M.; Ali, M. Numerical investigation on the delay of boundary layer separation by suction for NACA 4412. Procedia Engineering. **105** 329–334 (2015)

Bakırcı, M. Investigation of Turbulence Models in the Analysis of Two Different Airfoils with Computational Fluid Dynamics. Interdisciplinary studies on contemporary research practices in engineering in the 21st century. 62–99 (2023)

Balakumar, P. Direct numerical simulation of flows over an NACA-0012 airfoil at low and moderate Reynolds numbers. 47th AIAA Fluid Dynamics Conference, 2017. (757) 1–19 (2017)

Bardina, J. E.; Huang, P. G.; Coakley, T. J. Turbulence modeling validation. 28TH Fluid Dynamics Conference, 1997, American Institute of Aeronautics and Astronautics Inc, AIAA, 1997.

Bazdidi-Tehrani, F.; Masoumi-Verki, S.; Gholamalipour, P.; Kiamansouri, M. Large eddy simulation of pollutant dispersion in a naturally cross-ventilated model building: Comparison between sub-grid scale models. Building Simulation. **12** (5) 921–941 (2019)

Bolzon, M. D.; Kelso, R. M.; Arjomandi, M. Force Measurements and Wake Surveys of a Swept Tubercled Wing. Journal of Aerospace Engineering. **30** (3) 1–11 (2017)

Bolzon, M. D.; Kelso, R. M.; Arjomandi, M. The effects of tubercles on swept wing performance at low angles of attack. Proceedings of the 19th Australasian Fluid Mechanics Conference, AFMC 2014. (2014)

Bolzon, Michael. D.; Kelso, R. M.; Arjomandi, M. Tubercles and Their Applications. Journal of Aerospace Engineering. **29** (1) 1–10 (2016)

Boris, J. P.; Grinstein, F. F.; Oran, E. S.; Kolbe, R. L. New insights into large eddy simulation. Fluid Dynamics Research. **10** (4–6) 199–228 (1992)

Boughou, S.; Omar, A. A.; Elsyed, O. A.; Aldheeb, M. Numerical Investigations of Aerodynamic Characteristics Prediction of High-lift Low Reynolds Number Airfoil. CFD Letters. **14** (2) 111–121 (2022)

Brunner, C. E.; Kiefer, J.; Hansen, M. O. L.; Hultmark, M. Study of Reynolds number effects on the aerodynamics of a moderately thick airfoil using a high-pressure wind tunnel. Experiments in Fluids. **62** (8) 1–17 (2021)

Burnazzi, M.; Radespiel, R. Assessment of leading-edge devices for stall delay on an airfoil with active circulation control. CEAS Aeronautical Journal. **5** (4) 359–385 (2014)

Bush, R. H.; Chyczewski, T.; Duraisamy, K.; Eisfeld, B.; Rumsey, C. L.; Smith, B. R. Recommendations for future efforts in RANS modeling and simulation. AIAA Scitech 2019 Forum. 1–19 (2019)

Bush, R. H.; Chyczewski, T.; Duraisamy, K.; Eisfeld, B.; Rumsey, C. L.; Smith, B. R. Recommendations for future efforts in RANS modeling and simulation. AIAA Scitech 2019 Forum. 1–19 (2019)

Carmichael, B. H.; NASA. Low Reynolds number airfoil survey. NASA Contractor Report. **1** (1982)

Catalano, P.; Amato, M. An evaluation of RANS turbulence modelling for aerodynamic applications. Aerospace Science and Technology. **7** (7) 493–509 (2003)

Celik, I. B.; Cehreli, Z. N.; Yavuz, I. Index of resolution quality for large eddy simulations. Journal of Fluids Engineering, Transactions of the ASME. **127** (5) 949–958 (2005)

Chacksfield, J. E. Variable Camber Airfoils. Aeronautical Journal. **84** (832) 131–139 (1980)

Chen, Q.; Zhong, Q.; Qi, M.; Wang, X. Comparison of vortex identification criteria for planar velocity fields in wall turbulence. Physics of Fluids. **27** (8) (2015)

Chen, Z. J.; Qin, N.; Nowakowski, A. F. Three-dimensional laminar-separation bubble on a cambered thin wing at low Reynolds numbers. Journal of Aircraft. **50** (1) 152–163 (2013)

Cheng, W.; Pullin, D. I.; Samtaney, R. Wall-resolved and wall-modelled large-eddy simulation of plane Couette flow. Journal of Fluid Mechanics. **934** 1–31 (2022)

Chin, V. D.; Peters, D. W.; Spaid, F. W.; Mcghee, R. J. Flowfield measurements about a multi-element airfoil at high Reynolds numbers. In: AIAA 23rd Fluid Dynamics, Fluid Dynamics, And Lasers Conference, 1993. 1–15 (1993)

Choudhry, A.; Arjomandi, M.; Kelso, R. A study of long separation bubble on thick airfoils and its consequent effects. International Journal of Heat and Fluid Flow. **52** 84–96 (2015)

Ciliberti, D.; Della Vecchia, P.; Nicolosi, F.; De Marco, A. Aircraft directional stability and vertical tail design: A review of semi-empirical methods. Progress in Aerospace Sciences. **95** 140–172 (2017).

Corson, D.; Jaiman, R.; Shakib, F. Industrial application of RANS modelling: Capabilities and needs. International Journal of Computational Fluid Dynamics. **23** (4) 337–347 (2009)

Damiola, L.; Siddiqui, M. F.; Runacres, M. C.; De Troyer, T. Influence of free-stream turbulence intensity on static and dynamic stall of a NACA 0018 aerofoil. Journal of Wind Engineering and Industrial Aerodynamics. **232** 105270 (2023)

Diskin, B.; Galbraith, M. C. High-Fidelity CFD Verification Workshop 2024: Spalart-Allmaras QCR2020 Turbulence Model. 1–18 (2023)

Diskin, B.; Thomas, J. L.; Rumsey, C. L.; Schwöppe, A. Grid convergence for turbulent flows (invited). 53rd AIAA Aerospace Sciences Meeting. 1–50 (2015)

Dong, L.; Choi, K. S.; Mao, X.; Wang, Y. Development and interaction of vortices over a very low aspect-ratio wing under pitch-up motion. Journal of Fluid Mechanics. 943 1–25 (2022)

Douvi C. Eleni. Evaluation of the turbulence models for the simulation of the flow over a National Advisory Committee for Aeronautics (NACA) 0012 airfoil. Journal of Mechanical Engineering Research. **4** (3) 100–111 (2012)

Elgammi, M.; Sant, T.; Ateeah, A. A. The influence of the flow separation bubble and transition location on the profile drag of three 4-digit NACA aerofoil profiles. Wind Engineering. **46** (3) 796–817 (2022)

Falk, U.; Schäfer, M. A fully coupled finite volume solver for the solution of incompressible flows on locally refined non-matching block-structured grids. Adaptive Modeling and Simulation 2013 - Proceedings of the 6th International Conference on Adaptive Modeling and Simulation, ADMOS 2013. 235–246 (2013)

Fatahian, H.; Salarian, H.; Nimvari, M. E.; Khaleghinia, J. Computational fluid dynamics simulation of aerodynamic performance and flow separation by single element and slatted airfoils under rainfall conditions. Applied Mathematical Modelling. **83** 683–702 (2020)

Favier, J.; Pinelli, A.; Piomelli, U. Control of the separated flow around an airfoil using a wavy leading edge inspired by humpback whale flippers. Comptes Rendus - Mecanique. **340** (1–2) 107–114 (2012)

Feng, Z.; Qi, H.; Huang, X.; Liu, S.; Liu, J. Comparisons of Subgrid-Scale Models for OpenFoam Large- Eddy Simulation. IOP Conference Series: Earth and Environmental Science. **1802** (4) (2021)

Fernandes, E. C. R.; Belo, A. C.; Araújo, A. M.; Silva, A. A. C. da; Bezerra, C. C. de A.; Rocha, G. J. de A. M. an Assessment of Different Turbulence Models on a Cfd Simulation of Air Flow Past a S814 Airfoil. Brazilian Journal of Development. **6** (8) 58335–58348 (2020)

Fernandes, I.; Sapkota, Y.; Mammen, T.; Rasheed, A.; Rebello, C. L.; Kim, Y. H. Theoretical and experimental investigation of the leading-edge tubercles on the wing performance. 2013 Aviation Technology, Integration, and Operations Conference. (2013)

Fish, F. E.; Battle, J. M. Hydrodynamic design of the humpback whale flipper. Journal of Morphology. **225** (1) 51–60 (1995)

Fish, F. E.; Lauder, G. V. Passive and active flow control by swimming fishes and mammals. Annual Review of Fluid Mechanics. **38** 193–224 (2006)

Fish, F. E.; Weber, P. W.; Murray, M. M.; Howle, L. E. The tubercles on humpback whales' flippers: Application of bio-inspired technology. Integrative and Comparative Biology. **51** (1) 203–213 (2011)

Fureby, C. Towards the use of large eddy simulation in engineering. Progress in Aerospace Sciences. **44** (6) 381–396 (2008)

Gaster, M. The Structure and Behaviour of Laminar Separation Bubbles. Aeronautical Research Council Reports and Memoranda. No. 3595 1–31 (1967)

Genc, S. M.; Koca, K.; Demir, H. Traditional and new types of passive flow control techniques to pave the way for high maneuverability and Low Structural Weight for UAVs and MAVs. Unmanned Aerial Vehicles. 2020. 129–162 (2020)

Georgiadis, N. J.; Rizzetta, D. P.; Fureby, C. Large-eddy simulation: Current capabilities, recommended practices, and future research. AIAA Journal. **48** (8) 1772–1784 (2010)

Germano, M.; Piomelli, U.; Moin, P.; Cabot, W. H. A dynamic subgrid-scale eddy viscosity model. Physics of Fluids A. **3** (7) 1760–1765 (1991)

Gong, Y.; Wang, J.; Zhang, W.; Socha, J. J.; Dong, H. Computational analysis of vortex dynamics and aerodynamic performance in flying-snake-like gliding flight with horizontal undulation. Physics of Fluids. **34** (12) (2022)

Gopinathan, V. T.; Ralphin Rose, J. B. Aerodynamic performance characterization of bio-inspired wings with leading edge tubercles at low Reynolds number. Proceedings of the Institution of Mechanical Engineers, Part G: Journal of Aerospace Engineering. **237** (3) 561–586 (2023)

Guo, H.; Li, G.; Zou, Z. Numerical Simulation of the Flow around NACA0018 Airfoil at High Incidences by Using RANS and DES Methods. Journal of Marine Science and Engineering. **10** (7) (2022)

Guoqiang, L.; Shihe, Y. Large eddy simulation of dynamic stall flow control for wind turbine airfoil using plasma actuator. Energy. **212** 118753 (2020)

Gupta, A. K.; Aswatha Narayana, P. A.; Ramesh, G. Effect of turbulence intensity on low Reynolds number airfoil aerodynamics. International Journal of Engineering and Technology (UAE). **7** (4) 12–17 (2018)

Gupta, S.; Naveen, R.; Prathik, B. V.; Spurthy, S. CFD simulation of turbulent flow around multi-element airfoil. AIP Conference Proceedings. **2204** (2020)

Hansen, K. L.; Kelso, R. M.; Dally, B. B. Performance variations of leading-edge tubercles for distinct airfoil profiles. AIAA Journal. **49** (1) 185–194 (2011)

Haque, A. U.; Asrar, W.; Omar, A. A.; Sulaeman, E.; Ali, M. J. S. Comparison of data correction methods for blockage effects in semispan wing model testing. EPJ Web of Conferences. 114 1–7 (2016)

Hassan, T.; Islam, Md. T.; Rahman, Md. M.; Ali, A. R. I.; Ziyan, A. Al. Evaluation of Different Turbulence Models at Low Reynolds Number for the Flow over Symmetric and Cambered Airfoils. Journal of Engineering Advancements. **03** (01) 12–22 (2022)

Heffron, A. P.; Williams, J. J.; Avital, E. Flow separation and passive flow control on E387 Airfoil. 54th AIAA Aerospace Sciences Meeting. 1–11 (2016)

Hoburg, W.; Abbeel, P. Geometric programming for aircraft design optimization. AIAA Journal. **52** (11) 2414–2426 (2014)

Horton, H. P. Laminar separation bubbles in two and three dimensional incompressible flow. Ph.D. thesis,University of London. (1968)

Hu, H.; Yang, Z. An experimental study of the laminar flow separation on a low-Reynolds-number airfoil. Journal of Fluids Engineering, Transactions of the ASME. **130** (5) 0511011–05110111 (2008)

İlyas. K.; Sergen, T. The Turbulence Intensity Effect on the Flow Characteristics and Aerodynamics of a Circular Cylinder. Cukurova University Journal of Engineering.**36** 901–912 (2021)

Jo, Y.; Choi, S.; Zientarski, L. A.; Joo, J. J. Aerodynamic characteristics and optimization techniques of a variable camber compliant wing. 34th AIAA Applied Aerodynamics Conference, 2016, 2016.

Johari, H.; Henoch, C.; Custodio, D.; Levshin, A. Effects of leading-edge protuberances on airfoil performance. AIAA Journal. **45** (11) 2634–2642 (2007)

Jones, G.; Santer, M.; Debiasi, M.; Papadakis, G. Control of flow separation around an airfoil at low Reynolds numbers using periodic surface morphing. Journal of Fluids and Structures. **76** 536–557 (2018)

K. Jacob, D. S. A method for prediction of lift for multi-element airfoil systems with separation. AGARD Conf Proc. **143** 159–174 (1974)

Kakka, P.; Anupindi, K. Assessment of subgrid-scale models for large-eddy simulation of a planar turbulent wall-jet with heat transfer. International Journal of Heat and Mass Transfer. **153** 119593 (2020)

Kanazaki, M.; Tanaka, K.; Jeong, S.; Yamamoto, K. Multi-objective aerodynamic exploration of elements' setting for high-lift airfoil using kriging model. Journal of Aircraft. **44** (3) 858–864 (2007)

Kandula, M.; Wilcox, D. C. An examination of k-ω turbulence model for boundary layers, free shear layers and separated flows. In: 1995 Fluid Dynamics Conference, 1995, American Institute of Aeronautics and Astronautics Inc, AIAA. 1–15 (1995)

Karkoulias, D. G.; Tzoganis, E. D.; Panagiotopoulos, A. G.; Acheimastos, S. G. D.; Margaris, D. P. Computational Fluid Dynamics Study of Wing in Air Flow and Air–Solid Flow Using Three Different Meshing Techniques and Comparison with Experimental Results in Wind Tunnel. Computation. **10** (3) (2022)

Katz, J. Experimental Characterization of Separated Flows – A Review. STO - Meeting Proceedings Paper. 1–14 (2019)

Khalid, M. S. U.; Wang, J.; Akhtar, I.; Dong, H.; Liu, M.; Hemmati, A. Larger wavelengths suit hydrodynamics of carangiform swimmers. Physical Review Fluids. **6** (7) (2021)

Khan, S. A.; Bashir, M.; Baig, M. A. A.; Ali, F. A. G. M. Comparing the effect of different turbulence models on the CFD predictions of NACA0018 airfoil aerodynamics. CFD Letters. **12** (3) 1–10 (2020)

Kim, H. J.; Kwon, O. J. Numerical simulation of transitional flows using a blended IDDES and correlation-based transition model. Computers and Fluids. **222** (2021)

Kim, H.; Kim, J.; Choi, H. Flow structure modifications by leading-edge tubercles on a 3D wing. Bioinspiration and Biomimetics. **13** (6) (2018)

Kim, J.-H.; Choi, K.-S.; Lacagnina, G.; Chaitanya, P.; Joseph, P.; Hasheminejad, S. M.; Chong, T. P.; Shahab, M. F.; Omidyeganeh, M.; Pinelli, A. Aerodynamic and aeroacoustic optimization of leading-edge undulation of a NACA 65(12)-10 airfoil. AIAA Journal. **60** (4) 2342–2353 (2022)

Kim, M.; Lim, J.; Kim, S.; Jee, S.; Park, D. Assessment of the wall-adapting local eddy-viscosity model in transitional boundary layer. Computer Methods in Applied Mechanics and Engineering. **371** (2020)

Larkin, G.; Coates, G. A design analysis of vertical stabilisers for Blended Wing Body aircraft. Aerospace Science and Technology. **64** 237–252 (2017)

Lee, B. H. K. Vertical tail buffeting of fighter aircraft. Progress in Aerospace Sciences. **36** (3-4) 193-279 (2000).

Lee, C. Y.; Cant, S. Assessment of LES Subgrid-scale Models and Investigation of Hydrodynamic Behaviour for an Axisymmetrical Bluff Body Flow. Flow, Turbulence and Combustion. **98** (1) 155–176 (2017)

Lesieur, M.; Métais, O. New trends in large-eddy simulations of turbulence. Annual Review of Fluid Mechanics. **28** 45–82 (1996)

Li, L.; Hearst, R. J. The influence of freestream turbulence on the temporal pressure distribution and lift of an airfoil. Journal of Wind Engineering and Industrial Aerodynamics. **209** (October 2020) 104456 (2021)

Li, S. W.; Wang, S.; Wang, J. P.; Mi, J. C. Effect of turbulence intensity on airfoil flow: Numerical simulations and experimental measurements. Applied Mathematics and Mechanics (English Edition). **32** (8) 1029–1038 (2011)

Lin, J. C.; Andino, M. Y.; Alexander, M. G.; Whalen, E. A.; Spoor, M. A.; Tran, J. T.; Wygnanski, I. J. An Overview of Active Flow Control Enhanced Vertical Tail Technology Development. In: 54TH AIAA Aerospace Sciences Meeting, 2016, Reston, Virginia. Reston, Virginia: American Institute of Aeronautics and Astronautics. (2016).

Lin, J. C.; Dominik, C. J. Parametric investigation of a high-lift airfoil at high Reynolds numbers. Journal of Aircraft. **34** (4) 485–491 (1997)

Lin, J. C.; Robinson, S. K.; McGhee, R. J.; Valarezo, W. O. Separation control on high-lift airfoils via micro-vortex generators. Journal of Aircraft. **31** (6) 1317–1323 (1994)

Liu, Y.; Li, P.; Jiang, K. Comparative assessment of transitional turbulence models for airfoil aerodynamics in the low Reynolds number range. Journal of Wind Engineering and Industrial Aerodynamics. **217** 104726 (2021)

Lobo 1, G. J.; K2, A.; Vineeth 3, D.; Charan, M. S. Tubercles Effect on a Wing Performance for NACA 634-421 Aerofoil. International Journal of Science and Engineering Applications. **09** (04) 43–48 (2020)

Loughnane, F.; Mongin, M.; Gunasekaran, S. Effect of airfoil-preserved undulation placement on wing performance and wingtip vortex. AIAA Journal. **59** (5) 1598–1613 (2021)

Lu, S.; Liu, J.; Hekkenberg, R. Mesh properties for rans simulations of airfoil-shaped profiles: A case study of rudder hydrodynamics. Journal of Marine Science and Engineering. **9** (10) (2021)

Luo, D.; Huang, D.; Sun, X. Passive flow control of a stalled airfoil using a microcylinder. Journal of Wind Engineering and Industrial Aerodynamics. **170** 256–273 (2017)

Madhan Kumar, P.; Halder, P.; Samad, A.; Rhee, S. H. Wave energy harvesting turbine: Effect of hub-to-tip profile modification. International Journal of Fluid Machinery and Systems. **11** (1) 55–62 (2018)

Mandadzhiev, B. A.; Lynch, M. K.; Chamorro, L. P.; Wissa, A. A. An experimental study of an airfoil with a bio-inspired leading edge device at high angles of attack. Smart Materials and Structures. **26** (9) (2017)

Matyushenko, A. A.; Kotov, E. V.; Garbaruk, A. V. Calculations of flow around airfoils using two-dimensional RANS: an analysis of the reduction in accuracy. St. Petersburg Polytechnical University Journal: Physics and Mathematics. **3** (1) 15–21 (2017)

Maulik, R.; San, O.; Jacob, J. D.; Crick, C. Sub-grid scale model classification and blending through deep learning. Journal of Fluid Mechanics. **870** 784–812 (2019)

McGinley, C. B.; Anders, J. B.; Spaid, F. W. Measurements of Reynolds stress profiles on a high-lift airfoil. 16th AIAA Applied Aerodynamics Conference. **98–2620** 391–401 (1998)

McKinney, M. O.; Kuhn, R. E.; Reeder, J. P. Aerodynamics and flying qualities of jet V/STOL airplanes. SAE Technical Papers. (1964)

Menter, F. R. Two-equation eddy-viscosity turbulence models for engineering applications. AIAA Journal. **32** (8) 1598–1605 (1994)

Mereu, R.; Passoni, S.; Inzoli, F. Scale-resolving CFD modeling of a thick wind turbine airfoil with application of vortex generators: Validation and sensitivity analyses. Energy. **187** 115969 (2019)

Meunier, M.; Brunet, V. High-lift devices performance enhancement using mechanical and air-jet vortex generators. Journal of Aircraft. **45** (6) 2049–2061 (2008)

Miklosovic, D. S.; Murray, M. M.; Howle, L. E.; Fish, F. E. Leading-edge tubercles delay stall on humpback whale (Megaptera novaeangliae) flippers. Physics of Fluids. **16** (5) (2004)

Mikuž, B.; Tiselj, I. Wall-resolved Large Eddy Simulation in grid-free 5 × 5 rod bundle of MATiS-H experiment. Nuclear Engineering and Design. **298** 64–77 (2016)

Mishra, A.; De, A. Investigation of passive flow control over an airfoil using leading edge tubercles. 1–35 (2021)

Mishra, A.; Kumar, G.; De, A. Prediction of separation induced transition on thick airfoil using non-linear URANS based turbulence model. Journal of Mechanical Science and Technology. **33** (5) 2169–2180 (2019)

Moin P., K. J. Tackling turbulence with supercomputers. Scientific American. **276** (1) 62–68 (1997)

Monner, H. P.; Kintscher, M.; Lorkowski, T.; Storm, S. Design of a smart droop nose as leading-edge high lift system for transportation aircrafts. AIAA/ASME/ASCE/AHS/ASC Structures, Structural Dynamics and Materials Conference. 1–10 (2009)

Newman, A. J.; Clark, M. P.; Winstral, A.; Marks, D.; Seyfried, M. The use of similarity concepts to represent subgrid variability in land surface models: Case study in a snowmelt-dominated watershed. Journal of Hydrometeorology. **15** (5) 1717–1738 (2014)

Nguyen Van, E.; Alazard, D.; Döll, C.; Pastor, P. Co-design of aircraft vertical tail and control laws using distributed electric propulsion. IFAC-PAPERSONLINE, 2019, Elsevier B.V. **52** 514–519 (2019).

Nicolosi, F.; Ciliberti, D.; Della Vecchia, P. A Comprehensive Review of Vertical Tail Design. Aircraft Engineering and Aerospace Technology **89** (4), 547-557 (2017).

Nicoud, F.; Ducros, F. Subgrid-scale stress modelling based on the square of the velocity. Flow Measurement and Instrumentation. **62** 183–200 (1999)

O'meara, M. M.; Mueller, T. J. Laminar separation bubble characteristics on an airfoil at low Reynolds numbers. AIAA Journal. **25** (8) 1033–1041 (1987)

Obayashi, S. Multidisciplinary design optimization of aircraft wing planform based on evolutionary algorithms. International Conference on Systems, Man and Cybernetics, 1998, IEEE. **4** 3148–3153 (1998).

Olson, L. E.; McGowan, P. R.; Guest, C. J. Leading-Edge Slat Optimization for Maximum Airfoil Lift. NASA Tech Memo. (1979)

Ouchene, S.; Smaili, A.; Fellouah, H. Assessment of Turbulence Models for Unsteady Separated Flows Past an Oscillating NACA 0015 Airfoil in Deep Stall. Journal of Applied Fluid Mechanics. **16** (8) 1544–1559 (2023)

Pascau, A.; Pérez, C.; Serón, F. J. A comparison of segregated and coupled methods for the solution of the incompressible Navier-Stokes equations. Communications in Numerical Methods in Engineering. **12** (10) 617–630 (1996)

Pope, S. B. Ten questions concerning the large-eddy simulation of turbulent flows. New Journal of Physics. **6** (2004)

Pope, S. B. Ten questions concerning the large-eddy simulation of turbulent flows. New Journal of Physics. **6** (2004)

Qin, N. CFD for Better Understanding of Wind Tunnel Tests. 1st Symposium on Integrating CFD and Experiments in Aerodynamics, Glasgow, United Kingdom (2003)

Qin, N.; Vavalle, A.; Le Moigne, A.; Laban, M.; Hackett, K.; Weinerfelt, P. Aerodynamic considerations of blended wing body aircraft. Progress in Aerospace Sciences. 40 (6) 321–343 (2004)

Qin, S.; Koochesfahani, M.; Jaberi, F. Large eddy simulations of unsteady flows over a stationary airfoil. Computers and Fluids. **161** 155–170 (2018)

Rahimi, H.; Medjroubi, W.; Stoevesandt, B.; Peinke, J. 2D numerical investigation of the laminar and turbulent flow over different airfoils using openFOAM. Journal of Physics: Conference Series. **555** (1) (2014)

Rahmani, S.; Wang, Z. J. Passive flow control for the E423 airfoil utilizing an equilateral triangular trip. Physics of Fluids. **35** (12) (2023)

Raj Mohamed, M. A.; Kumar Reddy, K. S.; Sai Sri Vishnu, S. Bio-inspired optimization of leading edge slat. Aircraft Engineering and Aerospace Technology. **95** (5) 725–733 (2023)

Reynolds, W.C. The potential and limitations of direct and large eddy simulations. Whither Turbulence? Turbulence at the Crossroads. Lecture Notes. **357** 369-373 (1990)

Riella, M.; Kahraman, R.; Tabor, G. R. Fully-coupled pressure-based two-fluid solver for the solution of turbulent fluid-particle systems. Computers and Fluids. **192** (2019)

Rinoie, K.; Hata, K. Turbulent energy balances inside short bubble formed on NACA 0012 airfoil. AIAA Journal. **42** (6) 1261–1264 (2004)

Rizzetta, D. P.; Visbal, M. R.; Morgan, P. E. A high-order compact finite-difference scheme for large-eddy simulation of active flow control. Progress in Aerospace Sciences. **44** (6) 397–426 (2008)

Rizzi, A.; Luckring, J. M. Historical development and use of CFD for separated flow simulations relevant to military aircraft. Aerospace Science and Technology. 117 106940 (2021)

Rogowski, K.; Królak, G.; Bangga, G. Numerical study on the aerodynamic characteristics of the naca 0018 airfoil at low reynolds number for darrieus wind turbines using the transition sst model. Processes. **9** (3) 1–26 (2021)

Rokhsaz, K. A brief survey of wing tip devices for drag reduction. SAE Technical Papers. **102** 1901–1910 (1993)

Rumsey, C. L.; Vatsa, V. N. Comparison of the predictive capabilities of several turbulence models. Journal of Aircraft. **32** (3) 510–514 (1995)

Sadikin, A.; Yunus, N. A. M.; Hamid, S. A. A.; Ismail, A. E.; Salleh, S.; Ahmad, S.; Rahman, M. N. A.; Mahzan, S.; Ayop, S. S. A Comparative Study of Turbulence Models on Aerodynamics Characteristics of a NACA0012 Airfoil. International Journal of Integrated Engineering. **10** (1) 134–137 (2018)

Sadraey, M. Commercial Airplane Design. Commercial Airplane Design. 274–352 (2012).

Salimipour, E. A modification of the k-k L -ω turbulence model for simulation of short and long separation bubbles. Computers and Fluids. **181** 67–76 (2019)

Sarghini, F.; Felice, G.; Santini, S. Neural networks based subgrid scale modeling in large eddy simulations. Computers and Fluids. **32** (1) 97–108 (2003)

Sarlak, H. Large Eddy Simulation of an SD7003 Airfoil: Effects of Reynolds number and Subgrid-scale modeling. Journal of Physics: Conference Series. **854** (1) (2017)

Sathyabhama, A.; Sreejith, B. K. Numerical Investigation on the Effect of Leading-Edge Tubercles on the Laminar Separation Bubble. Journal of Applied Fluid Mechanics. **15** (3) 767–780 (2022)

Savory, E.; Toy, N.; Tahouri, B.; Dalley, S. Flow regimes in the cove regions between a slat and wing and between a wing and flap of a multielement airfoil. Experimental Thermal and Fluid Science. **5** (3) 307–316 (1992)

Sevant, N. E.; Bloor, M. I. G.; Wilson, M. J. A hierarchical approach to optimal aerodynamic design. In: 7TH AIAA/USAF/NASA/ISSMO Symposium On Multidisciplinary Analysis and Optimization, 1998, American Institute of Aeronautics and Astronautics Inc, AIAA, 1998. 1099–1107 (1998).

Shah, H.; Mathew, S.; Lim, C. M. Numerical simulation of flow over an airfoil for small wind turbines using the γ-Reθ model. International Journal of Energy and Environmental Engineering. **6** (4) 419–429 (2015)

Sheta, E. F.; Huttsell, L. J. Characteristics of F/A-18 vertical tail buffeting. Journal of Fluids and Structures. **17** (3) 461–477 (2003)

Shi, X.; Xu, S.; Ding, L.; Huang, D. Passive flow control of a stalled airfoil using an oscillating micro-cylinder. Computers and Fluids. **178** 152–165 (2019)

Shih T-H, Liou W.W, Shabbir A, Yang Z, Z. J. A New Kt Eddy Viscosity Model for High: Reynolds Number Turbulent Flows. Computers and Fluids. **24** (3) 227–238 (1995)

Shyam, V.; Ameri, A.; Poinsatte, P.; Thurman, D.; Wroblewski, A.; Snyder, C. Application of pinniped vibrissae to aeropropulsion. Proceedings of The ASME Turbo Expo. **2** (2015)

Siddharth, S.; Craig, C.; Hanifa, S. Computational Fluid Dynamics (CFD) Mesh Independency Study of a Straight Blade Horizontal Axis Tidal Turbine. 1–11 (2016)

Skillen, A.; Revell, A.; Favier, J.; Pinelli, A.; Piomelli, U. Investigation of wing stall delay effect due to an undulating leading edge: An les study. International symposium on turbulence and shear flow phenomena, TSFP. **3** (2013).

Skillen, A.; Revell, A.; Pinelli, A.; Piomelli, U.; Favier, J. Flow over a wing with leading-edge undulations. AIAA Journal. **53** (2) 464–472 (2015)

Smagorinsky, J. General Circulation Experiments with the Primitive Equations: I. The Basic Experiment. Monthly Weather Review. **91** 99-164 (1963).

Smith, H. College of Aeronautics Blended Wing Body Development Programme. Congress of International Council of Aeronautical Sciences. 114.1-114.10 (2000)

Spalart, P. R. Trends in turbulence treatments. FLUIDS 2000 Conference and Exhibit. 1–13 (2000)

Spalart, P. R.; Allmaras, S. R. One-equation turbulence model for aerodynamic flows. Recherche aerospatiale. (1) 5–21 (1994)

Sreejith, B. K.; Sathyabhama, A. Numerical study on effect of boundary layer trips on aerodynamic performance of E216 airfoil. Engineering Science and Technology, an International Journal. **21** (1) 77–88 (2018)

Srinivasan, G. R.; Ekaterinaris, J. A.; McCroskey, W. J. Evaluation of turbulence models for unsteady flows of an oscillating airfoil. Computers and Fluids. **24** (7) 833–861 (1995)

Steiner, J.; Viré, A.; Benetti, F.; Timmer, N.; Dwight, R. Parametric slat design study for thick-base airfoils at high Reynolds numbers. Wind Energy Science. **5** (3) 1075–1095 (2020)

Su, L.; Qiang, X.; Zheng, T.; Teng, J. Effect of undulating blades on highly loaded compressor cascade performance. Proceedings of the Institution of Mechanical Engineers, Part A: Journal of Power and Energy. **235** (1) 17–28 (2021)

Sudhakar, S.; Karthikeyan, N.; Suriyanarayanan, P. Experimental studies on the effect of leading-edge tubercles on laminar separation bubble. AIAA Journal. **57** (12) 5197–5207 (2019)

Sudhakar, S.; Venkatakrishnan, L.; Ramesh, O. N. The influence of leading-edge tubercles on airfoil performance at low reynolds numbers. AIAA SCITECH 2020 FORUM. **1** (2020)

TailSurf, P. Rear End Aerodynamic and Aeroelastic Studies. <https://cordis.europa.eu/project/id/864290>.

Tavakoli Dakhrabadi, M.; Seif, M. S. Influence of main and outer wings on aerodynamic characteristics of compound wing-in-ground effect. Aerospace Science and Technology. **55** 177–188 (2016)

Traub, L. W.; Kaula, M. P. Effect of leading-edge slats at low Reynolds numbers. Aerospace. **3** (4) (2016)

Van Dam, C. P. The aerodynamic design of multi-element high-lift systems for transport airplanes. Progress in Aerospace Sciences. **38** (2) 101–144 (2002)

Van Nierop, E. A.; Alben, S.; Brenner, M. P. How bumps on whale flippers delay stall: An aerodynamic model. Physical Review Letters. **100** (5) 1–4 (2008)

Vatsa, V. N.; Lin, J. C.; Melton, L. P.; Lockard, D. P.; Ferris, R. Computational investigation of conventional and active-flow-control-enabled high-lift configurations. Journal of Aircraft. **58** (5) 1137–1153 (2021)

Velkova, C.; Todorov, M. Study of the Influence of a Gap Between the Wing and Slotted Flap on the Aerodynamic Characteristics of Ultra-Light Aircraft Wing Airfoil. Review of the Air Force Academy. **13** (3) 39–44 (2015)

Volikas, A.; Nikas, K. S. Turbulence modeling investigation of airfoil designed for wind turbine applications. AIP Conference Proceedings. **2123** (2019)

Walters, D. K.; Cokljat, D. A three-equation eddy-viscosity model for Reynolds-averaged navier-stokes simulations of transitional flow. Journal of Fluids Engineering, Transactions of the ASME. **130** (12) 1214011–12140114 (2008)

Weber, C.; Ducros, F. Large Eddy and Reynolds-Averaged Navier-Stokes Simulations of Turbulent Flow over an Airfoil. International Journal of Computational Fluid Dynamics. **13** (4) 327–355 (2000)

Wei, Z.; New, T. H.; Cui, Y. D. Aerodynamic performance and surface flow structures of leading-edge tubercled tapered swept-back wings. AIAA Journal. **56** (1) 423–431 (2018)

Weickert, M.; Teike, G.; Schmidt, O.; Sommerfeld, M. Investigation of the LES WALE turbulence model within the lattice Boltzmann framework. Computers and Mathematics with Applications. **59** (7) 2200–2214 (2010)

Whitlock Mentor, M. E.; Jones, K. M. Analysis of a High-Lift Multi-Element Airfoil Using a Navier-Stokes Code 1995 LARSS Program Participant. 807-816 (1995)

Wokoeck, R.; Grote, A.; Krimmelbein, N.; Ortmanns, J.; Radespiel, R.; Krumbein, A. RANS simulation and experiments on the stall behaviour of a tailplane airfoil. Notes on Numerical Fluid Mechanics and Multidisciplinary Design. **92** (2006)

Wu, C.; Li, H.; Zhang, Y.; Chen, H. Prediction of Airfoil Stall Based on a Modified {formula-present} Turbulence Model. Mathematics. **10** (2) (2022)

Xiao, M.; Zhang, Y.; Zhou, F. Numerical investigation of the unsteady flow past an iced multi-element airfoil. AIAA Journal. **58** (9) 3848–3862 (2020)

Yang, X. I. A.; Griffin, K. P. Grid-point and time-step requirements for direct numerical simulation and large-eddy simulation. Physics of Fluids. **33** (1) (2021)

Yossri, W.; Ben Ayed, S.; Abdelkefi, A. Airfoil type and blade size effects on the aerodynamic performance of small-scale wind turbines: Computational fluid dynamics investigation. Energy. **229** 120739 (2021)

Zaki, A.; Abdelrahman, M. A.; Ayad, S. S.; Abdellatif, O. E. Effects of leading edge slat on the aerodynamic performance of low Reynolds number horizontal axis wind turbine. Energy. **239** (2022)

Zhang, H.; Yu, H.; Zhang, A.; Zheng, J. Large eddy simulation of dynamic stall over an airfoil and its control with plasma actuator. AIP Advances. **13** (2) (2023)

Zhang, M. M.; Wang, G. F.; Xu, J. Z. Aerodynamic control of low-Reynolds-number airfoil with leading-edge protuberances. AIAA Journal. **51** (8) 1960–1971 (2013)

Zhang, Y.; Zhou, Z.; Wang, K.; Li, X. Aerodynamic characteristics of different airfoils under varied turbulence intensities at low Reynolds numbers. Applied Sciences (Switzerland). **10** (5) (2020)

Zhi, H.; Zhu, Z.; Lu, Y.; Deng, S.; Xiao, T. Aerodynamic performance enhancement of co-flow jet airfoil with simple high-lift device. Chinese Journal of Aeronautics. (2021)

Zhiyin, Y. Large-eddy simulation: Past, present and the future. Chinese Journal of Aeronautics. **28** (1) 11–24 (2015)

Zhou, L., Gao, Z., & Du, Y. Flow-dependent DDES/γ– Re_ θt coupling model for the simulation of separated transitional flow. Aerospace Science and Technology. **87** 389-403 (2019).

Zhu, J.; Rodi, W. A low dispersion and bounded convection scheme. Computer Methods in Applied Mechanics and Engineering. **92** (1) 87–96 (1991)